Gate-tunable kinetic inductances for superconducting circuits

Splitthoff, L.J.

DOI
10.4233/uuid:2ee2a492-6588-46db-aa6a-7056fd37fd24

Publication date
2024

Document Version
Final published version

Citation (APA)
Splitthoff, L. J. (2024). *Gate-tunable kinetic inductances for superconducting circuits*. [Dissertation (TU Delft), Delft University of Technology]. https://doi.org/10.4233/uuid:2ee2a492-6588-46db-aa6a-7056fd37fd24

GATE-TUNABLE KINETIC INDUCTANCES FOR SUPERCONDUCTING CIRCUITS

Dissertation

for the purpose of obtaining the degree of doctor
at Delft University of Technology
by the authority of the Rector Magnificus, prof. dr. ir. T.H.J.J. van der Hagen,
chair of the Board for Doctorates
to be defended publicly on
Wednesday, 24. April 2024 at 12:30 o'clock

by

Lukas Johannes SPLITTHOFF

Master of Science in Physics,
University of Münster, Germany,
born in Wesel, Germany

This dissertation has been approved by the promotors.

Composition of the doctoral committee:

Rector Magnificus	chairperson
Promotors:	
Prof. dr. ir. L.P. Kouwenhoven	Delft University of Technology, promotor
Dr. C.K. Andersen	Delft University of Technology, copromotor
Independent members:	
Prof. dr. S. Gasparinetti	Chalmers University of Technology
Prof. dr. A. Kamal	University of Massachusetts Lowell
Prof. dr. N. Roch	University of Grenoble Alpes
Prof. dr. G. Steele	Delft University of Technology
Reserve member:	
Prof. dr. A.F. Otte	Delft University of Technology

Keywords: Gate-tunable superconducting circuits, Resonator-based parametric amplifiers, Topological metamaterials, Proximitized nanowires

Printed by: Gildeprint, Enschede, 2024

Cover: A SSH chain by Melanie Rieß, Esslingen am Neckar, 2023

ISBN 978-94-6384-540-3

CONTENTS

SUMMARY

Superconducting circuits in cryogenic environments form an excellent material platform for the realization and study of quantum systems. In this thesis, we continue the exploration of novel types of circuit elements which expand the circuit quantum electrodynamics toolbox to enable exotic, and potentially better circuit implementations. To this end, we combine the study of condensed matter systems and circuit quantum electrodynamics in what is called hybrid cQED experiments to arrive at the implementation of gate-tunable kinetic inductances for superconducting circuits. This discovery shed new light on the physics of gate-tunable kinetic inductances and enabled the observation of emergent phenomena in gate-tunable metamaterials, in particular the phase transition in a bosonic Su-Schrieffer-Heeger chain. Moreover, as gate-tunable kinetic inductances became available we realized tunable resonators and parametric amplifiers for enhanced control and readout of superconducting circuits.

1

INTRODUCTION: TUNABLE SUPERCONDUCTING CIRCUITS

Lukas Johannes Splitthoff

Superconducting circuits in cryogenic environments form an excellent material platform for the realization and study of quantum systems. As such, they are used at the frontier of the development of universal quantum computers and quantum simulators, but are as well suited for quantum sensing applications. Superconducting circuit also hold great promise for dissipation-less classical computing.
Even after half a century of circuit developments, we continue the exploration of novel types of circuit elements which expand the circuit quantum electrodynamics toolbox to enable exotic, and potentially better circuit implementations. In this thesis, we summarize the investigation of gate-tunable and magnetic field compatible superconducting circuits for the use in condensed matter experiments and densely packed, crosstalk-free quantum processors.

In the realm of superconducting circuits, the ability to precisely manipulate their properties, often referred to as "tunability," is a hallmark of their versatility and adaptability for various applications. This tunability can manifest itself through two distinct paradigms: flux control and charge control of either microscopic or macroscopic variables. Flux control involves manipulating the magnetic flux threading a superconducting loop or the spin polarization in a magnetic field, while charge control focuses on tuning the number of charge carriers in a system.

Historically, and since its discovery, the intrinsic properties of superconductors have been tested, and hence also controlled, by means of magnetic fields, temperature, or current. The Ginzburg-Landau theory describes the properties of the superconducting state close to the superconducting phase transition, quantified as superconducting gap Δ, as it is suppressed by external parameters at the critical temperature T_c, the critical magnetic field B_c, the critical current I_c, or a combination of them.

Consequently, circuits made out of superconductors can be globally controlled by these external parameters magnetic field, temperature or current. As a result of the circuit geometry, also magnetic flux can set the current running through a superconducting loop, and offset charge can affect the current across a superconducting island.

These control mechanisms represent the macroscopic tuning of superconducting circuits.

However, the intriguing nature of superconductors goes beyond these conventional macroscopic tuning methods. Imagine we could not just globally control the flux and charge, but we could also achieve localized and in-situ modifications of the material properties of the circuit components. More concretely, imagine a piece of a superconductor which we could locally deplete of charge carriers or those charge carriers we retard in their motion.

This level of fine-grained control would allow for the creation of tailored circuits with unprecedented flexibility and performance. The ability to tune the superconducting properties at the local level without crosstalk would open the door to a myriad of new possibilities and functionalities in the field of quantum computing, quantum electronics, and condensed matter physics.

This thesis is dedicated to exploring the fascinating world of gate-tunable kinetic inductances. While we are not the first research group dwelling on the local tunability of superconductors, we focus on a specific implementations using proximitized semiconducting nanowires and gate-tunable Josephson junctions. In the following sections, we will delve into the rich landscape of tunable circuit elements, highlighting six distinct mechanisms that enable this precise control over superconducting circuits: (1,2) Magnetic flux and offset charge control, (3,4) Gate-controlled supercurrents and current-biased conductors, (5,6) Gate-tunable Josephson junctions and kinetic inductances.

1.1. MAGNETIC FLUX AND OFFSET CHARGE CONTROL

Offset-charge-sensitive, flux-tunable superconducting qubits have been prominently employed as Cooper Pair Box or transmon qubits [1]. Both, the manipulation of the offset charge n_g on the charge island and the external flux ϕ_{ext} threaded through the superconducting loop allow for the control of the energy levels of these qubits, which are described by the following Hamiltonian

$$H = 4E_C(n - n_g)^2 - E_J \cos(\phi + \phi_{ext}) \tag{1.1}$$

with the charging energy E_C, Josephson energy E_J, and the charge n and flux ϕ variable. As a result the transition frequencies of the qubit varies versus the control parameters, see Fig. 1.1. The idea can also be applied to resonators and parametric amplifiers. Offset-charge-sensitive circuits have evaded modern implementations since any residual charge dispersion leads to unwanted qubit dephasing due to the presence of charge noise; hence the development of the transmon qubit.

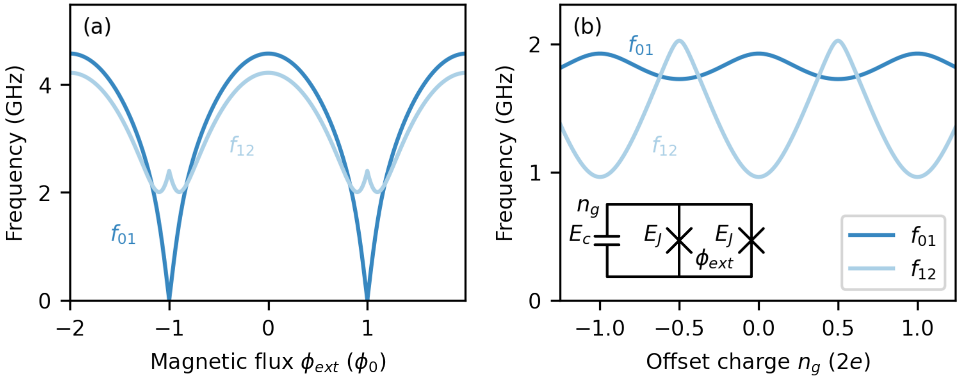

Figure 1.1.: Macroscopic circuit variables. (a) Transition frequencies of an offset-charge-sensitive, flux-tunable transmon qubit between the first three states versus external magnetic flux for $E_C = 0.3\,\mathrm{GHz}$, $E_J = 5\,\mathrm{GHz}$, and $n_g = 0.3\,\mathrm{GHz}$. (b) Transition frequencies versus offset charge for $E_C = 0.3\,\mathrm{GHz}$, $E_J = 1\,\mathrm{GHz}$, and $\phi_{ext} = 0$.

Thanks to the generally two orders of magnitude lower spectral amplitude of flux noise compared to charge noise [2], flux control has manifested as the main tuning knob for superconducting qubits, resonators and parametric amplifiers. It can be realized using superconducting loops, dc-SQUIDs or rf-SQUIDs placed at the voltage node of the circuit and manipulated by global magnetic fields or local flux bias lines. The flux control suffers from crosstalk with other flux-sensitive structures as well as heating introduced by the injected current in the coil or flux lines.

1.2. GATE-CONTROLLED SUPERCURRENTS AND CURRENT-BIASED CONDUCTORS

The potential energy of a superconducting circuit can be set by the material properties of the conductors in-situ, to which we refer to as microscopic control. This in turn sets the energy stored in an inductor E_L or a Josephson junction E_J. Well known is the case of a current-biased conductor: By injecting a current into a superconducting conductor, one increases its inductance due to the suppression of the superconducting gap. The inductive response of an inductor to a dc or rf bias current I_b can be approximated by

$$L_{kin} = L_0\left[1+\left(\frac{I_b}{I_*}\right)^2\right] \tag{1.2}$$

with linear inductance L_0 and relative current I_* which is close to the critical current I_c but depends on the exact material parameters. This approach yields frequency tunable resonators, see Fig. 1.2b, which can be used in parametric amplifiers [3]. An alternative approach constitutes the gate-controlled supercurrent: Researchers discovered that the critical current of a thin superconducting nanowires can be gate-controlled by a side gate in close proximity [4]. The sudden drop in critical current at a critical gate voltage V_c, which might arise from a change in the charge carrier density or by the injection of single electrons, so-called quasi-particles, translates into an increase in the conductor's inductance. This in turn can be used as switches or in frequency tunable resonators, see Fig. 1.2a.

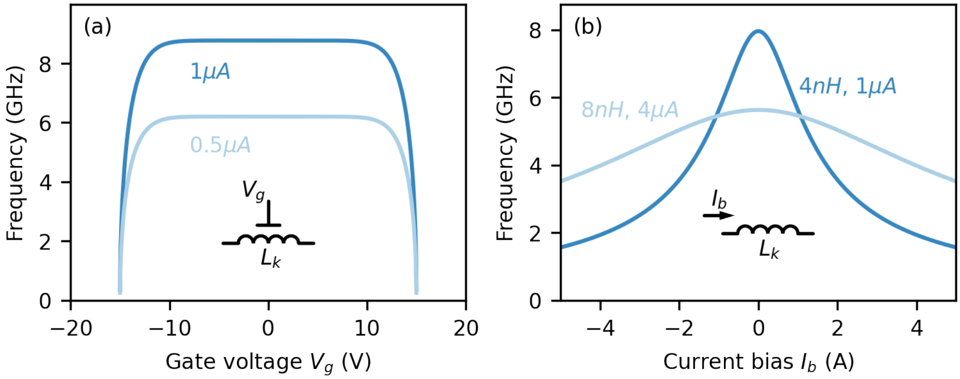

Figure 1.2.: Suppression of superconducting state. (a) Gate-controlled supercurrent with critical voltage $V_c = 15\,\mathrm{V}$ for two different critical currents I_c in LC resonator with capacitance $C = 1\,\mathrm{pF}$. (b) Current-biased conductors with different linear inductance L_0 and critical current I_* in LC resonator with capacitance $C = 0.1\,\mathrm{pF}$.

1.3. GATE-TUNABLE JOSEPHSON JUNCTIONS AND KINETIC INDUCTANCES

A new source of tunability became available with the development of proximitized semiconducting nanowires as the ones shown in Fig. 1.4. While these nanowires were originally exploited in the pursuit of realizing Majorana qubits, researchers soon build nanowire Josephson junctions from them. These SNS junctions host Andreev bound states which mediate the supercurrent across the junction. From the microscopic properties of these junctions (spin-orbit interaction, the g-factor, the chemical potential and the superconducting gap) the chemical potential, which is related to the charge carrier density, dominates the inductive response of the hybrid structure. The inductance of a nanowire Josephson junction, used in gatemon qubits, switches, and parametric amplifiers [5–7], can be understood from a single, normal conducting channel with increased conductance above a pinch-off voltage, see Fig. 1.3b, hence the frequency increase. In a real junction, accidental quantum dots lead to a nonmonotonic inductive response versus gate voltage.

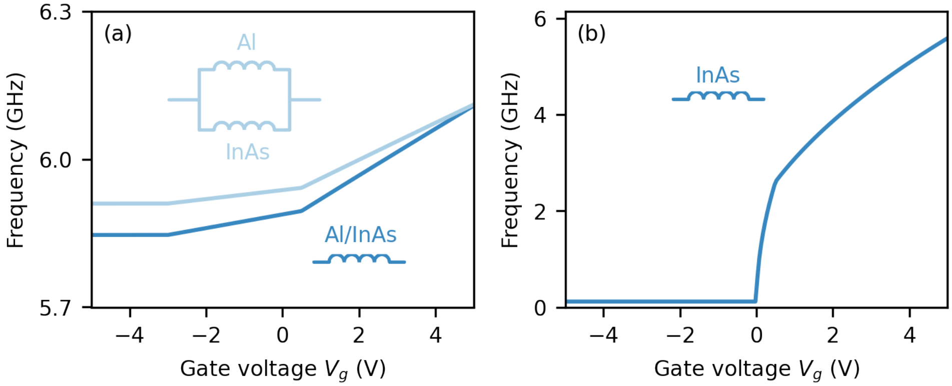

Figure 1.3.: Gate-tunable charge carrier density n including inversion, depletion and accumulation regime. (a) Single ($n_s \sim 6\times10^{28}$, $\mu_{Al} = 1.2\times10^{-3}\,\mathrm{cm}^2/\mathrm{Vs}$, $\Delta_{Al} = 300\,\mu\mathrm{eV}$, $r = 15\,\mathrm{nm}$) and two channel model ($n_{Al} = 6\times10^{28}$, $\mu_{Al} = 1.2\times10^{-3}\,\mathrm{cm}^2/\mathrm{Vs}$, $\Delta_{Al} = 300\,\mu\mathrm{eV}$, $r_{Al} = 6x110\,\mathrm{nm}^2$, $n_{InAs} \sim 4\times10^{24}$, $r_{InAs} = 55\,\mathrm{nm}$) for a $3\,\mu\mathrm{m}$ long, continuously proximitized nanowire as in Fig. 1.4a. (b) Single partially proximitized, 100 nm long InAs segment ($n_s \sim 1\times10^{22}$, $r = 55\,\mathrm{nm}$) as in Fig. 1.4b.

In this thesis we realized that also a Josephson junction-free proximitized nanowire can be gate-controlled [8]. It can either be understood as single hybrid kinetic inductance as discussed in Chapter III or as two parallel inductances arising from the kinetic inductance of Al and the normal inductance of InAs. Both models yield the same qualitative behaviour and cannot be distinguished from a resonator measurement. In all models, we consider inversion, depletion and accumulation regimes, which we approximate by a linear dependence in charge carrier density. Further modelling of the microwave response of proximitized nanostructures starting from first-principles is requested.

Cutback and outline

My four-year long doctoral research began in September 2019 in the cQED team of the Kouwenhoven lab at QuTech in the pursuit of realizing topologically protected qubits utilizing Majorana zero modes in proximitized semiconductors.

The original idea to observe the predicted topological phase transition in proximitized nanowires, see Fig. 1.4a, following the Lutchyn and Oreg model [9, 10], using superconducting resonators to precisely measure changes in the inductance and resistance upon changing the external magnetic field and chemical potential by adjusting the gate voltage never unfolded. Especially the magnetic field dependence remained poorly understood even after many consecutive cooldowns and sample inspections. Eventually, the observation of the topological phase transition remained elusive and forced us to changed the scope of our research from a fundamental physics question to an application, leading to the implementation of gate-tunable inductances in superconducting resonators [8]. Together with Christian K. Andersen, we then leveraged the gate-tunability and magnetic field compatibility of the previously studied hybrid material system to develop a gate-tunable, resonator-based parametric amplifier [11].

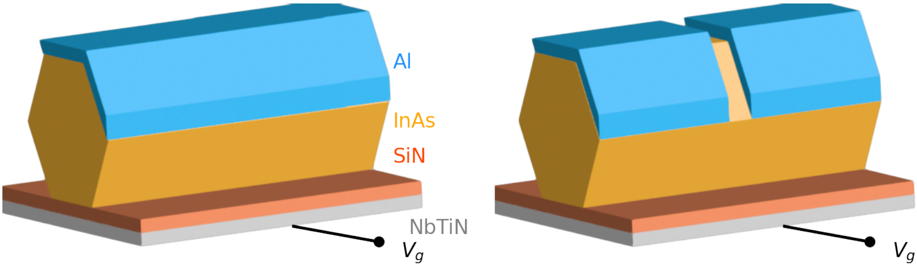

Figure 1.4.: Sketch of proximitized nanowires. (a) A 10 μm long and 100 nm wide, hexagonal Indium arsenide (InAs, III-V material) nanowire with continuous, 6 nm thick 2-facet Aluminum (Al) coverage. The charge carrier density in the semiconductor is controlled by a bottom gate voltage V_g applied to an Niobium-titanium-nitride (NbTiN) sheet separated by a Silicon nitride (SiN) gate dielectric. (b) An approximately 100 nm Aluminum segment has been etched out of the configuration shown in (a) to create a nanowire Josephson junction.

The better we understood the material system, the more we realized the potential benefits of gate-tunable superconducting circuits for quantum computing. Concretely, gate-tunable inductances offer local and nearly crosstalk-free control over superconducting circuits potentially enabling dense qubit packaging. However, open questions about the stability and introduced noise remain and need to be addressed in future research.

To demonstrate the concept of gate control further and to tie back in with the original research question of my PhD aiming to probe topological properties of extended states using cQED techniques, we engineered a gate-tunable resonator-based topological metamaterial based on nanowire Josephson junctions, shown in Fig. 1.4b, hosting different insulator states and probed the phase transition between them.

The main results of my doctoral studies are presented in the Chapters III, IV and V of the thesis. The content is supplemented by additional information about parametric amplifiers, presented in Chapter II, and about the operation of dilution refrigerators, see Method Chapter A. As overview:

- **Chapter II:** Implementation and characterization of superconducting parametric amplifiers
- **Chapter III:** Gate-tunable kinetic inductance in proximitized nanowires
- **Chapter IV:** Gate-tunable kinetic inductance parametric amplifier
- **Chapter V:** Gate-tunable phase transition in a bosonic Su-Schrieffer-Heeger chain

All code and data underlying this thesis document plus additional information is made available online [12].

2

IMPLEMENTATION AND CHARACTERIZATION OF SUPERCONDUCTING PARAMETRIC AMPLIFIERS

Lukas Johannes Splitthoff, Christian Kraglund Andersen

Amplifiers are electronic devices with a power gain greater than one and are typically employed to adjust the power level at the input of subsequent devices, such as other following amplifiers or detectors. Amplifiers can be characterized by various figures of merit. Optimal amplifiers feature high gain, wide bandwidth and large dynamic range at minimal added noise. Other properties such as the efficiency, the linearity, the slew rate or the stability are not typically specified for most amplifiers. While most of those properties are easily met in semiconductor amplifiers, such as High Electron Mobility Transistor (HEMT) amplifiers, these variants dissipate between 3 µW *and* 10 mW *of power [13, 14], which exceeds the available cooling power of about* 10 µW *at the* 20 mK *stage in dilution refrigerators, and they operate with an added noise far above the quantum limit.*

In the realm of superconducting circuits, superconducting parametric amplifiers became a key component at the first stage of the readout chain to boost the signal to noise ratio of weak signals, typically at microwave frequencies, because of negligible dissipated power and quantum-limited noise performance. Eventually, these amplifiers enabled single shot readout and fast feedback operation. In other use cases, they generate squeezed states of radiation.

In this chapter, we review the concept of parametric amplification and theoretically discuss the performance characteristics of gain, bandwidth, dynamic range and noise performance. Then, we describe the implementation of superconducting parametric

amplifiers based on Josephson junctions and on kinetic inductance materials in lumped element resonators and coplanar waveguide resonators. Finally, we present different characterisation methods and their pitfalls.

2.1. SUPERCONDUCTING PARAMETRIC AMPLIFIERS

The realization of superconducting parametric amplifiers operating at microwave frequencies requires three components: a nonlinear medium to enable wave mixing, a drive to supply power and a microwave circuit to guide the radiation. The nonlinear medium can be a Josephson junction or a kinetic inductance material. As drive serves an RF, or RF and DC tone. Suitable microwave circuits are resonators or waveguides; for simplicity we only focus on the former.

Using the three key components, different implementations of parametric amplifiers have been developed, which we summarize in the following paragraph and in Tab. 2.1: A good introduction to the field of parametric amplifiers is provided in Ref. [15]. The first observation of parametric amplification in superconducting circuits goes back to 1989 [16]. At first, but also down to the present day, resonator based-parametric amplifiers have been realized with increasing complexity to simultaneously meet several design objectives such as a large gain-bandwidth product and a large saturation power. While some first implementations were based on single junctions, researchers later explored flux biased SQUIDs made from SIS Josephson junctions [17–21], and current biased conductors in kinetic inductance materials [22]. A particularly well engineered variant, the SNAIL amplifier, gained some reputation for its robust and useful design [23, 24]. Later, gate-tunable parametric amplifiers became available [11, 25–27]. Yet other work focused on the realization of magnetic field compatible amplifiers [28–30]. In parallel to the research exploring the optimal non-linear medium, other researchers studied the coupling of the parametric amplifier to its environment [31] and the realization of broadband amplification windows [32–35]. As an opportunity for broadband amplification, travelling wave parametric amplifiers (TWPA) [36, 37] have been established, which often do not reach the quantum limit due to the complex and rich mode structure. Going beyond linear amplification, Josephson bifurcation amplifiers exist [38]. Resonator based parametric amplifiers are also a beautiful example for open quantum systems, which follow a non-Hermitian dynamic because of their driven and dissipative nature [39].

In this method chapter we will review the theory behind nonlinear resonators and how the wave-mixing comes into play and we will comment on the main design objectives for parametric amplifiers. Furthermore, we will present two implementations of Josephson parametric amplifiers and discuss how to characterize them in a test setup. While we are certainly not the first authors discussing the aforementioned aspects, we aim to prepare a self-contained document, which serves as a reference for young quantum engineers starting in the field of the parametric amplifier development. Inspiration for this section comes mainly from [40, 41].

Paper	Year	Co.	Des.	WM	f_r	GBW	P_{sat}	NLE	T	MF
					GHz	MHz	dBm			T
Castellanos [17]	2007	C	DE	4	7.8	3	-	SQUID A	F	-
Castellanos [19]	2008	C	DE	4	7	11	-	SQUID A	F	-
Yamamoto [18]	2008	C	CPW	3	11	63	-140	SQUID	F	-
Mutus [42]	2013	I	LE	3,4	7	-	-120	SQUID	F	-
Zhong [20]	2013	C	CPW	3	5.6	15	-136	SQUID A	F	-
Zhou [21]	2014	C	LE	3	6.0	60	-123	SQUID A	F	-
Mutus [31]	2014	K	LE	3	6.6	3900	-110	SQUID	F	-
Planat [43]	2019	D	DE	4	6.8	300	-117	SQUID A	F	-
Sivak [23]	2019	C	DE	3	7.2	250	-102	SNAILs	F	-
Sivak [44]	2020	C,I	DE	3	12	110	-108	SNAILs	F	-
Winkel [45]	2020	I	DE	4	8.0	150	-118	SQUID A	F	-
Grebel [32]	2021	ST	LE	3,4	5.3	3000	-116	SQUID	F	-
Lu [33]	2022	IM	LE	3	6.6	2500	-114	SQUID	F	-
White [34]	2022	K	LE	3	7	3000	-95	rf-SQUID A	F	-
Sarkar [26]	2022	D	LE	4	5.3	158	-130	graphene-JJ	G	-
Butseraen [25]	2022	C	CPW	4	6.2	33	-123	graphene-JJ	G	-
Ezenkova [24]	2022	ST	LE	3	6.4	2100	-100	SNAILs	F	-
Parker [22]	2022	BM	LE	3	6.4	53	-	NbTiN-KI	I	-
Qing [35]	2023	K	LE	3	7.1	3900	-110	SQUID	F	-
Xu [29]	2023	C	LE	4	7.5	59	-	NbN-KI	B	0.5
Khalifa [28]	2023	C	DE	4	4.6	-	-	NbTiN-KI	B	2
Phan [46]	2023	C	CPW	4	6.0	40	-125	2DEG-JJ	G	15m
Splitthoff [11]	2023	C	CPW	4	6.1	30	-120	NW-KI	G	0.5
Vaartjes [47]	2023	BM	LE	3	6.2	17	-86	NbTiN-KI	I	2
Frasca [48]	2023	ST	DE	3	5.8	21	-86	NbN-KI	I	6

Table 2.1.: Parameter Overview of some resonator parametric amplifiers: Coupling (Co): (I) Inductive/galvanic, (K) Klopfenstein, (D) Direct, (C) Capacitive, (ST) Step transformer, (IM) 'fishbone' impedance matching, (BM) Bragg mirror; Design (Des): (LE) Lumped element, (DE) Distributed element, (CPW) Coplanar-Waveguide; Wavemixing (WM), Highest amplifier frequency f_r, Gain-Bandwidth product GBW, Input saturation power P_{sat} for about 20 dB weak signal gain, and nonlinear element NLE (single SQUIDS, SQUID arrays (SQUID A), asymmetric SQUIDS as SNAILS, rf-SQUID arrays, graphene based Josephson junctions, InAs 2DEG Josephson junctions, InAs nanowire kinetic inductances, and kinetic inductances from NbN and NbTiN); frequency tunability (T) achieved by flux (F), electrostatic gate (G), magnetic field (B) or current (I); Tested magnetic field compatibility up to the specified in-plane magnetic field.

2.1.1. NOMENCLATURE

There exist different names for two different amplification processes regardless of the mixing scheme being three-wave mixing $f_p \approx 2 f_s$ or four-wave mixing $f_p \approx f_s$ [49]. They are summarized in Tab. 2.2.

term 1	term 2	minimal added noise
phase-sensitive	degenerate $f_s = f_i$	0 (in one quadrature)
phase-preserving/insensitive	non-degenerate $f_s \neq f_i$	$\frac{1}{2}$

Table 2.2.: Nomenclature in the context of single mode amplification

2.1.2. NONLINEAR RESONATOR

We begin the discussion about parametric amplifiers on a conceptual level without restricting the problem to a specific geometric implementation by studying a nonlinear resonator, whose nonlinearity arises from the 3rd order component of the electric susceptibility χ of the nonlinear medium and hence enables four-wave mixing. This type of resonator is often called Kerr resonator. However, a nonlinear resonator could also contain any other order of nonlinearity, which then might allow for three-wave mixing for example.

The Hamiltonian of this nonlinear resonator with 3rd order nonlinearity, which we call Kerr resonator in the following, with eigenfrequency ω_0 and Kerr coefficient K is given by

$$H_{JPA} = \hbar\omega_0 a^\dagger a + \frac{\hbar K}{2}(a^\dagger)^2(a)^2 \tag{2.1}$$

where $a^\dagger, a$ are the raising and lowering operators describing the intra-cavity field. Note that this Hamiltonian is in certain limits equivalent to the transmon qubit Hamiltonian. However, the Kerr coefficient differs between parametric amplifiers and transmon qubits. For the resonator-based parametric amplifier $|K|$ lies between 10 Hz and 100 kHz and between 150 MHz and 400 MHz for transmon qubits [50]. For resonator-based parametric amplifier the Kerr coefficient is negative, while in some TWPA implementations the Kerr coefficient can also be positive.

The dynamics or time-evolution of the Kerr resonator can be obtained when inserting the Hamiltonian in Eq. 2.1 into the Heisenberg-Langevin equation $\partial\rho/\partial t = -i/\hbar[H,\rho]$ and using the identity $[a, a^\dagger] = 1$. Then, the intra-cavity field, a, of the resonator is given by the equation of motion

$$\frac{\partial a}{\partial t} = -i\omega_0 a - iK a^\dagger (a)^2 - \frac{\kappa}{2} a + \sqrt{\kappa} a_{in} \tag{2.2}$$

a Lindblad equation, where the first two terms on the right hand side describe the unitary evolution of the uncoupled quantum system, while the remaining terms, which were added by hand, account for the driven, dissipative, non-unitary evolution due to the coupling to the environment. The coefficient κ quantifies the coupling strength to the transmission line with input and output field $a_{in/out}$. In this presentation of the input and output fields we neglect the presence of other loss channels, which is justified if the coupling strength to the transmission line is much larger than the coupling strength to loss channels $\kappa \gg \gamma$.

For a resonator coupled to a transmission line the input-output relation is given by:

$$a_{out} = \sqrt{\kappa} a - a_{in} \tag{2.3}$$

To solve the equation of motion, which is a differential equation, for the classical response of the nonlinear system, one would typically use a simple plane wave ansatz with single amplitude and frequency. However, we assume a superposition of the quantum field a and classical field α rotating at the pump frequency ω_p to account for the presence of the coherent drive field and the signal field. Hence, our ansatz takes the form

$$\begin{aligned} a &\to (a+\alpha)e^{-i\omega_p t} \\ a_{in} &\to (a_{in}+\alpha_{in})e^{-i\omega_p t} \\ a_{out} &\to (a_{out}+\alpha_{out})e^{-i\omega_p t} \end{aligned} \tag{2.4}$$

The classical response in the steady state $\dot{\alpha}=0$ is obtained after separating out all terms describing the classical field evolution. After regrouping the terms, we obtain the steady state for a coherent input field, also rewritten in terms of the reduced, dimensionless parameters pump detuning δ, drive strength ξ and input field $\tilde{\alpha}_{in}$

$$\begin{aligned} \Big(-i(\omega_p-\omega_0)+\frac{\kappa}{2}\Big)\alpha + iK\alpha^*\alpha^2 &= \sqrt{\kappa}\alpha_{in} \\ \Big(-i\delta+\frac{1}{2}+i\xi n\Big)\alpha &= \tilde{\alpha}_{in} \end{aligned} \tag{2.5}$$

To be explicit, we write out the dimensionless parameters pump detuning δ, drive strength ξ, the mean photon number in the resonator n and input field $\tilde{\alpha}_{in}$ and the later relevant signal detuning Δ:

$$\begin{aligned} \delta &= \frac{\omega_p-\omega_0}{\kappa} \\ \tilde{\alpha}_{in} &= \frac{\alpha_{in}}{\sqrt{\kappa}} \\ \xi &= \frac{|\tilde{\alpha}_{in}|^2 K}{\kappa} \\ n &= \frac{|\alpha|^2}{|\tilde{\alpha}_{in}|^2} \\ \Delta &= \frac{\omega_p-\omega_s}{\kappa} \end{aligned} \tag{2.6}$$

We translate from a field to a reduced photon number or power dependent description by multiplying Eq. 2.5 with its complex conjugate:

$$\begin{aligned} \Big(\delta^2+\frac{1}{4}\Big)n + 2\xi\delta n^2 + \xi^2 n^3 &= 1 \\ \frac{n}{4}(4(\delta-\xi n)^2+1) &= 1 \end{aligned} \tag{2.7}$$

We can numerically compute $n(\delta,\xi)$ as shown in Fig. 2.1b for four different values of ξ. Above a critical pump strength $\xi > \xi_{crit}$ the photon number inside the resonator bifurcates, hence several solutions exist and the computation of the exact numerical solution yields a distorted line shape. However, to better understand the conditions imposed on the resonator input field we shall study the cubic equation and its numerical solution in more detail. First, we notice from the regrouped form of Eq. 2.7 that the maximal resonator occupancy is $n = 4$ whenever $\delta = 4\xi$. Second, the cubic equation exhibits critical points, which can be derived from the roots of the derivative of Eq. 2.7 with respect to photon number $d/dn = 0$:

$$n_c = -\frac{2\delta}{3\xi} \pm \frac{1}{3\xi}\sqrt{\delta^2 - \frac{3}{4}} \tag{2.8}$$

At $\delta_c = \pm\frac{\sqrt{3}}{2}$ there exists only one critical point, which is the inflection point of the cubic function. For $\delta^2 > \delta_c^2$ there exist two real roots of the derivative, which indicates a bistability of the system leading to a bifurcation in the resonator response because the function $n(\delta, \xi)$ is multi-valued for a given δ. Instead, for $\delta^2 < \delta_c^2$ there exist two complex roots. Since the Kerr coefficient of the parametric amplifier is negative, hence $\omega_p < \omega_0$, we are only interested in $\delta_c = -\frac{\sqrt{3}}{2}$. Inserting $n_c(\delta_{crit})$ into Eq. 2.7 yields the critical drive strength $\xi_{crit} = -\frac{1}{\sqrt{27}}$.
In the experiment, we cannot directly probe the intra-cavity field, but instead we can only measure the reflection coefficient Γ, which is derived from the input-output relation in Eq. 2.3 and the solution for the intra-cavity field in Eq. 2.5:

$$\begin{aligned}\Gamma &= \frac{\alpha_{out}}{\alpha_{in}} \\ &= \frac{\sqrt{\kappa}\alpha}{\alpha_{in}} - 1 \\ &= \frac{1}{-i\delta + \frac{1}{2} + i\xi n} - 1\end{aligned} \tag{2.9}$$

In the here discussed, lossless case, the magnitude of the Kerr resonator response remains constant at $|\Gamma| = 1$, while only the reflected phase changes with the detuning and drive strength, see Fig. 2.1a. Hence, the response of the Kerr resonator measured in reflection should be studied versus phase, and not versus amplitude.

2.1.3. WAVE MIXING AND PARAMETRIC AMPLIFICATION

The wave mixing of the signal field with the pump field in the driven Kerr resonator that leads to the parametric amplification is described by the terms proportional to a in Eq. 2.2 after inserting the complex ansatz. Then, after separating out the terms corresponding to the weak field response assuming $|\langle a\rangle| \ll |\alpha|$, we obtain:

$$\begin{aligned}\dot{a} &= i\left(\omega_p - \omega_0 + i\frac{\kappa}{2}\right)a + \sqrt{\kappa}a_{in} - iK\left(2|\alpha|^2 a + \alpha^2 a^\dagger + \alpha a^\dagger a + \alpha^* a^2 + a^\dagger a^2\right) \\ &\approx i\left(\omega_p - \omega_0 - 2K|\alpha|^2 + i\frac{\kappa}{2}\right)a - iK|\alpha|^2 e^{i2\phi} a^\dagger + \sqrt{\kappa}a_{in} \\ &= \kappa\left[i\left(\delta - 2\xi n + \frac{i}{2}\right)a - i\xi n e^{i2\phi} a^\dagger + \tilde{a}_{in}\right]\end{aligned} \tag{2.10}$$

The first line of the equation above captures the dynamics of a weakly driven harmonic oscillator coupled to a waveguide. The last terms proportional to the Kerr

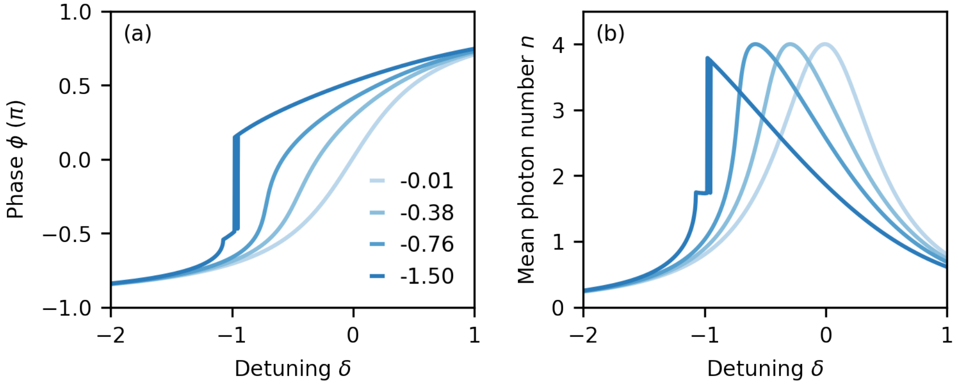

Figure 2.1.: (a) Reflected phase of the Kerr resonator $\phi(\Gamma)$ versus reduced detuning δ for four different drive strengths ξ/ξ_{crit} as indicated in (b). (b) Intra-cavity photon number n.

coefficient, K, mediate the four wave mixing between m pump fields and n weak fields $\alpha^m a^{n-1}$ with $m+n=4$. Subsequently, we neglect terms proportional to a^2 and a^3 because we assume $|\langle a\rangle| \ll |\alpha|$ by construction. This equation can also be rewritten in reduced variables as introduced in the previous subsection.

We solve this equation of motion in the frequency domain after a Fourier-transform of the form:

$$\begin{aligned} a &= \frac{\kappa}{\sqrt{2\pi}} \int_{-\infty}^{+\infty} e^{-i\Delta\kappa t} a_\Delta d\Delta \\ \dot{a} &= -i\Delta\kappa a_\Delta a \end{aligned} \tag{2.11}$$

and with $\Delta = (\omega_s - \omega_p)/\kappa$. As a result, the input field $\tilde{a}_{in,\Delta}$ is the superposition of the resonator field a_Δ and its conjugate $a^\dagger_{-\Delta}$:

$$\begin{pmatrix} \tilde{a}_{in,\Delta} \\ \tilde{a}^\dagger_{in,-\Delta} \end{pmatrix} = \begin{pmatrix} M_\Delta & M_\phi \\ M^*_\phi & M^*_{-\Delta} \end{pmatrix} \begin{pmatrix} a_\Delta \\ a^\dagger_{-\Delta} \end{pmatrix} \tag{2.12}$$

with $M_\Delta = i(-\delta + 2\xi n - \Delta) + 1/2$ and $M_\phi = i\xi n e^{i2\phi}$. This is the point where we understand the constraint imposed on the conjugate field. While the signal field oscillates at Δ around the pump field, the conjugate field, to which we refer to as idler field, oscillates at $-\Delta$. Consequently, the frequency of the idler tone is $\omega_I = 2\omega_P - \omega_S$.

To compute the input-output relation we invert the previous equation and obtain:

$$\begin{pmatrix} a_\Delta \\ a^\dagger_{-\Delta} \end{pmatrix} = \frac{1}{M_\Delta M^*_{-\Delta} - M_\phi M^*_\phi} \begin{pmatrix} M^*_{-\Delta} & -M_\phi \\ -M^*_\phi & M_\Delta \end{pmatrix} \begin{pmatrix} \tilde{a}_{in,\Delta} \\ \tilde{a}^\dagger_{in,-\Delta} \end{pmatrix} \tag{2.13}$$

The input-output relation for the signal field then reads

$$a_{out,\Delta} = g_{S,\Delta} a_{in,\Delta} + g_{I,\Delta} a^\dagger_{in,-\Delta} \tag{2.14}$$

with the gain coefficients for the two input fields

$$\begin{aligned} g_{S,\Delta} &= \frac{M^*_{-\Delta}}{M_\Delta M^*_{-\Delta} - M_\phi M^*_\phi} - 1 \\ g_{I,\Delta} &= \frac{-M_\phi}{M_\Delta M^*_{-\Delta} - M_\phi M^*_\phi} \end{aligned} \tag{2.15}$$

Subsequently, after multiplying the previous input-output field with its complex conjugate, we obtain the power gain at the signal frequency as:

$$G_\Delta = |g_{S,\Delta}|^2 \tag{2.16}$$

We visualize the amplification process in Fig. 2.2 and show the simulated data as it would be acquired in a real experiment. Fig. 2.2a shows the degenerate gain $G(\Delta = 0)$ versus detuning δ and drive strength ξ. Maximal gain is obtained along the grey line highlighting the optimal pump condition, which is approximately linear following $\xi \approx \delta/4$. Line cuts of the 2D map are shown Fig. 2.2b to highlight the sensitivity of the maximal gain to changes in the drive strength or the detuning. From this plot it is also clear that a gain of 20 dB, a desirable value to suppress the noise from subsequent components in the readout line, can be obtained in two different ways. One can either operate close the the optimal drive strength and shift the detuning, or alternatively, one can operate further away from the optimal drive strength and operate at the optimal detuning. The latter case, for example, corresponds to the intersection of the light blue dashed line with the grey line in Fig. 2.2a, while the former case corresponds to the detuning along the dark blue dashed line away from the intersection with the grey line. Fig. 2.2c shows the signal gain versus the signal frequency for a given drive strength (matching color shades with (a)) and the detuning maximizing the gain deduced from (b). The power gain approximately follows a Lorentzian line shape.

Based on the four wave mixing in the nonlinear resonator, we can in the following section discuss its properties, namely the gain-bandwidth product, the saturation power and the added noise.

2.1.4. GAIN-BANDWIDTH PRODUCT

The gain-bandwidth product is one important performance specification for resonator based parametric amplifiers, which states that the product of the maximal gain, G_0, and the instantaneous bandwidth, Δf, should be constant at different operation points leading to a different gain and bandwidth for each setting. In the literature, people refer to instantaneous bandwidth as the bandwidth given a certain operation point. Hence, by carefully choosing the operation point (ω_p, P_p), where ω_p is the pump frequency and P_p is the pump power, one can maximize the gain by compromising on the bandwidth of the amplification window.

We compute the gain and the bandwidth for different operation points from Eq. 2.16 numerically and summarize the results in Fig. 2.3. Along the grey line in Fig. 2.2a, corresponding to the optimal pump condition, the gain and the bandwidth, here as

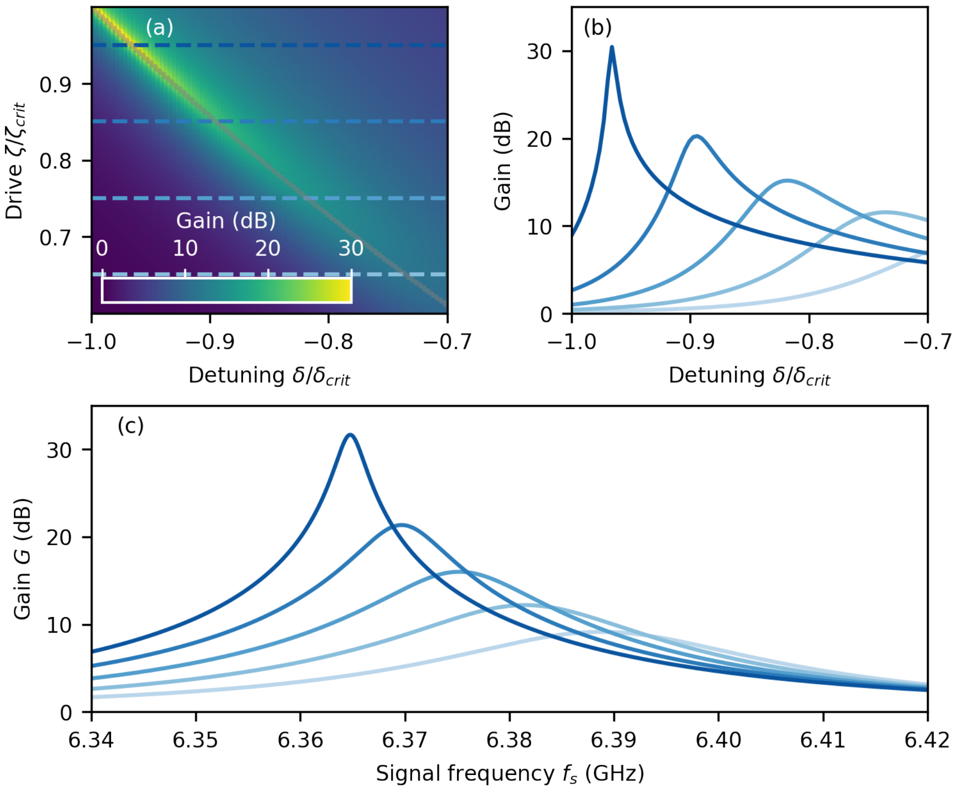

Figure 2.2.: (a) Signal gain versus drive strength ξ in units of the critical drive strength ξ_{crit} and detuning δ. The grey line highlights the point of maximal gain. (b) Signal gain versus detuning δ for different drive strength. The colors match the colors of the dashed lines in (a) to indicate the drive strength. (c) Signal gain versus the signal frequency for a given drive strength (matching colors with (a)) and the detuning maximizing the gain deduced from (b).

the full width at half maximum (FWHM) Δf of the gain curve, follow nearly linear slopes over a wide range of detunings that lead to $10-20$ dB gain, as shown in Fig. 2.3c. Over the same range, the gain-bandwidth product (GBWP), shown in Fig. 2.3a, remains nearly constant at around 90% of the coupling strength κ but rises outside of this regime as gain and bandwidth deviate from their linear slope.

An experimentally simpler measurement (only one drive parameter is swept) is presented as simulation in Fig. 2.3d, where we observe gain and bandwidth for a fixed detuning of $\delta = -0.78$ (leading to about 20 dB gain) versus drive strength ξ. We find a non-monotonic line shape of the gain-bandwidth product in Fig. 2.2b. Again, the resulting GPWB in Fig. 2.3b remains around 90% of the coupling strength κ around the point of maximal gain, but deviates significantly for lower drive strength.

The numerical result discussed above, which shows a nearly constant gain-bandwidth product over a wide parameter range, can be backed up with a simple inspection of a Lorentzian curve. We can approximate the line shape of the gain curve in Fig. 2.2c and Eq. 2.16 with an offset Lorentzian of the form:

$$|g_{S,\Delta}|^2 = \frac{\beta}{2\pi}\frac{A}{(f-f_0)^2+\frac{\beta^2}{4}}+1 = G(f) \tag{2.17}$$

with the full width at half maximum

$$\Delta f = \beta\sqrt{\frac{G_0}{G_0-2}} \tag{2.18}$$

where we define $G_0\pi\beta = 2A+\pi\beta$. In the large gain limit the product of gain and bandwidth is approximately constant

$$|g_{S,\Delta}|^2\Delta f = \left(\frac{2A}{\pi\beta}+1\right)\beta\sqrt{\frac{G_0}{G_0-2}} \approx \frac{2A}{\pi} = const. \tag{2.19}$$

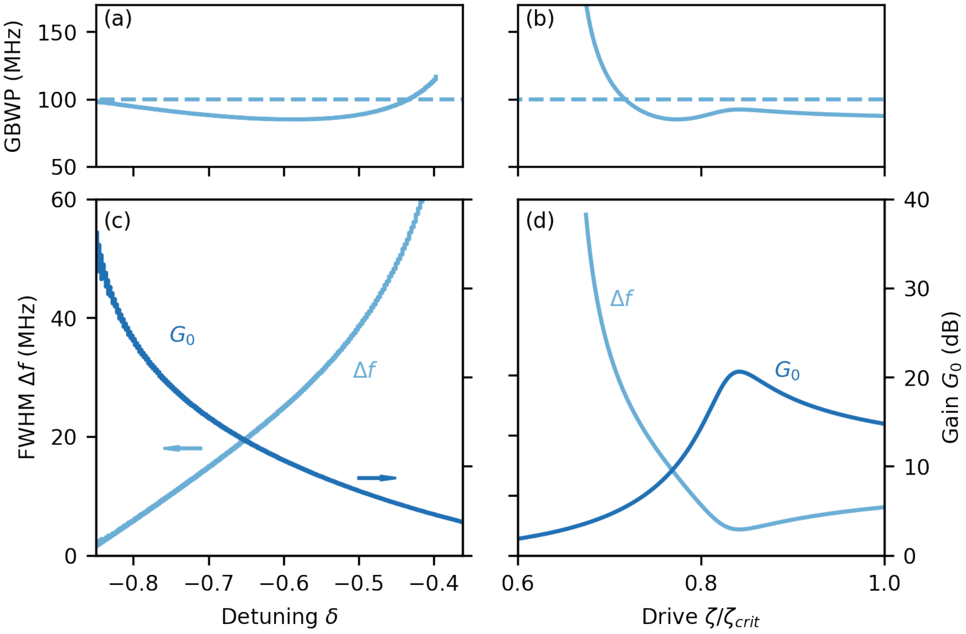

Figure 2.3.: Gain-bandwidth product. (a,c) GBWP together with FWHM Δf and maximal gain G_0 versus detuning δ while maintaining the optimal pump condition. (b,d) GBWP together with FWHM Δf and maximal gain G_0 versus drive strength ξ for a fixed detuning $\delta = -0.78$. The dashed line indicates the coupling strength κ.

2.1.5. SATURATION POWER

In the derivation of the four wave mixing following Eq. 2.10 we neglected terms proportional to a^2 and a^3 since these fields should be small compared to α^2. However, going beyond this weak field approximation employed here, which is often referred to as stiff pumping approximation, these remaining four wave mixing terms also contribute to the resonator field evolution and lead to a higher resonator occupation. Note that we, by construction of the Hamiltonian in Eq. 2.1, only consider four wave mixing. Higher or lower order wave mixing products, such as three or five wave mixing, arising from unwanted interactions in the actual circuit implementation are disregarded. Within this limitation, for a rigorous treatment of larger signal fields we could solve the equation of motion including the higher order terms. However, to a good approximation, we can also add the large signal field, α_s, to the already existing pump field for a given drive strength and detuning by hand and define a new variable for the resonator occupation n'

$$n \rightarrow n' = \frac{|\alpha + \alpha_s|^2}{|\alpha_{in}|^2} \tag{2.20}$$

that enters the computation of the gain coefficient from Eq. 2.16. We can relate the signal field to the signal power, P_S, at the amplifier input and inspect the signal gain versus signal power for different detunings Δ as shown in Fig. 2.4. We find that the signal gain is suppressed by the increasing signal power in case of degenerate gain $\Delta = 0$. We can specify a saturation power that corresponds to the 1 dB compression point, where the gain has reduced by 1 dB compared to the weak field limit. For a given coupling strength κ, Kerr coefficient K and detuning δ we find a saturation power of around -160 dB for different drive strengths ξ as presented in Fig. 2.4a. Noteworthy is the dependence on the signal detuning Δ which also leads to a suppression of the signal gain as shown in Fig. 2.4b,c as it effectively deviates the system away from the optimal pump condition. Interestingly, we find that for a positive detuning in Fig. 2.4b the signal gain recovers shortly around the saturation power and leads to a characteristic "shark fin" line shape, which is more or less expressed depending on the exact choice of parameters. This gain rise phenomenon has been experimentally observed [21, 51] and theoretically described [23, 52, 53].
We can compare the saturation power to the required pump power for given pump condition. The pump power at the input of the amplifier can be computed as

$$P_p = \hbar\omega_p \frac{\kappa^2}{\kappa} \frac{\kappa}{K} \xi \tag{2.21}$$

For the parameters $\xi/\xi_{crit} = 0.18$, $f_p = 6.37$ GHz, $K = 20$ kHz, $\kappa = 5$ MHz, the pump power ranges around -82.18 dBm.

2.1.6. ADDED NOISE

The superconducting parametric amplifier as the first amplifier in the readout chain should ideally operate with minimal added noise to the signal tone. The superconducting nature of the amplifier already reduces the added noise from any

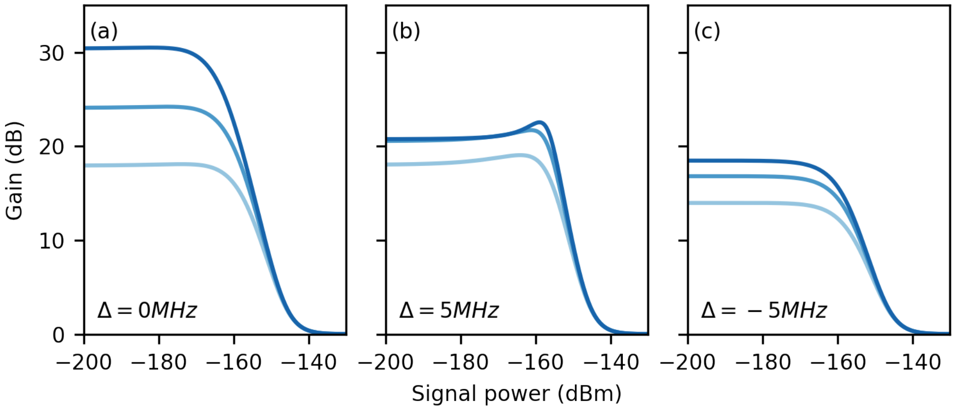

Figure 2.4.: Saturation power. Signal gain versus signal power for a given detuning δ and three different drive strength ξ and also for three different signal detunings Δ in (a-c).

resistive component to nearly zero. However, from the amplification process itself, there arises a lower bound on the added noise to which researchers typically refer to as the quantum limit [49, 54].

From Eq. 2.14 we know that the output field takes the form

$$a_{out,\Delta} = \sqrt{G} a_{in,\Delta} + \sqrt{G-1} a^\dagger_{in,-\Delta} \tag{2.22}$$

Already from this equation it is obvious that any noise added to the signal or idler tone will propagate to the output field at the signal frequency.

While it is already clear from the Fourier transform of the equation of motion of the weak field in the resonator, which leads to the equation above, that there exists a conjugate field with constrained frequency, that we name idler field, the output field must also obey the commutator relation:

$$[a_{out,\Delta}, a^\dagger_{out,-\Delta}] = [a_{in,\Delta}, a^\dagger_{in,-\Delta}] = 1 \tag{2.23}$$

Consequently, the input field must be a superposition of the signal and the idler field with certain gain coefficients. The noise of the output field can be computed by its variance, which is the sum of the variances of the input fields:

$$(\Delta a_{out,\Delta})^2 = G(\Delta a_{in,\Delta})^2 + (G-1)(\Delta a^\dagger_{in,-\Delta})^2 \tag{2.24}$$

For an unoccupied input mode, such as the idler mode, the variance is equal to the vacuum fluctuations $(\Delta a^\dagger_{in,-\Delta})^2 = \frac{1}{2}$. Note that the variance comes in units of photon number. This variance is added to the output field regardless of its occupation, hence it adds to the signal noise as added noise. We can express the noise coming from the parametric amplifier as noise temperature, which is the sum of the signal noise temperature T_S and the vacuum fluctuations from the idler mode:

$$T_{PA} = T_S + \frac{1}{2}\frac{\hbar\omega}{k_B} \tag{2.25}$$

since the equivalent temperature of a radiation field with photon number n and frequency ω is

$$T_{rad} = n\frac{\hbar\omega}{k_B} \tag{2.26}$$

The measurements of weak signals with noise temperate T_S require a very sensitive amplification chain composed out of several amplifiers with low noise to bring the effective noise temperature at the output close to the input noise temperature. A sketch of such a setup is depicted in Fig. 2.6. Concretely, we consider a readout line composed of a parametric amplifier followed by two HEMT amplifiers and a detector. Using the Frijs formula we can compute the effective noise temperature at the receiver

$$T_{eff} = T_{PA} + \frac{T_{HEMT}}{G_{PA}} + \frac{T_{RTamp}}{G_{PA}G_{HEMT}} + \frac{T_{det}}{G_{PA}G_{HEMT}G_{RTamp}} \tag{2.27}$$

as the noise propagates through an amplification chain. Note that the Frijs formula above does not take any losses originating from connectors, circulators or isolators into account. We can translate the noise temperature into noise power in a certain bandwidth Δf:

$$P_N = k_B T \Delta f \tag{2.28}$$

Based on Eq. 2.27 we calculate the effective noise temperature at the receiver for two different configurations, as shown in Fig. 2.5a. In both cases we assume the gain G and noise temperature T_N of the two HEMT amplifiers to have the specifications listed in Tab. 2.3 for one LNC HEMT amplifier and one LNR room temperature amplifier. Furthermore, we assume a vector network analyser as receiver with a noise floor of −115 dBm corresponding to a noise temperature of 22 MK. In this configuration, to which we refer to as the "ideal" configuration about 20 dB gain is required to suppress the noise temperature of the HEMT amplifier, which would otherwise be limiting the readout. In the case where further interconnects following the two HEMT amplifiers (here we assume twice 10 dB) effectively reduce the gain of the HEMT amplifiers, the noise temperature is significantly increased for the same gain of the parametric amplifier. Only a larger gain of the parametric amplifier or the first HEMT amplifier can compensate for the additional losses induced by long cables or many interconnects in this imperfect configuration.

During a measurement, the spectrum analyser used to record the power spectrum records the noise as noise power. The simulated result of such a measurement is presented in Fig. 2.5b for measurements limited by the HEMT noise temperature or the PA noise temperature given a noise floor of the spectrum analyser of −112 dBm. First of all, it is important to measure with a resolution bandwidth large enough for sufficient sensitivity above the noise floor, but smaller than the amplification bandwidth to record the gain correctly. Second, and very interestingly, this measurement can also be used to estimate the gain of the readout chain as the offset of this curve is set by the gain.

The gain and noise figure of any real amplifier depends on the input power. Both figures degrade significantly once the saturation power of the amplifier is reached.

Hence, it is important to maintain an input power level well below the 1 dB compression point for the input port, which is linked to the output compression power:

$$P_{out,1\,\mathrm{dB}} = P_{in,1\,\mathrm{dB}} + G_{dB} - 1\,\mathrm{dB} \tag{2.29}$$

The equation above is not particularly difficult to understand or derive, but very useful, since the relevant quantity for us is $P_{in,1\,\mathrm{dB}}$, while the specified quantity in most data sheets is $P_{out,1\,\mathrm{dB}}$. (In most data sheets for HEMT amplifiers and operational amplifiers, which consists of a chain of transistors or junctions, it is the last element of the chain that is compressed first. Hence the definition of the output saturation power. The output saturation power is also specified for amplifiers, which are used in high power applications, e.g. antenna circuits, where the power levels must be carefully handled to avoid subsequent gain compression or to maximize the transmission power of antennas. For parametric amplifier implementations in the context of quantum computing or quantum sensing applications, the specification of the input saturation power is more meaningful as it bounds the number of photons, which can be used for the readout of the superconducting qubits.) As the pump power level at the output of the parametric amplifier is on the order of −80 dBm in many realistic cases, the operation of the HEMT amplifier is generally not compressed by high input powers. But since the pump tone gets amplified by the HEMT amplifier by about 44 dB, it reaches a power level of −36 dBm, which is even above the input saturation power of the LNF LNR 4-8art amplifier listed in Tab. 2.3. Hence, the exact configuration of the readout chain has to be chosen carefully.

	range	G	T_N	$P_{1dB,O}$
	GHz	dB	K	dBm
LNF LNC 4-8c [14]	4-8	42	1.5	-12
LNF LNC 4-8f [55]	4-8	44	1.5	-8
LNF LNR 4-8art [56]	4-8	42	31.7	-2
AFS4-001008-14 [57]	0.1-8	36	110.3	10

Table 2.3.: Typical amplifier characteristics. The table lists two typically used LNF HEMT amplifiers for cryogenic operation, as well as two room temperature amplifiers, one provided by LNF, the other one provided by MITEQ. Earlier versions of the LNC amplifiers came with larger noise temperatures of around 2.2 K.

2.2. BUILDING A PARAMETRIC AMPLIFIER

Up to this point we have only considered a theoretical model of a nonlinear resonator in which a four wave mixing process is mediated. In this section, we want to present two different resonator implementations and two different nonlinear media, which could be combined together with some drive tone to compose a superconducting parametric amplifier. In particular, we will consider as nonlinear medium a standard superconductor-insulator-superconductor (SIS) Josephson junction. The results could be extended to a general kinetic inductance material in a similar way. For the

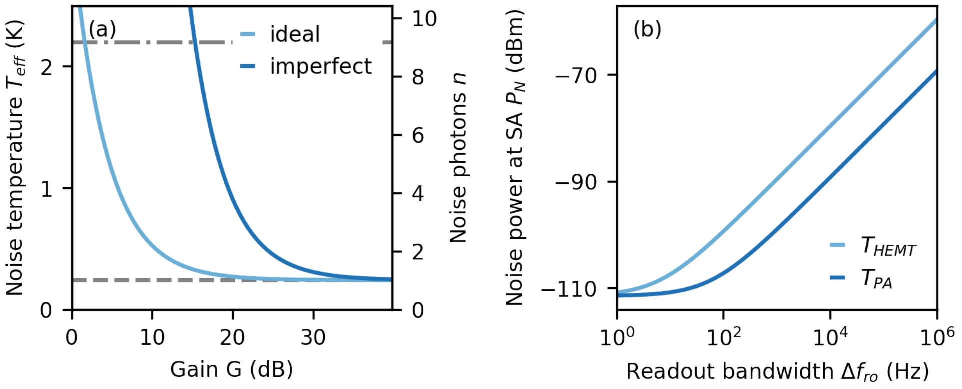

Figure 2.5.: Noise measurements. (a) Noise temperature for two different amplification chains assuming the gains, G, and noise temperatures, T_N, listed in Tab. 2.3. For the imperfect case, we additionally consider 10 dB of attenuation before the room temperature amplifier and before the receiver. The dashed line indicates the noise temperature equivalent to vacuum fluctuations in the signal and idler input mode. The dashed-dotted line corresponds to the noise temperature of a typical HEMT amplifier with $T_N = 2.2\,\mathrm{K}$. (b) Equivalent noise power measured at the spectrum analyser at the end of the amplification chain after total gain $G_{PA}G_{HEMT}G_{RTamp}$ for two different noise temperatures corresponding to the HEMT amplifier and the parametric amplifier as first amplifier assuming a noise floor of −112 dBm for the spectrum analyser.

resonator, we will model a lumped element resonator with a nonlinear element in parallel as well as a coplanar waveguide resonator, which is shunted by the nonlinear element.

2.2.1. NONLINEAR ELEMENTS

A superconducting circuit operating as a four wave mixing parametric amplifier requires a nonlinear element, which adds a term proportional to ϕ^4 to the Hamiltonian. Generally speaking, these elements must have an inductance-to-phase relation that is quadratic to first order. Here, we consider a SIS Josephson junction and a general kinetic inductance material.

JOSEPHSON JUNCTION

An SIS Josephson junction or Josephson tunnel junction is composed of two superconducting electrodes separated by a thin insulating barrier through which a supercurrent, a current of Cooper pairs, can tunnel. The dynamics of these junctions is described by the two Josephson equations depending on the current, I, the critical current, I_0, the voltage, V, and the phase difference between the superconductors across the junction, φ:

$$\begin{aligned} I &= I_0 \sin(\varphi) \\ \frac{d\varphi}{dt} &= \frac{2\pi V}{\phi_0} \end{aligned} \tag{2.30}$$

As we take the time derivative of the current-phase relation, we obtain the Josephson inductance as a function of the phase φ, which can also be expanded for small phase differences $\varphi \ll 1$:

$$L_J(\varphi) = V\left(\frac{dI}{dt}\right)^{-1} = \frac{\phi_0}{2\pi I_0}\frac{1}{\cos(\varphi)} \approx L_J\left(1 + \frac{\varphi^2}{2}\right) \tag{2.31}$$

The energy stored in the Josephson junction is given by:

$$\begin{aligned} E_J(\varphi) &= \int_0^{t_0} IV dt = \int_0^{t_0} I_0 sin(\varphi)\frac{\phi_0}{2\pi}\frac{d\varphi}{dt}dt \\ &= \frac{\phi_0 I_0}{2\pi}(1-\cos(\varphi)) = E_J\left(1 - \sum_{n=0}^{\infty}\frac{(-1)^n}{2n!}\varphi^{2n}\right) \\ &\approx E_J\left(\frac{\varphi^2}{2} - \frac{\varphi^4}{24}\right) = E_{NL,0}\varphi^2 + E_{NL,1}\varphi^4 \end{aligned} \tag{2.32}$$

The Josephson energy relates to the inductance as:

$$E_J = \frac{\phi_0 I_0}{2\pi} = \frac{\phi_0^2}{(2\pi)^2 L_J} \tag{2.33}$$

2.2.2. NONLINEAR, LUMPED ELEMENT CIRCUIT IMPLEMENTATION

We now consider a nonlinear, lumped element circuit, with parallel capacitor E_C, parallel inductor E_L and parallel nonlinear inductor E_{NL}. $E_{NL,0}$ is the linearized contribution to the inductance, and $E_{NL,1}$ is the quadratic contribution. The dynamics of such a circuit follows an anharmonic oscillator with the Hamiltonian

$$\begin{aligned} H_{AHO} &= 4E_C n^2 + (E_L + E_{NL,0})\varphi^2 + E_{NL,1}\varphi^4 \\ &\approx \hbar(\omega + K)\left(b^\dagger b + \frac{1}{2}\right) + \frac{\hbar K}{2} b^\dagger b^\dagger b b \end{aligned} \tag{2.34}$$

In order to solve the dynamics of the system, we first consider the linear Hamiltonian and then reintroduce the nonlinearity. The linear part of the Hamiltonian takes the form:

$$\begin{aligned} H_L &= 4E_C n^2 + (E_L + E_{NL,0})\varphi^2 \\ &= \omega_0\left(b^\dagger b + \frac{1}{2}\right) \end{aligned} \tag{2.35}$$

with the reduced flux and charge operators in second quantization

$$\begin{aligned} \varphi &= \sqrt{\frac{\zeta}{2}}(b + b^\dagger) \\ n &= \frac{i}{\sqrt{2\zeta}}(b - b^\dagger) \end{aligned} \tag{2.36}$$

and with the linear eigen-frequency and the energy ratio

$$\begin{aligned} \omega_0 &= 4\sqrt{E_C(E_L + E_{NL,0})} \\ \zeta &= \sqrt{\frac{4E_C}{E_L + E_{NL,0}}} \end{aligned} \tag{2.37}$$

The nonlinear part of the Hamiltonian takes the following form when restricting to only photon-number conserving terms, which is equivalent to applying a rotating wave approximation.

$$\begin{aligned} H_{NL} &= E_{NL,1}\varphi^4 \\ &= E_{NL,1}\frac{\zeta^2}{4}(b + b^\dagger)^4 \\ &\approx E_{NL,1}\frac{\zeta^2}{4}(3 + 12b^\dagger b + 6b^\dagger b^\dagger bb) \end{aligned} \tag{2.38}$$

In the case of vanishing shunt inductance, L, and a Josephson junction as nonlinear inductor, the Kerr coefficient can be simplified to

$$K_J = -\frac{E_J}{2}\frac{\zeta^2}{4} = -E_C \tag{2.39}$$

2.2.3. NONLINEAR, COPLANAR WAVEGUIDE RESONATOR IMPLEMENTATION

Going beyond the lumped element implementation treated above, we now consider a coplanar waveguide resonator with nonlinear shunt inductance as a Kerr resonator. We begin the mode analysis with a Lagrangian describing the waveguide chain of infinitely many short LC resonators and a linear inductive shunt (we only later include the nonlinear contribution)

$$\mathscr{L} = \lim_{n\to\infty}\sum_{m=1}^{n}\Delta x\left[\frac{c}{2}\dot{\phi}_m^2 - \frac{(\phi_m - \phi_{m-1})^2}{l\Delta x^2}\right] - E_{NL,0}\phi_n^2 \tag{2.40}$$

where we define $\phi_n = \phi(x = d)$ and the step size $\Delta x = d/n$. Computing the Euler-Lagrange equation from the Lagrangian at the position $x = d$ yields the equation of motion

$$\Delta x\frac{c}{2}\ddot{\phi}_n = 2\phi_n\left(\frac{1}{l\Delta x} - E_{NL,0}\right). \tag{2.41}$$

We solve the equation of motion with a wave ansatz in form of a normal mode decomposition

$$\phi(x) = \sum_{m=0}^{\infty}\phi_m\cos(k_m x). \tag{2.42}$$

Consequently, we obtain the transcendental equation for the wave number per mode k_m

$$k_m\tan(k_m d) = lE_{NL,0}. \tag{2.43}$$

Expanding the tangent around $k_m d = \pi/2$ yields the wave number for the fundamental mode

$$k_0 \approx \frac{\pi}{2d + \frac{2}{lE_{NL,0}}} \tag{2.44}$$

As a result of the derivation (not shown here), we find a Kerr coefficient of

$$K_{00} = -\frac{E_{NL,0}}{\hbar}\left(\frac{\phi_{zpf}}{\varphi_0}\right)^4 cos^4(k_0 d) \tag{2.45}$$

2.3. CHARACTERIZING A PARAMETRIC AMPLIFIER

2.3.1. MEASUREMENT SETUP

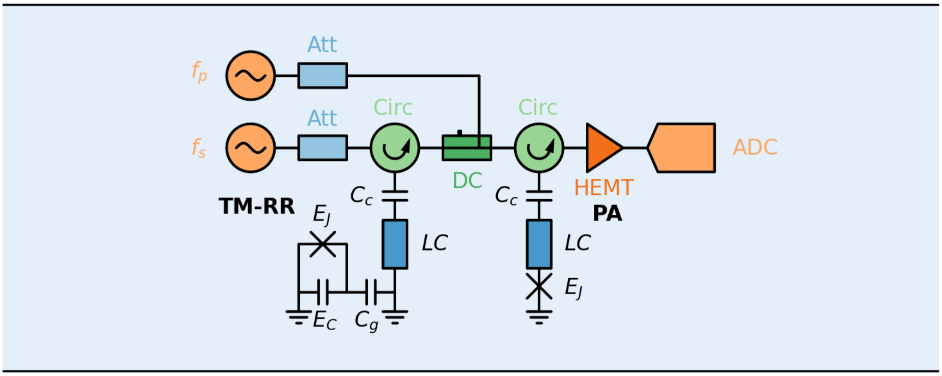

Figure 2.6.: Measurement setup for parametric amplifier allowing for noise performance and quantum efficiency measurements. PA Parametric Amplifier, TM Transmon qubit, RR Readout resonator, HEMT amplifier, Att in-line attenuation, Signal Generators with frequency f_p and f_s, ADC Analog-to-digital converter. The directional coupler and the two circulators ensure directionality and isolation between the qubit and the amplifier system.

The measurement setup for parametric amplifiers consists in the simplest case of a two port transmission setup, or for the full characterization of a three port transmission setup, see Fig. 2.6.
In both configurations, the attenuated input line combines the pump tone at f_p and the probe tone at f_s. The attenuation should be chosen such that the thermal radiation at the sample stage is well below the noise temperature of the parametric amplifier, which is on the order of one photon, which again is equivalent to approximately 300 mK. Otherwise, the noise temperature of the amplifier might be increased artificially due to the thermal occupation of the input modes. While this requirement has not been tested systematically in any experiment, the underlying consideration nonetheless suggests a distribution of attenuators along the input line of at least [20 dB, 10 dB, 10 dB, 20 dB] at [4 K, 1 K, 100 mK, 20 mK] [58]. At the same time, the responsible test engineer needs to ensure that the pump power at the

amplifier stage can be achieved with the given line attenuation and the dynamic range of the signal generator for the pump tone. Note that the line between the PA circulator and the PA should be kept at $50\,\Omega$ and as short as possible to avoid environmental effects as much as possible [31].
Eccosorb filters are not required for the test of amplifiers as the effect of pair breaking, high-frequency radiation should be negligible. The use of a low pass filter with a cut of frequency $f_c > f_s, f_p$ suppresses the amplification of spurious higher harmonics generated in the parametric amplifier or at higher amplification stages.
The amplifying output line should consist of two amplifiers, one at 4 K, and the other one at room temperature. The low-noise HEMT amplifier at 4 K should be specified with a noise temperature below $T_N < 3\,\mathrm{K}$ (modern devices seem to reach noise temperatures of around 1.5 K) to limit the rise in noise temperature to 10 % at 20 dB gain of the parametric amplifier compared to the T_S. The HEMT amplifier should also have a gain of $G_{HEMT} > 35\,\mathrm{dB}$ to suppress noise from subsequent stages over a bandwidth of $4-8\,\mathrm{GHz}$ and a saturation power that is much larger than the sum of pump power and amplified signal power $P_{sat} >> P_{pump} + G_{PA}P_{signal}$. The second amplifier at room temperature (not shown in Fig. 2.6) can have less stringent performance specifications, but must have a large saturation power to prevent saturation. If the pump tone cannot be filtered out with passive low pass filters prior to the room temperature amplifier, the use of a pump cancellation unit, which reduces the transmitted pump power by destructive interference with itself, is advisable.
For the full stack characterization including a sophisticated noise performance characterization, a third line should be added to the test setup. This additional line drives and probes a superconducting qubit dispersively coupled to a superconducting resonator, which will serve as sensitive power sensor or as test object for a quantum efficiency measurement. Ideally, the resonator is uni-directionally coupled towards the parametric amplifier to boost the collection efficiency of the readout resonator. The directional coupling can be achieved by an asymmetric coupling of a transmission line resonator or by a reflection measurement of a single port resonator with an additional circulator at its input. Moreover, the resonance frequency of the resonator must lay within the amplification window of the subsequent parametric amplifier. To prevent backaction from the amplifier drive to the qubit, one can isolate the two circuits in separate housings and by using directional couplers and additional isolators.

2.3.2. GAIN, BANDWIDTH, SATURATION POWER

The systematic tune-up of a resonator based parametric amplifier begins with a single tone VNA-based transmission measurement. The resonator, which itself is measured in reflection, manifests as a monotonic phase roll in the low power spectrum. Note that there is no dip in magnitude in the transmission spectrum for a lossless superconducting parametric amplifier. From a fit to the phase role versus frequency, one can extract the resonance frequency, f_0, the coupling strength, κ, and the loss rate, γ. Subsequently, one measures the Kerr coefficient, K, from the frequency shift versus probe tone power. Given the resonator parameters, one can estimate the photon number occupation of the resonator in the linear regime by

$$\bar{n} = \frac{1}{\kappa}\frac{P_{in}}{\omega_0} \tag{2.46}$$

for a given input power at the sample stage P_{in}, which can be sufficiently well estimated based on the input line attenuation. The Kerr coefficient is then computed by

$$K = \frac{\omega_0^* - \omega_0}{\bar{n}} \tag{2.47}$$

where ω_0^* is the frequency-shifted resonance frequency. After the single tone characterization of the Kerr resonator, one can now tune-up to the amplification regime and find the optimal pair (ω_p, P_p). The pump frequency below the bistable regime can be estimated by

$$\omega_p = \omega_0 - \kappa\frac{\sqrt{3}}{2}\beta \tag{2.48}$$

where β measures the detuning from the critical point and should be below unity. As a starting point for a first stable operation, one might choose $\beta = 0.9$. The required pump power for optimal amplification follows from Eq. 2.21.

While the here obtained estimate for (ω_p, P_p) will serve as a good starting point for the amplifier characterization, it does not take experimental imperfections into account, namely two-photon losses in the resonator in the high power regime and uncertainties in the line attenuation. In order to experimentally find the optimal pump condition systematically, one should measure the signal gain for a fixed detuning $\Delta = \omega_p - \omega_s$ versus pump frequency f_p and pump power P_p. The result of this measurement will look similar to Fig. 2.2a, but also take imperfections into account. Those will appear as instabilities or sudden jumps along the theoretically monotonic optimal pump condition line. It is recommended to operate at finite, but small detuning to ensure only non-degenerate gain and hence pump phase independence, but still high sensitivity to changes in gain. Hence, the detuning should be on the order of $\Delta/2\pi = 10 - 100\,\mathrm{kHz}$. A linear fit to the maximal gain per frequency and power point yields the experimental pump condition for various detunings δ.

Once the working point of the parametric amplifier has been approached, one can characterize the gain, bandwidth and saturation power versus any control parameter. For the gain-bandwidth measurement three different options exist: Gain versus signal frequency is measured versus (1) pump power for fixed pump frequency, (2) pump frequency for fixed pump power, or (3) pump power for adjusted pump frequency to meet the optimal pump condition found in the previous experiment. Every gain versus signal frequency trace can be fitted to a Lorentzian curve, which yields maximal gain G_0 and bandwidth $\Delta\omega$ for every tested pump condition. For the interpretation of the measurement results it is very important to distinguish between the different approaches, see Fig. 2.3. For the saturation power measurement, a certain ideal pump condition (ω_p, P_p) is chosen yielding the desired gain. Then the gain is measured for a small, but fixed detuning Δ versus the signal power P_s. The saturation power is specified as the 1 dB compression point, which is the corresponding signal power at which the amplifier gain is suppressed by 1 dB compared to the weak signal regime. In case of a non-monotonic line shape of the saturation power curve, as observed for example in Fig. 2.4b, the standard definition of saturation power becomes meaningless, and one should rather define a weak signal limit corresponding to a change in gain by ±1 dB compared to the weak signal regime.

2.3.3. NOISE PERFORMANCE MEASUREMENT

The noise performance of a parametric amplifier can be measured in various different quantities, such as the noise temperature, the noise figure, or the noise power in dBm or photon number. More indirect measures of the noise performance, but with more relevance for the experimental implementation, are the SNR improvement and the quantum efficiency measurements.

Different calibration methods exist to estimate the signal power level at the input of the parametric amplifier and the gain of the readout chain apart from the parametric amplifier. Most commonly used are four different methods based on (1) line calibrations, (2) shot-noise tunnel junctions, (3) hot-cold loads and (4) AC Stark shifts of qubits.

LINE CALIBRATION REFERRED POWER

The line calibration method is the most direct, but also the most error-prone method. As part of it, one measures the attenuation of the input line from the output of the VNA to the input of the PA and the amplification from the PA output to the VNA input at room temperature while the lines are accessible, when the dilution refrigerator is open for maintenance or sample exchange. In case of superconducting cables being present in either the input or the output line, a piece-wise calibration of every component is needed and the attenuation of the superconducting cables needs to be estimated based on the provided data sheets.

This calibration method assumes that the line attenuation remains constant between room temperature and cold temperatures and moreover, that the cable connections are robust against thermal expansion and contraction.

Already during the installation of the test setup, a proper 50 Ω impedance environment should be ensured, also on the short interconnects on the PCB to avoid impedance mismatches and unwanted back reflections.

TRANSMON-BASED REFERRED POWER

Likewise, a transmon qubit dispersively coupled to a readout resonator can be used to estimate the power level at the input of the parametric amplifier. First, one estimates the signal power output based on the readout resonator occupation n at f_r and the coupling strength κ by

$$P_{out} = \kappa n h f_r \tag{2.49}$$

The coupling strength is obtained from the bandwidth of the resonator line in the transmission spectrum. The resonator occupation for a given signal power at the signal generator output can be measured from the AC Stark shift of a qubit, where here we consider the workhorse of the superconducting qubit community, the transmon qubit. The photon number follows from

$$n = cP_{SG} = \frac{\Delta f_q}{2\chi} \tag{2.50}$$

where c is the power conversion factor, which depends on the line attenuation and the coupling rate of the resonator. P_{SG} is the power at the signal generator output. The dispersive shift, χ, can be extracted from the measurement-induced dephasing rate $\Gamma_\phi = \frac{8\chi^2 n}{\kappa}$ [59, 60] and the qubit frequency shift $\Delta f_q = 2\chi n$ as

$$\chi = \frac{\kappa}{4} \frac{\partial_P \Gamma_\phi}{\partial_P \Delta f_q}. \tag{2.51}$$

Both quantities can be simultaneously measured in a variable strength Ramsey experiment, which is composed of a standard Ramsey experiment to measure f_q and $\Gamma_\phi = \frac{1}{T_\phi}$ via T_2 (since we are only interested in the slope of Γ_ϕ versus input power, we might as well only consider the inverse of T_2 here) while a square measurement pulse with amplitude P_{SG} is played during the idling time of the Ramsey sequence.

Alternatively, one can estimate the frequency shift Δf_q from a power dependent qubit spectroscopy. However, the spectral resolution is typically worse than the one obtained in a Ramsey experiment. Alternatively, one can estimate the dispersive shift χ from the separation of the qubit-dependent resonator states in the IQ plane [36] after state dependent single shot readout as

$$\chi = \frac{\kappa}{2} \tan\left(\frac{\theta}{2}\right) \tag{2.52}$$

where θ is the angle between the resonator states in the rotated IQ plane. Ideally, the two different methods should yield the same photon number occupation.

The power level computed for the resonator output then needs to be referred to the input of the parametric amplifier. The attenuation between the output of the readout resonator and the input of the parametric amplifier can be measured with a VNA at room temperature and is on the order of 1.5 dB.

2.3.4. SNR IMPROVEMENT

The measurement of the signal-to-noise ratio (SNR) improvement

$$\Delta SNR = SNR_{on} - SNR_{off} = \left(\frac{T_{PA}}{T_{HEMT}} + \frac{1}{G}\right)^{-1} \tag{2.53}$$

between the SNR for the ON state with gain G and the OFF state of the parametric amplifier is a good approximation for the noise temperature. The three important approximations should be noted: First, the noise temperature of the readout chain is limited by the HEMT amplifier. Second, the noise temperature of the HEMT amplifier is exactly known. Third, the parametric amplifier is purely reactive, hence

the reflection in the off state is ideally $\Gamma = 1$.
Despite these strong assumptions and its indirect measurement of the noise temperature, the SNR improvement is an experimentally relevant quantity, because it measures what the experimentalists care about, the improvement of the readout in the presence of the parametric amplifier, which can be different from the point of maximal gain in case of imperfections, such as amplifier saturation. Consequently, the time-efficient measurement of the SNR improvement can be used during the tune-up of the parametric amplifier, once its working point has been approached.
The quantity SNR improvement is sometimes also referred to as noise visibility.

2.3.5. QUANTUM EFFICIENCY

The most holistic and convincing method characterizing the noise performance and backaction of a parametric amplifier as part of the entire readout chain is the measurement of the quantum efficiency [59–61]. Conceptually, the quantum efficiency or measurement efficiency quantifies the ratio between the obtained and the lost qubit state information. In other words, it quantifies the probability of detecting an emitted photon. Technically speaking, it is the ratio between the SNR of the obtained measurement outcome at the room temperature electronics and the dephasing of the qubit.

Following the formalism presented in Ref. [60], we can derive the ratio of SNR and dephasing starting from the equation of motion of the resonator field, which depends on the qubit state and the qubit drive as

$$\begin{aligned} \partial_t \alpha_1 &= -\epsilon(t) - i(\Delta+\chi)\alpha_1 - \frac{\kappa}{2}\alpha_1 \\ \partial_t \alpha_0 &= -\epsilon(t) - i(\Delta-\chi)\alpha_0 - \frac{\kappa}{2}\alpha_0 \end{aligned} \tag{2.54}$$

with the detuning Δ, the drive strength ϵ, the dispersive shift χ, and the resonator coupling strength κ. Furthermore, we make two assumptions: (1) The resonator fields α_i vanish at the beginning and end of the integration window. (2) Optimal integration weights are used.
Starting from assumption 1, we can then link the state dependent resonator evolution

to the dephasing:

$$\begin{aligned}
0 &= \Big[|\alpha_1-\alpha_0|^2\Big]_0^T \\
&= \int_0^T \partial_t|\alpha_1-\alpha_0|^2 \\
&= 2\int_0^T \Re\Big[(\alpha_1^*-\alpha_0^*)\partial_t(\alpha_1-\alpha_0)\Big]dt \\
&= 2\int_0^T \Re\Big[(\alpha_1^*-\alpha_0^*)\Big((-i\Delta-\frac{\kappa}{2})(\alpha_1-\alpha_0)-i\chi(\alpha_1+\alpha_0)\Big)\Big]dt \\
\frac{\kappa}{2}\int_0^T \Re\Big[(\alpha_1^*-\alpha_0^*)(\alpha_1-\alpha_0)\Big]dt &= -\chi\int_0^T \Re\Big[(\alpha_1^*-\alpha_0^*)i(\alpha_1+\alpha_0)\Big]dt \\
\frac{\kappa}{2}\int_0^T |\alpha_1-\alpha_0|^2 dt &= -\chi\int_0^T \Re\Big[i(|\alpha_1|^2-|\alpha_0|^2+2i\Im(\alpha_0\alpha_1^*))\Big]dt \\
&= 2\chi\int_0^T \Im(\alpha_0\alpha_1^*)dt \\
\frac{(SNR)^2}{4\eta} &= \beta_m
\end{aligned} \tag{2.55}$$

The measurement efficiency follows from the ratio between the two sides

$$\eta = \frac{(SNR)^2}{4\beta_m} \tag{2.56}$$

The transformations in the last two steps of the previous derivation might appear arbitrary. To clarify the link between the left hand side of the previous equation and the SNR and eventually to make this quantity experimentally accessible, we define the signal-to-noise ratio using optimal integration weights as

$$\begin{aligned}
SNR &= \sqrt{2\kappa\eta\int_0^T |\alpha_1-\alpha_0|^2 dt} \\
&= \frac{S}{N} \\
&= \frac{|\langle V_{int,1}-V_{int,0}\rangle|}{\langle V_{int}^2\rangle-\langle V_{int}\rangle^2} \\
&= a\epsilon
\end{aligned} \tag{2.57}$$

The SNR of the qubit measurement quantifies the state separation in the IQ plane for a given readout amplitude ϵ, hence we can look ahead and define a proportionality constant a quantifying the signal-to-noise ratio change versus drive strength. Some more background: Here $\langle V_{int}\rangle$ is the mean of the state dependent measurement outcome of state i and $\sigma = \sigma_0 = \sigma_1 = \langle V_{int}^2\rangle - \langle V_{int}\rangle^2$ is the standard deviation from the respective mean, assuming they are equal. To arrive at the previous equation, we need to define the optimal integration weights

$$V_{int,i} = \int_0^T \left[w_I V_{I,i} + w_Q V_{Q,i} \right] dt \tag{2.58}$$

with

$$\begin{aligned} V_{I,i} &= V_0(\sqrt{2\kappa\eta}\Re(\alpha_i) + n_I) \\ V_{Q,i} &= V_0(\sqrt{2\kappa\eta}\Im(\alpha_i) + n_Q) \end{aligned} \tag{2.59}$$

with

$$\begin{aligned} w_I = \langle V_{I,1} - V_{I,0} \rangle = V_0\sqrt{2\kappa\eta}\,\langle \Re(\alpha_1) - \Re(\alpha_0) \rangle \\ w_Q = \langle V_{Q,1} - V_{Q,0} \rangle = V_0\sqrt{2\kappa\eta}\,\langle \Im(\alpha_1) - \Im(\alpha_0) \rangle \end{aligned} \tag{2.60}$$

This yields the signal:

$$\begin{aligned} S &= |\langle V_{int,1} - V_{int,0} \rangle| \\ &= 2V_0^2\kappa\eta \int_0^T \left[\langle \Re(\alpha_1) - \Re(\alpha_0) \rangle \left(\Re(\alpha_1) - \Re(\alpha_0) \right) + \langle \Im(\alpha_1) - \Im(\alpha_0) \rangle \left(\Im(\alpha_1) - \Im(\alpha_0) \right) \right] dt \\ &= 2V_0^2\kappa\eta \int_0^T \left[\Re(\alpha_1\alpha_1 - \alpha_0\alpha_1 - \alpha_1\alpha_0 + \alpha_0\alpha_0) + \Im(\alpha_1\alpha_1 - \alpha_0\alpha_1 - \alpha_1\alpha_0 + \alpha_0\alpha_0) \right] dt \\ &= 2V_0^2\kappa\eta \int_0^T \left[(\alpha_1\alpha_1^* - \alpha_0\alpha_1^* - \alpha_1\alpha_0^* + \alpha_0\alpha_0^*) \right] dt \\ &= 2V_0^2\kappa\eta \int_0^T |\alpha_1 - \alpha_0|^2 dt \end{aligned} \tag{2.61}$$

A similar calculation can be done for the noise. Both expressions together then yield the SNR as defined above.

Following the effective stochastic master equation for qubits in the presence of a readout resonator, the off-diagonal element of the qubit density matrix is given by:

$$|\rho_{01}(\epsilon, T)| = e^{-\beta_m}|\rho_{01}(\epsilon = 0, T)| = e^{-\frac{\epsilon^2}{2\sigma^2}}|\rho_{01}(\epsilon = 0, T)| \tag{2.62}$$

Here $2\sigma^2$ is a proportionality constant quantifying the dephasing rate.

Bringing the SNR and the dephasing together, we arrive at the defintion of the measurment efficiency

$$\eta = \frac{SNR^2}{4\beta_m} = \frac{\sigma_m^2 a^2}{2} \tag{2.63}$$

which is experimentally accessible via a variable strength Ramsey experiment. Regarding the measurement, the coefficient a follows from a linear fit to the

SNR versus readout amplitude obtained in a state dependent single shot readout experiment repeated for variable strength. The coefficient σ_m can be deduced from an exponential fit to the coherence ρ_{01} obtained from a variable strength, constant time T, frame-rotation φ based Ramsey experiment. Note that T must be shorter than the dephasing time T_ϕ.

It should be noted that the quantum efficiency can be limited by imperfections other than the parametric amplifier under test. One dominant suppression effect is the detuning of the readout resonator frequency to readout frequency. Another effect comes from the usage of non-optimal integration weights during the measurement, which are often and simply set to a sinusoidal function of the demodulation phase. However, due to the resonator dynamics, time-variable integration weights can significantly boost the quantum efficiency.

ACKNOWLEDGEMENTS

We thank Taryn V. Stefanski (TU Delft) and Christoph Kissling (PTB Braunschweig) for stimulating input and a thorough proof reading of this method chapter.

DATA AVAILABILITY

The raw data and the analysis script underlying all figures in this chapter are available online [12].

3

GATE-TUNABLE KINETIC INDUCTANCE IN PROXIMITIZED NANOWIRES

Lukas Johannes Splitthoff, Arno Bargerbos, Lukas Grünhaupt, Marta Pita-Vidal, Jaap Joachim Wesdorp, Yu Liu, Angela Kou, Christian Kraglund Andersen, Bernard van Heck

We report the detection of a gate-tunable kinetic inductance in a hybrid InAs/Al nanowire. For this purpose, we have embedded the nanowire into a quarter-wave coplanar waveguide resonator and measured the resonance frequency of the circuit. We find that the resonance frequency can be changed via the gate voltage that controls the electron density of the proximitized semiconductor and thus the nanowire inductance. Applying Mattis-Bardeen theory, we extract the gate dependence of the normal state conductivity of the nanowire, as well as its superconducting gap. Our measurements complement existing characterization methods for hybrid nanowires and provide a new and useful tool for gate-controlled superconducting electronics.

This chapter has been published in Phys. Rev. Applied 18, 024074 (2022).

3.1. INTRODUCTION

Superconducting wires with high kinetic inductance [62–69] have found important applications as radiation detectors [70] and, more recently, in the field of quantum technology [71–73], where they are particularly beneficial for protected superconducting qubit designs [74–79].

Typically, the kinetic inductance of a nanofabricated sample is determined by the material composition and by the device geometry and, thus, is not tunable in-situ. Yet, some applications rely critically on the ability to tune the inductor of a quantum circuit after fabrication, e.g. for superconducting amplifiers [3, 18, 80]. Such tunability has commonly been achieved through the use of flux-biased dc-SQUIDs [81, 82] or current-biased conductors [3, 18, 63, 83–85].

A more recent source of tunability comes from the advent of hybrid semiconducting-superconducting nanostructures, which allow the realization of gate-tunable Josephson junctions [5–7]. Even a semiconducting nanowire proximitized by a continuous superconducting film, without any Josephson junction, can be controlled electrostatically. Nearby gates influence the electron density in the semiconductor as well as the induced superconducting gap [86–89], the two crucial parameters which control the inductive response. This electrostatic control over the properties of the proximitized nanowire suggests the possibility to realize a gate-tunable kinetic inductance by exploiting the proximitized transport channels. Such a circuit element could allow for a new class of frequency controllable resonators, amplifiers, qubits and detectors.

Here, we experimentally demonstrate a gate-tunable kinetic inductance using an InAs/Al nanowire shunting a NbTiN coplanar waveguide resonator. This system offers an easy-to-fabricate and magnetic field-compatible [90, 91] circuit element for superconducting electronics. Furthermore, facilitated by the absence of etched Al segments in the nanowire, we are able to extract bulk transport properties of the hybrid InAs/Al system, which has recently attracted lots of attention for its potential use in topologically protected qubits [92].

3.2. EXPERIMENTAL SETUP

We employ a quarter-wave coplanar waveguide resonator which is capacitively coupled to a feedline and shorted to ground by the proximitized nanowire, see Fig. 3.1a. The $l = 3\,\mu\mathrm{m}$ long nanowire section is galvanically connected to the central conductor of the resonator and to ground, see Fig. 3.1c. The nanowire is encapsulated by bottom and top gates for electrostatic control. In this experiment we use the bottom gate only, which extends along the entire nanowire section (optically hidden by top gate), as illustrated in Fig. 3.1d. Each gate line is filtered by on-chip LC filters [93]. The schematic longitudinal cross section in Fig. 3.1d highlights the continuous Al shell on two facets of the gated InAs nanowire, which is connected to the NbTiN circuit (App. 3.6).

To characterize the bare resonator properties, we use an identical reference resonator, in which the nanowire is replaced by a continuous 150 nm thick NbTiN film (App. 3.10.2). Multiple nanowire and reference resonators are frequency multiplexed on the same chip and measured at 15 mK base temperature inside a dilution refrigerator. In the main , we focus on one nanowire (two-facet Al-InAs nanowire, 110(5) nm diameter, 6 nm thick Al shell) and one reference resonator which exemplify trends observed in 12 different devices (App. 3.10.1).

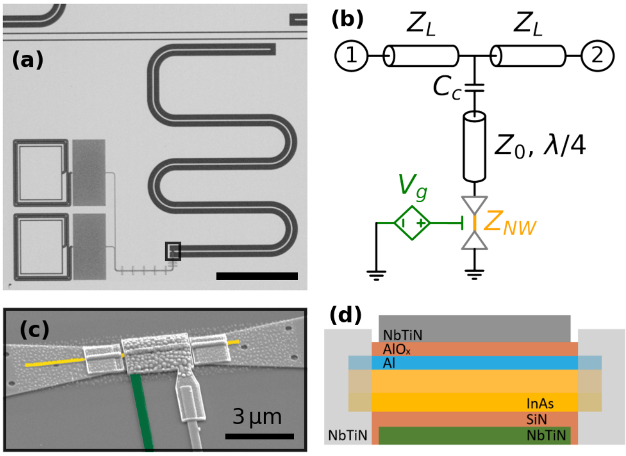

Figure 3.1.: Measured device and equivalent circuit. (a) Optical image of one quarter-wave coplanar waveguide resonator capacitively coupled to a feedline and shorted to ground via a proximitized nanowire. Two LC filtered pads left to the resonator connect to the gates in the vicinity of the nanowire. (scale bar 300 µm) (b) Circuit diagram of a measured device. The transmission line resonator with impedance Z_0 is shunted to ground by a hybrid nanowire with impedance Z_{NW}, which is voltage gate controlled (V_{g}), and capacitively coupled (C_{C}) to the feedline with characteristic impedance $Z_L = 50\,\Omega$. Port 1 and 2 connect to the external measurement setup. (c) False colored micrograph of a proximitized nanowire (orange) which is galvanically connected to the central conductor of the resonator [black box in (a)]. The 3 µm long nanowire section is encapsulated by bottom (green) and top (grey) gates. For this experiment we only use the bottom gate. (d) Schematic longitudinal cut away of InAs nanowire (yellow) with continuous Al shell (blue) between two NbTiN contacts. Bottom (green) and top (grey) gates with dielectric (orange) define the electrostatic potential at the nanowire.

3.3. GATE-TUNABLE KINETIC INDUCTANCE

The nanowire resonator system can be described by the circuit model in Fig. 3.1b: a transmission line with characteristic impedance Z_0 is shunted by a gate-voltage-dependent (V_{g}) impedance Z_{NW}, and capacitively coupled (C_{C}) to a common feedline ($Z_{\mathrm{L}} = 50\,\Omega$). We measure the transmission parameter S_{21} in the vicinity of the resonance frequency. The amplitude and phase of S_{21} display typical resonant behaviour, as shown in Fig. 3.2a,b. We use a linear resonator model [94, 95] to fit the resonance frequency f_r and internal quality factor Q_i.

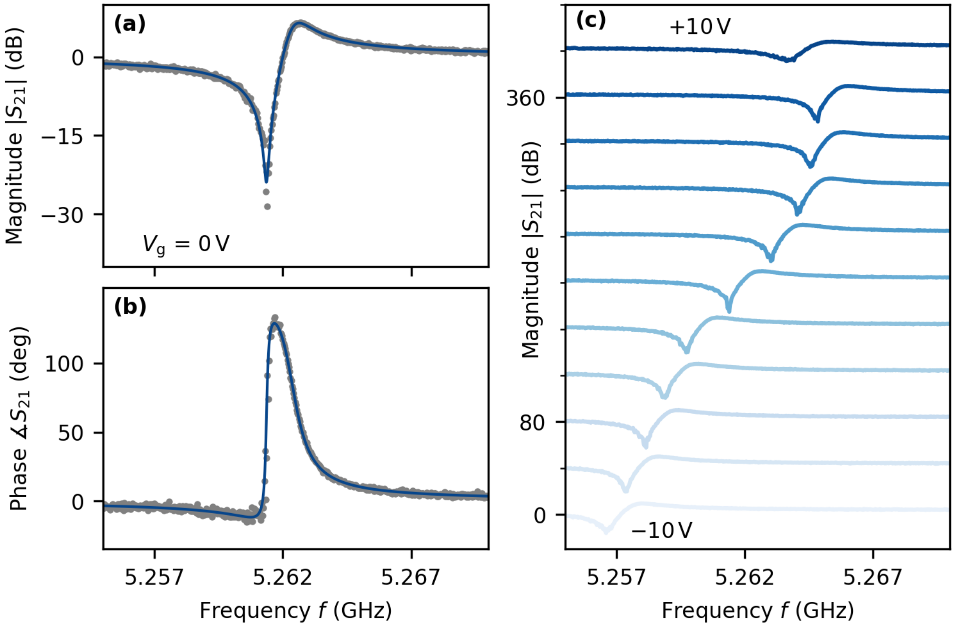

Figure 3.2.: Gate dependent frequency shift of the nanowire resonator. (a,b) Typical magnitude and phase of transmission parameter S_{21}, respectively, of a single nanowire resonator for a fixed gate voltage $V_0 = 0\,\mathrm{V}$. Blue lines show fit results. (c) Magnitude of the transmission S_{21} for 11 different, linear spaced gate voltages in the range from −10 V to 10 V. Each line with a fixed gate voltage is offset by 40 dB for better visibility.

We observe a monotonic increase in resonance frequency as a function of gate voltage up to 8 V (Fig. 3.2c). The shift is about 8 MHz over the total gate range available for measurement (−10 V to 10 V). In Fig. 3.3a,b, we show the extraction of f_r and Q_i as a function of gate voltage. The internal quality factor is nearly constant in the entire range, but it decreases sharply at large applied voltages, an effect which we attribute to the breakdown of the gate dielectric (App. 3.10.5).

When the temperature is increased, the resonance frequency and internal quality factor decrease, at all gate voltages, see Fig. 3.3c,d. We attribute this behaviour to the suppression of superconductivity in Al. Between 20 mK and 750 mK, the frequency is reduced by about 6 MHz, while Q_i drops by one order of magnitude. We notice that for both quantities the temperature response exhibits a gate dependence: it is stronger for positive gate voltages, which, as shown below, we attribute to a change in the induced superconducting gap in InAs. In contrast, in the same temperature range, the resonance frequency of the reference resonator remains approximately

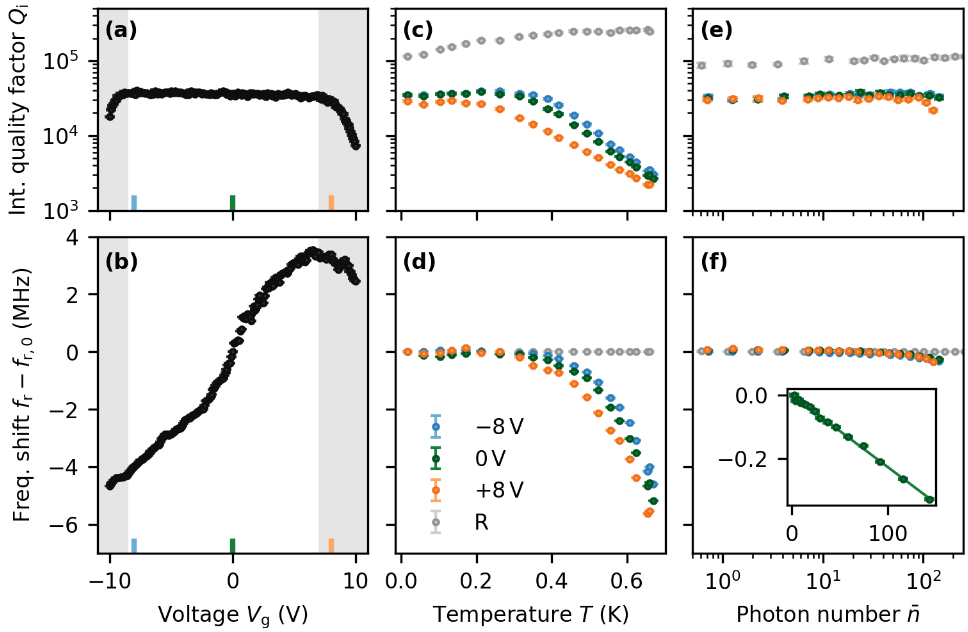

Figure 3.3.: Resonator response versus control parameters (a,b) Internal quality factor and frequency shift as function of gate voltages extracted from fits to S_{21} data (cf. Fig. 3.2a,b). The grey boxes indicate the regions of decreasing Q_i for $V_\mathrm{g} < -8.5\mathrm{V}$ and $V_\mathrm{g} > 7\mathrm{V}$ (see main text). Coloured lines at the bottom mark gate points used in panels (c-f). (c,d) Internal quality factor and frequency shift for the nanowire resonator versus temperature for different gate voltages relative to their zero temperature values. Reference resonator (R) data shown for comparison. (e,f) Internal quality factor and frequency shift for the nanowire resonator versus average intra-cavity photon number for different gate voltages. For higher photon number the nanowire resonator becomes increasingly non-linear and the linear fit model does not capture the measured data above $\bar{n} \gtrsim 200$. Reference resonator (R) data shown for comparison. The error bars indicate the 1σ confidence interval of fit. Inset: Zoom-in on frequency shift of nanowire resonator at 0 V with linear fit.

constant, while Q_i increases slightly. These observations are consistent with the much higher critical temperature of NbTiN and the saturation of two-level systems contributing to dielectric losses [96].

The resonance frequency decreases linearly with the number of intra-resonator photons, $\bar{n}$, as expected in the presence of a Kerr non-linearity arising from the inductance [97, 98]. The frequency shift relative to the single photon level (App. 3.7) is about 0.2 MHz at −120 dBm input power, corresponding to $\bar{n} \approx 100$ (Fig. 3.3e,f), one order of magnitude smaller than the frequency shifts observed versus gate voltage or temperature. We measure a Kerr coefficient $K/2\pi = (f_\mathrm{r} - f_{\mathrm{r},0})/\bar{n} = 2.28(3)\,\mathrm{kHz}$ (inset

Fig. 3.3f), which is sufficient for the realization of superconducting parametric amplifiers [97, 99]. For larger photon numbers, higher order non-linear processes set in and the resonator bifurcates [50, 100], thus the linear model does not capture the measured data for $\bar{n} \gtrsim 200$ (App. 3.10.4). The reference resonator inductance is not susceptible to these photon numbers, thus there is no frequency shift. Q_i increases with microwave power which is consistent with the saturation of two-level systems [96]. We thus choose 100 intra-resonator photons for the remaining measurements to have sufficient signal-to-noise ratio without inducing strong nonlinear effects on the nanowire.

3.4. BULK PROPERTIES OF THE PROXIMITIZED NANOWIRE

We use the measured frequency shifts to extract relevant physical properties of the hybrid nanowire. Assuming that the imaginary part of the nanowire impedance is purely inductive, $\Im(Z_\mathrm{NW}) = 2\pi f_\mathrm{NW} L_\mathrm{NW}$, which is justified given the electromagnetic field profile along the resonator in the limit $Z_\mathrm{NW} \ll Z_0$, a loaded transmission line resonator model (App. 3.9) yields the nanowire inductance $L_\mathrm{NW} = Z_0/4(f_\mathrm{NW}^{-1} - f_0^{-1})$, where f_NW is the resonance frequency of the loaded nanowire resonator and Z_0 and f_0 are the characteristic impedance and resonance frequency of the unloaded coplanar waveguide resonator. Using a conformal mapping technique [101] and the average kinetic sheet inductance of the NbTiN film obtained from the measurement of four reference resonators, we determine $Z_0 = 134.2(4)\,\Omega$ and $f_0 = 5.502(16)\,\mathrm{GHz}$. The uncertainties of these quantities mainly depend on the uncertainty of the NbTiN kinetic sheet inductance. Thus, we can extract L_NW from the measured f_NW, as shown in Fig. 3.4a.

At zero voltage, the nanowire inductance is $L_\mathrm{NW} = 278(17)\,\mathrm{pH}$ with about 6 % constant systematic error stemming from the uncertainties on Z_0 and f_0. L_NW varies by 3.5 % over the range from −10 V to 7 V before superconductivity is suppressed by gate leakage. The geometric inductance associated with the nanowire segment can be estimated to be $L_\mathrm{NW,geo} = 4.5\,\mathrm{pH}$ (App. 3.10.3), thus we conclude that the shunt impedance is dominated by the kinetic inductance of the hybrid nanowire.

Using the same method, we extract the temperature dependence of L_NW, as shown in Fig. 3.4b. For all gate voltages, the nanowire inductance increases with temperature. According to the Mattis-Bardeen theory [102, 103] in the low frequency limit, $hf \ll \Delta_0$, the kinetic inductance is given by

$$L_\mathrm{NW} = \frac{\hbar l}{\pi \sigma_\mathrm{n} \Delta_0} \tanh^{-1}\left(\frac{\Delta_0}{2k_\mathrm{B}T}\right), \tag{3.1}$$

where Δ_0 is the superconducting gap and σ_n is the one-dimensional normal state conductivity of the hybrid nanowire. Note that the latter absorbs the cross-sectional electron density distribution and has physical dimensions of conductance times length. The increase of L_NW with temperature can be used to extract Δ_0 as a function of gate voltage.

Increasing the gate voltage, the extracted superconducting gap decreases by 7 % from 270(1) µeV to 251(1) µeV (Fig. 3.4c). We note that at higher temperature, the onset of gate leakage shifts down to 5 V causing an increase in the fit uncertainty and interrupting the monotonous decrease of the gap with gate voltage. Moreover, we observe two distinct slopes: a shallow slope between −10 V and −2 V and a steeper slope between −2 V and 5 V. Similar observations have also been made in previous experiments on similar devices [86–89, 104]. We attribute the first regime to the strong hybridization of the InAs sub-bands with Al, and the second to an increase in the density in InAs with the occupation of new sub-bands. We do not observe a plateau in the bulk properties at negative gate voltages, which indicates that we have not reached the full depletion of the semiconductor. Whether the latter is possible at all depends on the value of the band-offset pinning the conduction band of InAs at the InAs/Al interface. If the band offset is too large, it may not be possible to reach full depletion by decreasing the gate voltage further, since eventually the gate may be screened by the accumulation of holes on the facets of the InAs nanowire closer to the gate electrode. [87]. We note that even over this large gate voltage range, the extracted gap remains finite. This observation does not rule out the possible onset, at positive gate voltages, of unproximitized states on the opposite side of Al-covered nanowire facets [89]. These states, if present, would not contribute considerably to the kinetic inductance.

Having determined the gate dependence of Δ_0, we can use Eq. (3.1) to extract σ_n using the values of L_NW measured at the lowest temperature (Fig. 3.4d). The resulting normal state conductivity increases by 10 % over the gate voltage range. This change in conductivity translates, for a nanowire length of 3 µm, to an increase in conductance of $\approx 3.9\, 2\mathrm{e}^2\mathrm{h}^{-1}$, giving a lower bound of 4 proximitized conduction channels added under the Al shell. Our measurement also yields a normal state resistance at −10 V of $R_\mathrm{n} = 365(1)\,\Omega$ or $R_\square = 13.4(1)\,\Omega\square^{-1}$, which is consistent with the expected values for a 3 µm long and 110 nm wide Al thin film [105]. The increase of conductivity with gate voltage overcompensates the simultaneous decrease of Δ_0 to determine the decrease of the inductance L_NW with gate voltage.

We note that the Mattis-Bardeen theory is formulated for a simple BCS superconductor and thus it does not capture the fact that the induced gap in the semiconductor could be different from that in the Al shell [106], and possibly varies among the proximitized sub-bands [87, 88, 107–109]. While these differences may cause strong deviations from the Mattis-Bardeen theory regarding the microwave absorption spectrum at frequencies comparable to the gap, the low-frequency inductive response of the condensate is likely to be less sensitive to the precise profile of the density of states. As a straightforward ansatz, it is therefore sensible to test the applicability of Eq. (3.1) to the data. A posteriori, the results reveal gate voltage trends that are consistent with those expected from detailed microscopic modeling of the field effect in the InAs/Al system [106, 109, 110], thus validating this simple approach. However, in order to fit the gate dependence of the data to microscopic parameters such as the hybridization strength between the two materials, an extension of the Mattis-Bardeen theory to proximitized systems would be required.

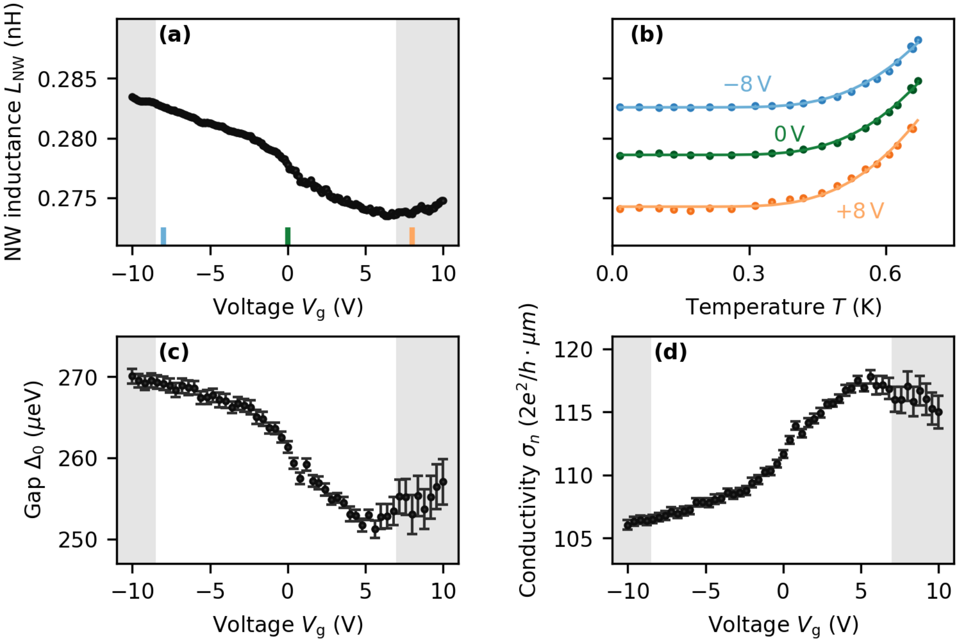

Figure 3.4.: Extracted nanowire parameters from resonator data shown in Fig 3.3. (a) Inductance of the nanowire resonator versus gate voltage extracted from loaded resonator model (see main text). (b) Nanowire resonator inductance versus temperature for three different gate voltages. Lines indicate fit to Matthis-Bardeen model. (c) Superconducting gap Δ_0 extracted from the fit to the temperature dependence for each gate voltage. (d) Normal state conductivity σ_n extracted from the fit to the temperature dependence for each gate voltage. The greyed-out areas indicate the regions of decreasing Q_i.

3.5. CONCLUSIONS

This experiment complements existing characterization methods for hybrid nanowires, which have been primarily based on low-frequency transport techniques [111–114]. The measurement of the microwave kinetic inductance allows us to directly probe the bulk properties of the hybrid nanowires, in contrast with measurement on devices with etched Josephson junctions, which are affected by the junction geometry and fabrication details. Given that the kinetic inductance gives access to the normal state conductivity in the proximitized nanowire, our method, if complemented with a capacitive measurement of the electron density via the bottom gate [115], could allow to extract the mobility of the semiconductor under the Al shell. Such a measurement could be of importance to determine whether the hybrid system meets the stringent disorder requirements for Majorana applications [116]. The value of resonator-based material characterisation in the context of hybrid systems has recently been demonstrated in 2DEGs [105].

Besides the fundamental interest to characterize hybrid nanowires, the presented approach offers a promising path towards gate-controlled superconducting electronics. In particular, the low loss and finite Kerr non-linearity will allow for frequency tunable resonators, switches, microwave detectors and parametric amplifiers [117]. In view of the potential application as frequency tunable resonators we report the frequency stability and hysteresis in the Appendix 3.10.6. The tunable frequency range can be enhanced by optimizing the choice of materials (e.g. including dielectrics with larger dielectric constants), the design of the gate electrodes, and the participation ratio of the nanowire inductance to the total resonator inductance.
The raw data and the data analysis code at the basis of the results presented in this work are available online [8].

ACKNOWLEDGEMENTS

We thank Peter Krogstrup for the supervision of the materials growth and Leo P. Kouwenhoven for support and discussion. We also thank Andrey Antipov and Andrew Higginbotham for their careful feedback on the manuscript. This research was co-funded by the allowance for Top consortia for Knowledge and Innovation (TKI) from the Dutch Ministry of Economic Affairs and the Microsoft Quantum initiative. CKA and BvH acknowledge financial support from the Dutch Research Council (NWO).

AUTHOR CONTRIBUTIONS

LJS, BvH and AK conceived the experiment. LJS fabricated the devices with help from MPV. Nanowires were grown by YL. LJS acquired and analysed the data with input from AB, LG, AK, CKA and BvH. LJS, CKA and BvH wrote the manuscript with input from all other co-authors. AK, CKA and BvH supervised the project.

3.6. FABRICATION

We fabricate the resonator circuit and the gate lines from a 35 nm-thick sputtered NbTiN film on low pressure chemical vapor deposition (LPCVD) SiN on Si. The kinetic sheet inductance of $5.31(5)\,\mathrm{pH}\square^{-1}$ has been measured using four reference resonators multiplexed to the same feedline, see Sec. 3.10.2. We pattern the ground plane using e-beam lithography and SF_6/O_2 based reactive ion etching. 30 nm-thick plasma enhanced chemical vapour deposition (PECVD) SiN serves as bottom gate dielectric. We transfer the two-facet InAs/Al nanowire on top of the SiN bottom gate with a nano-manipulator. The InAs nanowires were grown by vapor–liquid–solid (VLS) growth with a diameter of 110(5) nm, and nominal thickness of the Al of 6 nm [118]. We electrically contact the nanowires to the circuit via lift-off defined 150 nm-thick sputtered NbTiN leads after Ar milling which reduces the contact resistance. Similarly, we add top gates made from AlOx dielectrics and NbTiN to the design to overcome a possible lack of tunability due to the uncontrolled alignment of the Al shell with respect to the gates, but do not use them in this experiment as they got shorted to ground in a subsequent fabrication step. The grains visible in the SEM of the nanowire segment in the main text originate from polymer resist residuals.

3.7. MEASUREMENT SETUP

For the microwave spectroscopy, we use a RF transmission measurement setup installed in a dilution refrigerator operating at 15 mK base temperature, see Fig. 3.5. We probe the sample with resonators using a vector network analyser (VNA). The input line consists of microwave attenuators at room temperature (−20 dB) and at cryogenic temperatures (−70 dB). In addition, at each of the four temperature stages eccosorb filters with about 0.85 dB attenuation per 10 GHz are installed. The cables connecting the VNA to the 4 K plate add about 8 dB of attenuation. Then, NbTi cables connect to the 15 mK plate. We estimate the total input attenuation up to the sample plane to be −105(5) dB when accounting for the additional insertion loss of filters and other cable connections to the sample mount. The 5 dB uncertainty arises from the summation of the individual components measured at room temperature. Based on this attenuation we compute the intra-resonator photon number [96]

$$\bar{n} = \frac{2Q_t^2}{2\pi f_r Q_c} \frac{P_{in}}{h f_r}, \tag{3.2}$$

where Q_t is the total quality factor, Q_c is the coupling quality factor and P_in is the power at the input port of the sample. The intra-resonator photon number deviates from the true value by not more than a factor of 3.2 due to the uncertainty of the input attenuation.

The 2x7 mm chip on which the measurements are performed is glued with silver paint onto a gold plated copper mount and electrically connected to a printed circuit board using aluminium wire-bonds.

The output signal is amplified using a high electron mobility transistor amplifier at the 4 K stage. An isolator with 42 dB typical isolation prevents reflections. The directional coupler in the output line couples to an unused microwave line. The 10 GHz low pass filter at both input and output lines clean up the spectrum. DC blocks are placed at the breakout point of the fridge. A room temperature amplifier amplifies the signal before it enters the receiver port of the VNA.

The electrostatic gates are controlled via DC lines using a QuTech IVVI rack. The DC lines are low pass filtered at the mixing chamber stage.

3.8. RESONATOR FITTING

We use a background corrected linear notch type resonator model [119] to fit the acquired resonator data. The model is based on the scattering parameter of the resonator

$$S_{21} = 1 - \frac{Q_\mathrm{c}^{-1}(1+ia)}{Q_\mathrm{c}^{-1} + Q_\mathrm{i}^{-1} + 2idf}, \tag{3.3}$$

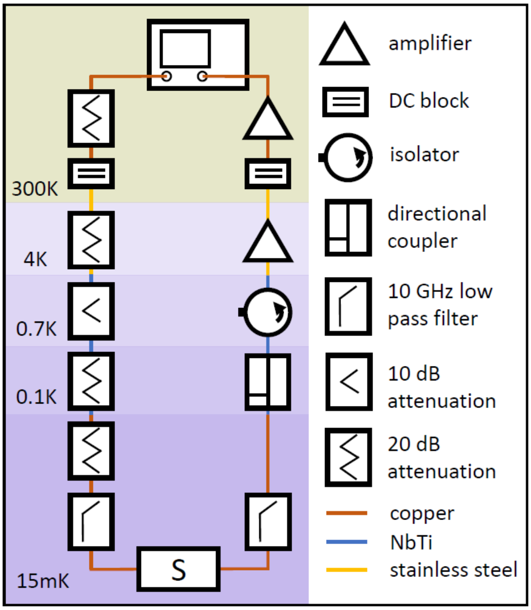

Figure 3.5.: Transmission measurement setup. A vector network analyser connected to highly attenuated input and amplified output line probes the sample (S) with resonators.

where $df = f/f_\mathrm{r} - 1$ is the frequency ratio, a is the asymmetry arising from the complex loading of the resonator, Q_c is the coupling quality factor and Q_i is the internal quality factor [94, 95]. We correct the scattering parameter of the resonator by multiplying a general background model to S_{21} and obtain the system scattering parameter

$$\tilde{S}_{21} = (m_0 + m_1 f)e^{2\pi i f\tau + i\varphi} S_{21}, \tag{3.4}$$

which we fit to the data. The background model includes a linear magnitude with offset m_0 and slope m_1 and a linear phase with offset φ and slope τ.

3.9. EXTRACTION OF NANOWIRE IMPEDANCE

We employ a loaded transmission line resonator model [120] to extract the impedance of the nanowire Z_NW from the measurement of the resonant frequency ω_NW and internal quality factor Q_i of the nanowire resonator. The input impedance of a transmission line of length l_0 loaded by an impedance Z_NW can be written as

$$Z_\mathrm{in} = Z_0 \frac{Z_\mathrm{NW} + Z_0 \tanh(\alpha_0 l_0 + i\beta l_0)}{Z_0 + Z_\mathrm{NW} \tanh(\alpha_0 l_0 + i\beta l_0)}. \tag{3.5}$$

Here, Z_0 is the frequency-dependent characteristic impedance of the transmission line, α_0 is the absorption coefficient, and β is the frequency-dependent propagation coefficient. The use of Eq. (3.5) is justified for our devices since the length of the nanowire is much shorter than that of the resonator.

We are interested in the input impedance close to the fundamental frequency of the nanowire resonator. In the limit of a small nanowire impedance, this frequency will be close to the fundamental frequency of the unloaded resonator, ω_0, which can be measured via the reference resonators, as discussed in the main text. We therefore expand Eq. (3.5) close to this frequency. Furthermore, we assume that the intrinsic losses are small, $\alpha_0 l_0 \ll 1$, thus the characteristic impedance reduces to $Z_0 = \sqrt{L/C}$, where L is the series inductance and C is the shunt capacitance per unit length of the transmission line. In the limit $|Z_{\mathrm{NW}}| \ll Z_0$ we obtain:

$$Z_{\mathrm{in}} \approx \frac{2\omega_0 Z_0}{\pi} \frac{1}{\frac{1}{2}\Gamma + i(\omega - \omega_{\mathrm{NW}})} \tag{3.6}$$

where ω_{NW} is the shifted resonant frequency of the nanowire resonator,

$$\omega_{\mathrm{NW}} = \omega_0 \left[1 - \frac{2}{\pi} \frac{\Im(Z_{\mathrm{NW}})}{Z_0}\right] \tag{3.7}$$

and Γ is the full-width at half-maximum, the sum of a contribution due to the intrinsic losses along the transmission line and a contribution coming from the nanowire:

$$\Gamma = \Gamma_0 + \Gamma_{\mathrm{NW}} = \frac{4\omega_0}{\pi} \left[\alpha_0 l_0 + \frac{\Re(Z_{\mathrm{NW}})}{Z_0}\right]. \tag{3.8}$$

The total internal quality factor of the nanowire resonator can therefore be given as:

$$Q_{\mathrm{i}}^{-1} = Q_0^{-1} + Q_{\mathrm{NW}}^{-1} \tag{3.9}$$

with $Q_0 = \omega_0/\Gamma_0$ and $Q_{\mathrm{NW}} = \omega_0/\Gamma_{\mathrm{NW}}$. Putting Eqs. (3.7) and (3.9) together, we obtain the nanowire impedance as a function of the measurable quantities $\omega_0, \omega_{\mathrm{NW}}, Q_{\mathrm{i}}, Q_0$:

$$Z_{\mathrm{NW}} = \frac{\pi Z_0}{4}\left(\frac{1}{Q_{\mathrm{i}}} - \frac{1}{Q_0}\right) + i\frac{\pi Z_0}{2}\frac{\omega_0 - \omega_{\mathrm{NW}}}{\omega_0} \tag{3.10}$$

This number has positive real and imaginary part for $Q_0 \geq Q_{\mathrm{i}}$ and $\omega_0 \geq \omega_{\mathrm{NW}}$.

3.10. COMPLEMENTARY MEASUREMENTS

3.10.1. NANOWIRE RESONATORS

During the course of this work, we prepared 11 samples with 4 nanowire resonators and 4 reference resonators each. In Tab. 3.1 and Fig. 3.6 and Fig. 3.7 we report the parameters and basic characterization of all 12 nanowire resonators exhibiting a gate voltage dependence. Other nanowire resonators were discarded because of shorted gates, highly resistive NbTiN to nanowire contacts or broken nanowires. The data which entered the main text is taken on a single nanowire resonator N2 and reference resonator R1 from sample S11. We consider the data set of S11 as representative for the entire set of measurements.

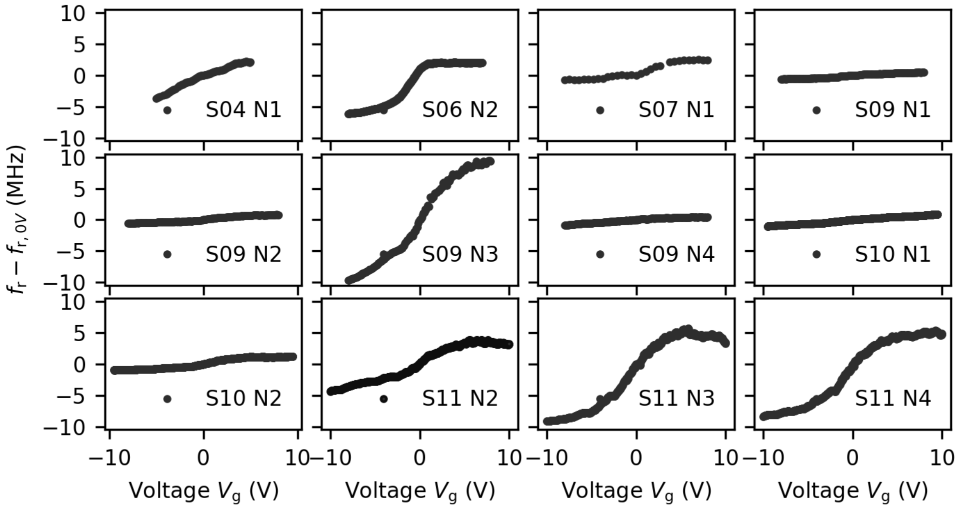

Figure 3.6.: Frequency shift as function of gate voltages extracted from fits to S_{21} data for 12 different nanowire resonators. The offset $f_{\mathrm{NW,0V}}$ is listed in Tab. 3.1.

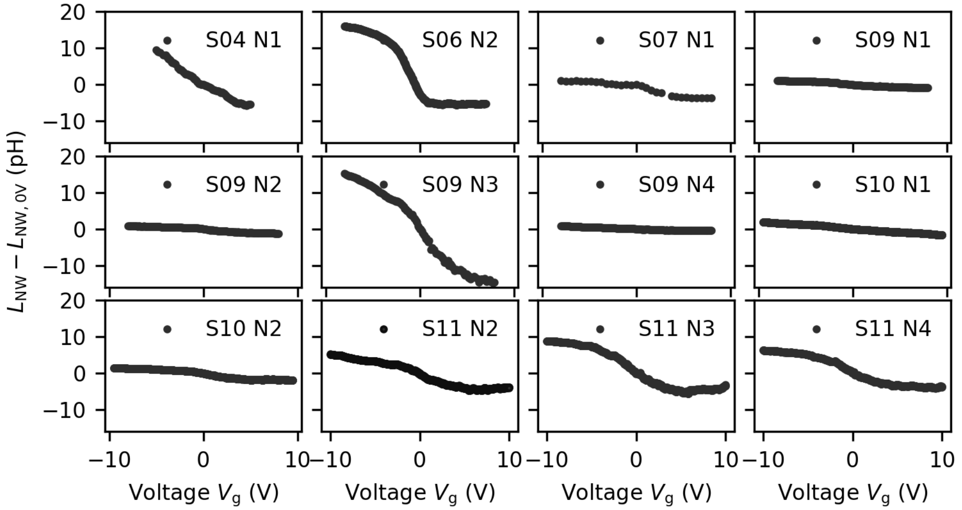

Figure 3.7.: Change in nanowire inductance as function of gate voltages for 12 different nanowire resonators. The offset $L_{\mathrm{NW,0V}}$ is different for each nanowire and listed in Tab. 3.1.

We design the nanowire resonators starting from the CPW resonators with $Z_0 \gg Z_{\mathrm{NW}}$ by adjusting the geometry, in particular width w, spacing s and length l of the CPW transmission line. The resonator parameters are listed in Tab. 3.1. For all nanowire resonator the coupling quality factor is $Q_c = 5.5 \times 10^3$. Based on the kinetic sheet inductance of NbTiN, we calculate the nanowire inductance. We also summarize further key quantities to compare the different nanowires.

label	w	s	l	L_k	L_{NW}	f_{NW}	ΔV_g	Δf_{NW}	ΔL_{NW}
	µm	µm	µm	$\mathrm{pH}\square^{-1}$	nH	GHz	V	MHz	pH
S04 N1	5	20	4898	5.50	0.45	3.629	10	5.9	15
S06 N2	5	20	4948	5.67	0.31	3.617	15	8.2	22
S07 N1	4	20	3200	5.45	0.62	5.087	16	3.2	5
S09 N1	5	20	3700	7.30	0.23	4.483	16	1.1	2
S09 N2	5	20	3290	7.30	0.31	4.973	16	1.4	2
S09 N3	5	20	2950	7.30	1.18	4.883	16	19.2	30
S09 N4	5	20	2650	7.30	0.37	6.046	16	1.3	1
S10 N1	5	20	3700	7.30	0.27	4.459	19	1.9	4
S10 N2	5	20	3290	7.30	0.30	4.978	19	2.2	3
S11 N2	5	20	3430	5.31	0.28	5.262	20	8.2	10
S11 N3	5	20	3030	5.31	0.33	5.873	20	14.9	15
S11 N4	5	20	2713	5.31	0.22	6.654	20	13.8	11

Table 3.1.: Overview of nanowire resonator parameters. In this paper we focus on the nanowire resonator denoted S11 N2. The designed width w, spacing s and length l of the CPW resonator as well as the kinetic sheet inductance per square of the NbTiN film L_k, the extracted inductance of the nanowire at 0 V, the measured resonance frequency at 0 V, the voltage range ΔV_g, the maximal change in frequency Δf_{NW} and the maximal change in inductance ΔL_{NW} are given.

In Fig. 3.6 we compare the gate voltage dependence of 12 nanowire resonators. We observe a monotonic increase in resonance frequency as a function of gate voltage. The frequency shift is quantified in Tab. 3.1 as Δf_{NW} over a voltage range of ΔV_g. The different magnitude of the frequency shift in the gate voltage scan arises from different participation ratios of nanowire to total inductance, but might also be a result of fluctuations between nanowires or due to the orientation of the Al shell relative to the bottom gate, potentially leading to gate screening for unfavourable orientations of the Al shell. We could not track the position of the Al shell relative to the bottom gate for each nanowire because of top gates encapsulating the nanowire.

The 12 measured nanowires differ in their configuration: they comprise devices with different gate geometries, different nanowire growths, and measurement in different cooldowns. In particular, S04 N1 and S06 N2 use a 2 µm long nanowire segment with a nanowire diameter of 80(5) nm, and a nominal thickness of the epitaxially grown Al of 6 nm. However, they all exhibit similar gate responses. From this observation, we conclude that the effect of gate-tunable kinetic inductance is reproducible in hybrid superconducting semiconducting nanowires from Al and InAs

label	w	s	l	L_k	f_r
	µm	µm	µm	pH$\square^{-1}$	GHz
S04 R1	5	20	2523	5.45	7.423
S04 R2	5	20	2573	5.55	7.239
S06 R1	5	20	2523	5.57	7.372
S06 R2	5	20	2573	5.77	7.155
S07 R1	4	20	4679	5.45	3.798
S09 R1	5	20	4600	7.3	3.704
S09 R2	5	20	2870	7.4	5.910
S10 R1	5	20	4600	7.3	3.709
S10 R2	5	20	2870	7.4	5.918
S11 R1	5	20	4662	5.35	4.042
S11 R2	5	20	4914	5.33	3.838
S11 R3	5	20	2561	5.34	7.360
S11 R4	5	20	2491	5.22	7.616

Table 3.2.: Overview of resonator parameters for all measured reference resonators labelled as sample SX with resonator RY. The designed width w, spacing s and length l of the CPW resonator as well as the extracted kinetic sheet inductance per square of the NbTiN film L_k, and the measured resonance frequency f_r are given. In this paper we focus on the reference resonator denoted S11 R1.

and not unique to a specific nanowire batch or fabrication process.

Fig. 3.7 shows the decreasing nanowire inductance versus gate voltage for 12 nanowire resonators. The change in inductance is quantified in Tab. 3.1 as ΔL_NW. Overall, the inductance values are similar within a factor of 2 for most nanowires. The variations between the experiments probably arise from different residual inductances at the NbTiN to nanowire interface. These residual inductances do not appear in the reference resonators and thus are specific to the nanowire resonator.

3.10.2. REFERENCE RESONATORS

The reference resonator consists of a quarter-wave coplanar waveguide resonators capacitively coupled to a feedline and shorted to ground via a thick NbTiN patch instead of a proximitized nanowire as shown in Fig. 3.8a. Two LC filtered pads left to the resonator connect to the electrostatic gates in the vicinity of the NbTiN patch. However, these gates are not used. The micrograph of the NbTiN film in Fig. 3.8c shows the 3 µm long and 1 µm wide NbTiN patch encapsulated by voltage bottom and top gates to mimic the same electromagnetic environment as for the nanowire resonator. The cut away in Fig. 3.8d illustrates the difference to the nanowire resonator shown in the main text in Fig. 1d. This direct comparison allows us to test the device quality in this multi-step fabrication and the superconducting NbTiN to NbTiN contact. The reference resonator can be modelled with the equivalent circuit in Fig. 3.8b. The transmission line resonator with characteristic impedance Z_0 identical to the nanowire resonator, but different resonator impedance is capacitively coupled (C_C) to the feedline with characteristic impedance $Z_\mathrm{L} = 50\,\Omega$. Port 1 and 2 connect to the external measurement setup.

For the experiment, we design CPW resonators with identical transmission line impedance as the nanowire resonator, but different length l. The resonator parameters are listed in Tab 3.2. We extract the kinetic sheet inductance per square of the NbTiN film L_k from the reference resonator by comparing the measured resonance frequencies with microwave simulations (AWR Microwave Office) of the full resonator design and numerical calculations based on a conformal mapping technique for CPW transmission lines [101]. We obtain the kinetic sheet inductance from the average over all reference resonators per sample.

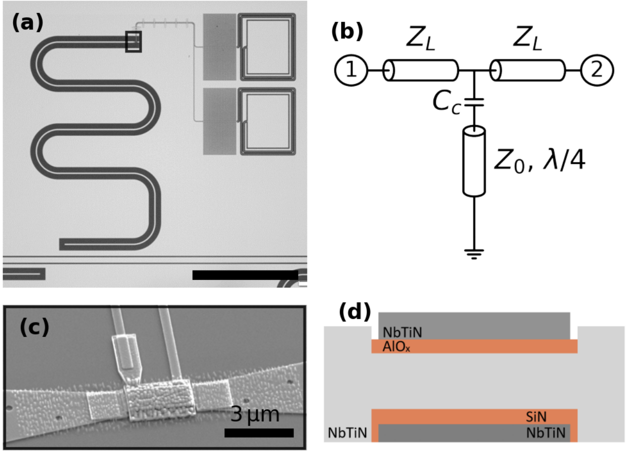

Figure 3.8.: Measured reference device. (a) Optical image of one quarter-wave coplanar waveguide resonator capacitively coupled to a feedline and shorted to ground via a thick NbTiN film instead of a proximitized nanowire. Two LC filtered pads left to the resonator connect to the electrostatic gates in the vicinity of the NbTiN film. (scale bar 300 µm) (b) Circuit diagram of a measured device. The transmission line resonator with impedance Z_0 is shunted to ground by a thick NbTiN film, and capacitively coupled (C_C) to the feedline with characteristic impedance $Z_\mathrm{L} = 50\,\Omega$. Port 1 and 2 connect to the external measurement setup. (c) Micrograph of the NbTiN film which is galvanically connected to the central conductor of the resonator [black box in (a)]. The 3 µm long NbTiN patch is encapsulated by voltage bottom and top gates. Here, neither of the gates is used. (d) Schematic longitudinal cut away of reference structure used for comparison with the nanowire resonator. The nanowire section is replaced by a continuous 150 nm thick NbTiN film.

3.10.3. GEOMETRIC INDUCTANCE OF NANOWIRE SEGMENT

We estimate the geometric inductance of the nanowire segment using a conformal mapping technique [101]. For a 100 nm wide and 3 µm long wire in a CPW geometry with 22 µm spacing to ground, we find a geometric inductance of 4.5 pH. This is about 2 % of the total nanowire inductance. This systematic error falls into the uncertainty of the nanowire inductance, thus we neglect the geometric contribution arising from the magnetic self-inductance.

3.10.4. RESONATOR BIFURCATION

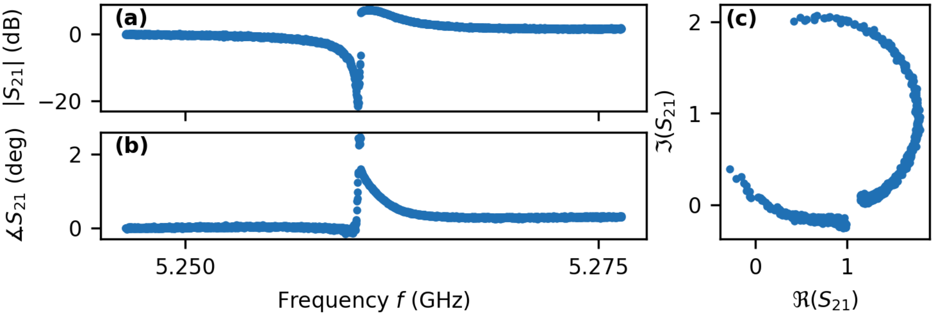

Figure 3.9.: Scattering parameter S_{21} of bifurcating nanowire resonance in magnitude (a), phase (b) versus frequency and in the complex plane (c) at −113 dBm input power at the reference plane of the resonator.

Superconducting resonators can exhibit nonlinear behaviour including bifurcation if driven with sufficiently large input power [121]. Fig. 3.9 shows the scattering parameter of a nanowire resonator in magnitude (a), phase (b) versus frequency and in the complex plane (c) at −113 dBm input power at the reference plane of the resonator. The discontinuity of the circle in Fig. 3.9 indicates a bifurcation behaviour at high readout powers. In the main text we limit our studies to the regime of few intra-cavity photons where the signal to noise ratio is sufficient for readout, but where the resonator does not bifurcate.

3.10.5. GATE LEAKAGE

Fig. 3.10a shows the frequency shift of about 13 MHz as function of gate voltages for nanowire resonator S11 N4 in the first scan of the experiment and after exceeding a gate voltage of |10 V| multiple times. Between the two experiments, we observe a different slope around 0 V, but otherwise the same magnitude of the frequency shift.

In Fig. 3.10b, while measuring the frequency response of S11 N4 between −12 V and 12 V, we record the leakage current through the bottom gate, which increases linearly by about 1 nA. We attribute the sharp drop in internal quality factor (see Fig. 3a) at large applied gate voltages to the point where the injection of quasi-particles through the bottom gate reduces the superconducting gap measurably. This is in

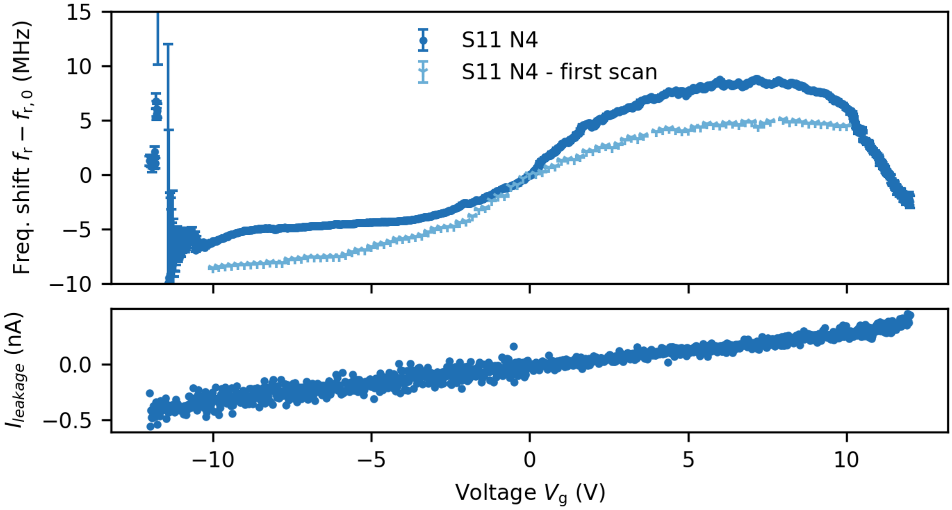

Figure 3.10.: Gate leakage of nanowire resonator 4. (a) Frequency shift as function of gate voltages extracted from fits to S_{21} data for resonator S11 N4 in the first scan of the experiment and later after exceeding a gate voltage of |10 V|. (b) Leakage current versus gate voltage measured during voltage sweep in the latter case.

line with the slightly asymmetric onset in the reduction of the internal quality factor for positive and negative voltages. The data shown in the main text has been taken after exceeding voltages of |10 V|. We note however that the trends in frequency and internal quality factor versus the control parameters do not seem to be affected in the voltage range from −8 V to 8 V.

3.10.6. GATE STABILITY AND HYSTERESIS

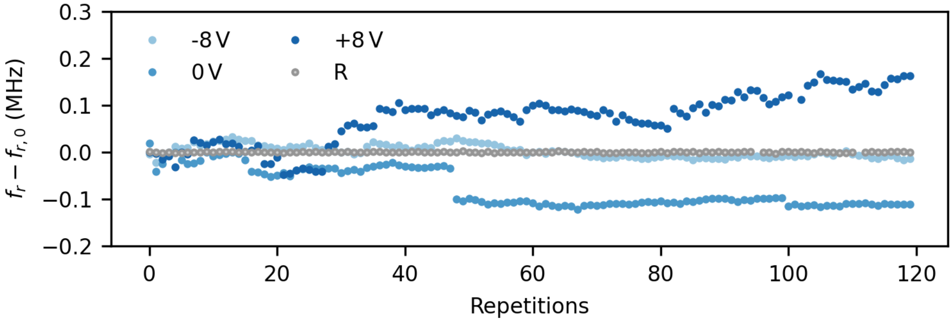

Figure 3.11.: Gate voltage stability. Frequency shift of nanowire resonator for three different gate voltages and frequency shift of reference resonator for 120 repetitions with 30 s waiting time between measurement point.

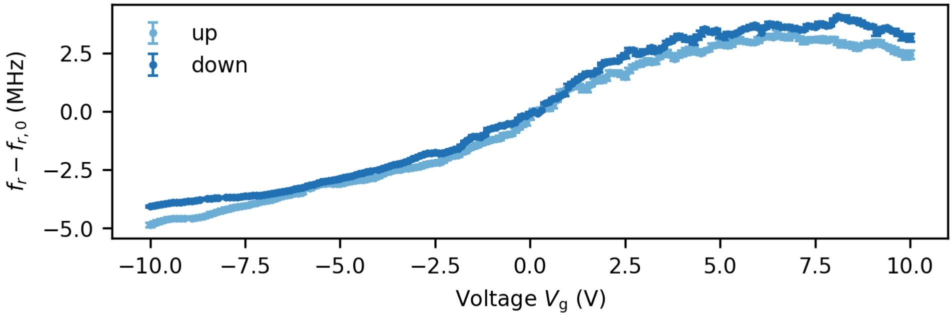

Figure 3.12.: Gate voltage hysteresis. Average frequency shift of nanowire resonator over 4 gate voltage scans per sweep direction.

In view of possible applications for frequency tunable resonators we study the frequency stability over time and the gate hysteresis. Fig. 3.11 shows the frequency shift of the nanowire resonator S11 N2 for three different gate voltages and the frequency shift of the reference resonator S11 R1 for 120 repetitions with 30 s waiting time between measurements point. The reference resonator exhibits a constant frequency in time. Only small variations on the few kHz scale can be observed. The behaviour of the nanowire resonator however differs from the reference resonator. For negative gate voltages, the fluctuations in time are on the order of 50 kHz, but the trend is relatively flat otherwise. The more positive we set the gate voltage, the more jumps and drifts appear in the time dependence. We speculate that at this gate voltage sudden reconfigurations of the charge carrier distribution in the nanowire happen.

Fig. 3.12 shows the average frequency shift of the nanowire resonator for four gate voltage scans per sweep direction with a reset to zero volt between each scan. The error bar represents the standard deviation and is small compared to the total frequency shift. The size of the error bar is nearly equal over the entire range of gate voltages. We note the offset between the up and down sweeps originating from gate hysteresis or a reconfiguration of the charge carrier distribution.

4

GATE-TUNABLE KINETIC INDUCTANCE PARAMETRIC AMPLIFIER

Lukas Johannes Splitthoff, Jaap Joachim Wesdorp, Marta Pita-Vidal, Arno Bargerbos, Yu Liu, Christian Kraglund Andersen

Superconducting parametric amplifiers play a crucial role in the preparation and readout of quantum states at microwave frequencies, enabling high-fidelity measurements of superconducting qubits. Most existing implementations of these amplifiers rely on the nonlinearity from Josephson junctions, superconducting quantum interference devices or disordered superconductors. Additionally, frequency tunability arises typically from either flux or current biasing. In contrast, semiconductor-based parametric amplifiers are tunable by local electric fields, which impose a smaller thermal load on the cryogenic setup than current and flux biasing and lead to vanishing crosstalk to other on-chip quantum systems. In this work, we present a gate-tunable parametric amplifier that operates without Josephson junctions, utilizing a proximitized semiconducting nanowire. This design achieves near-quantum-limited performance, featuring more than 20 dB *gain and a* 30 MHz *gain-bandwidth product. The absence of Josephson junctions allows for advantages, including substantial saturation powers of* −120 dBm, *magnetic field compatibility up to* 500 mT *and frequency tunability over a range of* 15 MHz. *Our realization of a parametric amplifier supplements efforts towards gate-controlled superconducting electronics, further advancing the abilities for high-performing quantum measurements of semiconductor-based and superconducting quantum devices.*

This chapter has been published in Phys. Rev. Applied 21, 014052 (2024) as editor's suggestion.

4.1. INTRODUCTION

In the pursuit of advancing quantum technologies, the extraction and amplification of weak quantum signals have emerged as crucial challenges in all known qubit platforms, especially those operating in cryogenic environments. The amplification chains required for weak signals must be carefully designed to exhibit specific characteristics, including high gain, wide amplification bandwidth, and large saturation power while maintaining minimal added noise, to maximize the signal-to-noise ratio (SNR) for high-performing readout [15, 40, 41]. Superconducting parametric amplifiers (PAs) based on Josephson junctions already play a pivotal role in the first stage of amplification chains in superconducting qubit platforms. By adding only the minimal amount of noise permitted by the laws of quantum mechanics, these amplifiers have proven invaluable for amplifying weak microwave signals encoding the quantum state of superconducting qubits [16, 54, 122–125]. Other quantum systems, including spin-qubit implementations [126–130], and novel types of hybrid semiconductor-superconductor qubits [5, 131–133], as well as condensed-matter experiments [134, 135] are generally operated under magnetic fields and therefore require magnetic-field-compatible parametric amplifiers. An additionally desired feature is minimal crosstalk to sensitive structures in the vicinity of the amplifier, such as flux-tunable qubits. However, conventional superconducting parametric amplifiers with flux-biased [17–21] or current-biased [22] control are impractical to operate near flux-sensitive elements. Surpassing these limitations necessitates the development of novel types of parametric amplifiers combining magnetic field compatibility with a new source of tunability.

Recent technological advances in the integration of exotic heterostructures into superconducting circuits, such as hybrid superconducting-semiconducting nanostructures [5, 7, 8, 90, 136–138], graphene Josephson junctions [134, 139, 140], or carbon-nanotube junctions [141], have enabled the realization of electrostatic control of supercurrents in superconducting circuits. This additional method of tunability has already opened up new avenues to build novel types of parametric amplifiers from graphene [25, 26] and proximitized semiconductors [27], further advancing the development of densely packed superconducting electronics due to minimal crosstalk. Concurrently, magnetic field compatibility of parametric amplifiers has been achieved through the use of superconducting thin films acting as kinetic inductance material [28–30].

In this work, we leverage the continuous superconducting aluminum thin film on an InAs nanowire, which can be seen as a chain of infinitesimally short, gate-tunable Josephson junctions to experimentally demonstrate a magnetic-field-compatible, gate-tunable kinetic inductance parametric amplifier composed of an InAs/Al nanowire shunting a NbTiN coplanar-waveguide resonator [8]. Notably, the parametric amplifier presented in this work features a gate-tunable amplification window, and magnetic field compatibility resulting from the superconducting thin film and the Josephson-junction-free design. Moreover, the amplifier exhibits a substantial saturation power and increased resilience against electrostatic discharge compared to Josephson-junction-based implementations, owing to the continuous superconducting film.

4.2. EXPERIMENTAL SETUP

In our realization, we use a quarter-wave coplanar-waveguide resonator that is capacitively coupled to a launch pad at one end and shorted to ground via a proximitized InAs/Al nanowire; see Fig. 4.1a. The frequency of the resonator is controlled using a dc voltage applied to the gate line (see purple structure in Fig. 4.1a). To minimize losses of the coplanar waveguide, we implement a fifth-order Chebyshev LC filter that suppresses coupling to the gate line by at least 50 dB within a frequency range of 4 – 8 GHz; see Appendix 4.5 for additional details on the device design and the LC filter. For electrostatic control, we follow Ref. [8] and place the nanowire of length $l = 4.5\,\mu\text{m}$ on an electrostatic voltage gate that extends for 3.5 µm below the nanowire segment; see Fig. 4.1b. The nanowire section is directly connected to the central conductor of the resonator and to ground via thick NbTiN patches. The schematic representation of the proximitized nanowire in Fig. 4.1c highlights the continuous Al shell covering two facets of the InAs nanowire [118]. We maximize the magnetic field compatibility by aligning the magnetic field parallel ($B_{\parallel}$) with the nanowire.

The nanowire-shunted resonator is expected to exhibit a nonlinear Kerr-type behavior when driven near resonance, where the resonance frequency shifts linearly with respect to the number of microwave photons occupying the resonator mode; see also Appendix 4.6. As a result, it is natural to use the nonlinear resonator as a parametric amplifier in the nondegenerate mode, which preserves the phase of the input signal. This mode of operation takes advantage of the four-wave-mixing process occurring within a Kerr oscillator. This process involves the interaction of two pump photons, at frequency f_p, and one signal photon, at frequency f_s, leading to the conversion of a pair of pump photons into an idler photon at f_i and an additional signal photon, which therefore leads to amplification of the signal tone (as illustrated in Fig. 4.1d). We integrate a circulator at the input to the device to ensure that the signal and pump photons pass through the parametric amplifier, while also maintaining the desired directionality from the input to the output spectrum. Overall, this experimental configuration enables efficient phase-preserving amplification of the input signal, see also Appendix 4.7 for a detailed description of the experimental setup.

4.3. EXPERIMENTAL RESULTS

4.3.1. GATE-TUNABLE NONLINEAR RESONATOR

To characterize the parametric amplifier, we start by measuring the complex transmission parameter S_{21} between input port and output port to extract the resonance frequency of the resonator as well as the internal and coupling quality factors. These quantities are extracted from a fit to a complex Lorentzian as expected for linear, reflection-type resonators [94, 95]. The resonance frequency is tunable with the gate voltage and we observe a monotonic increase in resonance frequency for voltages within the range of -3V to 7V; see Fig. 4.2a. The shift of about 15 MHz arises from a change in the kinetic inductance associated with the proximitized nanowire, as shown in Ref. [8]. The nearby voltage gate controls the charge carrier

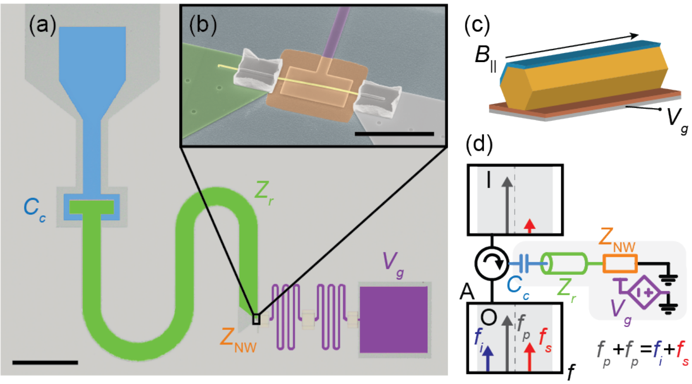

Figure 4.1.: Device and equivalent circuit. (a) False-color optical-microscope image of a gate-tunable parametric amplifier comprising a quarter-wave coplanar-waveguide resonator (green) that is capacitively coupled to the reflection port (blue) and shorted to ground (light gray) via a proximitized nanowire (yellow). The gate line with a fifth-order Chebyshev LC filter (purple) suppresses the crosstalk between the resonator and the gate line. (scale bar 250 µm). (b) Electron micrograph of the nanowire segment. The nanowire is connected with thick NbTiN patches to the resonator and ground. (scale bar 5 µm). (c) Schematic representation of the InAs nanowire (yellow) that is proximitized with a continuous Al shell (blue) on two facets and positioned on a voltage gate (gray) with a dielectric (orange). (d) Equivalent circuit of the parametric amplifier and representation of the four-wave mixing operation showing the signal amplitude A as a function of frequency f. At the input (I), a pump tone (gray) at a frequency f_p and a signal (red) with a frequency f_s enter the nonlinear resonator. At the output (O), the signal is amplified and there is an additional idler tone with frequency f_i. The dashed line indicates the central frequency of the undriven resonator and the gray box is the amplifier bandwidth.

density in the nanowire and hence the normal-state conductivity, which dominates the high-frequency response. At the same time, the superconducting gap closes only partially with increasing gate voltage. To characterize the nonlinearity of the resonator, we increase the power of the spectroscopy tone and we extract a Kerr coefficient K as the linear slope of the resonator frequency as a function of inferred photon number inside the resonator. We find $K \approx 20\,\mathrm{kHz}$ for all gate voltages, which lies between typical values reported for parametric amplifiers based on a single junction [25] and for kinetic-inductance-based amplifiers [28]. The flat response versus gate voltage facilitates a robust tune-up of the device in contrast to previous voltage-tunable junction-based systems, where the Kerr coefficient strongly depends on the gate voltage [25–27]. The internal quality factor increases slightly over the accessible gate-voltage range starting at $Q_i \sim 4000$, whereas the coupling quality factor stays nearly constant at $Q_c \sim 50$. The increase in Q_i could be attributed to the finite gap at all gate voltages and the addition of further conduction channels with more-positive gate voltage, although a detailed study of the internal-loss mechanism is beyond what can be extracted from simple spectroscopy measurements. In addition, we observe a small, although negligible for the applications considered here, reduction of Q_i due to nonlinear losses (see Fig. 4.7). Outside of the -3V to 7V voltage range, indicated by gray boxes in Fig. 4.2, the resonator coherence is suppressed by gate leakage. The n-doped Si substrate forms a Schottky junction below about -3V voltage bias leading to the injection of quasiparticles. Above 7V, we observe the breakdown of the SiN gate dielectric. These range limitations could be mitigated in the future by alternative material choices for the dielectric medium.

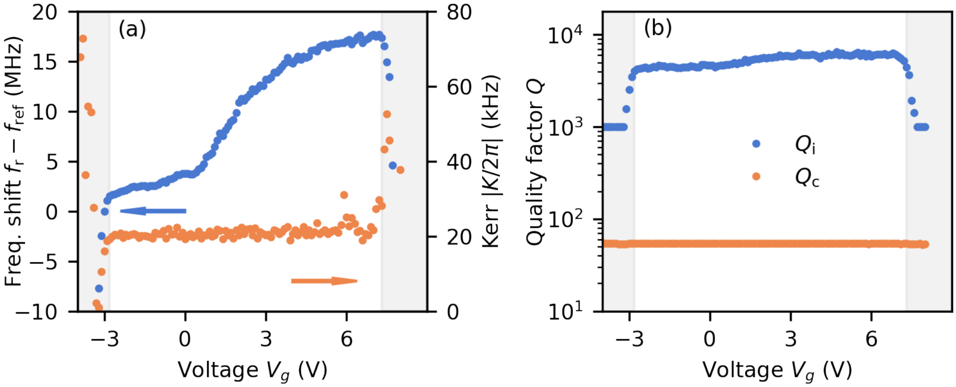

Figure 4.2.: Gate-tunable nonlinear resonator. (a) Frequency shift (blue, left axis) relative to the reference frequency f_{ref} measured at $V_g = -3$V and Kerr coefficient K (orange, right axis) as function of gate voltage, V_g. (b) Internal quality factor Q_i (blue) and coupling quality factor Q_c (orange) as a function of gate voltage V_g. The gray shaded areas indicate regions of suppressed resonator quality for gate voltages below -3V and above 7V.

4.3.2. AMPLIFIER CHARACTERISTICS

Next, we demonstrate that the nonlinear resonator can be operated as a parametric amplifier. We apply a strong pump tone slightly detuned from the bare resonance frequency and we measure the signal gain for signal frequencies in the vicinity of the pump; see Fig. 4.3(a). Notably, we find that by changing the gate voltage, the points of maximal gain shift to different frequencies, exemplified for five different gate voltages in Fig. 4.3(a). Specifically, we find that the amplifier exhibits more than 20dB gain in all tested configurations, yielding a gate-tunable amplification window of more than 15MHz. In nominally identical devices but different experimental realizations, we have observed accessible frequency tuning ranges of more than 70MHz. It is important to note that the gate dependence of the parametric amplifier's working point exhibits a nonmonotonic behavior, which is in contrast to the monotonic frequency response observed in Fig. 4.2a, resulting from an interplay between the linear and nonlinear inductances. However, while the gate dependence of the optimal working point cannot be a priori predicted, we find only a weak hysteresis versus gate voltage, as reported in earlier work [8], which allows a robust and efficient tune-up as well as stable operation over days of the parametric amplifier.

We fit the signal-gain curve with a double-Lorentzian model that captures both the up-to 15 dB broadband amplification window (orange) and the narrowband mode (purple) centered at the pump frequency; see Fig. 4.3a. This double-Lorentzian behavior may arise from the presence of a parasitic mode, most likely a box mode stemming from the sample enclosure. Note that the fit underestimates the maximal gain observed in the gain curve. Despite this complex mode structure, we extract the maximal signal gain G_0 of the fitted response versus pump power P_p and find a stable working range of 0.1 dB with more than 20 dB gain, see Fig. 4.3b, which exemplifies the trend at a gate setting of 4 V. The bandwidths of the two respective modes Δf_1 and Δf_2 evolve nonmonotonically as a function of power. While Δf_1 increases for pump powers above -1.25 dB, Δf_2 stays nearly constant. The trend of the gain curve (red) and the contribution to the bandwidth of the broad mode (orange) can be explained by considering a single-mode-Kerr-resonator model for a fixed pump frequency ω_p and a variable pump strength ξ. Since the optimal pump frequency depends on the pump power, the system deviates from the optimal pump condition and the low-order approximation yielding a constant gain-bandwidth product breaks down. Instead, we expect a minimal bandwidth (orange curve) at the point of maximal gain (red), which is in agreement with the data shown in Fig. 4.3b around -1.25 dBm. For larger pump powers, the bandwidth increases and the gain decreases as expected but because of the second mode we do not reach the coupling-limited gain-bandwidth product. This simple description does not capture the regime of pump powers below -1.4 dBm, when the distinction of the two modes becomes unreliable due to the small gain and small bandwidth. Consequently, the gain-bandwidth product of neither mode reaches the bandwidth limit of 128 MHz set by the coupling quality factor of the resonator, as would be expected for an ideal single-mode Kerr resonator close to the optimal pump condition. To characterize the dynamic range of amplification, we record the maximal signal gain G_0, directly extracted from the data, versus signal power, as shown in Fig. 4.3c for three different pump powers as indicated with colored dots in Fig. 4.3b. With increasing signal power the signal gain overall reduces due to a deviation from the stiff pumping condition [40, 41]. For a weak signal gain of 20 dB we observe a 1 dB compression point of -120 dBm, which is on par with the saturation powers reported in work on other capacitively coupled superconducting-quantum-interference-device (SQUID), SQUID-array, single-junction and gate-tunable-junction implementations [25–27] (see also Tab. 2.1) and should allow frequency-multiplexed qubit readout given a sufficiently large amplification bandwidth. The sharp rise in the signal gain before its overall decrease, sometimes referred to as a “shark fin”, results from an interplay between the input signal and the internal dynamics of the parametric amplifier due to higher-order nonlinear terms at negative pump detuning. This gain-rise phenomenon has been observed experimentally [21, 51] and has been described theoretically [23, 52, 53].

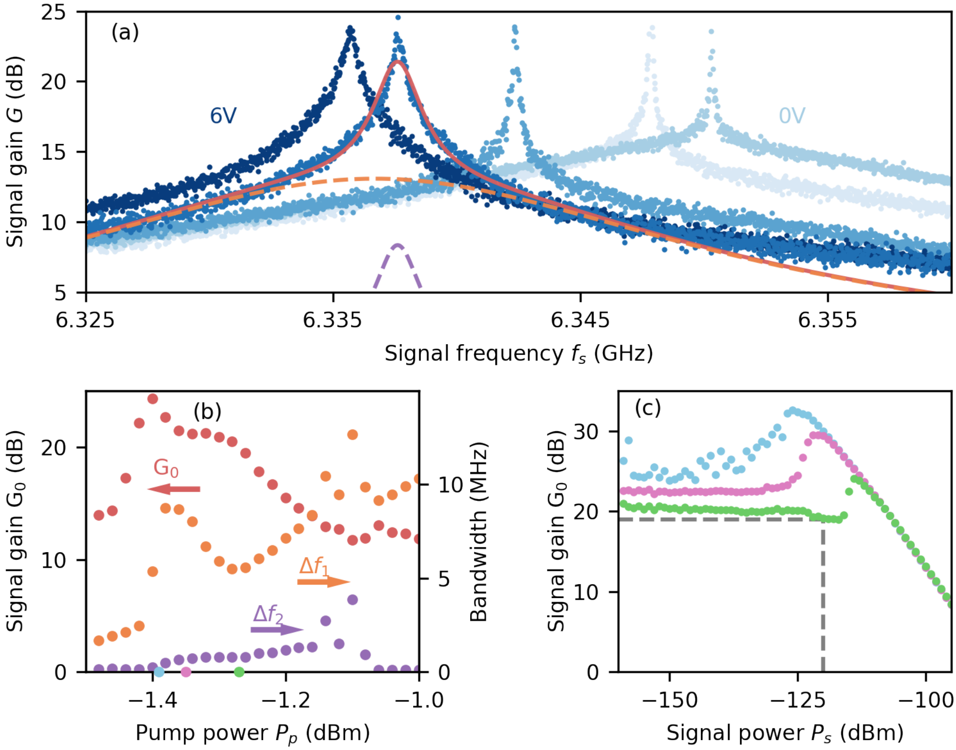

Figure 4.3.: Amplifier characteristics. (a) Signal gain versus signal frequency for different gate-voltage settings [6 V, 4 V, 2 V, 0 V, and −2 V] from dark to light shades. The solid red curve shows the best fit of a double Lorentzian to the gain curve. The dashed purple and orange curves show the individual single-Lorentzian curves composing the fits. (b) Signal gain, G_0 and bandwidths of the two Lorentzian curves, Δf_1 and Δf_2, as a function of pump power at the signal generator, P_p, at room temperature. (c) Signal gain as a function of referred signal power at the PA input, P_s, for three different pump powers indicated on the x axis of (b) with color-matching markers.

4.3.3. NOISE PERFORMANCE

While large gain is desirable for parametric amplifiers, it should come without the cost of additional added noise beyond the quantum limit, in order to not degrade the amplifier performance. We generally quantify the quality of a signal by considering the SNR. Specifically, we compare the power level of the signal to the power level when the signal is turned off or, more practically, the power level slightly detuned from the signal. For an amplifier, we can define the SNR improvement as the difference in the SNR between the ON and OFF state of the amplifier $\Delta\text{SNR} = \text{SNR}_{\text{on}} - \text{SNR}_{\text{off}}$ which serves as a good measure for its noise characteristic.

For the parametric amplifier that we study here, we find that the SNR improvement depends strongly on the pump power and pump frequency as shown in Fig. 4.4a, measured at a gate voltage of 4 V and at a signal-pump detuning of $\Delta = 0.5$ MHz. The SNR improvement reaches a maximum of about 7 dB, which is about 2 dB lower than the theoretical maximum set by the difference between the noise temperature of the high-electron-mobility-transistor (HEMT) amplifier and the quantum limit (QL) [49]; see Fig. 4.4(b). It is worth noting that the maximal SNR improvement versus pump power presented in Fig. 4.4c does not coincide with the maximum in the gain curve, but shows a peak at about 15 dB signal gain. Note that we slightly compress an amplifier at room temperature when maximal gain is being approached, which might have led to the slight shift between the point of maximal gain with respect to the point of maximal SNR improvement in Fig. 4.4c. Also note that the working point of the parametric amplifier has shifted by about 10 MHz compared with the data shown in Fig. 4.2a after many gate scans, which might have led to a different charge configuration in the nanowire [142] and hence to a slightly different working point. In Fig. 4.4b, we compare the spectrum obtained for a single pump tone between the driven state and undriven state of the parametric amplifier. In the undriven case, the noise is limited by HEMT amplifier at the 4K-stage of the cryostat. The referred power, and hence the effective noise temperature, is estimated on the basis of a line calibration supported by an estimate based on the dispersive shift of an adjacent on-chip transmon qubit connected to the input port (see Appendix 4.8). In the undriven case we observe the signal tone at 6.3134 GHz and the pump tone leaking through the output of the signal generator, while the noise floor is set by the noise temperature of the HEMT, which is close to the manufacturer-specified value of 2.2 K indicated as a horizontal gray line. In the driven case, the signal amplitude increases together with the appearance of an idler tone of about the same magnitude, while the noise floor drops below the noise floor of the HEMT, showcasing the usefulness of the parametric amplifier presented here. While the improvement in SNR is noteworthy, we also observe that the performance is not fully quantum limited as we do not reach the quantum limit of 303 mK, indicated by a dashed gray line. The inability to reach the quantum limit signals the presence of an additional loss channel in the system, which is consistent with the observations of an additional mode in Fig. 4.3.

4.3.4. MAGNETIC FIELD COMPATIBILITY

The continuous superconducting thin film renders amplification at high magnetic field strength possible, since the superconducting gap is not locally suppressed inside a Josephson junction potentially leading to interference effects. In particular, we are interested in magnetic fields of up to a few hundred milliteslas as used for a variety of spin-based devices [129] and hybrid superconductor-semiconductor devices [131, 133]. When the magnetic field, $B_{\parallel}$, is aligned with the nanowire direction, the compatibility with the magnetic field should be maximal and we observe up to 20 dB gain at fields up to 0.5 T; see Fig. 4.5. Moreover, at 0.5 T, we see maximal gain at a 170 MHz lower signal frequency compared with the zero field setting. The overall shift of the amplification window towards lower frequencies along with the increase in the

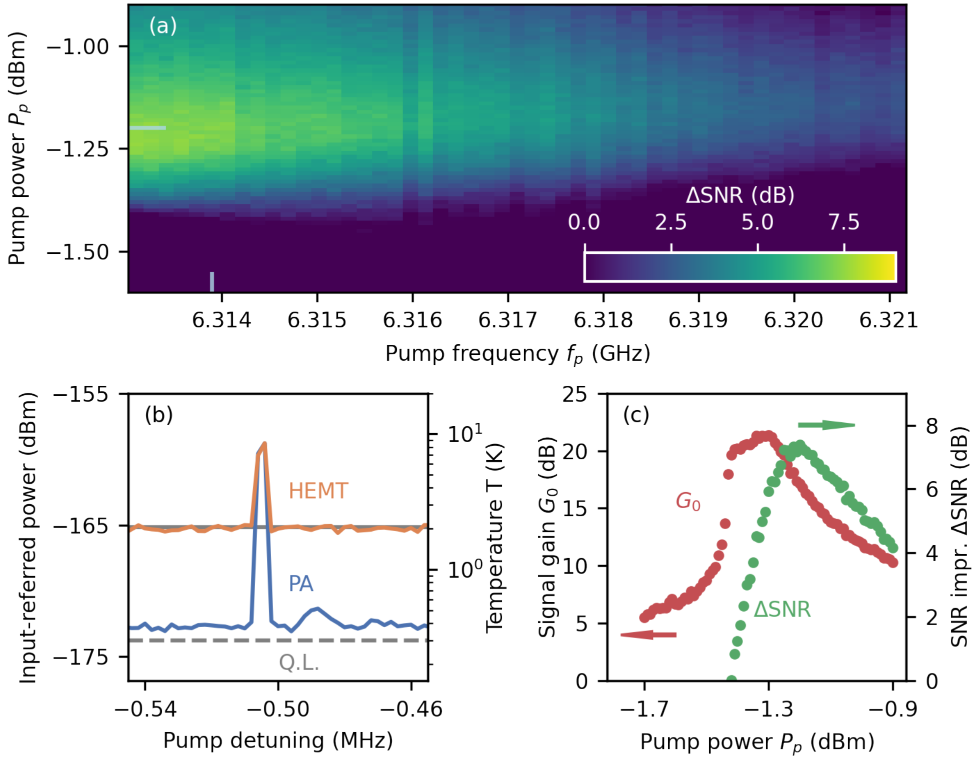

Figure 4.4.: SNR improvement. (a) Change in the SNR as a function of pump power, P_p, and pump frequency, f_p, for a fixed detuning between the signal frequency and pump frequency of 0.5 MHz. Light-blue lines indicate the working point used for the trace shown in (b). (b) Input-referred power spectrum with signal tone at 6.3134 GHz and pump tone at 6.3139 GHz in the undriven (orange) and driven (blue) cases. The dashed lines indicate the quantum limit (QL) and the specified noise temperature of the HEMT amplifier for a resolution bandwidth of 1 kHz. For comparison, the equivalent temperature is provided on the right axis. (c) Signal gain (red, left axis) and SNR improvement (green, right axis) versus pump power for $f_p = 6.3139$ GHz.

Kerr coefficients follows from the continuous suppression of the superconducting gap with increasing magnetic field [8]. The nonmonotonicity of the frequency shift and the lower maximal gain can be attributed to the nucleation of vortices in the heterostructure of finite thickness and to small field misalignments [143], a scenario that is most likely unavoidable in real applications of this amplifier. The distortion of the gain curves in Fig.4.5 arises most likely from a Fano interference with a broad box mode [144]. We did not explore the magnetic field dependence of the parametric amplifier beyond 0.5 T, nor did we characterise the noise performance at elevated magnetic fields due to technical limitations imposed by the dilution refrigerator that prevented us from maintaining an elevated field while keeping the base temperature cold. However, we do not expect a significant change in the noise performance as the resonator loss rate γ remains smaller than the coupling strength κ. While an increase in the resonator loss rate γ is unavoidable, previous work on similar hybrid systems allowed the realization of a transmon qubit operated at 1 T [91], which shows that the fabrication of coherent devices at elevated magnetic field is possible. Note that this dataset was taken in a consequent cooldown, which again led to a different charge configuration in the nanowire and hence a different working point.

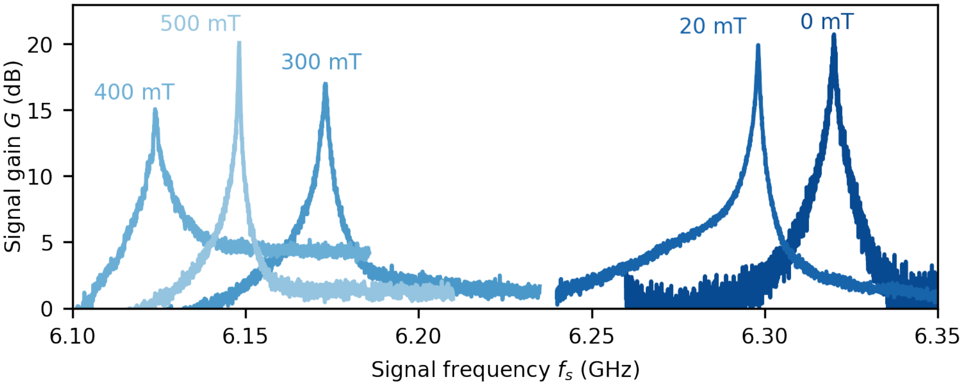

Figure 4.5.: Magnetic field compatibility. Signal gain versus signal frequency for different parallel-magnetic-field strengths of 0 mT, 20 mT, 300 mT, 400 mT, and 500 mT.

4.4. CONCLUSION

We experimentally demonstrated a prototype of a gate-tunable kinetic inductance parametric amplifier. This system features a gate-tunable amplification window of up to 15 MHz due to the hybrid superconducting-semiconducting nanostructure, magnetic field compatibility up to at least 500 mT due to the superconducting thin film, a sizeable saturation power of −120 dBm and minimal electrostatic discharge sensitivity due to the continuous superconducting film. The tuning range of the amplification window should already be sufficient to render frequency matching with other superconducting resonators made from low-kinetic-inductance films and hence low fabrication-induced frequency variability [145] possible. Furthermore, we expect that the local gate-voltage control, as demonstrated here, will exhibit minimal crosstalk to other voltage-controlled element due to the absence of finite and long-range supercurrents induced by the dc control. Thus, this ability to tune the nonlinear resonator might render large-scale implementations of voltage-controlled superconducting electronics with dense packing possible.

While this demonstration of a gate-tunable kinetic inductance parametric amplifier achieves the main objectives of magnetic field compatibility, gate tunability and a useful saturation power, further improvements must be made without additionally compromising any of these features. Therefore, further work should be devoted to the improvement of the dielectric environment to widen the tuning range without being limited by current leakage at higher voltages. Moreover, the optimization of the inductance ratio of the proximitized nanowire and the resonator is required to further increase the saturation power of the amplifier. In this work, we study only four-wave-mixing operations, but three-wave mixing should be accessible by driving the nonlinear resonator via an oscillating voltage gate connected to the proximitized nanowire or alternatively a dc current bias through the nonlinear inductor. We expect that three-wave mixing will allow for a large spectral separation of the pump tone and the signal tone, alleviating frequency crowding in the amplification window and saturation of higher amplification stages.

ACKNOWLEDGEMENTS

We thank Peter Krogstrup for the nanowire growth. We also thank Alessandro Miano, Patrick Winkel, Nicolas Zapata González and Ioan Pop for valuable discussions. This research was cofunded by the allowance for Top consortia for Knowledge and Innovation (TKI) from the Dutch Ministry of Economic Affairs and the Microsoft Quantum initiative. CKA acknowledges financial support from the Dutch Research Council (NWO).

AUTHOR CONTRIBUTIONS

LJS, and CKA conceived the experiment. LJS fabricated the devices, and acquired and analysed the data with help from JJW, MPV and AB. LJS and CKA wrote the manuscript with input from all other co-authors. CKA supervised the project.

DATA AVAILABILITY

The raw data and the analysis script underlying all figures in this manuscript are available online [11].

4.5. DESIGN AND FABRICATION

4.5.1. DESIGN

We design the circuitry using a customised design framework [146]. The loaded quarter-wave resonator is designed to have a total capacitance of $C_0 = 511\,\mathrm{fF}$, a total inductance of $L_0 = 1.07\,\mathrm{nH}$ for the unloaded transmission-line resonator, a capacitance to the input port of $C_c = 55\,\mathrm{fF}$ and an inductance of $L_{NW} = 0.79\,\mathrm{nH}$ for the proximitized nanowire. We note that if the nanowire segment was a single Josephson junction, we would expect a critical current of $I_c = \frac{\Phi_0}{2\pi L_{\mathrm{NW}}} \approx 0.42\,\mu\mathrm{A}$ for this inductance. Instead, in dc experiments on nanowires from the same batch, we measured a critical current of around $3-17\,\mu\mathrm{A}$, which quantitatively supports the description of the nanowire as kinetic inductance element. The nanowire inductance fraction in this configuration is $\alpha = \frac{L_{NW}}{L_{NW}+L_0} = 0.42$. The quarter-wave transmission-line design frequency separates best the fundamental mode from higher harmonics simulated to be above 19.2 GHz. To suppress crosstalk between the amplifier mode and the voltage gate, we add a fifth-order Chebyshev low-pass filter in between. The filter is composed of three parallel-plate capacitors and two meandering inductors as shown in Fig. 4.1a. As expected for a low-pass filter, we find that the filter suppresses high-frequency transmission, see Fig. 4.6, which shows the low-pass-filter response from finite element simulations for three different thicknesses of the dielectric material SiN separating the two superconducting plates. The filter therefore suppresses the coupling between amplifier and gate by more than 50 dB in the 4-8 GHz range (gray box) also in the case of small fabrication imperfections potentially resulting in the SiN film thickness. The filter structure also exhibits self-resonances due to its finite length at around 15.5 GHz. In microwave simulations, we do not find any additional or common mode due to the filter structure around the resonance frequency of the undriven amplifier that could explain the appearance of an additional mode in the driven case.

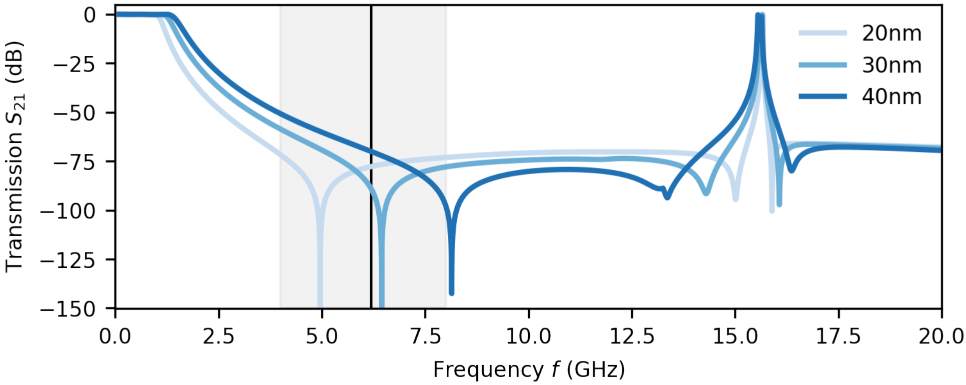

Figure 4.6.: Filter response. Simulated transmission parameter S_{21} versus frequency of a fifth-order Chebyshev filter for three different dielectric layer thicknesses. The gray box indicates the 4-8 GHz range. The black vertical line indicates the resonance frequency of the undriven amplifier.

4.5.2. Fabrication

We fabricate the resonator circuit and the gate lines from a 40 nm-thick sputtered NbTiN film (kinetic inductance 4 pH$\square^{-1}$) on high resistivity n-doped Si. We pattern the NbTiN film using electron-beam lithography and SF_6/O_2-based reactive-ion etching. 30 nm-thick plasma enhanced chemical vapour deposition (PECVD) SiN defined by a buffered oxide etch serves as bottom gate dielectric. We transfer the two-facet InAs/Al nanowire on top of the SiN bottom gate using a nanomanipulator. The InAs nanowires are grown by vapor–liquid–solid (VLS) growth with a diameter of 110(5) nm and nominal thickness of the Al of 6 nm [118]. We electrically contact the nanowires to the circuit via lift-off defined 150 nm-thick sputtered NbTiN leads after prior Ar milling to minimize the contact resistance.

4.5.3. REPRODUCIBILITY

We have prepared 13 samples with four amplifiers each. Of those, we have measured seven samples with in total 12 parametric amplifiers in 12 cooldowns, of which six amplifiers exhibit more than 20 dB gain. The remaining devices were discarded because of fabrication imperfections or excluded because of high room-temperature resistances of the nanowire segment due to high nanowire-to-NbTiN contact resistance.

4.6. KERR COEFFICIENT

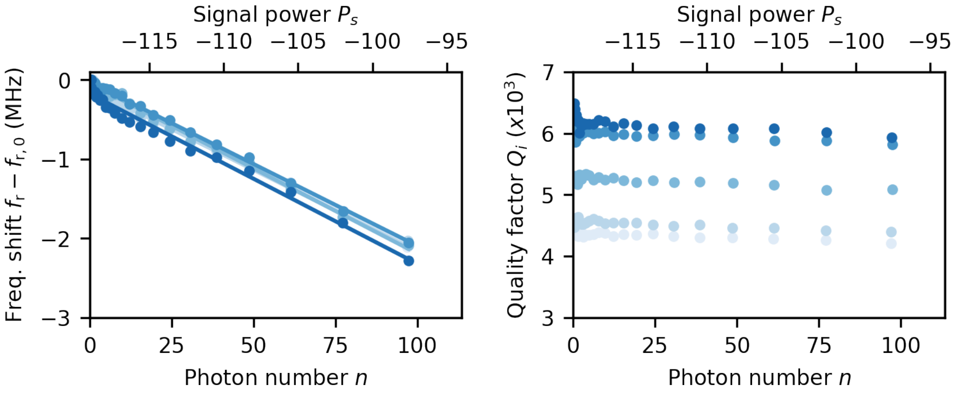

Figure 4.7.: Nonlinear resonator. (a) Frequency shift and (b) internal quality factor for five different gate voltages between −2.5 V and 5.5 V versus intra-cavity photon number.

The parametric amplifier is a nonlinear resonator where the nonlinearity, as explained in the main text, manifests itself as a frequency shift proportional to the number of photons in the resonators. We extract this proportionality constant, the Kerr coefficient K, from a measurement of the frequency shift versus intra-resonator photon number, see Fig. 4.7, which shows this measurement for different gate voltages. The frequency shifts are displayed here with respect to the resonator frequency measured at the weakest signal power f_r,0. We observe a similar slope for all gate voltage between −2.5 V and 5.5 V which results in a Kerr coefficient of about 20 kHz. As shown in Fig. 4.7, the internal quality factor increases with gate voltage from $Q_{i,-2.5\,\mathrm{V}} = 4363$ to $Q_{i,5.5\,\mathrm{V}} = 6483$ and for all gate voltages, we see a weak dependence of Q_i on the intra-resonator photon number.

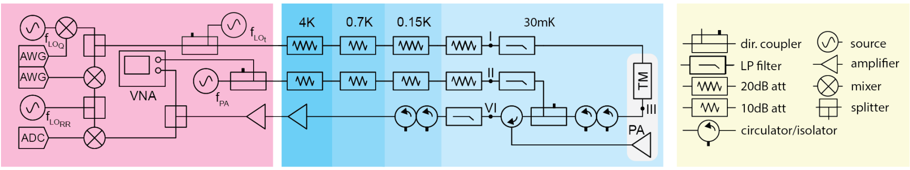

Figure 4.8.: Experimental setup. Left: Room-temperature control and readout electronics: A signal generator, f_{PA} and a VNA are combined with a directional coupler and connected to the drive line of the parametric amplifier. Two arbitrary-waveform generators (AWGs) provide modulated waveforms that are up-converted to microwave frequencies with the local oscillators set by two signal generators, f_{LO_Q} and $f_{LO_{RR}}$, for the transmon qubit drive and the readout. The output signal is split into a signal path to the vector network analyer and towards the analog to digital convertor (ADC). Middle: Microwave components installed in the dilution refrigerator, including two input lines and one output line. The sample (gray) hosts the readout resonator, the transmon qubit and the parametric amplifier. Two strongly attenuated and low-pass-filtered input lines serve as a readout resonator and transmon qubit drive line and as parametric amplifier drive line. The output line is amplified using one cryogenic HEMT amplifier and one room-temperature HEMT amplifier.

4.7. MEASUREMENT SETUP

The 6x6 mm^2 chip hosting the parametric amplifier, and also a readout resonator and transmon qubit (see Sec. 4.8), is glued with GE varnish onto a gold-plated copper mount and electrically connected to a printed circuit board using Al wire-bonds.

The room-temperature control and readout electronics (red box in Fig. 4.8) control the sample under test. A signal generator and a vector network analyzer (VNA) are connected to the drive line for the parametric amplifier. Amplitude-modulated waveforms provided by the two other signal generators and two baseband arbitrary-waveform generators drive the transmon qubit and the readout resonator. The output signal is split into a signal path to the vector network analyer and towards the amplitude-demodulation unit. The microwave components installed in the dilution refrigerator (blue areas in Fig. 4.8) include two strongly attenuated and low-pass-filtered input lines and one output line, and the sample hosting the readout resonator, the transmon qubit and the parametric amplifier. The output line is amplified using one HEMT operating at cryogenic temperatures (4 K) and one HEMT operating at room temperature as well as the parametric amplifier under test.

The estimation of the line attenuation and amplification between room-temperature electronics and the parametric amplifier is based on a combination of transmission measurements at cold temperature and room temperature is summarized in Fig. 4.9. The probe line between the VNA and the PA has −99 dB of attenuation at 6.4 GHz, which is composed of 50 dB cold attenuation between the VNA output and the PA input, 40 dB from the two directional couplers, 3.3 dB attenuation from the Eccosorb filters at 6.4 GHz, 3.2 dB cable and connector loss at room temperature, and the

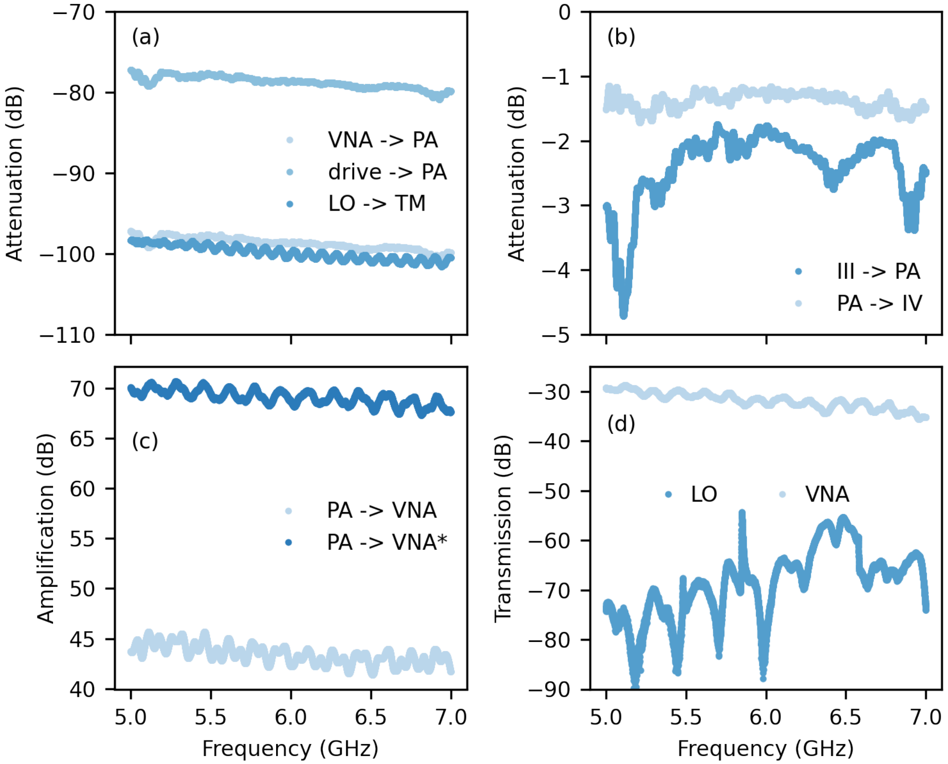

Figure 4.9.: Transmission calibration of measurement chain and individual components measured with a VNA. (a) Input-line transmission at room temperature from the VNA to the PA input (blue), from the PA drive-signal generator to the PA input (orange) and from the test tone signal generator to the TM input (green). (b) Interconnection transmission at room temperature from the TM output (III in Fig. 4.8) to the PA input and from the PA output to the HEMT input (IV in Fig. 4.8). (c) Net amplification of the readout chain between the PA output and the VNA input for two different configurations. (d) Transmission measurement in the cold state with the PA OFF from the VNA output port to the VNA input port (blue) and from the local oscillator (LO) signal generator generating the test tone to the VNA input (green).

insertion loss of low-pass filter, circulator and copper cables connecting to the PA of about 2.5 dB; see the blue line in Fig. 4.9a . The connection between the PA drive-signal generator and the parametric amplifier has 20 dB less attenuation due to the through connection through the first directional coupler at room temperature. The attenuation between the LO signal generator (LO), that generates the test tone for the SNR improvement measurement, and the input to the transmon readout resonator is −100 dB. Figure 4.9b shows the attenuation of the interconnections before and after the parametric amplifier, in particular the connection from the transmon readout resonator output (III) to the parametric amplifier input (PA) with $-2.5\,\mathrm{dB}$ attenuation and the connection between the PA output and the HEMT input (IV) with $-1.3\,\mathrm{dB}$ attenuation. Figure 4.9c shows the net amplification of the readout chain for two different tested configurations. The data presented in this paper is based on the "PA → VNA*" configuration with 70.7 dB gain provided by the cryo-HEMT (LNF-LNC4_8C serial number 844H, $P_{1dB,out,cryo} = -8\,\mathrm{dBm}$) and the LNF room-temperature HEMT (LNF-LNR4_8F_ART, $P_{1dB,out,rt} = 0\,\mathrm{dBm}$), which we tested componentwise at room temperature. Finally, we can compare the componentwise characterization for the input lines (Fig. 4.9a) and output line (Fig. 4.9c) at room temperature with the transmission measurement through the entire setup in the cold state, presented in Fig. 4.9d. The sum of the individual input-line and output-line characterizations agrees up to 4 dB with the total transmission measurement from the VNA output port to the VNA input port as shown in the wiring diagram in Fig. 4.8. This discrepancy might arise from multiple reconnections between the components and a different thermal state of the components in the respective measurements.

This line calibration suggests that the typically used pump power level at the PA of $P_p = -1.2\,\mathrm{dBm} - 78.9\,\mathrm{dB} = -80.1\,\mathrm{dBm}$ does not compress the cyro-HEMT with input saturation power $P_{1dB,in,cryo} \approx -48\,\mathrm{dBm}$. However, the pump power level after the cryo-amplifier is about $P_p \approx -40\,\mathrm{dBm}$ which is on the level as the 1 dB input compression power of the room-temperature HEMT of $P_{1dB,in,rt} \approx -42\,\mathrm{dBm}$. Consequently, the pump tone together with the amplified signal tone may saturate the room-temperature amplifier in this configuration of the measurement setup, which may distort the gain curves and also cause the shift between the point of maximal gain and the point of maximal SNR improvement, observed in Fig. 4.4c. To mitigate the saturation of the room-temperature amplifier, we considered an alternative configuration of the readout chain including a 20 dB attenuator before an alternative room-temperature amplifier with lower gain, but also lower 1 dB compression point. The net amplification of this readout chain is shown as blue curve in Fig. 4.9c. While the gain curves remained the same, we noticed that the readout chain is not limited by the HEMT noise temperature anymore but rather by the noise temperature of the spectrum analyzer, which would have complicated the interpretation of the noise characterization considerably.

4.8. CAVITY-REFERRED POWER ESTIMATED USING A TRANSMON QUBIT COUPLED TO A READOUT RESONATOR

To further characterize the noise performance of the parametric amplifier and to showcase its usefulness in terms of co-operation with other quantum devices, we integrate two transmon qubits, which are dispersively coupled to a common readout resonator on the same device chip as the parametric amplifier. Fig. 4.10a shows a false-color optical image of the transmission-line readout resonator which is weakly coupled to the input port (C_{C_1} small) and strongly coupled (C_{C_2} large) to the output port. Two single-island transmon qubits [147] are capacitively coupled close to the current nodes of the resonator; see Fig. 4.10b for the equivalent-circuit diagram. The Josephson junctions of the two transmon qubits are formed by electrostatically controlled proximitized nanowires with an etched segment as displayed in the schematic representation in Fig. 4.10c. The gate-voltage controls the critical current of the Josephson junction, and hence the Josephson energy E_J, but also a global magnetic field affects the Josephson energy. This tuning knob allows us to tune the transmon frequency f_q in-situ as $hf_q(V_g) \approx \sqrt{8E_cE_J(V_g)} - E_c$ under the assumption of many low-transparency channels in the nanowire junction [148]. Here E_c is the charging energy of the transmon island.

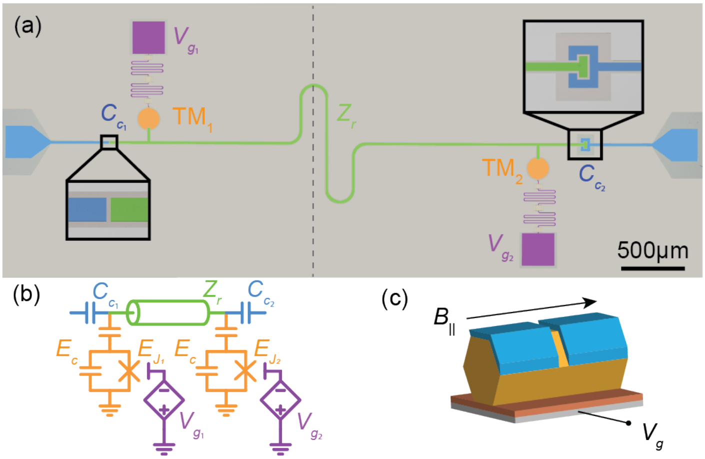

Figure 4.10.: Transmon qubit and readout resonator. (a) False-color optical microscope image of a readout resonator in transmission-line configuration (green) that is capacitively connected to a weakly coupled input port (blue, left) and a strongly coupled output port (blue, right). Two single-island transmon qubits (orange) are capacitively coupled around the current nodes of readout resonator. The nanowire Josephson junctions of the transmon qubits are electrostatically controlled via low-pass filtered voltage gates (purple). The optical image has been cropped at the dashed gray line for better visibility, which reduces the displayed length of the resonator. (b) The equivalent-circuit diagram of the device shown in (a). (c) Schematic representation of the nanowire Josephson junction formed by an InAs nanowire that is partially proximitized with an Al shell on two facets and positioned on a voltage gate.

To estimate the cavity-referred power P_{out}, we independently measure the dispersive shift χ and the cavity coupling rate κ. We obtain χ from a variable-strength Ramsey experiment [36, 60], which allows us to extract the measurement-induced dephasing rate $\Gamma_\phi = \frac{8\chi^2 n}{\kappa}$ and the qubit frequency shift $\Delta f_q = 2\chi n$ as a function of a weak test tone at the readout resonator frequency applied using a signal generator at frequency f_{LO_t} during the idling time of the qubit in the equal superposition state; see Fig. 4.11b. From a linear fit to the dephasing rate Γ_ϕ versus input power at the signal-generator output P_{SG}, we obtain the slope $\partial_P \Gamma_\phi$. Similarly, a linear fit to the frequency shift Δf_q yields $\partial_P \Delta f_q$. Their ratio yields the dispersive shift χ expressed in the following equation:

$$\chi = \frac{\kappa}{4} \frac{\partial_P \Gamma_\phi}{\partial_P \Delta f_q} \tag{4.1}$$

From a linear fit to the frequency shift $\Delta f_q = 2\chi c P_{SG}$ we obtain the conversion factor c, which allows us to compute the intra-resonator photon number as $n = cP_{SG}$. Finally, the cavity-referred power at the resonator output is given by $P_{out} = \kappa h f_r n$. Because of the directional design of the transmission-line resonator with $C_{C_2} \gg C_{C_1}$ and high internal quality factor $Q_i > Q_c$, we can approximate the coupling rate as $\kappa = \frac{f_r}{Q_{tot}}$, which is equivalent to the FWHM of the peak in the transmission measurement extracted from the double-Lorentzian fit in Fig. 4.11a. At one specific gate set point for transmon qubit 1 ($V_{g_1} = 0.75\,\mathrm{V}$) and while transmon qubit 2 is frequency detuned with the pinched-off nanowire Josephson junction ($V_{g_2} = -2\,\mathrm{V}$), we find a dispersive shift of $\chi = 1.33\,\mathrm{MHz}$ and a cavity coupling rate of $\kappa = 11.34\,\mathrm{MHz}$ and a setup-specific conversion factor $c = 5.65\,\mathrm{mW}^{-1}$, see Fig. 4.11. For this configuration, the other system parameters are the resonator frequency $f_r = 5.862\,\mathrm{GHz}$, the qubit frequency $f_{q_1} = 4.827\,\mathrm{GHz}$ and the coherence time $T_1 = 1.3\,\mu\mathrm{s}$. Consequently, a signal-generator input power of $P_{in} = -20\,\mathrm{dBm}$ corresponds to a cavity output power of $P_{out} = -138.09\,\mathrm{dBm}$ at a frequency of $f_r = 5.862\,\mathrm{GHz}$. Since the transmon readout resonator is not resonant with the parametric amplifier, the SNR measurements presented in Fig. 4.4 were performed with a signal tone far detuned from the readout resonator frequency. Away from the passband of the readout resonator, we find that the transmission through the resonator is suppressed between 20 and 25 dB. Therefore, the effective power level at the input of the parametric amplifier, when driven at a signal frequency of around 6.3 GHz with $P_{in} = -20\,\mathrm{dBm}$ at the signal generator, is expected to be in the range from $-158\,\mathrm{dBm}$ to $-163\,\mathrm{dBm}$, which is consistent with the power level inferred from the line calibration and used in Fig. 4.4b. Note that we were not able to accurately estimate the precise transmission at the signal frequency of the parametric amplifier due to an unexplained background signal in the transmission spectrum when measured through the readout resonator. Thus, we base the power-level calibration in the main text solely on the line-calibration data.

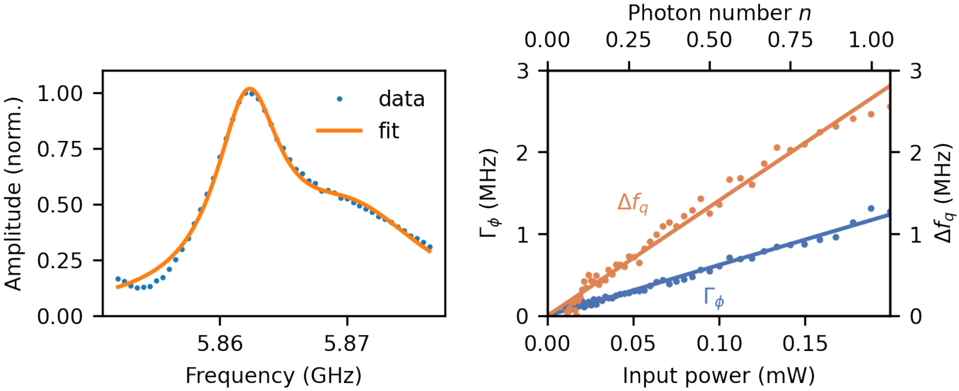

Figure 4.11.: Estimation of intra-cavity photon number. (a) Transmission spectrum of the readout resonator with double-Lorentzian fit. (b) Measurement-induced dephasing (blue, left axis) and frequency shift (orange, right axis) as a function of input power of a readout tone with frequency f_{LO_t} applied during a Ramsey experiment. The data are shown with a linear fit to extract the slope. The equivalent intra-cavity photon number is indicated on the top axis.

5

GATE-TUNABLE PHASE TRANSITION IN A BOSONIC SU-SCHRIEFFER-HEEGER CHAIN

Lukas Johannes Splitthoff, Miguel Carrera Belo, Guliuxin Jin, Yu Li, Eliska Greplova, Christian Kraglund Andersen

Metamaterials engineered to host topological states of matter in controllable quantum systems might hold promise for advancement of quantum simulations and quantum computing technologies. In this context, the Su-Schrieffer-Heeger (SSH) model has gained prominence due to its simplicity and practical applications, including entanglement stabilization in superconducting quantum circuits. Here, we present the implementation of a gate-tunable, five-unit-cell bosonic SSH chain on a one-dimensional lattice of superconducting resonators. We achieve electrostatic control over the inductive intra-cell coupling using semiconductor nanowire junctions, which enables the spectroscopic observation of a trivial-to-topological phase transition in the engineered topological metamaterial. Our approach offers precise and independent in-situ tuning of the coupling parameters – a feature that has eluded previous work. To this end, we will discuss the robustness of the topological edge state against various disorder realizations. Our results supplement efforts towards gate-controlled superconducting electronics and larger controllable bosonic lattices to enable quantum simulations.

This chapter is currently prepared for publication.

5.1. INTRODUCTION

Metamaterials are engineered assemblies of simple constituents, which exhibit exotic functionalities, that would otherwise be absent. This transferable concept entered the realm of quantum systems and stimulated efforts to engineer metamaterials which host topological states of matter that remain robust against imperfections and are therefore suited for quantum computing and simulation.

Among all topological metamaterials especially those resembling the Su-Schrieffer-Heeger (SSH) model [149] attracted recent attention [150–153] as the model predicts a phase transition of a finite, 2N-site chain with alternating coupling strength between a band insulator and a topological insulator with localized edge states. The SSH model finds applications in the entanglement stabilization of quantum states [154], the long-range interaction of qubits [155–158] and the study of non-hermitian light-matter interaction [159–161].

Due to the generality of the concept, topological metamaterials can be realized in various material platforms and efforts materialized in spin qubits [162], Rydberg atoms [163], adatoms [164] and integrated photonics [165]. The idea has also been taken to classical electrical circuits made out of surface mount components on printed circuit boards [166–168], which challenge the correspondence between classical circuits and superconducting quantum circuits. Thanks to the mature fabrication and design techniques of superconducting circuits, the reliable large scale implementation of superconducting qubits and resonators is feasible leading to experiments with engineered photonic baths [52, 169–178], topological electrical circuits [179], and qubit-to-topological waveguide coupling [153, 156, 180–182].

While all of the aforementioned efforts resemble static realizations of metamaterials, the engineering of topological metamaterials from superconducting circuits with tunable spectral bandgap and controllable dissipative and dispersive interaction remains an open challenge due to the necessary integration of crosstalk-free tunability. Those efforts would enable quantum simulation of novel states of matter [183, 184] or the development of new circuit components such as on-chip isolators [185] or long-range couplers. The required tunability could enter the topological circuit via flux control [81] or current biased conductors [22, 82, 84, 186]. However, it has been shown that flux-crosstalk between SQUID loops significantly complicates the device tune-up [187, 188]. We also expect that long range supercurrents arising from current biased conductors lead to crosstalk between otherwise independent sites.

To alleviate the need for advanced control strategies which eliminate this type of crosstalk between mesoscopic circuit elements by device design or tune-up algorithms, one could instead leverage the local control over the microscopic properties of circuit elements. Such source of tunability became available with the local electrostatic control of the supercurrents in hybrid superconducting semiconducting structures [5, 6, 46, 189] or other hybrid structures, which should enable the crosstalk-free integration of tunability. Based on this concept of gate-tunability, gate-tunable transmon qubits [5, 189], bus resonators [6] and parametric amplifiers [11, 46] have been realized in previous work in which the accessible tuning range and stability depends on the material quality and the presence of Josephson junctions.

In this paper, we present the implementation of a five-unit-cell bosonic SSH chain comprised of two resonators per unit-cell forming a one-dimensional lattice of superconducting resonators. By taking the idea of electrostatic control from the single element level, like a gatemon, to scale, we achieve in-situ, electrostatic control over several inductive intra-cell coupling elements using semiconductor nanowire junctions, which enables the spectroscopic observation of a trivial-to-topological phase transition in the engineered topological metamaterial.

5.2. SSH CHAIN IMPLEMENTATION

We implement a five unit-cell tight-binding SSH model, shown in Fig. 5.1a, as a chain of 10 lumped-element, high-kinetic inductance, superconducting resonators with alternating variable inductive intra-cell coupling v and static capacitive inter-cell coupling w, see Fig. 5.1b. One unit-cell is comprised of two resonators with intra-cell coupling v as highlighted in Fig. 5.1a,b,d with a grey box. The capacitive inter-cell coupling is set by the geometry of the neighboring resonators between unit cells. The inductive intra-cell coupling is realized by five gate-tunable Josephson junctions formed in five proximitized semiconducting nanowires, which intra-connect the two resonators of a unit cell. The gate voltages, which are applied via Chebyshev-filtered gate lines, control the Andreev bound states carrying the super-current between the superconducting leads of the nanowire junctions separately by changing the chemical potential and in turn set the respective Josephson energies E_J. Eventually, the coupling inductance is then given by the Josephson inductance $L_v(V_g) = \phi_0(2\pi I_c(V_g))^{-1} = \phi_0^2(E_J(V_g))^{-1}$. The inductance is infinite, when the nanowire Josephson junction gated below the pinched-off voltage $V_g < V_p$, and finite on the order of a few nanohenry otherwise when charge carriers are accumulated in the junction region.

The resonators are made from a high kinetic inductance film to reduce their footprints and avoid spurious modes. Within a unit cell, the resonators are spatially separated to minimize the residual capacitive intra-cell coupling and are arranged in a mirrored configuration to suppress the residual capacitive second nearest neighbor coupling. The chain is terminated to either side by resonator-like coupling sites with an open inductor to maintain a coupling strength w on both ends to preserve the chiral symmetry. These coupling sites themselves connect directly to the input port S and the output port D, which enable transmission measurements.

A zoom-in on such a nanowire Josephson junction is provided in Fig. 5.1c. The thin Aluminum film on two facets of the InAs nanowire has been selectively etched to form a 110 nm long Josephson junction, which directly connects to resonators on either side via NbTiN contacts. The voltage gate is surrounded by two narrow ground lines to ensure equal ground potentials on the upper and lower half of the SSH chain.

The equivalent circuit model of a single unit cell is shown in Fig. 5.1d displaying the four relevant circuit parameters: the resonator capacitance C_0, the resonator inductance L_0, the capacitive inter-cell coupling C_w, and the inductive intra-cell coupling L_v on the two sub-lattice sites A and B. The relation between v and L_v and between w and C_w is discussed in Sec. 5.5.2. In this approximation we neglect the residual capacitive intra-cell C_v and the residual capacitive second nearest neighbor coupling C_{SNN}.

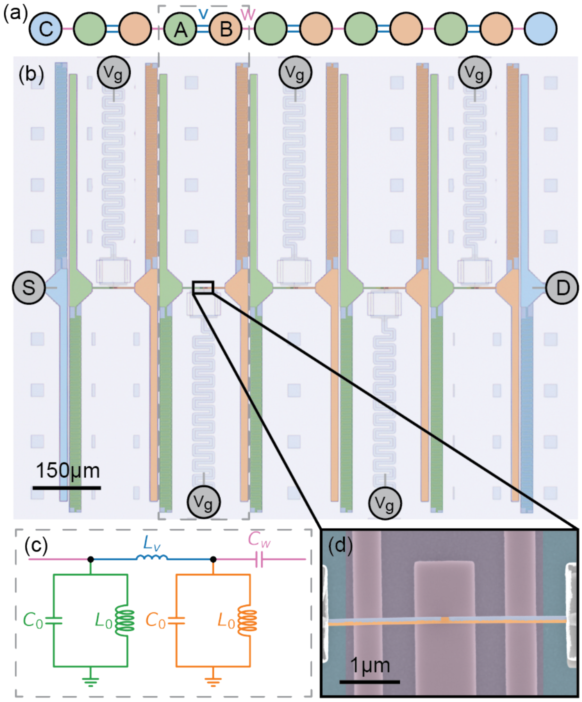

Figure 5.1.: Superconducting resonator-based SSH chain implementation. (a) Illustration of the SSH tight-binding model with two-site unit cell A,B, intra-cell coupling v and inter-cell coupling w. The finite chain is terminated to coupling sites C. (b) False-colored microscope image of the five unit cell SSH chain composed of lumped element resonators with alternating variable inductive coupling and static capacitive coupling. The chain is measured from port S to port D in transmission. The inductive coupling, mediated by proximitized nanowire Josephson junctions, is controlled via five independence voltage gates. One unit cell is highlighted within the dashed box. (c) Equivalent circuit of a single unit cell in (b). (d) False-colored micrograph images of a single gate controlled proximitized nanowire Josephson junction. Orange: InAs semiconductor, blue: Al thin film, purple: SiN gate dielectric on NbTiN gate electrodes, turquoise: Si substrate, grey: NbTiN contacts.

Our circuit implementations shares the same tight-binding geometry as the original SSH model with identical on-site potentials and alternating coupling strengths v and w, as highlighted with a corresponding color code in Fig. 5.1a,b. To further affirm the correspondence between the SSH model and our implementation we derive the real space Hamiltonian from the circuit Lagrangian (see App. 5.5.2). The diagonalization of the real space Hamiltonian for realistic circuit parameters then yields the eigenvalues for uniformly varied coupling strength L_v, see Fig. 5.2.

The energy spectrum in Fig. 5.2a shows the evolution of 10 circuit modes versus the coupling strength L_v. In the case of large inductances, $L_v > 22\,\mathrm{nH}$, corresponding to $v < w$ the spectrum exhibits two nearly degenerate mid-gap modes (red) centered around the eight bulk modes (black), which is the characteristic feature of the topological insulator state. Hence, we find the system to be in the topological insulator state if the nanowire junctions are pinched-off. As the coupling inductance decreases and the coupling ratio crosses over to $v > w$, see Fig. 5.2b, the mid-gap modes split and approach the bulk modes, which eventually leads to a fully gaped spectrum corresponding to the trivial insulator state. Particular for this implementation is the blue shift of the entire spectrum for smaller coupling inductances as the change in L_v also renormalizes the on-site potential, here the resonator frequency ω_r. Consequently, also w increases slightly following the increase in ω_r (see Fig.!5.2b). Note that the spectrum remains symmetric around the instantaneous resonator frequency ω_r (see App. 5.5.3), which is characteristic for a system obeying chiral symmetry. To highlight the spectral evolution further, we present the free spectral range between one mid-gap mode and the nearest bulk mode as well as the separation between the two mid-gap modes in Fig. 5.2c. The system undergoes a phase transition between the topological and the trivial state as the order of the coupling strength v and w inverts. At the point where $v = w$, the free spectral range between the mid-gap modes and the nearest bulk modes is equal, see Fig. 5.2c, but remains finite due to the finite system size.

Despite the presence of on-site and coupling strength disorder in this simulation, which represents the actual experimental circuit implementation, the spectrum is nearly indistinguishable from an ideal SSH chain, which shows the robustness of this implementation method. The only difference appears in the symmetry of some bulk modes (see App. 5.5.2).

5.3. RESULTS

We experimentally resolve the energy spectrum of the 10 site SSH chain implementation via a transmission measurement at microwave frequencies through the chain from port S to port D for different gate voltages applied to nanowire junctions measured at the base temperature of a dilution refrigerator. In this measurement, eigenmodes of the SSH chain manifest as peaks in the transmission spectrum. Their linewidth is proportional to the respective wavefunction weight on the outer sites of the chain $|\psi_{0,2N}|^2$.

5.3.1. TOPOLOGICAL REGIME

We begin the measurement by pinching off the Josephson junctions mediating the intra-cell coupling v. At a gate voltage of $V_g = -1\mathrm{V}$ on all gates, we observed a transmission spectrum with 9 peaks corresponding to the eight bulk modes and the two quasi-degenerate edge modes occupying the lower band, the gap, and the upper band of the spectrum shown in Fig. 5.3a-c. The red crosses indicated the

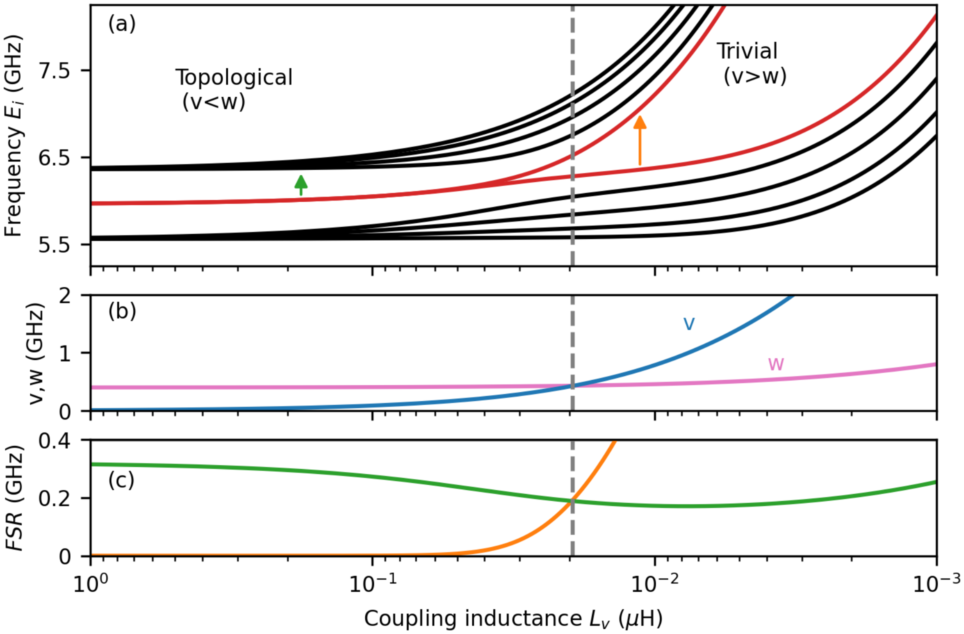

Figure 5.2.: Simulated spectrum versus the coupling inductance L_v of a bosonic SSH chain with the circuit parameters used in the experiment. (a) Energy spectrum of the bulk modes (black) and the edge modes (red) versus the coupling inductance L_v. The dashed line indicates the phase transition point between the topological and the trivial phase where $v = w$. (b) Coupling coefficients v (blue), w (pink) versus coupling inductance L_v. (c) Free spectral range FSR between the edge states and the bulk (green, arrow in (a)) and between the two edge modes (orange, arrow in (a)).

frequency points of the individual modes. The linewidth of a mode depends on its coupling strength to the measurement ports. Hence, modes with more wavefunction weight on lattice sites close to the edge of the chain $|\psi_{0,2N}|^2$ couple more strongly to the measurement ports and appear as broader modes in the spectrum. By this logic, we can assign the narrow modes in range 5.68 GHz to 5.72 GHz and 6.38 GHz to 6.42 GHz as bulk modes. The wider, central peak then corresponds to the quasi-degenerate mid-gap modes. The reduced transmission amplitude of the mid-gap modes compared to the maximal transmission results from the localization on either site of the chain. The asymmetric and distorted lineshapes of the SSH chain modes originate from Fano resonances of these relatively narrow modes with a broad box mode centered around 6.3 GHz formed by the sample enclosure.

The sorted eigenfrequencies versus mode index in Fig. 5.3d shows the gaped spectrum with quasi-degenerate zero energy modes, which is characteristic for the topological insulator state expected for this system. After the mode assignment, we can estimate the on-site energies and the coupling strength of each individual site along the SSH chain to obtain an estimate of the circuit parameters by fitting the full 10 dimensional Hamiltonian to the extracted eigenfrequencies (see App. 5.5.2). The average values of the estimated circuit parameters C_0, L_0, C_w and L_v deviate from the design parameters by less than 10 %. Moreover, we find a parameter variation of less than 1 % along the chain. The obtained parameters were used to generate the simulated data shown in Fig. 5.2.

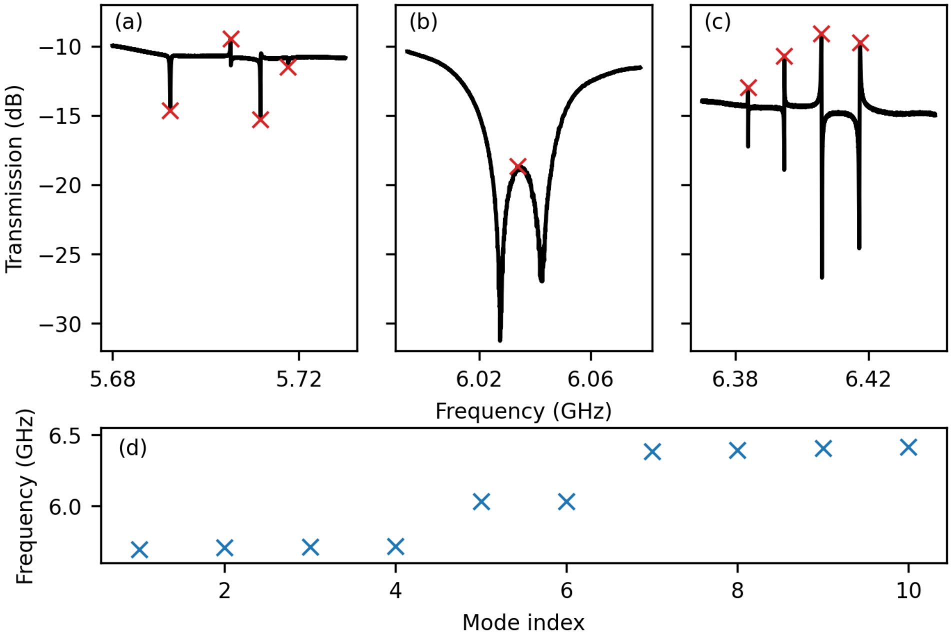

Figure 5.3.: Parameter estimation of the SSH chain in the topological phase. (a-c) Transmission spectrum of the lower band, the gap and the upper band. The red crosses mark the 10 modes of the five unit cell SSH chain. (d) Eigenfrequency of the 10 modes in the topological phase sorted by mode index. The simulated eigenfrequencies based on the parameter extraction (orange) overlap with the measurement results (blue) with 1 kHz precision.

5.3.2. PHASE TRANSITION

Having established the circuit parameters in the topological regime, we now leverage the tunability per unit cell to observe the phase transition predicted for a SSH chain. To prepare for a measurement of the energy spectrum of the SSH chain versus a simultaneous change of all coupling inductances L_v, we first characterize the dependence of each individual nanowire junction on the spectrum. Hence, we repeatedly record the spectrum for a wide range of gate voltages per nanowire junction to identify the pinch-off voltage V_{p_i}, that suppresses the supercurrent across the junction, and the open voltage V_{o_i}, that maximizes the supercurrent of

the respective junction, while the other junctions remain in the pinch-off regime $V_{g_i} < V_{p_i}$. For the measurement of the energy spectrum of the SSH chain along a synchronous evolution of the coupling inductances L_v we compose a joint gate control as linear interpolation between V_o and V_p per junction based on the five individual gate dependencies. Here we assume that each nanowire junction opens at a similar rate between V_o and V_p such that the joint gate control mimics the synchronous tuning of L_v in all junctions. The resulting spectrum over 1 GHz with a 70 kHz resolution in the few photon regime is shown in Fig. 5.4a after background correction (see App. 5.9). Three linecuts, color-coded relative to their respective gate setting, shown in Fig. 5.4 exhibit the three different SSH states, which as accessible experimentally upon in-situ tuning.
The overall spectral fan-out of the SSH modes with increasing gate voltages, hence decreasing coupling inductances, qualitatively follows the simulation presented in Fig. 5.2a. For the initial gate settings close to V_p shown in Fig. 5.4b, we obtain a gaped spectrum with mid-gap modes and a free spectral range of $FSR = 350\,\mathrm{MHz}$, which we previously identified as topological insulator state in Fig. 5.3. As the gate voltages increase towards V_o, the initially quasi-degenerate mid-gap modes with relatively wide linewidth and maximal prominence split and approach the lower and upper bundle of four modes. Eventually, close to V_o the lines in the spectrum form two bundles, are narrow in linewidth and of low prominence, see Fig. 5.4d. We identify this single gaped spectrum with a free spectral range of $\Delta = 240\,\mathrm{MHz}$ as trivial insulator state.
The phase transition of the SSH chain manifests in this experiment in two ways: The first observable is the free spectral range between the mid-gap and the nearest bulk modes. Starting from the topological insulator state with a free spectral range of $\Delta = 350\,\mathrm{MHz}$ between the mid-gap modes and the nearest bulk mode, this spectral gap continuously closes. Around the intermediate regime corresponding to the trace in Fig. 5.4c, the gap between the mid-gap modes and the gap to the nearest bulk modes is approximately equal. This change in FSR is in qualitative agreement with the simulated trend shown in Fig. 5.2c. Also note that the entire spectrum blue shifts as the coupling inductance is reduced as expected from the simulations. The second observable is the linewidth together with the transmission amplitude of the modes, which measures the localization of the wave function on the edges of the chain. As it can be seen from the comparison of the Fig. 5.4b and Fig. 5.4d, the bulk mode resonances widen from the topological to the trivial state, while the mid-gap mode resonances appear narrower. Additionally, the transmission amplitude of the mid-gap modes increases towards the trivial state. As a result the total transmission in the trivial state is higher than in the topological state.
While the nonlinear frequency shift of the system is not directly related to the phase transition and kept small by choosing a low probe power, it serves as additional state indication to verify that the nanowire junctions are open. While the system in the topological regime remains nearly unchanged versus changes in the probe power, the system frequencies lower drastically as the trivial regime is more susceptible to current passing through the system due to added Kerr nonlinearity arising from the presence of the open Josephson junctions.

However, there remains a caveat arising from the nature of nanowire Josephson junctions. As observed in earlier work on nanowire Josephson junctions [5, 86, 131, 136], the functional dependence of the inductance on the individual gate voltage is non-monotonic and hysteretic over time, which prevents us from observing a smooth transition. The effect of disorder and disorder induced phase transitions can further be studied, following ideas presented in Ref. [190, 191].

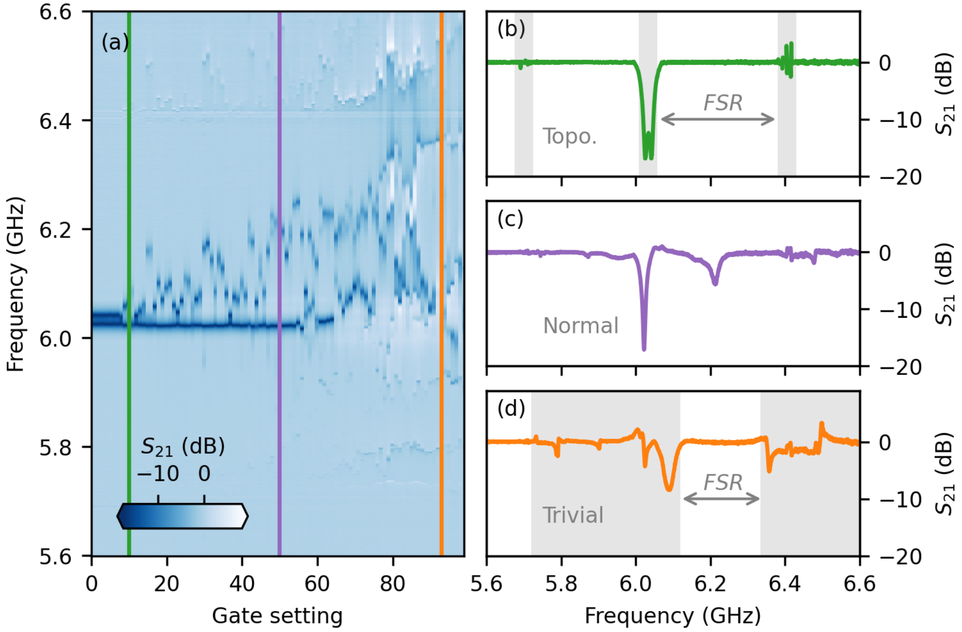

Figure 5.4.: Gate-tunable phase transition. (a) SSH chain spectrum versus individual gate voltage V_{g_i} aggregated in a joint gate setting sweep (more information in the text). The shades indicate the S_{21} transmission through the chain. (b-d) SSH chain spectrum for a given gate setting indicated as colored line in (a). The greyed out regions in (b) and (d) highlight the width of the bands. The arrows indicate the largest free spectral range in these traces.

5.4. CONCLUSION

We have realized a macroscopic SSH chain out of a 1d lattice of superconducting resonators, which inherits the tunability from the microscopic properties of nanowire Josephson junctions. We have characterized the system in the topological regime and mapped our bosonic implementation onto the original spin-less, single particle SSH Hamiltonian. Eventually, we leveraged the unit cell tunability and the engineered robustness against disorder to control the extended states along the SSH chain, which lead to the observation of the topological insulator phase transition in the macroscopic, gate-tunable resonator based SSH chain from the topological to the trivial insulator phase.

Our experiment takes the idea of gate-tunable superconducting circuits [192] from a single gate-tunable element to scale and proves that the implementation of several nanowire Josephson junctions in cQED experiments is possible. This result encourages further research on gate-tunable qubits, such as $cos(2\phi)$ gatemon qubits [193], Andreev spin qubits [131] or Kitaev chain qubits [133]. Also the composition of 2d lattices [194] of gate-tunable superconducting resonators seems feasible.

However, our findings also suggest that further material development of the hybrid superconductor-semiconductor stack is required to enable a smooth and reproducible gate control and exploit full potential of the microscopic properties of nanowire junctions in superconducting circuits.

In future realization of this tunable system we intend to probe the on-site wavefunction with qubits as local probes via their affected decoherence and qubit frequency arising from an AC Start shift [154, 156, 195]. Going beyond the current implementation, one can study the nonlinear coupling [196, 197] between unit cells. Other work might focus on the long-range coupling of qubit to a 1d-chain, more complex 1d systems like the Rice-Mele model [198] or the the Kitaev model [199]. The microwave transmission spectroscopy used in this work might also find application in the characterization of topological insulators and other material systems.

ACKNOWLEDGEMENTS

We thank Isidora Araya Day, Anton Akhmerov and Dmitry Oriekhov for insightful discussions and Peter Krogstrup for the nanowire growth. This research was co-funded by the Dutch Research Council (NWO) and by the Top consortia for Knowledge and Innovation (TKI) from the Dutch Ministry of Economic Affair.

AUTHOR CONTRIBUTIONS

LJS, and CKA conceived the experiment with help from GJ and EG. LJS and MCB designed and acquired and analysed the data the sample. LJS fabricated the device. YL provided the proximitized nanowires. LJS, MCB and CKA wrote the manuscript with input from all other co-authors. CKA supervised the project.

DATA AVAILABILITY

The raw data and the analysis script underlying all figures in this manuscript are available online.

5.5. SSH CHAIN MODEL

The Appendix contains further information on the implementation of the SSH chain. Our implementation has been derived from the SSH model presented in App. 5.5.1. We then compare the model with the ideal implementation in App. 5.5.2 and discuss its symmetries and the localisation of the wavefunctions in App. 5.5.3 and App. 5.5.3. We present the fabrication in App. 5.8.

5.5.1. CONDENSED MATTER HAMILTONIAN

The condensed matter system inspired tight-binding Hamiltonian of the SSH chain with on-site potential ϵ, intra-cell hopping v and inter-cell hopping w yields a tri-diagonal real space Hamiltonian of dimension $2N$, where N is the number of unit cells in the system. The basis of this real space Hamiltonian is formed by the sites along the chain. The Hamiltonian reads

$$\begin{aligned} H_{CM} &= \sum_{n=1}^{2N} \epsilon \left|n\right\rangle \left\langle n\right| \\ &+ \sum_{n}^{N} \left[v \left|2n-1\right\rangle \left\langle 2n\right| \right. \\ &+ \left. w \left|2n\right\rangle \left\langle 2n+1\right| + h.c. \right] \\ &= \begin{pmatrix} \epsilon & v & & & & & \\ v & \epsilon & w & & & & \\ & w & \epsilon & & & & \\ & & & \ddots & & & \\ & & & & \epsilon & w & \\ & & & & w & \epsilon & v \\ & & & & & v & \epsilon \end{pmatrix} \end{aligned} \tag{5.1}$$

The spectral properties of this system and its eigenstates are displayed in Fig. 5.5.1. The key feature is the symmetrically gaped spectrum span by the bulk modes (black) with mid-gap modes in the topological insulator phase for $v < w$. The appearance of the symmetric spectrum is linked to the chiral or sublattice symmetry of the system, which can be tested by computing the anti-commutator

$$\{c, H\} = cH + Hc = 0 \tag{5.2}$$

with

$$c = \mathbf{I}_5 \otimes \sigma_z \tag{5.3}$$

The spectral properties of this system and its eigenstates are displayed in Fig. 5.5.1. The key feature is the symmetrically gaped spectrum spanned by the bulk modes (black) with mid-gap modes in the topological insulator phase for $v < w$. The appearance of the symmetric spectrum is linked to the chiral or sublattice symmetry of the system, which can be tested by computing the anti-commutator

$$\{c, H\} = cH + Hc = 0 \tag{5.4}$$

with

$$c = \mathbf{I}_5 \otimes \sigma_z \tag{5.5}$$

where the chiral symmetry operator c is given by the outer product of N dimensional identity matrix $\mathbf{I_5}$ and the Pauli-z matrix σ_z. For this tri-diagonal real space Hamiltonian described above the anti-commutator is indeed zero. The spectral gap never closes due to the finite size of the system, in contrast to the infinite limit in which the spectral gap is given by $|v-w|$. Instead, the transition point at $v=w$ is signaled by the equal free spectral range between the mid-gap modes and one of the mid-gap modes and the first bulk mode. Beyond the transition, the system enters a trivial phase where $v>w$ eventually leading to a full dimerization. The corresponding eigenstates of the mid-gap modes are localized around the edges of the chain, as exemplified for a specific configuration in Fig. 5.5.1d, hence the name edge mode. An exponential fit to the wavefunction supported on either sublattice A or B yields the localization length ξ in Fig. 5.5.1b. As long as the edge modes are quasi-degenerate, the localization length extracted from the fit follows the theoretical limit $\log(w/v)^{-1}$, but the fit does not capture the divergence of the localization length well. For a finite system length, the inverse participation ratio appears to be a better measure for the localization of the wave function.

5.5.2. Lumped element, superconducting circuit Hamiltonian

The design of the lumped element, superconducting circuit implementation of the SSH chain follows a simple guiding principle. We realize every site as lumped element resonator with frequency ω and the coupling terms as capacitors C_w or inductors L_v. We then derive the circuit Hamiltonian from a classical circuit Lagrangian formalism as part of a standard circuit quantization [200]. The resulting Hamiltonian H_{LC} indeed takes the form of the tight-binding Hamiltonian

$$\begin{aligned}
H_{LC} &= \sum_{n=1}^{2N} \hbar\omega \left|n\right\rangle \left\langle n\right| \\
&+ \hbar\omega \sum_{n}^{N} \left[\frac{L_T}{2L_v} \left|2n-1\right\rangle \left\langle 2n\right| \right. \\
&+ \left. \frac{C_w}{2C_T} \left|2n\right\rangle \left\langle 2n+1\right| + h.c. \right] \\
&= \hbar\omega \begin{pmatrix}
1 & \frac{L_T}{2L_v} & & & & & \\
\frac{L_T}{2L_v} & 1 & \frac{C_w}{2C_T} & & & & \\
& \frac{C_w}{2C_T} & 1 & & & & \\
& & & \ddots & & & \\
& & & & 1 & \frac{C_w}{2C_T} & \\
& & & & \frac{C_w}{2C_T} & 1 & \frac{L_T}{2L_v} \\
& & & & & \frac{L_T}{2L_v} & 1
\end{pmatrix}
\end{aligned} \tag{5.6}$$

Based on the correspondence between the two systems, we can compare the coefficients in the Hamiltonian and formalize the mapping between the on-site energy ϵ and the resonator frequency ω, between the coupling strength v and the Josephson inductance L_v, and between the the coupling strength w and the capacitive coupling C_w

$$\begin{aligned} \epsilon &= \hbar\omega \\ v &= \frac{\hbar\omega}{2}\frac{L_T}{L_v} \\ w &= \frac{\hbar\omega}{2}\frac{C_w}{C_T} \end{aligned} \tag{5.7}$$

It should be noted that $\omega = \omega(L_v)$ which leads to a small increase in w, but a significant shift in the on-site potential ϵ causing the upwards shift of the spectrum as L_v decreases. For further visual comparison we also show the spectral properties and the eigenstates of the ideal SSH chain implementation in Fig. 5.5.1.

5.5.3. TOPOLOGICAL PROPERTIES OF SSH IMPLEMENTATION

REAL SPACE WINDING NUMBER

Generally, a topological invariant characterize the topological properties of topological insulators. In case of the SSH model, the momentum space winding number is used as topological invariant, which takes a state-dependent binary value: 0 in the trivial insulator state and 1 in the topological insulator state. In the finite-size SSH chain, where access to momentum space winding number is limited, the real space winding number (RSWN) serves as an approximation for a topological invariant. In our study, we compute the RSWN versus the coupling strength v/w for various chain lengths N and for $w = 0.5$, see Fig. 5.5.2 (a). On either end of the coupling strength range ($v = 0, 1$), the system approaches the the topological and trivial state with RSWN=1 and RSWN=0, respectively, regardless of the chain length. In-between $v = 0, 1$, the RSWN indicates a cross-over between the two different insulator states, but only in the thermodynamic limit $N \to \infty$ the RSWN correctly predicts the phase transition point. For small N, the RSWN does not capture the phase transition, which is spectroscopically still defined, due to finite size effects.

Additionally, we investigate the robustness of the topological state by examining the RSWN under varying levels of disorder in the coupling parameter v for three different intra-cell couplings $v = 0, 0.2, 1$ and for $w = 0.5$.

This study of the RSWN does not aim at benchmarking the system but at characterizing its behavior in comparison to the thermodynamic limit, providing valuable insights into the topological phase transition in finite systems.

SYMMETRIES

To further strengthen the claim that the chiral symmetry persists in our implementation, we present the spectrum of Fig. 5.5.1c normalized by the instantaneous resonator frequency $\omega(L_v)$ in Fig. 5.5.3a. This normalized spectrum is clear symmetric around the on-site energy. Moreover, we can again compute the anti-commutator and find that it vanishes $\{c, H_{LC}\} = 0$.

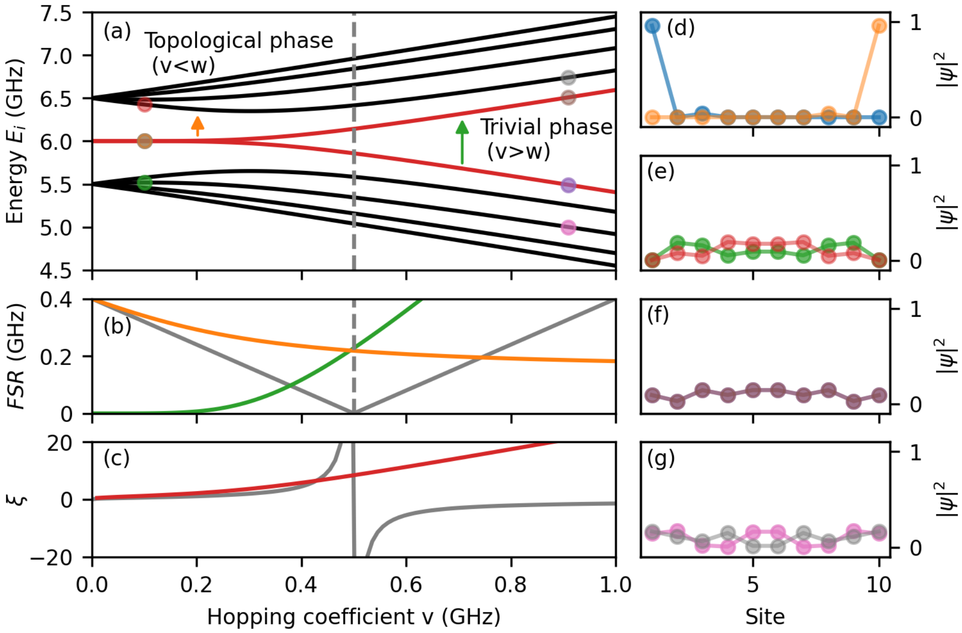

Figure 5.5.1.: Simulated spectrum and states of a tight-binding SSH model with on-site potential $\epsilon = 6.5\,\text{GHz}$ and hopping coefficient $w = 0.5\,\text{GHz}$ (a) Energy spectrum of the bulk modes (black) and the edge modes (red) versus the coupling strength v. (b) Free spectral range Δ between the edge states and the bulk (blue, arrow in (a)) and between the two edge modes (orange, arrow in (a)) versus hopping strength v. The dashed line indicates the phase transition point between the topological and the trivial phase where $v = w$. The spectral gap $|v - w|$ (grey) only closes in the infinite length system (c) Localization length ξ extracted as exponential decay fit to the wave functions of the edge modes. The grey line shows the theoretical limit $\log(w/v)^{-1}$. (c) Energy spectrum of the bulk modes (black) and the edge modes (red) versus the coupling strength v. (d-g) Real space wave function $|\psi|^2$ on the resonator lattice for the topological and the trivial phase of the bulk and the edge states. The colors correspond to the markers in (a).

LOCALIZATION

The localization of the wavefunctions of the edge states is a characteristic of the SSH chain. For finite chain lengths however, the localization length defined as exponential decay $\exp(-x/\xi)$ does not capture the delocalization of the edge modes as the system undergoes the phase transition, as seen in Fig. 5.5.1b. Instead, for finite chain length we can define an inverse participation ratio (IPR) [201], which measures the support of a wave function on a specific site and is defined as

$$IPR = \frac{\sum_x |\psi(x)|^4}{(\sum_x |\psi(x)|^2)^2} \tag{5.8}$$

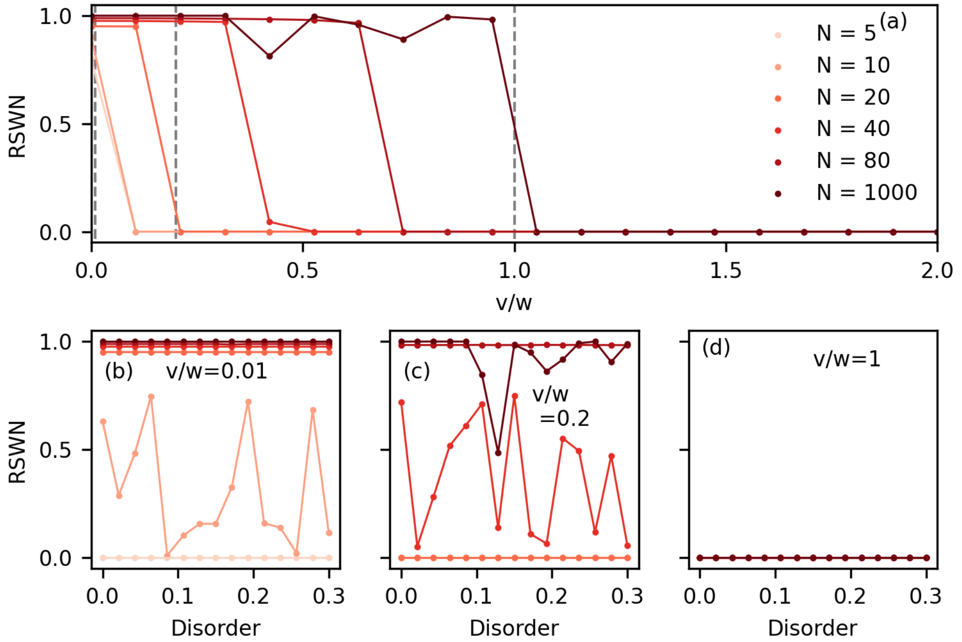

Figure 5.5.2.: Real space winding number. (a) RSWN versus coupling strength ratio. (b-d) RSWN versus disorder strength for three different coupling strength.

We observe that the IPR of the edge modes is finite and larger than for the bulk modes in the topological phase. As the system undergoes the phase transition, the IPR decreases and approaches the delocalization limit $1/L = 1/10$ of the bulk modes at $v = w$, see Fig. 5.5.3b,c.

5.6. CIRCUIT PARAMETER ESTIMATION

From the presence of the bulk and gap modes in the spectrum for a given L_v configuration, we can extract the circuit parameters C_0, L_0, C_w and L_v. First, we identify and list the eigenmodes of the system. Then, we fit the 10 dimensional Hamiltonian H_{LC} to the list of eigenmodes while allowing for free variation of all circuit parameters along the chain. For completeness, we also take the two C_w couplings to the coupling sites C into account, which expands the C_w list from four to six elements. Since the eigenfrequencies of the coupling sites are far detuned from the SSH spectrum, we do not consider them in the system Hamiltonian. The circuit parameters obtained from this optimization routine in the topological phase are shown in Fig. 5.6.1. We assume the design parameters as start parameters for the Nelder–Mead optimization. The variation of the obtained parameters is smaller than 1%. Finally, we input the obtained circuit parameters into the full Hamiltonian to compute the spectrum and the eigenstates to simulate the data in Fig. 5.2 and

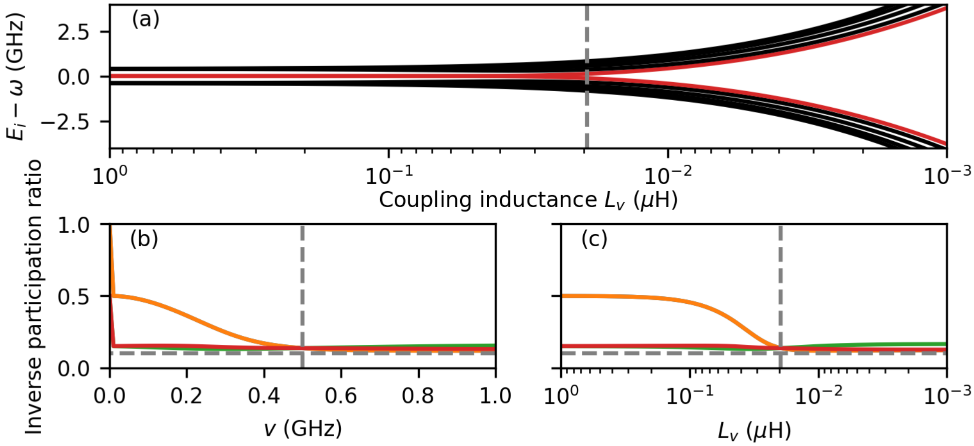

Figure 5.5.3.: (a) Normalized simulated spectrum of the bosonic SSH chain with ideal the on-site and coupling energies as in Fig. 5.5.1. (b,c) Inverse participation ratio for different states for the tight-binding model (b) and the ideal SSH chain implementation (c) versus the coupling strength v. The dashed line indicates the $1/L$ limit. The colors correspond to the respective wave functions in Fig. 5.5.1.

Fig. 5.3d. The agreement of this optimization with the measurement results is on the order of a few kHz, which is also the spectral resolution of the measurement. This parameter estimation yields the static parameters C_0, L_0, and C_w. The optimization routine can then be repeated for different L_v configurations to the trivial phase.

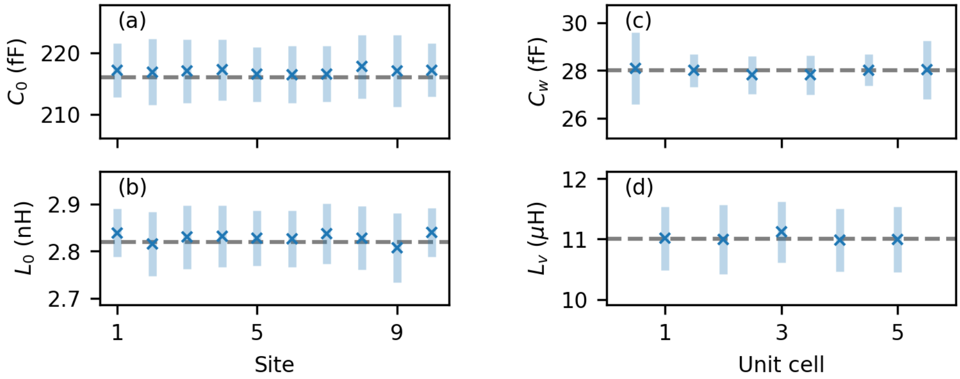

Figure 5.6.1.: Extracted circuit parameters in the topological phase. (a,b) Resonator capacitance C_0 and inductance L_0 per site. (c,d) Coupling capacitance C_w and coupling inductance L_v per coupling site.

5.7. SINGLE GATE DEPENDENCE

A transmission measurement through the 5 unit cell SSH chain allows for a site specific tune-up of every unit cell in order to prepare for a joint gate scan as presented in the main text.

We run single gate scans for every nanowire Josephson junction over a wide gate voltage range, while we keep all other gates at the pinch-off voltage V_p. Hence, all scans begin deep in the topological regime. For the bulk gates NW_i with $i \in [2,3,4]$ we zoom on the low band in the topological state, while we focus on the gap for the edge gates NW_i with $i \in [1,5]$, as we expect the biggest change in frequency in those spectral ranges.

The first important observation from the single gate dependence is that the modes in the spectrum do not monotonically move. In fact, we observes discontinuities due to jumps in the microscopic properties of the junctions. Repetitions of these scans reveal that the slopes change over time. Hence, even these single gate dependencies cannot be used as calibration for a joint gate scan across the phase transition point. However, from the single gate dependencies we can extract the voltage V_o, which correspond maximal supercurrent, hence minimal L_J or, expressed in Josephson energy, maximal E_J. This voltage point seem robust enough and constant over time and over several gate scans.

5.8. FABRICATION

We fabricate the SSH chain circuit and the gate lines from a 40 nm-thick sputtered NbTiN film (kinetic inductance $4\,\mathrm{pH}\square^{-1}$) on high resistivity n-doped Si. We pattern the NbTiN film using e-beam lithography and SF_6/O_2 based reactive ion etching. 30 nm-thick plasma enhanced chemical vapour deposition (PECVD) SiN defined by a buffered oxide etch serves as bottom gate dielectric. We transfer the two-facet InAs/Al nanowire on top of the SiN bottom gate using a nano-manipulator. The InAs nanowires were grown by vapor–liquid–solid (VLS) growth with a diameter of 110(5) nm, and nominal thickness of the Al of 6 nm [118]. We selectively etch the 110 nm long Josephson junctions into Al film. Then, we electrically contact the nanowires to the circuit via lift-off defined 150 nm-thick sputtered NbTiN leads after prior Ar milling to minimize the contact resistance.

5.9. SSH CHAIN ENVIRONMENT

We measure the transmission spectrum of the SSH chain in the topological state over the accessible frequency range (4 – 8 GHz), see Fig. 5.9.1. We observe a non-monotonic and peaked background transmission with a finer modulation and with a maximal transmission close to the expected transmission. We attribute the resonance-like peak at around 6.2 GHz to a box mode hosted byt the PCB enclosure spanning between the two test ports S and D, which acts as a band pass filter in parallel to the SSH chain, which in turn affects the overall transmission. We also observe that the transmission spectrum recorded in several experimental runs and on different samples, but within the same enclosure differs from the expected

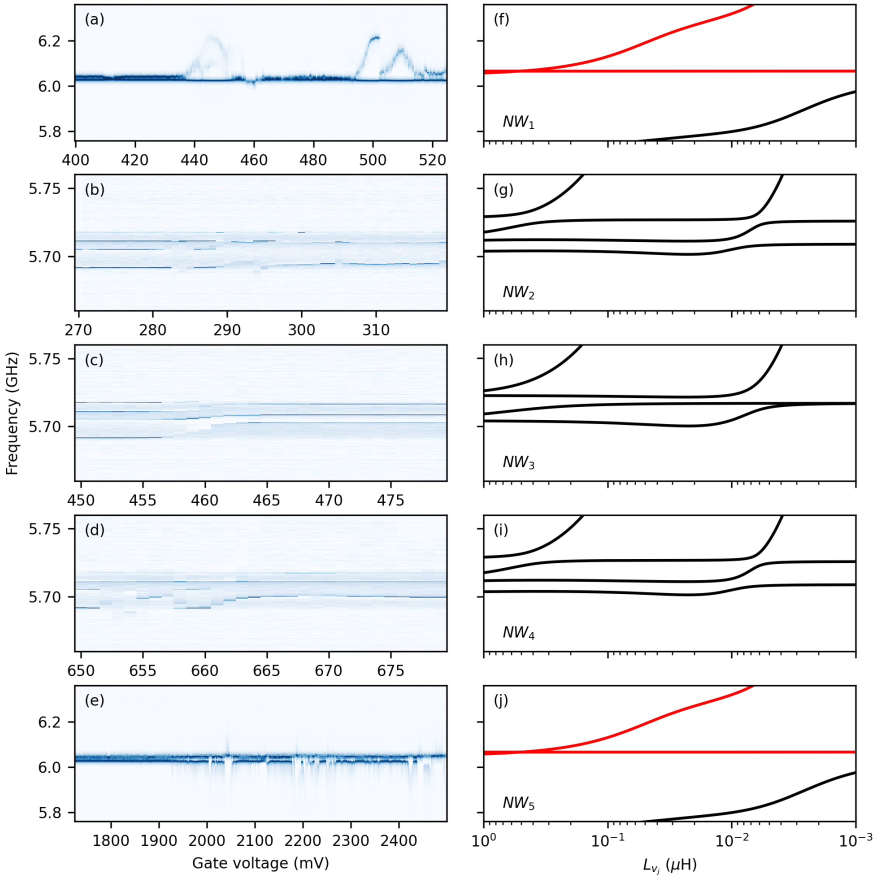

Figure 5.7.1.: Single gate dependence. (a-e) Measured spectrum per gate while the other gates are set to V_p. Zoom-in on low band for bulk gates and zoom-in on gap for edge gates. The data is normalized on the background to enhance the visibility of the change. (f-j) Corresponding simulated spectrum.

transmission spectrum with two or three well resolved transmission bands. We highlight the resemblance of the transmission spectrum with a broad band resonator with a fit to a Lorentzian. The finer modulation of the transmission probably arises from impedance mismatches along the lines connecting to the measurement electronics.

To simplify the data analysis in the presence of the box mode, we obtain a linearly interpolated background transmission spectrum Fig. 5.9.1 onto which we normalize the all measurement data to better identify the transmission peaks and dips of the SSH chain spectrum.

While we cannot extract the exact effective inductance and capacitance leading to the box mode formed by the enclosure, we can approximate its effect in a lumped element simulation in which we assume a resonator in parallel to the SSH chain. The results of these lumped element simulations are presented in Fig. 5.9.2(top) for the ideal case and in Fig. 5.9.2(bottom) for the case in presence of a box mode. In the ideal case, we expect two, or three well defined bands with in total 10 modes and otherwise suppressed background transmission. However, a box mode yields a higher overall transmission due its band pass filter like nature and distorts the measured line shape of the modes due to is capacitive contribution on the rising edge and its inductive contribution on the falling edge. Consequently, the bulk modes appear as dips and peaks and the mid gap modes in the topological state appear as deep dip with a shallow peak in the center.

The box mode does not affect the SSH chain, but it does complicate the interpretation of the overall transmission spectrum. To overcome the effect, a new sample enclose should be carefully designed [202], or the current sample enclosure should be modified.

Going beyond the current experiment, one could also intentionally coupled a SSH chain to a resonator as described in Ref. [170].

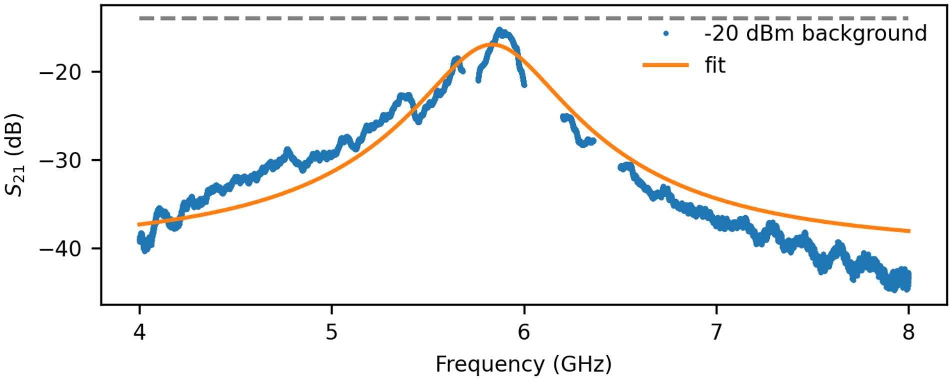

Figure 5.9.1.: Box mode. S_{21} transmission spectrum over the accessible frequency range 4 – 8 GHz without the SSH modes (blue). A Lorentzian fit to the data highlights the presence of a box mode (orange). The dashed lines indicates the expected transmission given the input attenuation and output amplification.

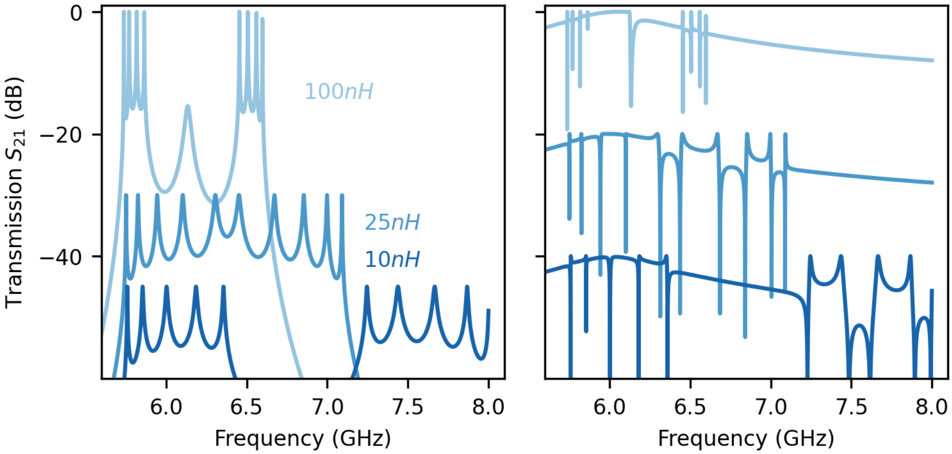

Figure 5.9.2.: Lumped element simulation of the three regimes topological, normal, trivial for different tuning scenarios. (a) Expected, ideal SSH chain spectrum for a joint synchronous sweep of L_v. (b) Same device tuning as in (a), but accounting for the presence of a box mode modelled as transmission resonator in parallel to the SSH chain. Note that all spectra per panel are offset for better visibility.

6

CONCLUSION

"Do not judge me by my successes,
judge me by how many times I fell down
and got back up again."

Nelson Mandela

6.1. GATE TUNABLE INDUCTANCES FOR SUPERCONDUCTING CIRCUITS

In this thesis, we combine the study of condensed matter systems and circuit quantum electrodynamics in what is called hybrid cQED experiments. We explore the concept of gate-tunable kinetic inductances for superconducting circuits along two dimensions: (1) the fundamental physics of gate-tunable kinetic inductances and emergent phenomena thereof, (2) the applications derived from the gate-tunable kinetic inductance.

Along the first dimension, we have investigated the gate-tunability of the bulk properties of continuously proximitized semiconducting nanowires, and we have studied the phase transition of an SSH metamaterial.

Along the second dimension, we have realized gate-tunable resonators, gate-tunable parametric amplifiers, gate-tunable transmon qubits and eventually gate-tunable resonator lattices forming metamaterials.

While the work presented in this thesis mainly focuses on gate-tunable kinetic inductances made from hybrid superconducting-semiconducting nanowires, the underlying concept is directly transferable to other hybrid material systems such as proximitized 2 dimensional electron gases (2DEG) of InAs or InSb, hole gases (2DHG) of Ge, or other 2 dimensional materials such as graphene or other van der Waals materials.

For my own record: The projects required meticulous lab work. In particular, I deposited more than 250 nanowires, for the projects I was involved in and on samples that actually got measured. And I executed more than 46 cooldowns of dilution refrigerators, see Tab. 6.1.

project	samples	nanowires	CD
NWres	11	44	11
NWPA	13	88	24
NWSSH	6	10	11
SQDS		40	
ASQ-ASQ		16	
QPP		40	
ABS		12	

Table 6.1.: Project statistics including the number of measured samples, deposited nanowires, and executed cooldowns in "B3" (except for 2 CD in "Mira", 8 CD in "K1").

6.1.1. NW RESONATOR

Our research introduces the previously unexplored concept of gate-tunable superconductivity in the bulk of hybrid nanowires, distinct from conventional tuning observed in gate-tunable nanowire Josephson junctions. We emphasize that the conventional wisdom prior to our work, that extracting the gate dependence of the normal-state conductivity of the InAs/Al nanowires would be impossible due to the dominant contribution of the Al-shell, was wrong - and yet, we have precisely achieved this measurement by relying on low-noise, high-energy resolution microwave techniques. Important to note is that the inductance of the circuit connecting to the nanowire closely approximates the nanowire inductance. Consequently, the contribution of the contact inductance significantly influences the total inductance of the circuit, which can complicate the interpretation of the measurement results.

Hence, it's worth highlighting that the examination of reproducibility in this study involved an unprecedented scale - we investigating over 20 experimental realizations to understand the consistency of the observed effect.

Eventually, the research outcome lead to the development of a parametric amplifier and strongly motivated the efforts of implementing a Kitaev chain, which critically relies on the control of the bulk properties of the nanowire.

On the distinction between nanowire junction and nanowire inductance: The comparison between the bulk kinetic inductance measured in our pristine nanowires and the local Josephson inductance typical using in gatemon devices reveals significant differences in their length dependence and their dependence on local properties. While both types of inductances can be understood as kinetic inductances, there are important differences. As we write in the manuscript, using Mattis-Bardeen theory, the kinetic inductance at low temperature reads $L_{NW} \sim l/(\sigma_n \Delta_n)$ where σ_n is the gate dependent normal state conductivity, Δ_0 the induced superconducting gap and l the length of the nanowire segment. In contrast, following for simplicity the Ambegaokar-Baratoff formula for tunnel junctions, we can express the Josephson inductance of a nanowire-based Josephson junction via its Josephson energy as $L_J \sim 1/E_J \sim 1/\Delta G$ where G is the gate-dependent conductance of the junction and Δ the superconducting gap. We see the crucial difference that L_{NW} depends on the bulk properties of the nanowire and, consequently, is an extensive property, scaling linearly with the length of the proximitized wire. Via the dependence on σ_n, it reflects important properties of the bulk system, such as the mean free path in the semiconductor under the Al shell or the number of occupied sub-bands in InAs. In contrast, L_J only depends on local properties (such as the barrier transparency) and is independent of the length of proximitized nanowire (though of course it may depend on the length of the junction itself). A measurement of L_J, or equivalently G, does not provide information about the bulk properties of the InAs/Al wire since it depends on the junction geometry and fabrication details.

Notably, the continuous Al shell of the proximitized nanowires exhibits a substantial critical current and reduced normal state resistance. For a $3\,\mu$m long, proximitized nanowire with continuous shell we observe a critical current of $I_C \sim 10\,\mu$A and a normal state resistance of $R_N \sim 350\,\Omega$. Measurements on 100 nm long, nanowire-based Josephson junctions such as those used in gatemons typically yield $I_C \sim 100\,$nA and a normal state resistance of $R_N \sim 5\,\mathrm{k}\Omega$. The relatively large critical current and the small normal state resistance of the proximitized nanowire arise from the presence of the uninterrupted Al shell, which also diminishes the gate tunability of the bulk properties of the proximitized nanowire compared to a nanowire-based Josephson junction. Regarding the gatemon, the nonlinearity of the proximitized nanowire reported in the manuscript is sufficiently large to realize parametric amplifiers but does not allow the realization of transmon qubits.

Future efforts in the material development should address the limited tuning range of the hybrid devices.

6.1.2. NANOWIRE PARAMETRIC AMPLIFIER

We present a pioneering study on a new class of superconducting parametric amplifiers that deviates from traditional SQUID-based or Josephson-junction-based implementations. Building upon our prior work on gate-tunable kinetic inductances in proximitized nanowires, our innovative design leverages the nonlinear response of the gate-tunable kinetic inductance in proximitized semiconducting nanowires, eliminating the need for Josephson junctions. Achieving a remarkable 20 dB gain and a 30 MHz gain-bandwidth product, our amplifier is en par with conventional designs while is also remains compatible with magnetic fields up to 500 mT. The device not only exceeds near-quantum-noise-limited measurement requirements but also holds promise for enhancing the readout of semiconductor-based spin-qubits and other hybrid systems, thanks to its magnetic field compatibility and minimal crosstalk compared to conventional flux control.

Our design objectives were tailored to fill a critical gap in amplifier development for quantum and condensed matter experiments involving sensitive components susceptible to stray magnetic fields. By minimizing magnetic crosstalk through electrostatic tuning, our Josephson-junction-free design optimally balances three key objectives: large saturation power, magnetic field compatibility, and gate tunability. The absence of a Josephson junction facilitates reaching a sizable saturation power of −120 dB and enhanced magnetic field compatibility by enabling operation within the superconducting thin film plane. While acknowledging potential improvements, our implementation represents a significant step forward in achieving these objectives, laying the foundation for broader applications in research.

Gate tunability, though certainly smaller (15 MHz) compared to state-of-the-art resonator-based amplifiers using SQUIDs, offers distinctive advantages. The properties of our semiconductor nanowire-based implementation remain nearly constant over the accessible frequency range, unlike other designs with varying characteristics. Furthermore, the tunability scales linearly with the nanowire segment length, suggesting future enhancements by increasing segment length. Although improvements are envisioned, the current tunability proves useful, particularly in scenarios where a fine-tuning around a target frequency is sufficient, such as in devices with low kinetic inductance superconducting resonators.

Magnetic field compatibility emerges as a pivotal feature of our design, aris-

ing from the choice of superconducting thin films. While the non-monotonic behavior of nanowire inductance versus magnetic field requires further investigation, our device demonstrates compatibility up to 500 mT. Technical limitations prevented exploring higher magnetic field dependence and noise performance in our experiment, but the groundwork laid here sets the stage for future investigations in these directions.
While preparing this thesis, I got aware of three other works on magnetic field compatible parametric amplifiers [29, 47, 48], which, compared to the magnetic field compatibility objective, clearly outperform our implementation of a nanowire based parametric amplifier.

Finally, I want to say, that tuning up an amplifier and carefully calibrating out its noise performance poses a much harder challenge than measuring the coherence properties of a superconducting qubit under the same constrains as gate tunability and magnetic field compatibility due to the required carefulness. Or in short: Measuring open, dissipative and driven quantum systems is hard.

6.1.3. NANOWIRE SSH CHAIN

We have realized a macroscopic SSH chain out of a chain of superconducting resonators, which inherit the tunability from the microscopic properties of nanowire Josephson junctions. We have carefully characterized the system in the topological regime and mapped our bosonic implementation onto the original spin-less, single particle SSH chain Hamiltonian. Eventually, we leveraged the unit cell tunability to observe the SSH chain phase transition in the macroscopic, gate-tunable resonator based SSH chain.
Our experiments takes the idea of gate-tunable superconducting circuits [192] to scale and proves that the implementation of several nanowire Josephson junctions in cQED experiments is possible. This result encourages further research on gate-tunable qubits and Kitaev chain systems.
However, our findings also suggest that in order to fully exploit the microscopic properties of SNS junctions for stable operation and reliable applications, advances in the material development of the hybrid superconductor-semiconductor stack have to be made.
In future realization of this tunable system we intend to probe the on-site wavefunction with qubits as local probes via their affected decoherence and qubit frequency arising from an AC Start shift [154, 156, 195]. Going beyond the current implementation, one can study the nonlinear coupling [196, 197] between unit cells. Other work might focus on distant coupling of quantum emitters to a 1d-chain or the extension to 2D lattices [194] or more complex 1d systems like the Rice-Mele model [198] or the the Kitaev model [199].

This project allowed me to eventually observe a phase transition of an extended state in a macroscopic system, and helped me to achieve the goal of my PhD for which I came to Delft. While the initial project on proximitized nanowires failed because of disorder and poorly understood experimental requirements, we managed to engineer a system that is robust enough against disorder.

6.2. OUTLOOK

There are of course many ideas around, but we will present only a few core concepts and concrete research directions within those. Disclaimer: The ideas should again be scrutinized before the start of any actual research endeavour.

6.2.1. MATERIAL DEVELOPMENT FOR GATE TUNABLE INDUCTANCES

In this thesis, we presented the concept of gate-tunable inductances based on the hyrbid Al-InAs stack. Similarly, also other semiconductors such as InAs, InSb, and more recently, Ge, which have been proximitized with Al or other superconductors could be used for this purpose. This innovative approach opens the door to a myriad of experiments that probe the microscopic properties of these materials. However, our investigations into the use of proximitized semiconductors revealed certain limitations in tuning range, stability, and hysteresis during experiments.

While we observed a monotonic and stable kinetic inductance as a function of gate voltage in Chapter 3 and Chapter 4, we faced a problem of instability and hysteresis in the NW SSH chain implementation in Chapter 5 based on nanowire junctions.

The precise requirements for improving the properties of nanowire junctions for cQED experiments remain uncertain. Potential avenues for improvement include achieving a low-resistance interface to the circuit, establishing a clean, wide and disorder-free junction to avoid accidental quantum dots (potentially using 2DEG implementations), and enhancing charge carrier mobility. Equally crucial is ensuring chemical robustness for large-scale implementation.

6.2.2. AC-GATE CONTROLLED SUPERCONDUCTING CIRCUITS

The coupling between gate-tunable nanowire inductances and Josephson junctions and superconducting resonators can exhibit rich and novel physics. In this section we contemplate three different research projects: we suggest to optimize gate-tunable parametric amplifiers, we suggest to build an on-chip microwave generator, and we suggest to implement a phase gate for protected qubits. The all-encompassing research question thus is: What kind of quantum states can be prepared, observed and manipulated in the coupled junction-cavity system?

NANOWIRE LASER

Exploiting the nonlinear dynamics of the strongly coupled Josephson junction-cavity system can result in meaningful applications, such as an on-chip microwave generator. First experiments [203, 204] have already demonstrated parts of the physical phenomena in the high quality, high nonlinearity limit. Here, we suggest investigating the effect of lasing independent of the exact finite bias voltage by measuring the relative amplitude and phase at different cavity harmonics in the steady-state and pulsed drive mode. This extension of previous work will answer open questions in the current theoretical model and pave the way towards a controllable on-chip microwave source with a short pulse duration and high repetition rate for the coherent manipulation of artificial two-level systems, in particular superconducting charge qubits such as transmons [1].

Introduction Within the last 30 years of qubit development, the coherence time T_1 for single qubits has been increased significantly from first 8 ns for the Cooper pair box to 5 ms for Fock-state encodes qubits in 3d cavities [205]. This progressive improvement brings medium scale architectures of qubit networks into sight [206]. In order to operate interesting algorithms on multiple physical qubits, typical qubit infrastructures rely on large dilution refrigerators with multiple superconducting RF drive lines [207], which are hardly scalable due to the thermal load of RF cables and connections.

Consequently, researchers try to fold the architecture in 3d as well as down-scale and better thermalize the RF control. An alternative proposal is to bring as much of the qubit control on-chip. Therefore, we propose to further investigate tunable on-chip microwave generators based on the ac Josephson junction laser [203] demonstrated in 2017 and its continuous wave (CW), hybrid semiconductor-superconductor nanowire extension [204] in 2018. This strategic addition to the cQED toolbox could enable fast qubit operations when neatly integrated in existing qubit designs. Furthermore, the omission of RF lines breaks the thermal link between base temperature and room temperature and prevents the injection of high energetic radiation.

As a long-term goal, we envision an on-chip microwave generator consisting of a DC voltage biased and gated nanowire Josephson junction strongly coupled to a transmission line cavity, which enables the microwave frequency generation up to the superconducting gap and pulse generation with arbitrary shape and width down to 10 ps resulting for possibly 50 GHz controllable bandwidth. Thus, no RF lines are required for microwave experiments according to this proposal. Besides waveform generation for qubit operations, a short pulse and high repetition rate on-chip microwave source enables frequency comb generation used in metrology.

This motivation goes hand in hand with the exploration of the underlying physics. From an academic perspective, studying the emission of radiation of a DC voltage biased Josephson junction coupled to different environments is of great interest because it adds a new functionality to the Josephson junction as circuit element. In the past, research focused on Josephson junctions coupled to transmission lines or lossy transmission line cavities. The experiment in [203] explored the high quality cavity, high nonlinearity junction limit, which leads to a strongly coupled system. In our work, we want to observe the emission characteristics of the strongly coupled system at multiple harmonics of the fundamental resonance frequency as a function of bias voltage, and junction nonlinearity in order to use it for pulse generation.

With this proposal, we suggest four project phases: reproduction of previous

work, investigation of lasing at higher harmonics, short-pulse detection, and complete on-chip microwave generator for qubit operations.
The second experimental phase requires adjustments to the system design. First, we design the cavity such that multiple harmonics starting from the fundamental mode fall into the accessible measurement bandwidth of 4 GHz to 16 GHz. Second, the capacitance of the coplanar waveguide is minimized such that the nonlinearity of the system can be widely tuned by the Josephson energy E_J. Third, the gate is connected to a fast DC line in order to modulate E_J in time for studying the time dynamics of the emission process and for active mode locking. Also, it helps to change the emission intensity. Fourth, the DC voltage bias is further stabilized in the small voltage range to facilitate the observation of harmonics.
The third experimental phase requires phase correlation measurements of different harmonics after down-conversion through frequency mixing. For this, the dispersion of the amplification chain must be precisely known. We investigate active and passive mode-locking techniques, such as active injection locking or passive Q-switching in order to reach ps pulse duration.
Eventually, this system could be integrated together with a qubit, like a transmon, on a single chip.

Coherent light from junction-cavity system Josephson junctions can be coupled to different environments. One realization is the Josephson-junction-embedded transmission-line resonator [208], which can be operated in a certain regime as a nanowire laser. The general equivalent circuit with DC voltage biasing is depicted in Fig. 6.2.1a. The cavity is illustrated as a transmission line. Mathematically, the time evolution of the phase of the resonator modes φ_n is described by a coupled, nonlinear differential equation [209–211]

$$\ddot{\phi}_n + \gamma\dot{\phi}_n + n^2\omega_0^2\phi_n = -\lambda\omega_0^2 \sin\left(\sum_n \phi_n + \omega_J t\right) \tag{6.1}$$

with the mode dependent cavity frequency $n\omega_0$, dissipation rate γ, the superconducting magnetic flux quantum $\Phi_0 = \frac{\hbar}{2e}$, time t, total capacitance C and the Josephson frequency $\omega_J = \frac{2eV}{\hbar}$. The right side of the equation is called the forcing function. It is convenient to introduce a forcing strength $\lambda = \frac{E_J}{\Phi_0^2 C\omega_0^2}$. For a fixed capacitance, λ is only set by E_J which itself can be tuned by a nanowire gate.

For a high quality junction-cavity system, we can describe the dynamics as a function of the forcing strength.
The linear regime with $\lambda \ll 1$, meaning small E_J, is dominated by spontaneous emission of radiation close the cavity resonances. Intuitively speaking, photons emitted by the junction into the cavity do not undergo a nonlinear interaction with the junction after one cavity round-trip. Thus, neither higher harmonic generation nor down-conversion takes place. The emission is enhanced around the quantized resonances of the cavity, i.e. at voltages $2eV_b = hf_n$. This is also called the Purcell effect, see Fig. 6.2.2a,b.

The nonlinear regime with $\lambda > 1$, meaning large E_J, is dominated by stimulated emission of radiation at all frequencies independent of the finite bias voltage, see Fig. 6.2.2d (Fig. 6.2.2c shows the same parameter settings as in d, but modes are considered as uncoupled). This is also the regime that we want to further investigate in experiments by recording a large frequency span for each DC bias voltage. The underlying processes are sketched in Fig. 6.2.1b,c. For $V_b = 0$ the junction allows dissipationless transport, but no emission. For $eV_b < \Delta$ the system is lasing by stimulated emission of radiation due to back-action. In a simplified picture, one can think of a photon emitted by spontaneous emission of the junction into the cavity. After one round-trip in the low loss cavity, the photon interacts again with the nonlinearity of the junction, which results in frequency mixing and the generation of all harmonics by higher harmonic generation and down-conversion. The modes in the cavity combine coherently due to the junction-cavity back action and form discrete pulses. This is the concept of a mode-locked pulsed laser. Thus, we will observe the emission of light at many harmonics independent of the voltage bias.

Due to the resonator line broadening and the frequency mixing of these frequency components, we also observe frequency components further detuned from the cavity harmonics and with lower intensity.

As a result, the emission spectrum will eventually be continuous with some intensity modulation up to a cutoff, above which the nonlinearity is not strong enough to mediate frequency mixing and only disconnected peaks remain. In the experiment, we can probably realize a few resonator modes within the measurement bandwidth, but are limited in the range of the coupling strength λ.

For $eV_b > \Delta$ incoherent quasi-particles are generated and damp the junction, leading to a higher loss rate and a reduced emission. For $eV_b > 2\Delta$, only resistive transport can be observed.

In the literature, we can find further examples for junctions embedded in different environments. A general overview on junction-cavity systems is given in [208]. The high quality, high nonlinearity limit is studied theoretically in [209–211] and experimentally in [203, 204]. A realizations of parametric amplifier can be found here [212]. The low quality factor limit was explored in [213]. The emission of nonclassical radiation was shown in [214]. On-demand antibunched radiation was generated in [215, 216].

Up to the present day, research on the junction-cavity system focused on the voltage dependence of the continuous emission of radiation with constant intensity into the fundamental cavity mode. The previous experiments on the system have not observed the expected generation of higher harmonics independent of bias voltage. Our research objective follows up on these results. Here, we suggest to investigate the radiation emitted into higher harmonic cavity modes and their coupling via the junction as nonlinear circuit element. We expect phase coherent emission of all modes. Once we achieve the coherent superposition of several cavity modes by active or passive mode locking, the mode beating should result in a modulation of the emission intensity in form of a pulse train, characterized by a certain pulse duration and pulse repetition rate.

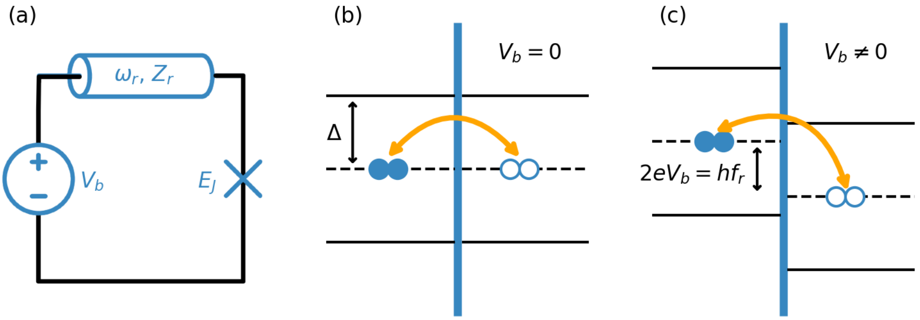

Figure 6.2.1.: (a) General circuit diagram for the Josephson junction laser consisting out of a voltage source, a resonator, and a Josephson junction. (b) Unbiased Josephson junction leading to no emission of radiation. (c) Biased Josephson junction emitting radiation.

Design and Fabrication As demonstrated in [203], the junction-cavity system can be composed of a half-wave coplanar waveguide transmission-line resonator between input and output port and a Josephson junction connecting the central conductor of the CPW to ground at one current node of the cavity.

In order to exploit the full application range, the system has to be adjusted in the parameter range. For maximal control over the nonlinear forcing function of the differential equation, we wish to tune the forcing strength in the range $\lambda = 0$ to 10. From preceding experiments, we can estimate the Josephson energy to be adjustable within the range $E_J = h * 0\,\mathrm{GHz}$ to $50\,\mathrm{GHz}$ [204, 217] using a gate. In contrast, the capacitance is fixed by the geometry. Based on this requirement, the total capacitance should be

$$C = \frac{E_{J,max}}{\lambda_{max}\Phi_0^2\omega^2} \approx 0.1\,\mathrm{pF}$$

for $f_0 = 3.5\,\mathrm{GHz}$. It is dominated by the total CPW resonator capacitance (capacitance per unit length times length). The junction and the coupling capacitance are of the order of 10 fF and thus can be neglected. For a minimal resonator length of $l_{res,min} = 5.8\,\mathrm{mm}$, we can calculate the maximally allowed capacitance per length of $C'_{res,max} = 17\,\mathrm{pF/m}$, which heavily restricts the design.
The controlled DC voltage biasing with integrated current measurement is an essential part of the experimental design. The wiring must optimized for stable voltage supply, precise current readout and minimal filter-cavity interaction. Therefore, they consist of a voltage divider and an off-chip π-RC low-pass filter used

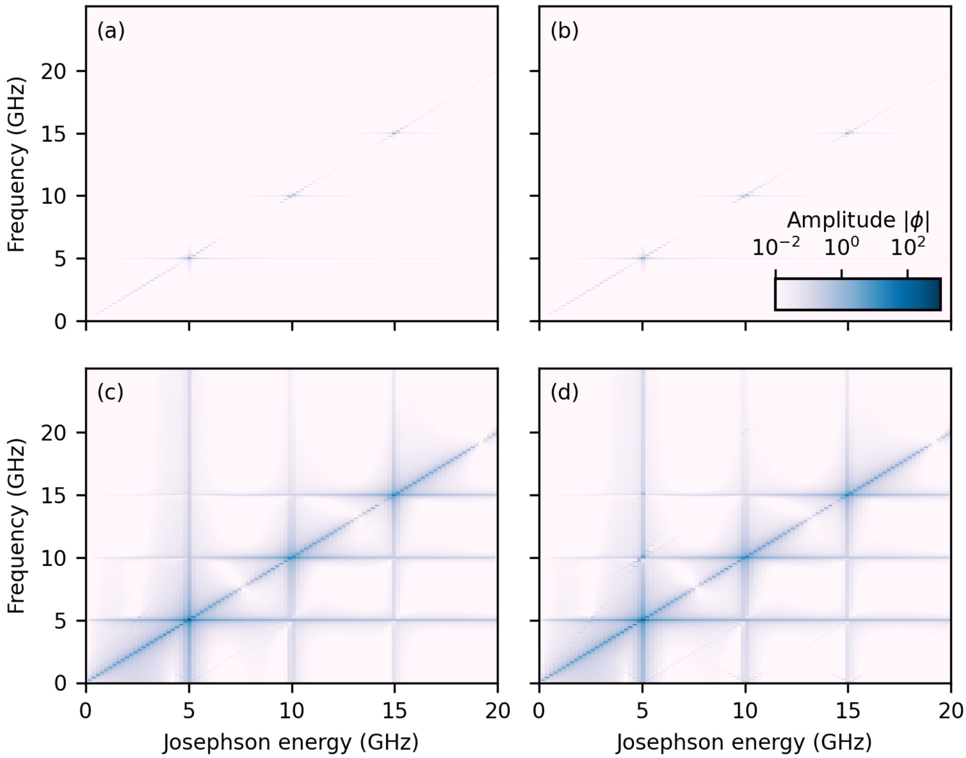

Figure 6.2.2.: Simulation of the emission spectra for different coupling strength λ (low: a,b vs high: c,d) and assuming three uncoupled modes (a,c) as well as three coupled modes (b,d). In the low λ limit, the coupling of the modes does not change the spectrum. In the high λ limit, the back-action leads to the emission of higher harmonics for the coupled modes system, compared to the uncoupled mode system.

also for current measurement. The properties of the aluminium PCB to on-chip bond cannot be well controlled. Next, the on-chip low-pass T-LC filter consisting of a spiral inductor and an interdigitated capacitor to ground and again an inductive microstrip connect to the resonator. This filter helps to reduce the energy leakage of microwave radiation into the DC bias line. Typical values are $C_{filter} = 1\,\mathrm{pF}$ and $L = L_{filter} + L_{spiral} = 13\,\mathrm{nH}$ with a cutoff at $f_{LC} = 3.5\,\mathrm{GHz}$. The exact DC voltage biasing still needs to be discussed. Especially the known problem of instabilities of the load circuit at low bias voltages needs to be mitigated.

One approach for active mode locking in view of a pulsed NW laser is based on a fast gate for few MHz to perhaps even GHz modulations of the gate voltage in order to orchestrate the emission of all modes and thus force coherent emission. This requires again a low-pass filter in order to minimize the coupling of microwave radiation to the gate line. The cutoff frequency still needs to be determined.

Experimental stages and measurement plan The proposed experiments fall into three project phases, which should be conducted sequentially in order to explore the physics between the current continuous wave nanowire laser and the tunable on-chip microwave source:

1. Spontaneous and stimulated emission of Josephson radiation to individual microwave cavity modes
2. Injection-locking at different harmonics for active mode locking
3. Fast backgate modulation for fast tune of nonlinearity and active mode locking

The following subsections contain a more detailed description of measurement plan and a discussion of the possible results.

Spontaneous and stimulated emission of Josephson radiation to individual microwave cavity modes We will observe the spontaneous and stimulated emission of Josephson radiation by measuring the emission spectrum for different values of the DC voltage bias depending on the gate voltage, which sets the nonlinearity and E_J. The goal of this measurement phase is the reproduction of the simulation presented in Fig. 6.2.2b,d.

The sequence of experiments starts with the acquisition of the cavity spectrum with the Josephson junction being in pinch-off in a standard CW VNA measurement. From this, we extract the bare resonance frequencies as well as the internal and coupling quality factors for different modes. Next, we focus on the junction only and measure an IV curve for different gate voltages and extract the superconducting gap.

The reproduction of the experiment is important to establish the fabrication techniques and set up the measurement electronics.
Then, we will sweep the DC voltage bias V_b and observe the full spectrum in the range 4 GHz to 16 GHz, including 4 resonator modes, for different backgate voltages tuning E_J between pinch-off and open. This measurement requires a new HEMT and new circulators suitable for this frequency range as well as an output line without TWPA in order to circumvent its dispersive feature. For each DC voltage bias we will acquire the full emission spectrum and readout its bandwidth as a function of the junction nonlinearity in terms of E_J. From this, we can calculate the power conversion efficiency. This could help us to understand the order of nonlinear processes involved in the cavity-junction back-action.
Using IQ demodulation, we investigate the coherence of the emitted light at different frequencies. In this state of the free running system, we will observe a "donut" shape in the IQ plane indicating superposition of different time evolutions of a coherent state. For higher harmonics closer to the superconducting gap, an additional peak

around zero will appear in the IQ plane, which originates from non-coherent thermal radiations. The acquisition of a time trace of these higher modes will show an on/off switching behaviour, which can probably be explained by quasi-particle poisoning of the emission process.
By frequency down-conversion of higher modes to the fundamental mode, we can also study the phase correlation of different modes. We would like to investigate the bandwidth and the phase coherence of all frequency components within this bandwidth for a fixed DC voltage bias in order to better understand the emission process.

Theoretically, one can expect the functionality of a multi-mode laser when operated in the strong coupling limit. Under the assumption, that the light emission into different modes happens coherently, we can then further expect passive mode-locking by stimulated emission, which should result in short pulse generation due to mode beating. The pulse width and repetition rate should be set by the number of harmonics included in the spectrum. The emission amplitude can be set by the junction nonlinearity.

Injection-locking at different harmonics for active mode locking By injection-locking we can control the time evolution of different modes. Typically, this leads to a narrowing of the emitted line width. The effect has been observed for the fundamental harmonic, but not for their multiples. It is of interest to individually probe the harmonics and study their phase evolution in the IQ plane.

Moreover, one could actively mode-lock the system by injecting four RF tones, called seed, tuned to the different harmonics. The relative phase tuning of the seed can lead to a coherent and stable superposition of different modes, which then itself results in mode beating and eventually short pulse generation. This technique should allow for maximal adjustability of the relative phase of the four different harmonics in the measurement bandwidth. However, this approach contradicts the original proposal of having a gate-line tuned (thus no RF line required) microwave-source.

Fast backgate modulation for fast tune of nonlinearity and active mode locking The backgate voltage can serve as a fast tunable knob for the emission characteristic and can probably be driven with tens of MHz to few of GHz rate, when connected to fast gate lines or on-chip bias-T after RF lines. This technique enables us the investigate the dynamics of the emission process.
First, while acquiring time traces, we set step function pulses to the back gate. With this method, we can derive the response function of the fast gate.
Second, we apply backgate pulses and record time traces of the emitted signal at different harmonics individually. We can study the phase correlation of the signal as well as the pulse width.
Third, we apply backgate pulses and record time traces of the emitted signal at all harmonics at a time. This way, we can follow the emission process and potentially

observe the time evolution of the cavity mode population. This will offer valuable clues about the order of nonlinearity involved in the back-action process.
Potentially, this technique can serve as active mode-locking for short pulse generation.

Possible extensions of the project The main research goals described in this proposal are the observation of higher harmonics and the operation of a pulsed nanowire laser. However, we already envision possible extensions based on the same or similar geometries, which are briefly adumbrated hereafter:

Interferometric on-chip intensity auto-correlation of short pulses: We would like to integrate a on-chip intensity auto-correlation using heterodyne detection in a nonlinear medium, again a Josephson junction, in order to determine the ps pulse width with high accuracy right after the laser. This way we would like to avoid the potential pulse shaping due to the amplification chain in the fridge read out line. This technique requires a redesign of the current chip and readout design.

Transmon control: The final goal of the project is to drive a transmon qubit from an on-chip microwave source. In the past, transmon qubits with coherence times of about 100 μs in T_1 and T_2 have been realized [205], also here in Delft. In order to reach this device and measurement quality, further improvements on the qubit shielding are required. Another challenge is the simultaneous fabrication of qubit and laser devices with high quality on the same chip. However, the fabrication for individual devices should be well established. The qubit could be integrated into the laser and coupled to the same central conductor or places behind the cavity.

Further ideas: Possible extensions of the project rely on the integration of further Josephson junctions. We are thinking of Josephson junction positioned along the transmission line in order to modulate the participation ratio of each junction with the propagating mode. This could increase the laser intensity.
Other than that, we can place a second junction at the opposite end of the junction and run pump-and-probe experiments between the two junctions. In this proposal we envision the emission of light at one junction, which then excites the next junction. Possible effects are retarded propagation of light and junction-junction back-action. This experiment will further shed some light on the excitation and emission process of Josephson junctions.

In this project, we would like to further explore the junction-cavity system in the lasing regime at higher cavity harmonics. Starting from individual harmonics, we would like to coherently control multiple harmonics as the ones shown in Fig. 6.2.2 by clever design and measurement in order to construct and operate a tunable microwave generator.

From a technical point of view [203], a few questions remain: First, how can we build a stable on- and off-chip DC voltage bias scheme, that does not show any bifurcations in the low bias voltage regime? Second, how can we readout and control the envelop of generated pulses? Can we also observe the chirp within the pulse? Third, can we implement 2DEG nanowire-based junctions to allow for a well-defined and adjustable E_J? Another idea is to use shadowed junctions instead of etched junctions to increase the junction quality and eliminate the presence of unwanted resonances or subgap states. [1]

TOWARDS PROTECTED GATES: JOSEPHSON SWITCH AND GRID STATE PREPARATION

Quantum systems suffer from decoherence of various origins, which impedes the development of scalable quantum computers and can be overcome by the integration of either error-correction or fault-tolerant computation schemes. The latter can be achieved by robust encoding of information in a particular superconducting circuit, the so-called 0-π qubit, which can be manipulated using the $\exp(i\frac{4}{\pi}Z)$ phase gate. It can be implemented as a tunable Josephson coupling between a 0-π qubit and a LC resonator with high impedance. As part of the phase gate protocol, the coupling is varied by a square pulse with fast raising and falling edge, which creates and annihilates grid states in the LC oscillator. Apart from the gate operations, grid states are an important resource in quantum error-correction and therefore interesting by themselves.
Here, we propose to demonstrate the fast switching and the grid state generation, which does not require a working 0-π qubit. For the fast tunable coupling, we envision the use of a fast gated nanowire Josephson junction.

Protected qubit gate One implementation of protected qubits, which are less or not susceptible to various sources of decoherence, is the 0-π qubit theoretically proposed in [218–220]. The main characteristic of this two terminal superconducting circuit depicted as a back-box with label Qubit in Fig. 6.2.3a is the π periodic energy dispersion as a function of the phase difference across the qubit θ with energy degenerate minima at $\theta = 0$ or π. The barrier between the minima defines two energy degenerate eigenstates $|0\rangle$ and $|1\rangle$. In this scheme, bit-flip errors are suppressed by the potential barrier between the two eigenstates. Phase-flip errors associated with quantum tunnelling from one to the other terminal are suppressed by the energy degeneracy of states.

For manipulations of the $0-\pi$ qubit, Brooks, Kitaev, and Preskill [221] invented the single-qubit phase gate $\exp(i\frac{4}{\pi}Z)$, which could become part of a full universal fault-tolerant scheme. As phase gate, they consider a 0-π qubit coupled to a LC circuit via a fast gate-tunable nanowire Josephson junction. The junction is operated as a switch between pinch-off and open. The circuit is shown in Fig. 6.2.3a

---

[1] This project proposal stems from my GoNoGo meeting in 2020 and was developed together with Bernard van Heck. I acknowledge the helpful discussion with Anton Akhmerov, Fabian Hassler, Yevheniia Cheipesh, and Willemijn Uilhoorn.

and its Hamiltonian can be written as

$$H(t) = \frac{Q^2}{2C} + \frac{\varphi^2}{2L} - J(t)\cos(\varphi - \theta) + H_{0-\pi} \tag{6.2}$$

with the time dependent Josephson coupling $J(t) \sim E_J$, the inductance L, the capacitance C, the phase across the qubit θ, and the resonator phase variable φ. The Hamiltonian of the qubit $H_{0-\pi}$ is neglected here as its only function is to set θ. The main requirement for the phase gate is a large LC resonator impedance $L/C \gg 1$ leading to a shallow harmonic potential. For the ground state of the resonator, the wave function is broadened in φ space and confined in Q space.
Based on this circuit, the phase gate follows the scheme illustrated in Fig. 6.2.3b

1. On-ramp
2. Evolution in time
3. Off-ramp

On-ramp: We want to evolve the ground state into a grid state by a fast change of the Josephson coupling. The time evolution of the switching process is shown in Fig. 6.2.3b with a pulse duration $t \approx L\pi$ (in renormalized units here) depending on the inductance and with a switching time $\tau_J \sim \sqrt{LC}$.
When the ramp-on time is well selected, the broad LC resonator ground state φ from the shallow harmonic potential will collapse into the different minima of the cosine dominated potential upon switching of the Josephson coupling. In detail, the ramp-on has to be slowly enough to adiabatically prepare the ground state in each local minimum of the harmonic-cos potential of the LCJ circuit, but also fast enough to prevent a collapse of the LC resonator ground state wave function into in only a few harmonic-cos potential wells of the LCJ resonator.
For a qubit phase $\theta = 0$, the projection on the φ space of the grid state leads to grid states with maxima at even multiples of π. Otherwise in the $\theta = \pi$ case, but not shown here, the maxima fall on odd multiples of π. A representation in Q space would show a different ratio of peak width to spacing. The grid states shall be denominated $|0_L\rangle$ and $|1_L\rangle$ for the two logical states.

Evolution in time: After the ramp, an arbitrary initial state has evolved into a superposition of grid states

$$(\alpha|0\rangle + \beta|1\rangle)|\Psi_{in}\rangle \rightarrow \alpha|0\rangle \otimes |0_L\rangle + \beta|1\rangle \otimes |1_L\rangle . \tag{6.3}$$

For a constant Josephson coupling over a certain hold time t, this new state evolves under the harmonic-cos potential. Besides an overall geometric phase, each peak in the grid state accumulates a relative phase under the action of the Gaussian operator $e^{-it\varphi^2/2L}$. If the hold time is well chosen, the evolving state comes back to its initial state up to an overall phase shift and reads:

$$\alpha|0\rangle \otimes |0_L\rangle + \beta|1\rangle \otimes |1_L\rangle \rightarrow \alpha|0\rangle \otimes |0_L\rangle - i\beta|1\rangle \otimes |1_L\rangle . \tag{6.4}$$

Moreover, the grid state can be squeezed to a central wave function by dissipation, mode interaction, and tunnelling through the cos potential barriers. The effect of squeezing depends on the device quality and its design.

The phase gate is completed by a ramp-off under the same conditions as the ramp-on that brings the superposition of grid states in a new superposition of LC oscillator states

$$\alpha\,|0\rangle \otimes |0L\rangle + \beta\,|1\rangle \otimes |1_L\rangle \rightarrow \alpha\,|0\rangle \otimes |\Psi_0^{fin}\rangle - i\beta\,|1\rangle \otimes |\Psi_1^{fin}\rangle\,. \tag{6.5}$$

Now, we can read out the final state of the LC resonator $|\Psi_{0,1}^{fin}\rangle$ which ideally only weakly depends on the original state of the qubit.

The phase gate for 0-π qubits thus requires the fast control of Josephson junctions, and the readout of the final resonator state. Note that in the full implementation, the phase gate fidelity will not only depend on the phase gate errors, but also on the qubit decoherence. In addition, for the purpose of characterization of the full gate operation, the readout of the grid state is important. Beside the gate application, the preparation of these grid states is interesting by itself, as grid states can be seen as basis for other quantum error-correction codes [222].

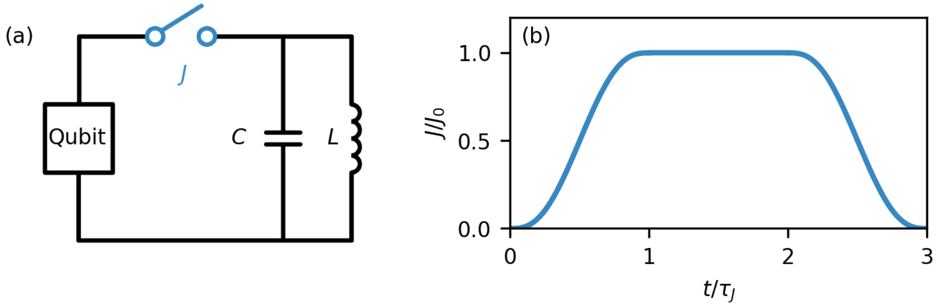

Figure 6.2.3.: Phase gate for a "0-π" qubit (a) Circuit consisting of a LC resonator connected via a Josephson junction switch to the qubit. (b) Time evolution of the coupling rate J mediated via the switch with the maximal Josephson coupling $J_0 \sim E_J$ and characteristic raising and falling time τ_J.

Experimental stages and measurement plan The central idea is to demonstrate the fast switching of a gated nanowire Josephson junction and to observe the generation of grid states in a phase-gate prototype, which does not require a working 0-π qubit.

The experimental realization of this project encompassed two technological challenges. First, we must build a fast nanowire gate based on an on-chip bias-T.

Second, we have to readout the quantum state of the LC and LCJ resonator in order to reconstruct the evolution from a Gaussian LC resonator state to a grid state.

Circuit design The equivalent circuit model looks like the circuit shown in Fig. 6.2.3a but without the qubit. So to say, we restrict the experiment to the $\theta = 0$ state. Theoretically, this device behaves like a fluxonium qubit in the $L/C \gg 1$ limit and at GHz frequencies [223].

The design of the LC resonator requires the integration of a "super-inductance" L and small capacitance C in order to fulfil the requirement $L/C \gg 1$. Ideally, we achieve a resonator impedance, which is 100 or 1k times larger than the resistance quantum $\hbar/e^2$, because the magnitude of Z determines the number of peaks in the grid state after the ramp. In this limit, we can almost neglect the broad harmonic potential of the LC resonator, thus the LCJ potential is dominated by the cos potential of the junction.

Fast backgate controlled nanowire Josephson junction The fast backgate control of the nanowire Josephson junction is a common theme in the previous and present project. One possible implementation relies on a bias-T, which is a three terminal device setting the DC and AC components individually. In our experiment, the low-frequency port is connected to the standard DC lines up to the MHz regime, and the high-frequency port is linked to an attenuated and filtered RF line in the dilution refrigerator. The output port of this device is then connected to the backgate. In addition, we need arbitrary waveform generators with ns resolution to reach the times scales required for the phase gate operated at GHz frequencies. With this gate configuration, we should be able to send arbitrary waves to the junction gate.
During the final design process, we will also revise the use of a wrap gate for a more reliable junction control.

The fast nanowire gate is characterized through the reconstruction of the resulting grid state after the on-ramp. Depending on the raising time of the gate, we will find the LCJ resonator in different grid states. Except for an overall phase accumulated during state evolution, we should be able to hold and observe the grid state for enough time to run the tomography. Then, we can plot the raising time of the Josephson coupling vs. LCJ state. Prior to this experiment, we will simulate the time dependence of the state preparation and better understand the different time scales.

Reconstruction of grid state After the on-ramp, we will find the state in some grid state depending on the raising time of the step function as discussed above. In order to characterize the state after the ramp and to study the state evolution during the hold time, we want to reconstruct the wave function of the grid state. A visualization of the wave function of such a grid state is shown in Fig. 6.2.4. Note that we will measure the $|0_L\rangle$ state only in our experiment without the $0-\pi$ qubit. This reconstruction can first be done by IQ demodulation or by mapping out the Wigner function in tomography for different ramping and hold times. The Wigner function is a quasi-probability distribution, which completely represents the wave function. Therefore, we want to implement a Wigner tomography to observe the grid state.

In cQED experiments, this Wigner tomography can be realized in different ways. One approach is based on a homodyne detection scheme [224–226]. The RF signal is split, one half propagates through the fridge, the other half propagated through a phase shifter and serves as local oscillator. Both signals are recombined at another beamsplitter and directed to intensity detectors. This experiment is repeated for many configurations of the phase shifter.
Depending on the system under investigation, other different proposals exist in the literature [222, 227–233]. Among the established techniques, we still have to find and design the most suitable realization for our problem.

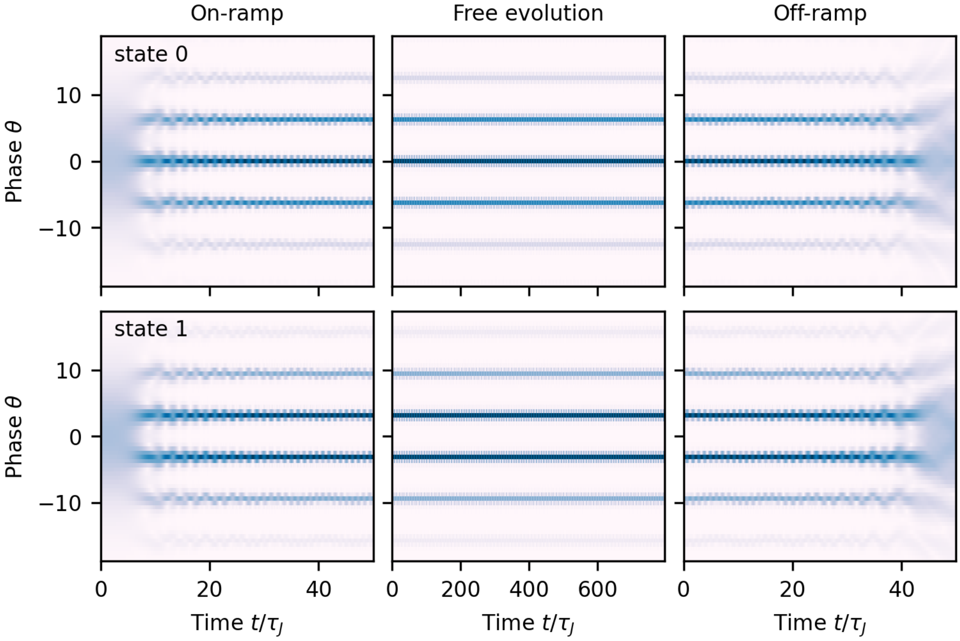

Figure 6.2.4.: Visualization of the time evolution of the Gaussian ground state into grid states and back with even or odd weights depending on the state of the qubit.

With this proposal we want to proof the principle of a phase gate for the "0-π" qubit. On this way, we will explore the switching behaviour of Josephson junctions under fast gating and the preparation and readout of grid states generated in the same LC-LCJ system.
These technological advances could potentially merge with the current development of protected qubits, but are by itself interesting for the scientific community in view of quantum error correction and quantum information processing with bosonic

qubits in cQED [234, 235]. [2]

6.2.3. WIDE-BANDWIDTH PARAMETRIC AMPLIFIERS

In the realm of superconducting qubit readout schemes and RF conductance experiments, the indispensability of parametric amplifiers is evident. These amplifiers play a pivotal role in enhancing readout capabilities for superconducting qubits. However, the pursuit is not merely for any amplifier but specifically for a wide-bandwidth, high-gain parametric amplifier characterized by a simple mode structure. The complexity and inability to reach the quantum limit associated with traveling-wave parametric amplifiers (TWPAs) prompt the exploration of alternative approaches. One promising avenue involves replacing the coupling capacitor of a resonator-based parametric amplifier as the coupling impedance with a Klopfenstein taper (or other LC filter based implementation), effectively augmenting the bandwidth κ. This, coupled with the utilization of a flux-biased superconducting quantum interference device (SQUID) or a gated nanowire junction enabling three-wave mixing, presents a simpler alternative known as impedance-matched parametric amplifiers (IMPAs). While initial implementations of IMPAs exist, there is a pressing need for further optimization to fully harness their potential. Additionally, a comprehensive understanding of the environmental impact on these strongly coupled amplifiers is imperative for advancing their practical applications in quantum information processing and beyond.

---

[2] This project proposal stems from my GoNoGo meeting in 2020 and was developed together with Bernard van Heck.

A

STANDARD OPERATION PROCEDURE FOR LEIDEN CRYOGENICS DILUTION REFRIGERATOR B3

Lukas Johannes Splitthoff

A.1. HARDWARE OF CUSTOMIZED CF-CS110 2PT 2000

The dilution refrigerator described here was provided by Leiden Cryogenics BV, Kenauweg 11, 2331BA Leiden, The Netherlands (info@leidencryogenics.com) in March 2019 [236]. Originally designed for experiments with electron temperatures below $T_e < 10\,\mathrm{mK}$ by Wolfgang Pfaff and Leo P. Kouwenhoven it was meant for braiding experiments of Majorana Zero Modes, hence the name Braiding 3 or short B3. Soon after its arrival, it got modified for RF conductance measurements by Lin Han and Filip K. Malinowski, but never used for experiments. In September and October 2020, the fridge moved to its current position in the QC1 lab where it was taken into use for cQED type measurements in November 2020 by Lukas J. Splitthoff. Olaf W.B. Benningshof supervised and assisted with the installation. He also remains the point of contact for fridge related questions. In addition to the default configuration, Olaf W.B. Benningshof added a third trap in series to the two parallel traps in the default configuration in spring 2023.

This dilution refrigerator is comprised of an outer, multi-shield fridge vessel and an inner probe hosting experiments, which are cooled via two cooling circuits, the pulse tube cooling unit and the He_3/He_4 dilution unit, see Fig. A.1.1. Additionally, there is a control rack (not shown) with fridge computer, impedance bridge and heater power supply.

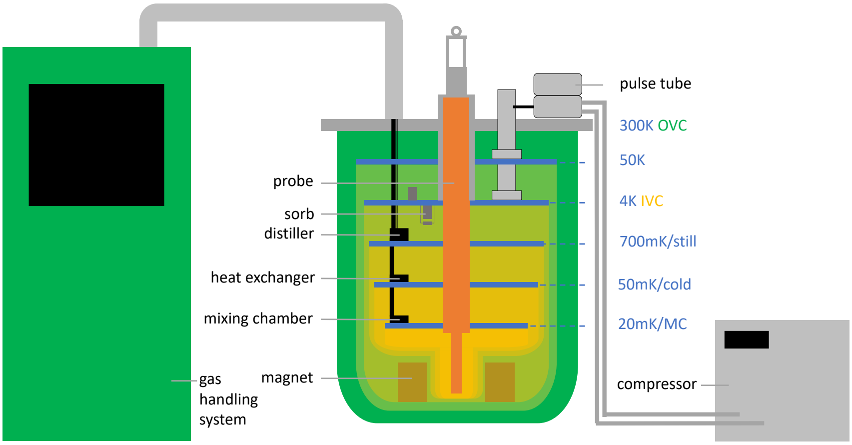

Figure A.1.1.: Hardware overview with focus on the cooling mechanisms. Fridge vessel with probe, gas handling system and pulse tube compressor.

A.1.1. Outer fridge vessel

The outer, multi-shield fridge vessel is composed of an outer vacuum chamber (OVC) and an inner vacuum chamber (IVC). The OVC hosts the 300 K and the 50 K radiation shield connected to the respective temperature plates. The IVC hosts the 4 K, 700 mK, 50 mK and 20 mK radiation shields. When not referred to the temperature, but to their function the lowest three plates are also called still, cold and base or mixing chamber (MC) plate. Every temperature stage is equipped with thermometers. For precise temperature control, heaters are installed on the still plate and on the 4 K plate. The latter heater also acts as sorb heater to control the He_4 exchange gas in the IVC which in turn makes thermal contact between all temperature plates in the IVC. If the sorb heater is off, all the exchange gas is trapped in the sorb, otherwise when 30 mA are applied to the heater exchange gas is released. During normal operation, the fridge vessel rests on two damping blocks elevated by some metal frame. A four pillar screw jack (4 spindles, 2 motors) functions as fridge lift to facilitate sample loading, but also to enable maintenance on the inside of the fridge vessel.

A.1.2. Cold insertable, top loading probe

The probe hosts the experiment and thus has the same temperature stages as the fridge vessel. The experiment is typically placed at the end of a mounting bracket, which is enclosed by a tight gold-plated copper can and screwed onto the MC plate of the probe. 12 RF lines and 48 DC lines run through the probe between the mounting bracket at the bottom and the breakout box at the top. There is an additional line to bias a cryo-HEMT. Every temperature stage is equipped with thermometers. For precise temperature controll, heaters are installed on the MC and still plate. Thus, the breakout box has 5 Fischer connectors for heaters, thermometers, DC control (2x) and cryo-HEMT biasing, plus 12 SMA connectors. The probe is designed as a movable object that can be inserted into or retracted from the fridge vessel via a top loader. A four pillar screw jack (2 spindles, 1 motor) functions as probe lift. An elastic metal bellow connects between the top of the probe and the top plate of the fridge vessel to enable the insertion or retraction of the probe while maintaining a closed vacuum chamber around it. Once inserted into the fridge, pneumatically actuated mechanical clamps on the probe make thermal contact with the fridge vessel. The clamping mechanism is pressurized via a high-pressure line to an external N2 gas cylinder. To insert or retract the probe into the fully extended metal bellow a manual tripod crane (not shown) is used, which can be attached to the top of the probe.

A.1.3. PULSE TUBE COOLING UNIT

Two two-stage pulse tube coolers connected to the 50 K and the 4 K plate provide each about 70 W and 1.5 W of cooling power at the respective temperature stage. The two pulse tube coolers are driven by two water-cooled cryomec pulse tube compressors, each drawing about 7.2 kW power in steady state. Further information on the concept of pulse tube cooling can be found in Ref. [237].

When turning off compressor 1, then also turn off its PMC linear drive (step motion controller to synchronize the operation of the two compressors) positioned on top of it. Go in reverse to turn it on again.

A.1.4. HELIUM DILUTION CIRCUIT

The He_3/He_4 dilution circuit is composed of an external circuit in the gas handling system and two parallel dilution units, each comprised of a still, a continuous heat exchanger, a silver sinter step heat exchanger and a mixing chamber in the fridge vessel. Note that He_3 is a rare resource since its only produced in nuclear reactions such as tritium decay or deuterium-deuterium fusion. The gas handling system is comprised of two parallel turbo pumps to pump on the distiller, a scroll pump to maintain a certain flow, a compressor to increase the flow during condensation, two parallel, liquid N2 cooled traps followed by one liquid N2 cooled trap in series to filter the mixture and two dumps to store the He_3/He_4 gas. Additional lines connected to the dilution circuit serve as by-pass or emergency recovery line. Other lines outside of the dilution circuit allow to access and pump on the IVC, the OVC and the probe, when positioned in the bellow, separately.

During operation all He_3/He_4 is condensed in the dilution unit. By pumping on the distiller on the still plate, He_3 is removed from the diluted phase. This allows other He_3 atoms to cross the phase boundary in the mixing chamber which allows for the heat transfer. Further information on the concept of dilution refrigeration can be found in Ref. [237].

MC temperature	19.6 mK	103 mK	115 mK
Cooling power (fridge)	25 μW	1600 μW	2000 μW
Cooling power (probe)	n.a.	n.a.	196 μW

Table A.1.: Cooling power on mixing chamber plate of fridge vessel and probe measured by applying different powers to the respective mixing chamber heaters.

A.1.5. MAGNETIC FIELD CONTROL

Magnetic fields can be applied to the device under test with a 9-1-1 T three axis vector magnet, based on a Helmholtz coil per axis. The magnet configuration was provided by American Magnetics Inc. Box 2509, 112 Flint Road, Oak Ridge (http://americanmagnetics.com) in February 2016 to Leiden Cryogenics as cryogen-free MAxes Vector magnet and AMI Magnet number 14540. All magnet specifications are provided in the Leiden Cryogenics data sheet, Appendix A [236].

Note that the fridge is only rated for the simultaneous operation of multiple magnet coils yielding a resulting field magnitude below 1 T. Hence 9 T should only be applied in independent operation of the z-axis.

The center of the PCB holding the device under test on the mounting bracket should be aligned with the origin of the vector magnet when the probe is inserted into the fridge vessel to a position of 307 mm above the fridge base plate (this position has been determined from CAD drawings and might have changed over time). The alignment of the device under test mounted on the PCB to the magnet needs to be determined experimentally via a three-axis rotation and corrected for by inversion of the rotation matrix. We generally observed good alignment of the z-axis of the sample to the z-axis of the magnet, but notice some rotation in the xy-plane.

The magnet power supply must be turned on and off in a specific order. First power on the main control module and subsequently start the slave power supply units upon request of the main controller. To turn the power supply off, ramp the field to zero, then turn off the power supplies and finally the controller.

The three axes are separately addressed with individual IPv4 addresses that can be read out on the main controller.

	x-axis	y-axis	z-axis
Rated central field	1 T	1 T	9 T
Rated operating current	57.64 A	57.54 A	85.55 A
Maximal ramp rate	0.085 As^{-1}	0.084 As^{-1}	0.042 As^{-1}
Inductance	11.6 H	11.8 H	24 H

Table A.2.: Magnet specifications provided by the supplier and rated at 4.2 K.

A.1.6. TEMPERATURE READOUT AND HEATER CONTROL

The temperature control software comes as a LabView program, see Fig. A.4.1a, that reads out the Lakeshore impedance bridge and controls the four heaters (sorb, still in/out and MC). While many settings can be adjusted, it is not recommended to change anything aside from activating or deactivating the thermometer and heater channels (green panels, controlled by double-click) and from setting heater bias currents (selected by double-click). The individual temperature graphs of channel 0-9 can be accessed via the tabs 0-9 in the top row, which are useful for monitoring the temperature trends. All temperature data is logged and time-stamped in a log file per week saved under C:\avs-47 on the fridge computer.

The different temperature sensors on the various temperature plates are only rated for specific ranges, listed in Tab. A.3. The Pt1000 is useful to monitor the pre-cooling or warm-up of the fridge vessel. The RuO_2 and TT thermometers should be read during the condensation and collection of the mixture. The new RuO_2 thermometer can also be used to follow the pre-cooling of the cold inserted probe. The CMN precision thermometers help to monitor the normal circulation after condensation.

	T_{min}	T_{max}
Pt1000	18 K	400 K
$RuO_2$10k	150 mK	4.2 K
$RuO_2$10k (new)	10 mK	40 K
$RuO_2$1k5	20 mK	4.2 K
$RuO_2$1k5	20 mK	4.2 K
TT-1903	9 mK	4.2 K
TT-1811	10 mK	4.0 K
CMN 1020-097	8 mK	2 K
CMN 1020-100	18 mK	2 K

Table A.3.: Temperature sensor range based on calibration data.

A.1.7. PRESSURE READOUT AND GAS HANDLING

The pressure control software comes as a LabView program, see Fig. A.4.1c,f, that reads the MaxiGauge (channel 3: p_{probe}, channel 4: p_{OVC}, channel 5: p_{IVC}, channel 6: p_{still}) and the gauges P1-P8 (reference points indicated in circuit diagram) plus the pressure after the compressor (P COMP or PC) and the flow into the dilution unit (Flow). The MaxiGauge uses TPR/PCR (TPR: Compact Pirani Gauge, PCR: Compact Pirani Capacitance Gauge, cal-factor 1 referring to N_2, range: 1000-5×10^{-5} mbar). The individual pressure graphs of MaxiGauge and the other gauges can be accessed via the tabs "Pressure Graphs" in the top row. All pressure data is logged and time-stamped in a log file per week saved under C:\avs-47 on the fridge computer (data logging is set under the tab "settings").

The software also controls all automatic, pneumatically actuated valves (auxiliary valves A0-A10, dilution circuit 0-18 and AUX1 (not to confuse with AUX PORT 1)) and the pumps (turbo S1-S2, scroll S3-S4, compressor S6), which can be activated/deactivated with a single click on the software or the front panel on the gas handling system itself. All manual valves (M1-M5, OVC) are clearly labelled on the fridge itself to avoid confusion. Note that M4 is placed between P1 and "from probe", but not shown in the circuit diagram. Also the two gates M5 and OVC are not shown in the circuit diagram, since they connect to auxiliary port for external pump stations. All automatic valves and build-in pumps can be controlled individually, but also via automatic routines started and stopped by AUTO. The two important routines are condensation/normal circulation (START) and recovery (RECOVERY). To close all valves and stop all pumps press RESET.

A.1.8. PROBE MOTION CONTROL

The probe motion control software comes as a LabView program, see Fig. A.4.1b,d, that remote controls the motor of the four pillar screw jack by continuously pressing the four control buttons or single clicking on Stop. In case of deviation set and save the actual position in "Preset Position". The position refers to the distance between the top most fridge plate and the top most probe plate and can be measured best with a ruler when close to full insertion. The probe motion control has a build in limit, set to 307 mm to stop the probe automatically at the sweet spot where the origin of the magnet aligns with the center of the samples holder. Unfortunately, this automatic break only functions when the limit is approached slowly enough, otherwise the probe overshoots into the IVC.

When opening the probe control software, it prompts the communication settings, which are printed here in Fig. A.4.1d for reference.

A.2. STANDARD OPERATION FOR SAMPLE EXCHANGE

This standard operation procedure was written with greatest care. Nonetheless, even a thorough study of this manual can not replace a hands-on training on the device by an experienced user to familiarize with the operation. The manual should be regarded as a guide and reference for new, but also experienced users. Please read the relevant sections of this manual carefully from the first to the last line before operating the machine.

When all three cool-down steps are operated very efficiently, the probe can reach base temperature in about 26 h. More comfortable for the user is a cool-down over 1.5 days. In return, from base temperature to room temperature it takes minimally 8 h or better about 17 h.

Fig. A.2.1 shows the temperature and pressure trends during a warm-up and cool-down cycle from July 2023 between base temperature and 4K for sample exchange. Note that the P5 pressure is oscillating during normal circulation due to a constant switching of the compressor when reaching threshold values probably indicating a blockage in the dilution unit. Ideally P5 should be relatively flat over time and the compressor should be off. To stabilize the P5 pressure and the flow through the condensing lines, open the second cold trap and the second dilution unit, then start the compressor to create a second channel for the mixture, which reduces the pressure.

A.2.1. LOADING: INSERTION OF THE PROBE INTO THE BELLOW

In this step the probe is inserted into probe bellow, which acts as a load lock, to evacuate the probe space while the probe is still at room temperature. The step requires about 1h of manual work on the fridge and 12-16 h of pumping.

1. Wear gloves to keep all parts of the probe clean while loading.
2. Check that the super-insulation and all cables are fixed to the probe, otherwise tighten them.
3. Screw the can on the mixing chamber plate.
4. Clean the clamps, that make thermal contact between the probe and the fridge plates, with acetone and iso-propanoal. Also clean the can with acetone and iso-propanoal.
5. Remove the lid in the floor and surround the opening with a colored chain.
6. Double-check that the gate valve is closed.
7. Vent the probe space by opening M4, A3.
8. Lift the fridge plate slowly using the remote control until the top of the probe bellow aligns with the floor above. Ensure that the four screws engage with their counterparts in the plate. Watch cables and tubes connected to the fridge plate.

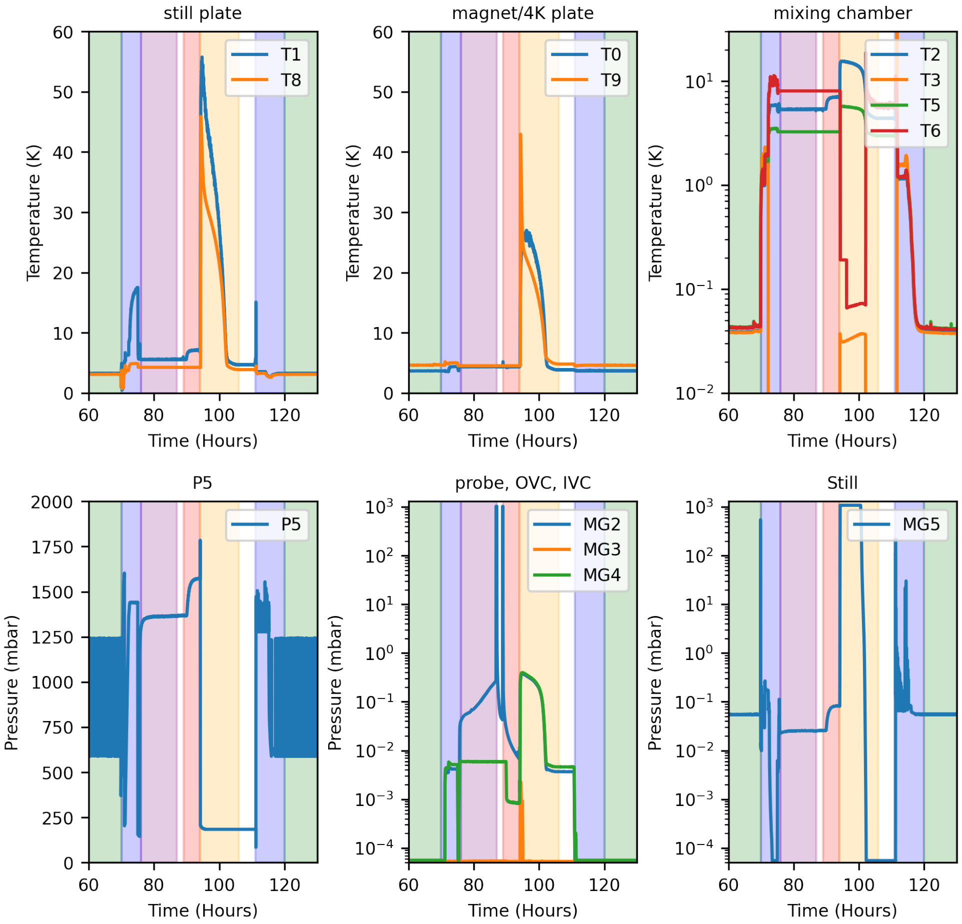

Figure A.2.1.: Temperature and pressure trends during a warm-up and cool-down cycle between base temperature and 4K for sample exchange. Green: normal circulation, blue: collection/condensation, purple: warm-up of probe in bellow, red: pumping on probe space with sorb heaters turned off already, orange: pre-cooling of probe to 4 K.

9. Unscrew and remove the blank lid covering the bellow.

10. Clean the o-ring and the matching surface on the probe with iso-propanol. Apply a small amount of vacuum grease to o-ring.

11. Center the probe above the bellow by correctly positioning the tripod crane. Lower the probe slowly and carefully into the bellow. Match the alignment marks. Have a buddy help you watch the cables and the correct positioning, interrupt the lifting if needed.

12. Screw the probe to the bellow.

13. Detach the hook of the tripod crane from the probe.

14. Lower the fridge plate to its lowest position. Disengage the screws from the fridge plate to avoid ground loops.

15. Evacuate the probe space, thus close A3, keep M4 open, open A6 and start S4.

16. Connect an external pump station to M5 with a long bellow. Ensure that the pump station is vented to atmospheric pressure. Open the gate valve of the pump station to connect the bellow with turbo pump. Start pumping with the pump station. Once the pressure gauge on the pump station reads 1×10^{-1} mbar, open M5. Alternatively, pump on the probe space only with the external turbo pump via M5.

17. Close M4, then A3. Turn off S4.

18. Close the opening in the floor above.

19. Pump down the probe space to at least 1×10^{-2} mbar. The probe pressure typically reaches $p_{probe} = 8 \times 10^{-3}$ mbar after 12h, and $p_{probe} = 4 \times 10^{-3}$ mbar after 16 h.

A.2.2. PRE-COOLING OF PROBE TO 4K

In this step, the pre-cooling of the probe to 4K is initiated. As part of it, the probe is first transferred from the bellow into the IVC, then thermally connected to the fridge vessel and eventually pre-cooled using exchange gas. The step requires about 0.5 h of manual work on the fridge and 6-10 h of pre-cooling, depending on the thermal load on the probe and the exchange gas pressure in the IVC.

1. Once the probe pressure has reached the desired value, close M5. Monitor the probe pressure for about 1 min. The probe pressure should not exceed $p_{probe} = 1$ mbar, otherwise the pressure rise indicates a leak. Typically it rises to $p_{probe} = 5 \times 10^{-2}$ mbar due to outgasing.

2. Open the gate valve connecting the IVC and the probe bellow (about 5.5 turns).

3. Open the probe control software "probe motion". Check the settings.

4. Lower the probe slowly until the position reads 307 mm. Have a buddy help you watch the cables, interrupt the lifting if needed. In case of doubt, check the position with a ruler.

5. Pressurize the clamps: Connect the N2 line to the top of the probe by pushing down the orange ring and inserting the line. Turn the T-gate in parallel with the N2 line. Open the N2 tank and the pressure regulator valve. Set the pressure regulator to 25 bar (slow clockwise rotation).

6. Close the probe control software, press EXIT → DISCONNECT → CLOSE.

7. Attach the heater and probe thermometry cables (Fischer connectors) to the probe breakout box. Start the reading of thermometer channels 5-9 in the temperature control software.

8. Apply 30 mA to the sorb heater to release the exchange gas and reach thermal equilibrium between the plates.

9. Connect an external pump station to the OVC valve with a long bellow. Ensure that the pump station is vented to atmospheric pressure. Open the gate valve of the pump station to connect the bellow with turbo pump. Start pumping with the pump station. Once the pressure gauge on the pump station reads 5×10^{-5} mbar, open the OVC gate valve. Keep pumping until the pre-cooling has finished ($T_{magnet} < 4\,\mathrm{K}$ and $T_{still} < 5\,\mathrm{K}$), but not longer to avoid unwanted cryo-pumping from the turbo pump into the cold OVC.

A.2.3. CONDENSATION: COOL-DOWN FROM 4K TO BASE TEMPERATURE

Once the pre-cooling has finished and the exchange gas has been collected in the sorb, the condensation of the He_3/He_4 mixture can be initiated. The step requires about 0.5 h of manual work on the fridge and 4-8 h for the condensation. With full wiring and under otherwise optimal conditions, the base temperature on the mixing chamber of the fridge vessel can be as low as 9.5 mK, while the base temperature of the probe is 12.3 mK according to the test report. Lately we observed base temperatures of 20-40 mK. We suspect that the increase of the base temperature has to do with the amount and ratio of the mixture circulating through the dilution unit. The mixture ratio can be controlled via the end set-points for He set in the condensation routine.

1. Wait until the pre-cooling has finished, $T_{magnet} < 4\,\mathrm{K}$ and $T_{still} < 5\,\mathrm{K}$, to provide sufficient cooling power for the subsequent condensation.

2. Stop pumping on the OVC: Close the gate valve to the OVC, close the gate valve to the turbo pump, stop the pumps, disconnect the bellow at the OVC gate, wait until the pump span down and move the pump station back to the corridor.

3. Collect the exchange gas in IVC by turning off the sorb heater (approx. 30min). Wait until probe and IVC pressure reach their minimal reading, $p_{probe} = 5 \times 10^{-5}$ mbar and $p_{IVC} = 5 \times 10^{-5}$ mbar.

4. Open the manual valves to the dumps (M1, M2).

5. Start the automatic condensation routine, press RESET → START → AUTO.

A.2.4. OPERATION AT BASE TEMPERATURE

Once the condensation has finished, the normal circulation routine continues. Experiments can be conducted, while monitoring the fridge especially when large currents, or large powers or fast magnetic field ramps are applied.

- Refill the LN2 traps weekly during normal operation.
- Monitor the P5 pressure to foresee a potential blockage in the dilution unit.

A.2.5. COLLECTION: WARM-UP TO 4K

To return the fridge to 4K, all procedures are run in reverse order. First comes the collection of the mixture in two steps, which takes about 4-5 h.

1. Finish the experiment: Set the magnet power supply and the DACs to zero. Turn off all RF source outputs and turn off the cryo-HEMT (gate, drain, ground to ground).
2. Check that the dump valves M1, M2 are open.
3. Run recovery routine, press → AUTO → RECOVERY → AUTO.
4. During the He_3 collection, apply 10 mA to the three heaters: MC and still in/out.
5. Once the He_4 collection has started (when automatic valve 11 has opened), apply 30 mA to the four heaters: sorb, MC and still in/out.
6. Wait until the still pressure $p_{still} = 5 \times 10^{-5}$ mbar (approx. 3h). Press AUTO → RESET to stop the collection of the mixture.
7. Turn off all four heaters, sorb, MC and still in/out.
8. Close the manual dump valves (M1, M2).

- To check if all the mixture has been collected, monitor the still pressure after stopping the recovery routine. If the still pressure remains low, the collecting of the mixture was successful.
- Optionally, keep pumping to the cold traps to trap any contamination in case of leakage. Thus open 4, 15, 19, AUX 1, S3, 3, 2, 8, 0, 1, S1, S2, 18, 6, 7. Optionally also open 11, 14, 9 if M2 is definitely closed. Keep 5, 16 closed.

A.2.6. WARM-UP OF PROBE TO ROOM TEMPERATURE

Further in reverse, the probe needs to be lifted out of the IVC into the metal bellow to thermalize with the room temperature. The thermalization can be accelerated by using Helium as exchange gas. However, this procedure might be more detrimental to the metal bellow because of induced thermal stress. This step requires about 0.5 h of manual work on the fridge.

1. Check that the heaters are off, otherwise turn them off. Check that the IVC and probe pressure reach their minimal reading, $P_{probe} = 5 \times 10^{-5}\,\mathrm{mbar}$ and $P_{IVC} = 5 \times 10^{-5}\,\mathrm{mbar}$, otherwise wait and monitor.
2. Disconnect the heater and probe thermometer cables from the breakout box (Fischer connector). Stop the reading of thermometer channels 5-9 in the temperature control software. Disconnect the RF coax cables from the breakout box.
3. Depressurize the clamps: Close the N2 tank, close the pressure regulator valve, regulate the pressure to its minimum (anti-clockwise rotation till the end), turn the T-gate in the line by 90 deg to depressurize the clamps, disconnect the N2 line at the top of the probe by pushing down the orange ring and retracting the line.
4. Open the probe control software "probe motion". Check the settings. Check that the position reading is at 307 mm, otherwise check and correct accordingly.
5. Lift the probe via the probe control software. Have a buddy help you watch the cables, interrupt the lifting if needed.
6. Stop the lifting before the top of the probe hits the frame. The end value the probe should reach is about 1668 mm, if the position reading is set correctly and functions.
7. Close the gate valve between IVC and probe bellow (about 5.5 turns).
8. Close the probe control software, press EXIT → DISCONNECT → CLOSE.
9. Apply 30 mA to the sorb heater to release the exchange gas and reach thermal equilibrium between the plates.
10. Wait until the probe reaches room temperature (approx. 10-12h).

- Alternatively to the slow warm-up suggested above, add the amount of one balloon of He_4 as exchange gas to the probe space via M5. Set up hairdryers to blow at the probe bellow from the outside to prevent freezing or condensation on the outside. This faster procedure takes about 4 hours.
- Unfortunately, there is no direct way to read the probe temperature once the short probe thermometer cable has been disconnected.

A.2.7. UNLOADING: EXTRACTION OF PROBE FROM BELLOW

The final step: The probe is lifted out of the metal bellow to access the sample or modify the wiring. This step requires about 0.5 h of manual work on the fridge.

1. Double-check that the gate valve is closed.
2. Vent the probe space via valve M4, A3. Keep A3 open.

3. Remove the lid in the floor and surround the opening with a colored chain.
4. Lift the fridge plate slowly using the remote control until the top of the probe bellow aligns with the floor above. Ensure that the four screws engage with their counterparts in the plate. Watch cables and tubes connected to the fridge plate.
5. Unscrew the probe from the bellows.
6. Attach the hook of the tripod crane to the probe.
7. Wear gloves to keep all parts of the probe clean while unloading.
8. Lift the probe slowly and carefully out of the bellow. (The crane cable slips when not curled up correctly.)
9. Close the bellow immediately with the blank lid to prevent anything from falling in. Fix the lid with at least two screws.
10. Close A3, open A6. Evacuate the bellow using S4 until the probe pressure reads $p_{probe} = 1 \times 10^{-1}$ mbar. Then stop pumping via S4 and close A6.
11. Lower the fridge plate sufficiently such that opening in the floor can be closed with the lid.
12. Close the opening with the lid.

A.3. STANDARD OPERATION FOR FRIDGE MAINTENANCE

A.3.1. PRE-COOLING OF FRIDGE FROM ROOM TEMPERATURE TO 4K

For example after maintenance, the fridge will be at room temperature and needs to be pre-cooled to 4 K for operation. The pre-cooling to 4K without LN2 and full wiring including the magnet takes approximately 3 days.

1. Start pumping IVC and OVC with an external pump station via A0, A2, A1, A5 and the AUX PORT-1 in the auxiliary circuit of the gas handling circuit until $p_{OVC} < 1 \times 10^{-1}$ mbar and $p_{IVC} < 1 \times 10^{-1}$ mbar. Optionally, pump on the IVC and OVC via the additional K25 ports on the fridge base plate.
2. Close all open valves and disconnect the external pump from the AUX PORT-1.
3. Connect a high pressure He line to the AUX PORT-1. Flush the line via A8 and S4 at least 3 times by closing and reopening the values M3 and A8 alternately.
4. Add 10-15 mbar (aim for 12 mbar) of He as exchange gas to the IVC via A0, A2 and M3 while monitoring MG5.
5. Circulate small amount of 4He in the dilution unit to pump any remaining contamination into the cold traps while the fridge is cooling down. You can simply use the leftover gas surrounding S3. Don't use the compressor, and open the bypass 19.

6. Turn on both pulse tube compressors and the linear drive.
7. Start pumping on the OVC with an external pump station until the pre-cooling has finished (cryo-pumping has never been a severe during operation, but likely occurs at this stage below $T < 20\,\mathrm{K}$). Close the OVC valve and disconnected once the pumping has finished.
8. Check the compressor pressure and temperature regularly. Monitor the cool-down using the PT1000 thermometer.
9. Turn on the sorb heater to 30 mA.

- Optional: Get full LN2 Dewar and pressurize it to 1.5 bar, start pre-cooling with LN2 via the pre-cooling lines on the top fridge plate. Replace with another full dewar if LN2 cooling still makes sense to accelerate the pre-cooling. (This procedure has never been tested on B3.)

A.3.2. WARM-UP OF FRIDGE TO ROOM TEMPERATURE

For maintenance or cleaning the dilution it might be needed to warm-up the entire fridge to room temperature. Warm-up from 4K to room temperature takes about 48 h.

1. Ensure that all the mixture has been collected, i.e. the still pressure has dropped to 5×10^{-5} mbar after collection and the still pressure does not increase significantly when closing the valves 6,7, and 18.
2. Ensure that the manual valves to the dumps (M1, M2) are closed.
3. Turn off the two pulse tube compressors and the linear drive.
4. Apply 30 mA to the sorb heater.
5. Turn on the 3 K and 50 K heaters via the black control box below the fridge computer and set the time to 20h. Restart the timer whenever needed.
6. Monitor the warm-up using the PT1000 thermometer.
7. Once the warm-up reaches about 100 K (not earlier to avoid mechanical stress due to thermal expansion), add 20 mbar of He as exchange gas to the IVC and OVC via A0, A1, A2, A5, M3 and AUX-PORT 1 with a high pressure He line connected to it. Keep A0, A1, and A2 open to monitor the pressure build-up due to thermal expansion on P2 and P3.

A.3.3. CLEANING THE LN2 TRAPS

The LN2 traps need to be cleaned regularly, in the past there has not been a clear maintenance cycle for this operation.

1. Ensure that all the mixture has been collected, i.e. the still pressure has dropped to 5×10^{-5} mbar after collection and the still pressure does not increase significantly when closing the valves 6,7, and 18.

2. Empty the volume between A2, A5 and A8 and close all valves.

3. Open 5, 16 and A9. Observe the P3 pressure.

4. Lift the traps out of the LN2 dewar and gently warm them up with a hairdryer. Monitor the P3 pressure. If the P3 pressure exceeds 1 bar, pump via A8 on the volume with S4.

5. Once the P3 pressure saturates, note down the value in the logbook. A typical value is 400 mbar, when using a hair dryer.

6. Start pumping on the traps with S4. Additionally, use an external pump station connected to AUX PORT-1 to accelerate the pumping.

7. Pump for about 12 h.

8. Finally, close 5, 16, A9, A8 and M3 if needed. Insert the traps back into the dewar and refill LN2.

A.3.4. CLEANING THE LN2 TRAPS AND THE DILUTION UNIT

In case of a blockage of the dilution unit, its cleaning is recommended. In the past, we cleaned the DU very 6 to 12 months.

1. Ensure the fridge is at room temperature and all the mixture had been collected.

2. Open 5, 6, 7, 16, 17 and A9. Observe the P3 pressure.

3. Lift the traps out of the LN2 dewar and gently warm them up with a hairdryer. Monitor the P3 pressure. If the P3 pressure exceeds 1 bar, pump via A8 on the volume with S4.

4. Once the P3 pressure saturates, note down the value in the logbook. A typical value is 400 mbar, when using a hair dryer.

5. Start pumping on the traps with S4. Additionally, use an external pump station connected to AUX PORT-1 to accelerate the pumping.

6. Pump for about 12 h with an external pump station.

7. Finally, 5, 6, 7, 16, 17, A9, A8 and M3 if needed. Insert the traps back into the dewar and refill LN2.

A.4. REOCCURRING PROBLEMS DURING OPERATION

A.4.1. COOLING WATER OUTAGE

In case of a cooling water outage, the two pulse tube compressors will stop working and the 4K plate of the fridge vessel will warm up slowly to room temperature. If the normal circulation is running, the insufficient cooling power on the 4K plate will leads to a boil-off of the mixture and consequently the pressure in the condensation line will increase significantly. To prevent over-pressure and a potentially loss of mixture, the mixture recovery into the dumps must be initiated immediately. In principle, the automation should handle this case and automatically fall into the recovery mode, but it is better to check than to trust the system.

A.4.2. INCREASING P5 PRESSURE

Over time the P5 pressure increases, which typically indicates a blockage at the constriction in the dilution unit. The blockage arises from a polluted mixture, due to hydrogen contamination. When the P5 pressure exceeds $p_5 = 1300\,\mathrm{mbar}$, the path through the auxiliary trap (automatic valve 15-16) and the wider, second dilution unit is automatically opened. The normal circulation should stabilize in a short time. When the P5 pressure then again raises and exceeds $p_5 = 1650\,\mathrm{mbar}$ an alarm goes off, which alerts for the automatic mixture recovery when the P5 pressure then exceeds $p_5 = 1750\,\mathrm{mbar}$. It is recommended to not rely on this automatic recovery, but instead to recover the mixture manually. The blockage in the dilution unit can often be mitigated in the short-term (helps you for a few weeks typically) by recovering and re-condensing the mixture as a short term solution. To remove the blockage ultimately the LN2 traps and the dilution unit should be cleaned, see Sec. A.3.4.

A.4.3. LOSS OF MIXTURE

Since the installation of Braiding 3 in December 2020 and August 2023, the total dump pressure reduced by 50 mbar, which only shows as a decrease in the He_4 dump pressure due to the settings of the recovery routine, see Fig. A.4.1. This value corresponds to about 7 l of lost Helium in 3 years, while a loss of 1-2 l is considered as normal due to the diffusion through o-rings. A reduction of mixture by this amount might affect the cooling power of the dilution unit and thus lead to an elevated MC temperature.

At the moment, we suspect that some faction of the mixture is leaking through A9 into the volume measured as P3 since the P3 pressure is increasing during normal operation over time.

A.4.4. FOUR PILLAR SCREW JACK OF FRIDGE PLATE DOES NOT START

One of the two motors (the one closer to the corridor) of four pillar screw jack moving the fridge vessel up and down does not start occasionally, especially when completely retracted to the minimal position. To unlock the motor, hand crank the

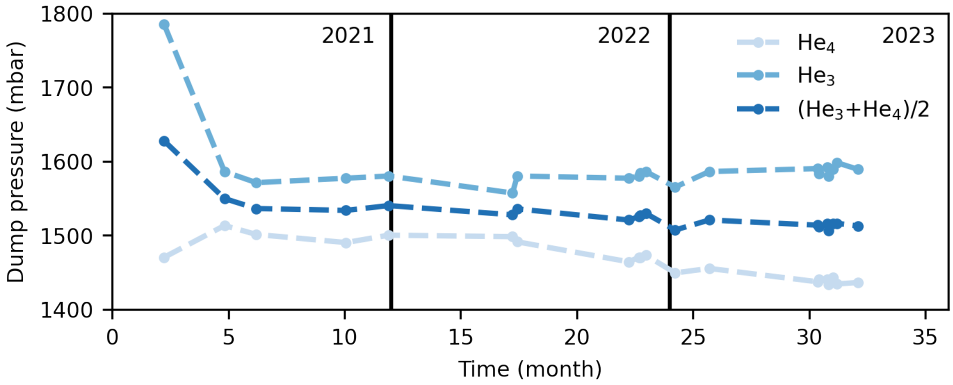

Figure A.4.1.: Dump pressure over time starting in March 2021. Most interesting to monitor is the sum of both dump values over time.

motor axis while pressing up on the yellow remote control. Watch out to not clamp your hand between the motor axis and the fridge plate!

A.4.5. ABSORBER DOES NOT ABSORB EXCHANGE GAS

Occasionally, the absorber does not absorb the exchange gas, or only part of it, from the IVC after turning off the sorb heater. For a while we suspected that the absorber might be saturated or polluted, but later found it functioning again. Alternatively, there might have been a residual current biasing the sorb heater effectively. Reconnecting and restarting the sorb heater might help in some cases.

To mitigate further problems in the future, it might be advisable to install the latest version of the Leiden Cryogenics heat switches in the fridge vessel to not rely on exchange gas anymore.

A.4.6. LABVIEW SOFTWARE ON FRIDGE COMPUTER CRASHES

Frequently, the control software on the fridge computer crashes. In some cases the computer freezes. In those cases the computer seemed to be overloaded. The problem is solved by restarting the software or rebooting the computer and restarting the software. Or by rewriting the software.

A.4.7. TEMPERATURE READING FROZEN

The temperature reading via the impedance bridge stops occasionally about once or twice a year without clear reason. We at the moment suspect the USB port settings. To overcome this problem, close the temperature control software, disconnect the USB connection to the impedance bridge and power it down. Then go in reverse, power up and connect the impedance bridge, open and start the temperature control software.

A.4.8. TOP-LOADER DESIGN

Washing machines can be top-loaders, dilution refrigerators not. The design of B3 as a top-loader increases the changes that items unintentionally fall into the open metal bellow during a sample exchange. Hence, special care has to be taken during sample exchange by keeping the metal bellow closed as much as possible. In case an item falls into the bellow, it needs to be unmounted from the bottom mount to remove item before the gate valve can be opened.
Another problem arising from the top-loader design: The probe slides back into the IVC following the gravitational force, whenever the screw jack probe lift powers off during operation. The only way to prevent the probe from damage is to catch the probe by hand and stop the retarded fall.

ACKNOWLEDGEMENT

Lukas J. Splitthoff thanks Filip K. Malinowski for a first draft of the standard operation procedure for the sample exchange in 2020 and Olaf W.B. Benningshof for continuous support with the fridge operation and Francesco Zatelli for proof-reading. Jaap J. Wesdorp, Marta Pita-Vidal and Miguel Carrera Belo tested and confirmed the usefulness of the manual.

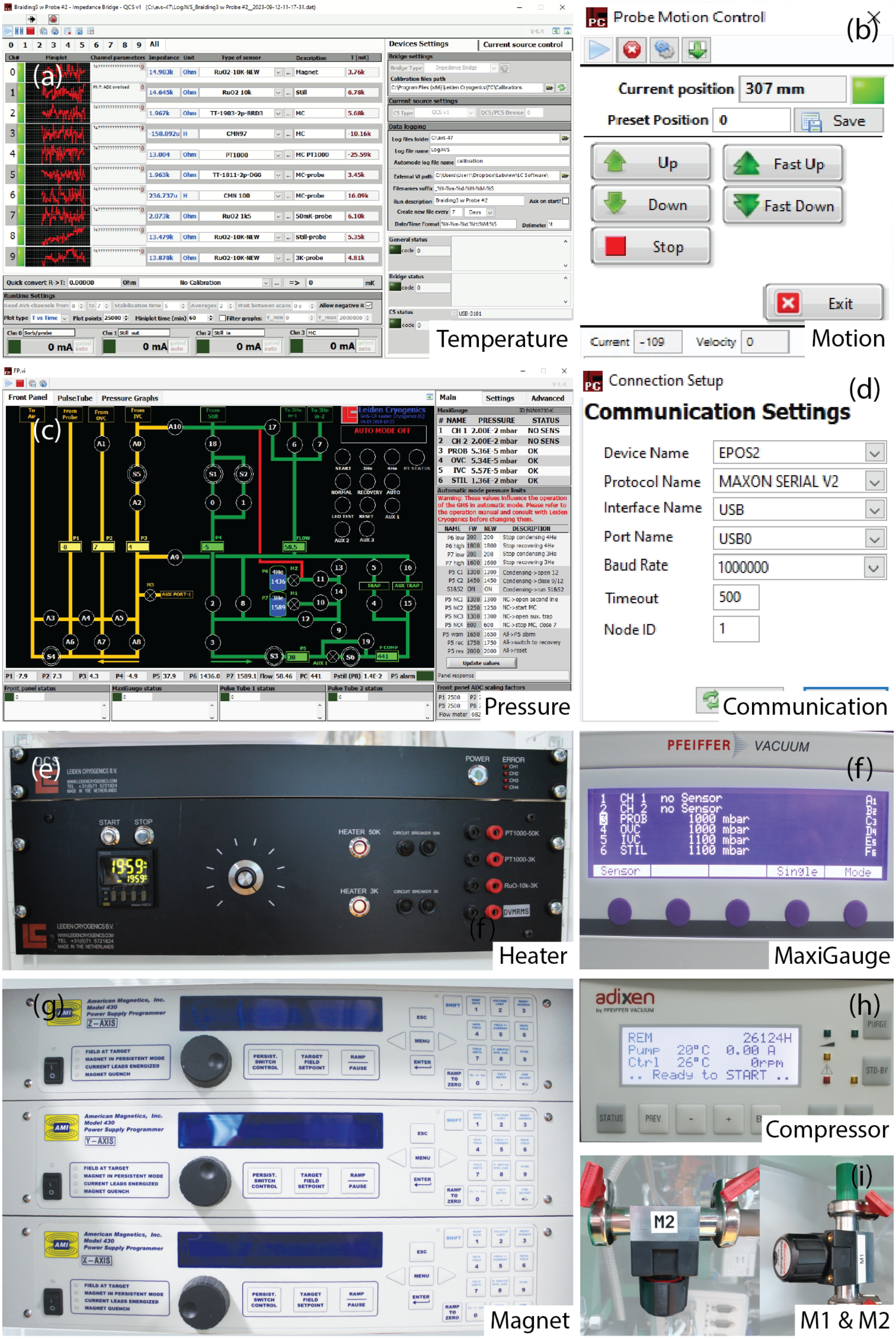

Current position: 307 mm

Preset Position: 0

Current: -109

Velocity: 0

Device Name: EPOS2

Protocol Name: MAXON SERIAL V2

Interface Name: USB

Port Name: USB0

Baud Rate: 1000000

Timeout: 500

Node ID: 1

```
1  CH 1  no Sensor
2  CH 2  no Sensor
3  PROB    1000 mbar
4  OVC     1000 mbar
5  IVC     1100 mbar
6  STIL    1100 mbar
```

```
REM          26124H
Pump   20°C  0.00 A
Ctrl   26°C   0rpm
.. Ready to START ..
```

Figure A.4.1.: Screen capture of LabView software for temperature and pressure readout and control.

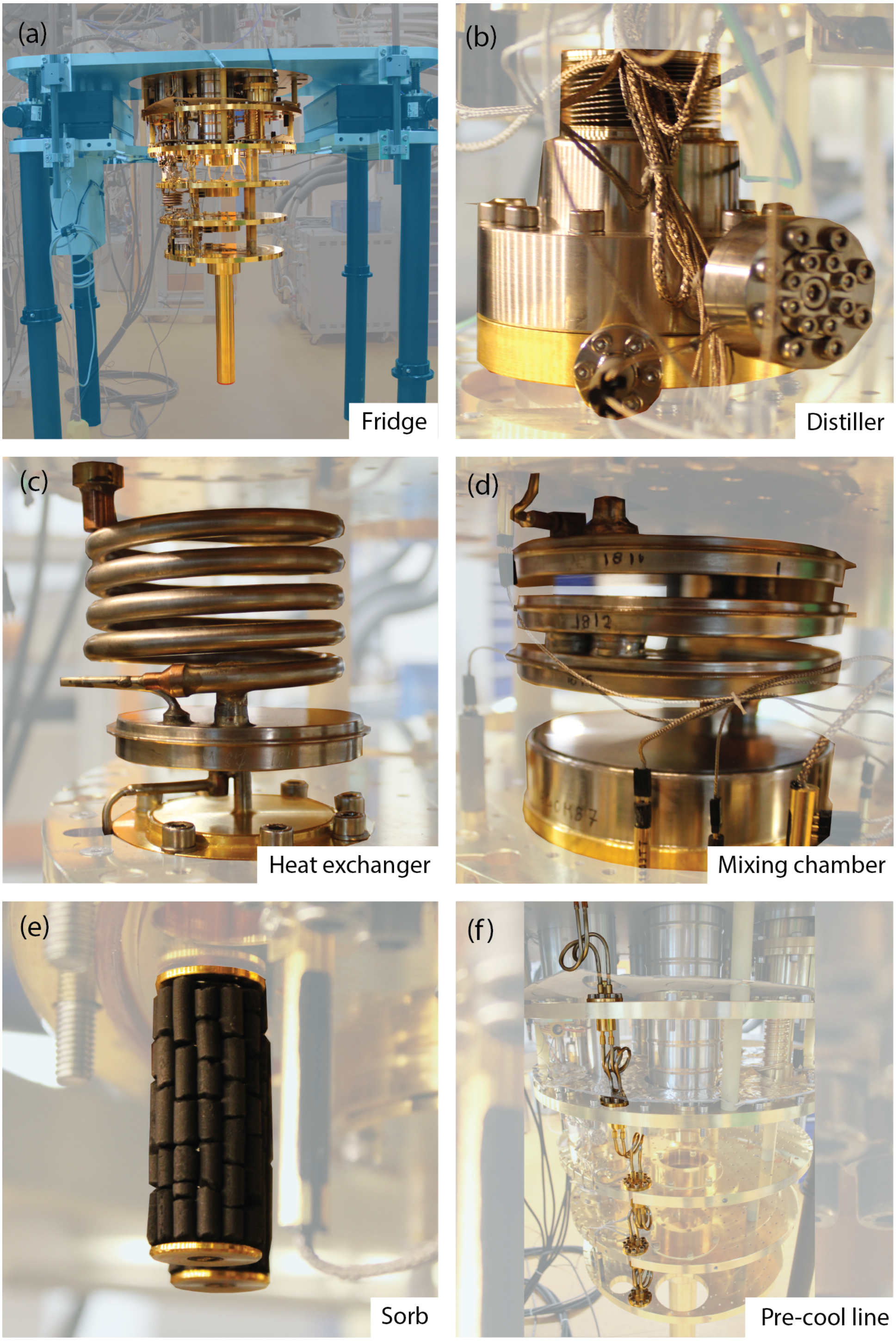

Figure A.4.2.: B3 hardware components inside the fridge vessel.

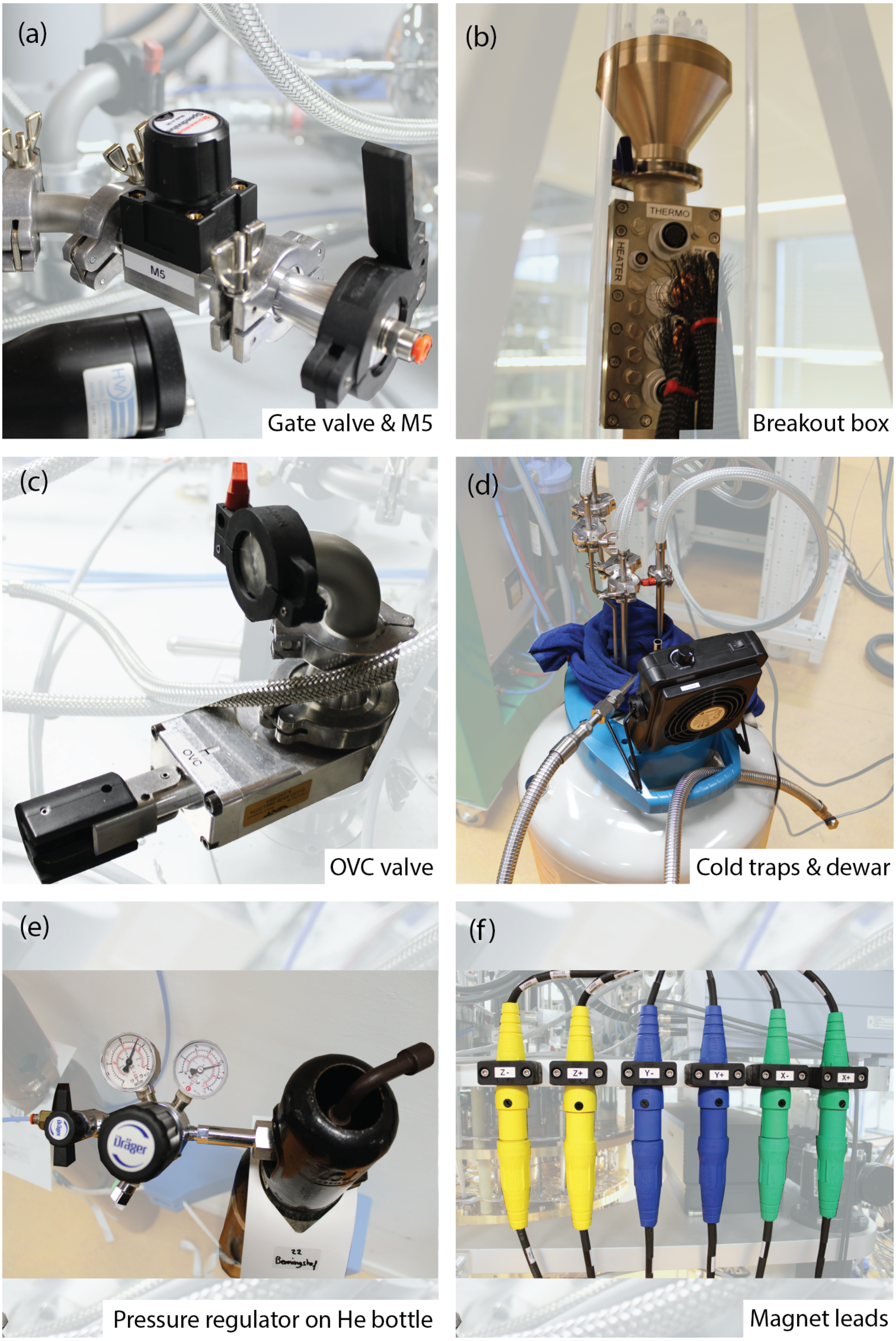

Figure A.4.3.: B3 hardware components at room temperature

B

METHOD: OTHER TECHNICALITIES

Lukas Johannes Splitthoff

B.1. NANOWIRE BATCHES AND TRANSFER

The proximitized nanowires used during the reported research projects were fabricated by Yu Liu and coworkers at Qdev in Copenhagen. The micrographs in Fig. B.1.1 give an impression of the size of these nanowires. Their growth information is provided in Tab. B.1.

We used Qdev 758 in the the beginning when trying to observe the topological phase transition in the long Majorana nanowire limit. However, we soon realized that the nanowire-to-nanowire variation and relatively short length limited our experimental progress. Most of the data from Qdev 758 nanowires used for the topological phase transition project remains unpublished. Later we requested the growth of thicker nanowires, which can also be grown longer, for the Andreev spin qubit project led by Arno Bargerbos and Marta Pita-Vidal. This new nanowire batch Qdev 1042 was then used for all following projects. Further information about the growth can be found in Ref. [118].

The nanowires are transferred from a growth chip to a sample with superconducting circuit using a manual nano-manipulator in a pick-and-place method. The manipulator consists of an optical microscope, an xy-table for the sample and growth chip translation and an xyz-stage to control the Tungsten needle (American Probe & Technology Inc. Model 72X-G3/01, Radius 0.1 μm). The transfer requires time and a long training. In my best times, I could deposit 10 nanowires per hour. Further information about the nanowire transfer can be found in the PhD thesis of Willemijn Uilhoorn, Nick van Loo and Marta Pita-Vidal.

During the NWPA project, we encountered significant challenges in connecting the nanowires to the circuitry, resulting in a delay of three months over the summer 2022. To better understand these issues, we conducted extensive measurements of nanowire resistance at room temperature across various configurations, including

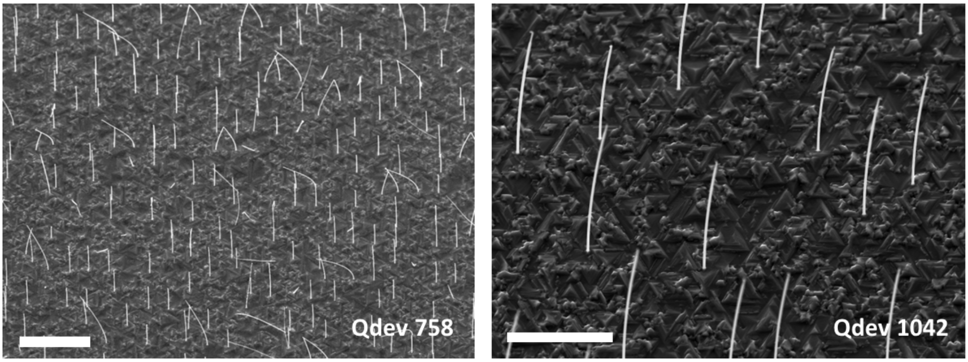

Figure B.1.1.: Micrograph of two nanowire batches Qdev 758 and Qdev 1042 after growth on their substrate. The scale bar indicates 10 μm in the left and 5 μm in the right figure.

identifier	Qdev 1042	Qdev 758
grower	Yu Liu	Rawa Tanta, Yu Liu, Joachim Sestoft, Peter Krogstrup
date	Jul 12, 2020	May 24, 2018
substrate	InAs (111)B RC2	-
pre-growth	in-situ Au	-
thickness InAs	111(5) nm	80(5) nm
thickness Al	6 nm	6 nm
length	10(1) μm	7(2) μm
covered facets	2	2
usage	NWres, NWPA, NWSSH	NWres

Table B.1.: Growth information about the two nanowires batches used in this thesis work. "NWres" abbreviates the work on gate-tunable inductances, "NWPA" stands for the work on gate-tunable parametric amplifier, and "NWSSH" for the work on the gate-tunable phase transition in a SSH chain.

samples from the NWres project, nanowire Josephson junctions (NWTM), and the NWPA project both with and without argon milling (nAr) prior to the NbTiN contact deposition. Our observations revealed distinct families of resistance values: continuous nanowires exhibited a resistance of approximately 3 kΩ, while nanowire Josephson junctions and imperfectly contacted nanowires (NWPA-nc), possibly with accidental junctions, demonstrated resistance on the order of 20-30 kΩ. In contrast, uncontacted nanowires (NWPA-open) and nanowires without prior argon milling exhibited resistance around 100 kΩ. Crucially, we determined that a 120-second, in-situ argon milling process (power 50 W, Ar flow 50 sccm, pressure 3 mTorr) before NbTiN deposition is crucial for reducing contact resistance to the nanowires and enabling superconducting contacts. It is very important to ensure the absence

of silicon nitride residuals stemming from the gate dielectric or polymer residuals from the PMMA soft mask around the nanowire contacts to achieve low resistance contacts. We further noted that expired resist can hinder achieving good contacts, rendering even a descum step prior to deposition ineffective in such cases.
The circuit fabrication has been extensively documented in Arno Bargerbos's and Marta Pita-Vidal's PhD thesis. The essential information is also provided in the appendix of chapter III, IV, V.

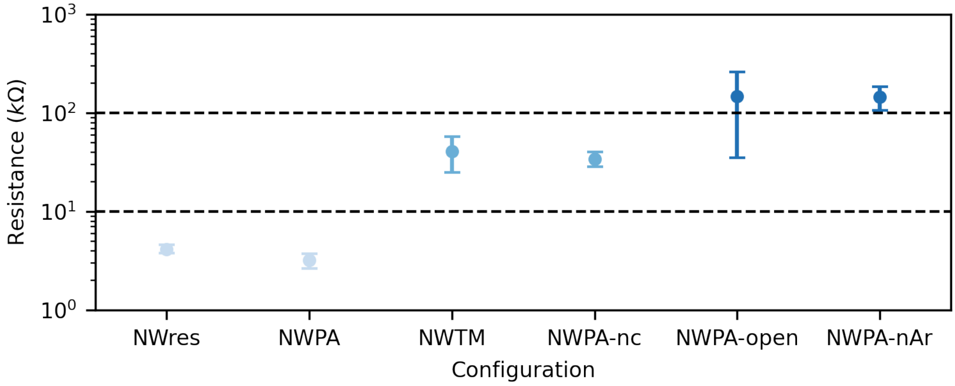

Figure B.1.2.: Nanowire resistance statistics over 40 Qdev 1042 nanowires characterized for the NWres (Chapter III) and NWPA (Chapter IV) project.

B.2. SUBSTRATE MATERIAL FOR GATE-TUNABLE CIRCUITS

The samples fabricated for the experiments presented in Chapter 3 on gate-tunable inductances in proximitized nanowires used a 525 μm thick high resistivity, n-doped Si substrate with a 100 nm LPCVD grown SiN film. The samples used for the experiments presented in Chapter 4 on gate-tunable parametric amplifiers and in Chapter 5 on a gate-tunable SSH chain came without the LPVCD grown SiN following the consideration that the presence of SiN might reduce the resonator coherence. However, we could never prove the expected improvement experimentally, either because of imperfect surface treatment of the substrate material prior to the metal deposition, or because of losses to the environment due to the presence of spurious modes on the PCB.
However, after reviewing the three thesis projects, we conclude that LPCVD grown SiN on n-doped Si is necessary as an insulating barrier to reliably fabricate versatile gate-tunable, hybrid semiconducting-superconducting circuits. First, we do not observe a significant improvement of the bare resonator quality factor as we move from the SiN to the Si interface, when comparing the resonator data from the NWresonator and the NWPA or NWSSH chain project, and Marta Pita-Vidal's lumped element comparison. Second, n-doped Si in conjunction with NbTiN seems to form a Schottky barrier, which under reverse bias voltage of approximately −3 V breaks and subsequently prohibits experiments at large negative bias due to gate leakage.

This limitation of the accessible voltage range in turn limited the tuning range of the nanowire parametric amplifiers. Third, the absence of SiN complicates the probing of the nanowire, contact or junction resistance at room temperature as both Si and n-doped Si show a finite conductance at room temperature. Due to the photo-electric effect, this conductance also depends on the intensity of light at which it is probed. Fourth, (LPCVD) SiN acts as a perfect etch stop layer compared to NbTiN during the reactive ion etching as part of the circuit lithography, and as such facilitates the etching process.

If very high coherence, hybrid circuits are required and necessitate a different substrate material, the aforementioned concerns should be considered carefully.

B.3. SPURIOUS MODES IN SAMPLE ENCLOSURE

Despite being a highly challenging and important issue for superconducting qubit measurements, there are very few works [202, 238] addressing spurious modes and optimal design of the microwave packaging of superconducting circuits. These unwanted modes can arise from various sources such as the sample enclosure, the printed circuit board (PCB), and the chip itself. They pose significant problem to qubit performance, as they contribute to Purcell decay (effect on T1) and dephasing due to residual photons (effect on T2). To mitigate these effects, spurious modes can be detected through transmission measurements using a vector network analyzer, preferably at liquid nitrogen temperatures to minimize conduction losses. These modes typically manifest as peaks or dips relative to the background transmission. Alternatively, coherence measurements of a fixed-frequency qubit while sweeping a probe tone across the measurement window can reveal points of reduced coherence indicative of spurious modes. Consequently, box modes can impose limitations on resonator and qubit coherence. Adhering to certain design principles is essential. For instance in our case, increasing the space to the metal sidewalls and burying the $50\,\Omega$ CPW lines between two layers of ground can help to avoid antenna modes in the cavity, thus improving the overall performance of the system. In the measurement of the sample enclosure depicted in Fig. B.3.1, we compare various configurations, including one with a bottom plate, PCB, lid, and top lid with the chip, another with the same setup but without the chip, see Fig. B.3.2, and a third configuration featuring silver plating in comparison to gold plating. Two notable observations emerge from our analysis. Firstly, the overall transmission levels are notably high [202], ranging between -60 to -40 dB. This suggests a strong coupling between the input and output ports, potentially attributable to antenna modes and other spurious modes. It's important to note that our transmission measurements primarily capture modes directly coupling to the input and output ports. Secondly, the transmission profile exhibits nonmonotonic behavior, showcasing several resonances within the range of interest, specifically between 4 and 8 GHz. Notably, the eigenfrequency of these modes may shift with temperature variations as sidewall conduction increases at lower temperatures.

Furthermore, our observations indicate that the presence of the chip enhances overall transmission, even at room temperature. Interestingly, it appears that

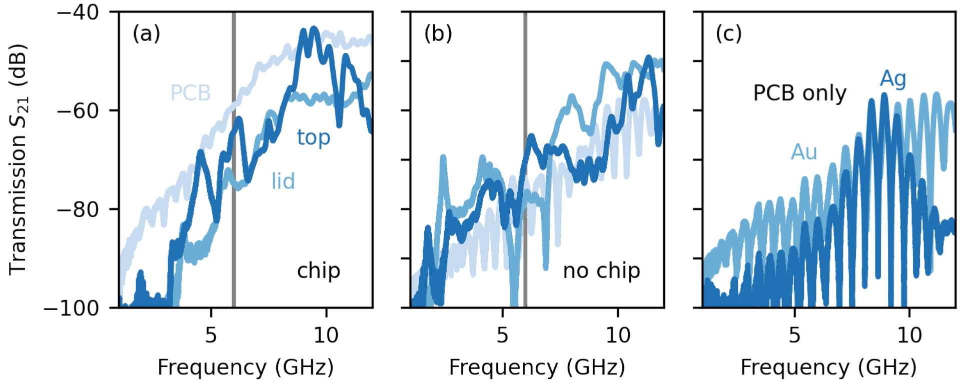

Figure B.3.1.: Transmission measurement from input to output port through sample enclosure at room temperature. (a) For gold plated PCB on bottom plate, plus lid and plus top lid with NWPA sample wirebonded in place. (b) same as in (a) but different PCB without sample. The grey line indicates 6 GHz in the spectrum. (c) Comparison between gold and silver plated PCBs on bottom plate.

the silver-plated PCB outperforms the gold-plated counterpart, at least within the measurement window. This suggests that material choice and configuration play a crucial role in optimizing transmission characteristics and minimizing spurious mode interference.

If I had a second chance to complete my PhD, I would begin by optimizing the sample enclosure and make it spurious-mode-free right from the start. This problem impeded all three projects documented in this thesis and gave me quite a head-ache. Unfortunately, I only understood the consequences of this problem at the very end of my PhD.

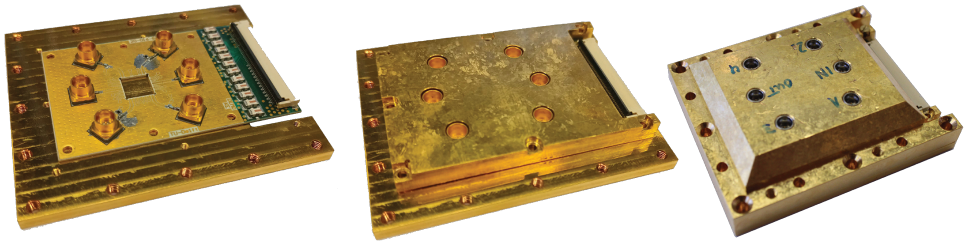

Figure B.3.2.: Sample enclosure. (Left) Bottom plate with PCB, (middle) plus lid, (right) plus top lid. The enclosure is fully described in Marta Pita-Vidal's thesis.

B.4. POWER COMPUTATION

For me to never forget: We can move from linear to logarithmic scale and back using the following two equations:

$$\begin{aligned} P_{mW} &= 10^{\frac{P_{dBm}}{10}} \\ P_{dBm} &= 10\log_{10}\left(\frac{P_{mW}}{1\,\mathrm{mW}}\right). \end{aligned} \tag{B.1}$$

Remember also that we can translate between power values and field values by

$$P \sim |V|^2. \tag{B.2}$$

ACKNOWLEDGEMENTS

First and foremost, I want to thank the whole **QuTech** research institute at the Delft University of Technology for providing an exceptional research environment in which this work was conducted.

I am profoundly grateful to **Christian Kraglund Andersen**, who adopted me into his research group in 2021 and became my copromotor. His unwavering support, his mentorship, and the inspiring work culture he fostered were invaluable in my research journey. He left his fingerprints behind on our work on superconducting parametric amplifiers and on the engineering of topological SSH chain.
I also extend my thanks to **Bernard van Heck** and **Angela Kou**, whose contributions initiated our work on gate-tunable inductances.
I am also indebted to **Leo Kouwenhoven** for his role in establishing the research environment that made this thesis possible.
I thank the external committee members, **Simone Gasparinetti, Archana Kamal, Nicolas Roch, Garry Steele**, and **Sander Otte**, for their critical evaluation and assessment of my PhD thesis.

I would like to extend my gratitude to the cQED team, including **Marta**, **Jaap**, **Arno**, and **Lukas G.**, for not only providing me with a welcoming and supportive home throughout my PhD but also for being an integral part of a resilient team. Together, we successfully navigated through changes in supervision and persevered through the challenges posed by the Covid pandemic. Our collaborative efforts led to the publication of high-impact research across a wide range of topics. Additionally, the moments we shared outside the lab like during our road trip across the United States were unforgettable and greatly contributed to the overall positive experience of my doctoral journey. Thank you for your camaraderie and support!
My thanks are also directed to my second family, the spirited members of the Andersen lab, including **Siddharth**, **Taryn**, **Figen**, **Martijn**, **Eugene**, **Natasha**, **Yen-An**, and **Jinlun**. Your diverse work attitudes, and your zest for life injected a sense of joy and vitality into the occasionally dry and monotonous academic lab environment. Our existing collaborations have been highly fruitful, and I look forward to continuing our work in both the fluxonium and the hybrid devices domain. To the co-opted member **Santi**, thanks for our great physics discussions, which often accompanied me on my way home.
I want to acknowledge the collaboration with our Master students **Duiquan**, **Miguel**, and **Doruk**.
I would like to give a special mention to **Taryn** and **Miguel** for their remarkable contributions to our research on parametric amplifiers, eccosorb filters, and the SSH chain. Your engaging questions, and the inspiring physics discussions we had not only enriched my

own understanding but also added immense joy to my PhD trajectory. Thanks for being my paranymphs on the last day of my PhD journey!

To conclude my acknowledgments to my scientific collaborators, I express my sincere appreciation to **Yu** for the growth of proximitized nanowires, and to **Jin** and **Eliska** for their significant contributions to the SSH chain project.

Not to forget, I want to thank all my colleagues from the lab and the corridor whose interactions have continuously stimulated my thought processes, and from whom I have greatly benefited through insightful discussions, idea revisions, and robust arguments. I refer to this collective group as the "**QuRe division**" to express my gratitude to everyone involved and to avoid inadvertently excluding anyone from this long list of appreciations. Thank you all for your contributions to my growth and learning.

Beyond my scientific collaborators, I would like to express my gratitude to the invaluable support staff, including the dedicated technicians **Olaf** and **Jason**, the efficient administrative team, including **Jenny** and **Csilla**, and all the enablers from the **Kavli cleanroom team**. Your clear commitment and expertise have been fundamental for our device fabrication and experiments in our unique and exceptional lab facilities.

To maintain the vital symbiosis between my body and mind, the role of sports has been paramount. Physical activity has not only aided in processing the challenges of academic life but also allowed me to savor the simple joys of existence. I am profoundly indebted to my sport companions who have shared these endeavors with me. From the early days when **Qing** and **Christian** joined me for runs through the Ackerdijk, turning 10 kilometers into a piece of cake, to the establishment of a QuTech-wide running group with **Luc**, and numerous others, and our jaunty participation in events like the Leiden Marathon and the Bruggenloop in Rotterdam, these moments have been a source of strength and delight in my journey.

What are legs without arms? **Isidora** and the other QuantumTinkers, including **Kostas**, **Johanna**, and **Anton**, answered that question by introducing me to the world of bouldering. With their enthusiasm, climbing became a weekly habit for me, and we even took our skills to Fontainebleau, creating unforgettable memories on the rocks. I am grateful for their friendship and the adventurous spirit they brought to my life.

To my other faithful companions **Melanie, Cyril, Murad, Matthias, Vinicius, Haowen, Kolja, Philipp, Alex, Frederik, Gabriel, Sven, Sebastian, Julian** and **Sabrina**: Thank you!

My current character is undeniably a superposition of countless influences and inputs from friends, colleagues, sports buddies, and even disquieters. However, at the core of my heart and soul, it is my family who has provided unwavering guidance and served as my anchor throughout the past decade of scientific pursuit. I extend my heartfelt thanks to my brother **Sebastian**, my parents **Helga** and **Alfred**, and all of my extended family. A special mention is reserved for my grandparents, **Gerd**, **Magda**, **Elke**, and **Dieter**, who not only generously provided me with waffles, dried fruits, and sweets but also extended their kindness to my colleagues, and motorized me with 4 wheels. I am also deeply grateful to my uncle **Otger**, who helped me in refitting my sailing boat, ensuring that I would always feel at home in the Netherlands.

CURRICULUM VITÆ

Lukas Johannes SPLITTHOFF

20-06-1995 Born in Wesel, Germany.

EDUCATION

2005–2014 Secondary School
Anne Frank-Gesamtschule, Havixbeck

2014–2017 Bachelor of Sciences in Physics
University of Münster
Thesis: Control of quasi-phase-matching of high-harmonics in a spatially structured plasma
Supervisor: Prof. Dr. H. Zacharias

2017–2019 Master of Sciences in Physics
Université Paris-Saclay (2017–2018)
Internship: Development of NbTiN quantum circuits resilient to magnetic field
Supervisor: Dr. D. Vion

University of Münster (2018–2019)
Thesis: Tantalum pentoxide based nanophotonic platform for integrated quantum technology
Supervisor: Prof. Dr. C. Schuck

2019–2024 PhD in Physics
QuTech, Delft University of Technology
Thesis: Gate-tunable kinetic inductances for superconducting circuits
Promotor: Prof. dr. ir. L.P. Kouwenhoven
Copromotor: Dr. C.K. Andersen

LIST OF CONTRIBUTIONS

During my time as PhD student at the Delft University of Technology, spanning from September 2019 to April 2024, I had the privilege of contributing to a diverse range of academic publications. In total, my research efforts culminated in 11 publications covering the engineering of gate tunable superconducting circuits, the investigation of Andreev bound states in nanowire Josephson junctions and the development of nano-photonic circuits.

My dissertation primarily focuses on three pivotal publications featured in the topical chapters, which align closely with the central theme of my dissertation, the engineering of gate-tunable inductances for superconducting circuits. These chapters delve into gate-tunable kinetic inductances, gate-tunable parametric amplifiers and a gate-tunable bosonic Su-Schrieffer-Heeger chain.

1. **L.J. Splitthoff**, M.A. Wolff, T. Grottke, C. Schuck, "Tantalum pentoxide nanophotonic circuits for integrated quantum technology", *Opt. Express 28, 11921-11932 (2020)*
2. M.A. Wolff, S. Vogel, **L.J. Splitthoff**, C. Schuck, "Superconducting nanowire single-photon detectors integrated with tantalum pentoxide waveguides", *Sci Rep 10, 17170 (2020)*
3. J. J. Wesdorp, L. Grünhaupt, A. Vaartjes, M. Pita-Vidal, A. Bargerbos, **L.J. Splitthoff**, P. Krogstrup, B. van Heck, G. de Lange, "Dynamical polarization of the fermion parity in a nanowire Josephson junction", *Phys. Rev. Lett. 131, 117001 (2023)*
4. **L.J. Splitthoff**, A. Bargerbos, L. Grünhaupt, M. Pita-Vidal, J.J. Wesdorp, Y. Liu, A. Kou, C.K. Andersen, B. van Heck, "Gate-tunable kinetic inductance in proximitized nanowires", *Phys. Rev. Applied 18, 024074 (2022)*
5. A. Bargerbos, M. Pita-Vidal, R. Žitko, J. Ávila, **L.J. Splitthoff**, L. Grünhaupt, J.J. Wesdorp, C.K. Andersen, Y. Liu, L.P. Kouwenhoven, R. Aguado, A. Kou, B. van Heck, "Singlet-doublet transitions of a quantum dot Josephson junction detected in a transmon circuit", *PRX QUANTUM 3, 030311 (2022)*
6. A. Bargerbos, M. Pita-Vidal, R. Žitko, **L.J. Splitthoff**, L. Grünhaupt, J.J. Wesdorp, Y. Liu, L.P. Kouwenhoven, R. Aguado, C.K. Andersen, A. Kou, B. van Heck, "Spectroscopy of spin-split Andreev levels in a quantum dot with superconducting leads", *Phys. Rev. Lett. 131, 097001 (2023)*
7. J.J. Wesdorp, F.J. Matute-Cañadas, A. Vaartjes, L. Grünhaupt, T. Laeven, S. Roelofs, **L.J. Splitthoff**, M. Pita-Vidal, A. Bargerbos, D.J. van Woerkom, P. Krogstrup, L.P. Kouwenhoven, C.K. Andersen, A. Levy Yeyati, B. van Heck, G. de Lange, "Microwave spectroscopy of interacting Andreev spins", *Phys. Rev. B 109, 045302 (2024)*
8. A. Bargerbos, **L.J. Splitthoff**, M. Pita-Vidal, J.J. Wesdorp, Y. Liu, P. Krogstrup, L.P. Kouwenhoven, C.K. Andersen, L. Grünhaupt, "Mitigation of quasiparticle loss in superconducting qubits by phonon scattering", *Phys. Rev. Applied 19, 024014 (2023)*

9. M. Pita-Vidal, A. Bargerbos, R. Žitko, **L.J. Splitthoff**, L. Grünhaupt, J.J. Wesdorp, Y. Liu, L.P. Kouwenhoven, R. Aguado, B. van Heck, A. Kou, C.K. Andersen, “Direct manipulation of a superconducting spin qubit strongly coupled to a transmon qubit”, *Nat. Phys. 19, 1110–1115 (2023)*
10. M. Pita-Vidal, J.J. Wesdorp, **L.J. Splitthoff**, A. Bargerbos, Y. Liu, L.P. Kouwenhoven, C.K. Andersen, "Strong tunable coupling between two distant superconducting spin qubits", *arXiv 2307.15654 (2023)*
11. **L.J. Splitthoff**, J.J. Wesdorp, M. Pita-Vidal, A. Bargerbos, C.K. Andersen, "Gate-tunable kinetic inductance parametric amplifier", *Phys. Rev. Applied 21.014052 (2024)*
12. **L.J. Splitthoff**, Miguel Carrera Belo, Guliuxin Jin, Yu Li, Eliska Greplova, Christian Kraglund Andersen, "Phase transition in a gate-tunable bosonic Su-Schrieffer-Heeger chain", (in preparation) (2024)

PATENT APPLICATION

1. **L.J.Splitthoff**, C.K. Andersen, "Microwave devices comprising a tunable nonlinear kinetic inductance element", Pending patent application filed to Dutch Patent Office (March 2023)

CONFERENCE CONTRIBUTIONS

1. **L.J. Splitthoff**, A. Bargerbos, L. Grünhaupt, J.J. Wesdorp, M. Pita-Vidal, J. Kroll, Y. Liu, P. Krogstrup, L.P. Kouwenhoven, A. Kou, B. van Heck, "Measurement of microwave impedance of proximitized nanowire using resonators" (*talk*), APS March meeting, March 2021 (online)
2. **L.J. Splitthoff**, A. Bargerbos, L. Grünhaupt, J.J. Wesdorp, M. Pita-Vidal, Y. Liu, A. Kou, C.K. Andersen, B. van Heck, "Gate-tunable kinetic inductance in proximitized nanowires" (*talk*), APS March meeting, March 2022 (Chicago)
3. **L.J. Splitthoff**, A. Bargerbos, L. Grünhaupt, J.J. Wesdorp, M. Pita-Vidal, Y. Liu, A. Kou, C.K. Andersen, B. van Heck, "Gate-tunable kinetic inductance in proximitized nanowires" (*poster*), CRC183 International Conference on "Entangled States of Matter", May 2022 (Berlin)
4. **L.J. Splitthoff**, A. Bargerbos, L. Grünhaupt, J.J. Wesdorp, M. Pita-Vidal, Y. Liu, A. Kou, C.K. Andersen, B. van Heck, "Gate-tunable kinetic inductance in proximitized nanowires" (*talk*), DPG Spring Meeting of the Condensed Matter Section, September 2022 (Regensburg)
5. **L.J. Splitthoff**, J.J. Wesdorp, M. Pita-Vidal, A. Bargerbos, C.K. Andersen, "Gate-tunable kinetic inductance parametric amplifier" (*talk*), APS March meeting, March 2023 (Las Vegas)
6. **L.J. Splitthoff**, J.J. Wesdorp, M. Pita-Vidal, A. Bargerbos, C.K. Andersen, "Gate-tunable kinetic inductance parametric amplifier" (*poster*), SQA conference, July 2023 (Munich)

7. **L.J. Splitthoff**, Miguel Carrera Belo, Guliuxin Jin, Yu Li, Eliska Greplova, Christian Kraglund Andersen, "Phase transition in a gate-tunable bosonic Su-Schrieffer-Heeger chain" (talk), APS March meeting, March 2024 (Minneapolis)
8. **L.J. Splitthoff**, Miguel Carrera Belo, Guliuxin Jin, Yu Li, Eliska Greplova, Christian Kraglund Andersen, "Phase transition in a gate-tunable bosonic Su-Schrieffer-Heeger chain" (talk), DPG Spring Meeting of the Condensed Matter Section, March 2024 (Berlin)

EXTRA-CURRICULAR ACTIVITIES

1. **Referee** for Physical Review Letters, Physical Review Applied, Physical Review Research, Optics Express, and Optics Continuum
2. **Teaching assistant** for lecture "Quantum Hardware II" of the Applied Science Master program (2022,2023)
3. Supervision of 3 **Master students** during their nine month long Masters End Projects
4. Member of the **Onderdeelcommissie** (OdC, "personnel committee") of QuTech (Jul 2022 - Oct 2023)
5. Member of the **Health and Well-being initiative** of QuTech (2023)
6. Contribution to the **Kavli Newsletter** Fall 2021, Self-Interview with Lukas Splitthoff presenting the research of the group and addressing issues such as the housing problem for students
7. Coordination of the participation of the **QuTech runners group** in several local running competitions (Oct 2021, Dec 2022, Dec 2023)
8. Organisation of a **QuTech broadcasting station** for the online APS March Meeting 2021 (Mar 2021)

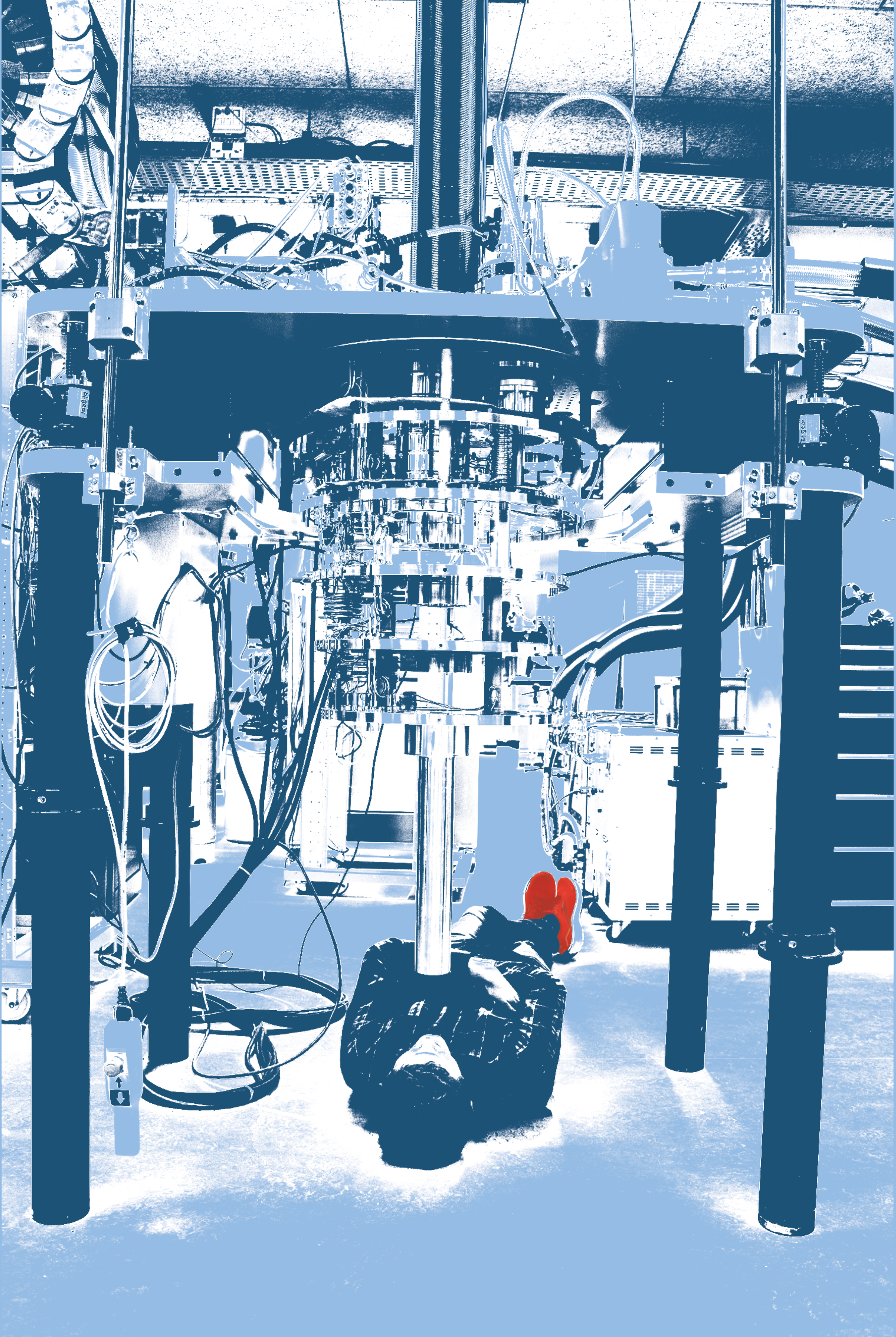

BIBLIOGRAPHY

[1] J. Koch, T. M. Yu, J. Gambetta, A. A. Houck, D. I. Schuster, J. Majer, A. Blais, M. H. Devoret, S. M. Girvin, and R. J. Schoelkopf, “Charge-insensitive qubit design derived from the cooper pair box”, Phys. Rev. A **76**, 042319 (2007).

[2] W. C. Smith, A. Kou, X. Xiao, U. Vool, and M. H. Devoret, “Superconducting circuit protected by two-cooper-pair tunneling”, npj Quantum Information **6**, 8 (2020).

[3] D. J. Parker, M. Savytskyi, W. Vine, A. Laucht, T. Duty, A. Morello, A. L. Grimsmo, and J. J. Pla, “Degenerate Parametric Amplification via Three-Wave Mixing Using Kinetic Inductance”, Phys. Rev. Applied **17**, 034064 (2022).

[4] L. Ruf, C. Puglia, T. Elalaily, G. D. Simoni, F. Joint, M. Berke, J. Koch, A. Iorio, S. Khorshidian, P. Makk, S. Gasparinetti, S. Csonka, W. Belzig, M. Cuoco, F. Giazotto, E. Scheer, and A. D. Bernardo, “Gate-control of superconducting current: mechanisms, parameters and technological potential”, arXiv, 2302.13734 (2024).

[5] G. de Lange, B. van Heck, A. Bruno, D. J. van Woerkom, A. Geresdi, S. R. Plissard, E. P. A. M. Bakkers, A. R. Akhmerov, and L. DiCarlo, “Realization of microwave quantum circuits using hybrid superconducting-semiconducting nanowire Josephson elements”, Phys. Rev. Lett. **115**, 127002 (2015).

[6] L. Casparis, N. J. Pearson, A. Kringhøj, T. W. Larsen, F. Kuemmeth, J. Nygård, P. Krogstrup, K. D. Petersson, and C. M. Marcus, “Voltage-controlled superconducting quantum bus”, Phys. Rev. B **99**, 085434 (2019).

[7] T. W. Larsen, K. D. Petersson, F. Kuemmeth, T. S. Jespersen, P. Krogstrup, J. Nygård, and C. M. Marcus, “Semiconductor-Nanowire-Based Superconducting Qubit”, Phys. Rev. Lett. **115**, 127001 (2015).

[8] L. J. Splitthoff, A. Bargerbos, L. Grünhaupt, M. Pita-Vidal, J. J. Wesdorp, Y. Liu, A. Kou, C. K. Andersen, and B. van Heck, “Gate-tunable kinetic inductance in proximitized nanowires”, Phys. Rev. Appl. **18**, 024074 (2022).

[9] Y. Oreg, G. Refael, and F. von Oppen, “Helical Liquids and Majorana Bound States in Quantum Wires”, Phys. Rev. Lett. **105**, 177002 (2010).

[10] R. M. Lutchyn, J. D. Sau, and S. Das Sarma, “Majorana Fermions and a Topological Phase Transition in Semiconductor-Superconductor Heterostructures”, Phys. Rev. Lett. **105**, 077001 (2010).

[11] L. J. Splitthoff, J. J. Wesdorp, M. Pita-Vidal, A. Bargerbos, Y. Liu, and C. K. Andersen, “Gate-tunable kinetic inductance parametric amplifier”, Phys. Rev. Appl. **21**, 014052 (2024).

[12] L. J. Splitthoff, “Gate-tunable kinetic inductances for superconducting circuits: data and code”, 4TUdatabase, 10.4121/1f759383-0b33-454f-afa7-936f02e4f0d2 (2024).

[13] A. Korolev, V. Shulga, and S. Tarapov, “Extra-low power consumption amplifier based on hemt in unsaturated mode for use at subkelvin ambient temperatures”, Cryogenics **60**, 76–79 (2014).

[14] L. N. Factory, *Datasheet LNF-LNC4_8C*, (2022) https://lownoisefactory.com/wp-content/uploads/2022/03/lnf-lnc4_8c.pdfd, (accessed: 27.09.2023).

[15] J. Aumentado, “Superconducting parametric amplifiers: the state of the art in Josephson parametric amplifiers”, IEEE Microwave Magazine **21**, 45–59 (2020).

[16] B. Yurke, L. R. Corruccini, P. G. Kaminsky, L. W. Rupp, A. D. Smith, A. H. Silver, R. W. Simon, and E. A. Whittaker, “Observation of parametric amplification and deamplification in a Josephson parametric amplifier”, Phys. Rev. A **39**, 2519–2533 (1989).

[17] M. A. Castellanos-Beltran and K. W. Lehnert, “Widely tunable parametric amplifier based on a superconducting quantum interference device array resonator”, Applied Physics Letters **91**, 083509 (2007).

[18] T. Yamamoto, K. Inomata, M. Watanabe, K. Matsuba, T. Miyazaki, W. D. Oliver, Y. Nakamura, and J. S. Tsai, “Flux-driven Josephson parametric amplifier”, Applied Physics Letters **93**, 042510 (2008).

[19] M. A. Castellanos-Beltran, K. D. Irwin, G. C. Hilton, L. R. Vale, and K. W. Lehnert, “Amplification and squeezing of quantum noise with a tunable Josephson metamaterial”, Nature Physics **4**, 929–931 (2008).

[20] L. Zhong, E. P. Menzel, R. D. Candia, P. Eder, M. Ihmig, A. Baust, M. Haeberlein, E. Hoffmann, K. Inomata, T. Yamamoto, Y. Nakamura, E. Solano, F. Deppe, A. Marx, and R. Gross, “Squeezing with a flux-driven Josephson parametric amplifier”, New Journal of Physics **15**, 125013 (2013).

[21] X. Zhou, V. Schmitt, P. Bertet, D. Vion, W. Wustmann, V. Shumeiko, and D. Esteve, “High-gain weakly nonlinear flux-modulated Josephson parametric amplifier using a squid array”, Phys. Rev. B **89**, 214517 (2014).

[22] D. J. Parker, M. Savytskyi, W. Vine, A. Laucht, T. Duty, A. Morello, A. L. Grimsmo, and J. J. Pla, “Degenerate parametric amplification via three-wave mixing using kinetic inductance”, Phys. Rev. Appl. **17**, 034064 (2022).

[23] V. Sivak, N. Frattini, V. Joshi, A. Lingenfelter, S. Shankar, and M. Devoret, “Kerr-free three-wave mixing in superconducting quantum circuits”, Phys. Rev. Appl. **11**, 054060 (2019).

[24] D. Ezenkova, D. Moskalev, N. Smirnov, A. Ivanov, A. Matanin, V. Polozov, V. Echeistov, E. Malevannaya, A. Samoylov, E. Zikiy, and I. Rodionov, “Broadband SNAIL parametric amplifier with microstrip impedance transformer”, Applied Physics Letters **121**, 232601 (2022).

[25] G. Butseraen, A. Ranadive, N. Aparicio, K. Rafsanjani Amin, A. Juyal, M. Esposito, K. Watanabe, T. Taniguchi, N. Roch, F. Lefloch, and J. Renard, “A gate-tunable graphene Josephson parametric amplifier”, Nature Nanotechnology **17**, 1153–1158 (2022).

[26] J. Sarkar, K. V. Salunkhe, S. Mandal, S. Ghatak, A. H. Marchawala, I. Das, K. Watanabe, T. Taniguchi, R. Vijay, and M. M. Deshmukh, “Quantum-noise-limited microwave amplification using a graphene Josephson junction”, Nature Nanotechnology **17**, 1147–1152 (2022).

[27] D. Phan, P. Falthansl-Scheinecker, U. Mishra, W. M. Strickland, D. Langone, J. Shabani, and A. P. Higginbotham, “Semiconductor quantum-limited amplifier”, arXiv (2022).

[28] M. Khalifa and J. Salfi, “Nonlinearity and parametric amplification of superconducting nanowire resonators in magnetic field”, Phys. Rev. Appl. **19**, 034024 (2023).

[29] M. Xu, R. Cheng, Y. Wu, G. Liu, and H. X. Tang, “Magnetic field-resilient quantum-limited parametric amplifier”, PRX Quantum **4**, 010322 (2023).

[30] W. Vine, M. Savytskyi, A. Vaartjes, A. Kringhøj, D. Parker, J. Slack-Smith, T. Schenkel, K. Mølmer, J. C. McCallum, B. C. Johnson, A. Morello, and J. J. Pla, “In situ amplification of spin echoes within a kinetic inductance parametric amplifier”, Science Advances **9**, eadg1593 (2023).

[31] J. Y. Mutus, T. C. White, R. Barends, Y. Chen, Z. Chen, B. Chiaro, A. Dunsworth, E. Jeffrey, J. Kelly, A. Megrant, C. Neill, P. J. J. O’Malley, P. Roushan, D. Sank, A. Vainsencher, J. Wenner, K. M. Sundqvist, A. N. Cleland, and J. M. Martinis, “Strong environmental coupling in a Josephson parametric amplifier”, Applied Physics Letters **104**, 263513 (2014).

[32] J. Grebel, A. Bienfait, E. Dumur, H.-S. Chang, M.-H. Chou, C. R. Conner, G. A. Peairs, R. G. Povey, Y. P. Zhong, and A. N. Cleland, “Flux-pumped impedance-engineered broadband Josephson parametric amplifier”, Applied Physics Letters **118**, 142601 (2021).

[33] Y. Lu, W. Xu, Q. Zuo, J. Pan, X. Wei, J. Jiang, Z. Li, K. Zhang, T. Guo, S. Wang, C. Cao, H. Wang, W. Xu, G. Sun, and P. Wu, “Broadband Josephson parametric amplifier using lumped-element transmission line impedance matching architecture”, Applied Physics Letters **120**, 082601 (2022).

[34] T. e. a. White, “Readout of a quantum processor with high dynamic range Josephson parametric amplifiers”, Applied Physics Letters **122**, 014001, 10.1063/5.0127375 (2023).

[35] B. Qing, L. B. Nguyen, X. Liu, H. Ren, W. P. Livingston, N. Goss, A. Hajr, T. Chistolini, Z. Pedramrazi, D. I. Santiago, J. Luo, and I. Siddiqi, “Broadband cpw-based impedance-transformed Josephson parametric amplifier”, arXiv, 2310.17084 (2023).

[36] C. Macklin, K. O’Brien, D. Hover, M. E. Schwartz, V. Bolkhovsky, X. Zhang, W. D. Oliver, and I. Siddiqi, “A near quantum-limited Josephson traveling-wave parametric amplifier”, Science **350**, 307–310 (2015).

[37] M. Esposito, A. Ranadive, L. Planat, and N. Roch, “Perspective on traveling wave microwave parametric amplifiers”, Applied Physics Letters **119**, 120501 (2021).

[38] V. E. Manucharyan, E. Boaknin, M. Metcalfe, R. Vijay, I. Siddiqi, and M. Devoret, “Microwave bifurcation of a Josephson junction: embedding-circuit requirements”, Phys. Rev. B **76**, 014524 (2007).

[39] Y.-X. Wang and A. A. Clerk, “Non-hermitian dynamics without dissipation in quantum systems”, Phys. Rev. A **99**, 063834 (2019).

[40] C. Eichler and A. Wallraff, “Controlling the dynamic range of a Josephson parametric amplifier”, EPJ Quantum Technology **1**, 2 (2014).

[41] A. Roy and M. Devoret, “Introduction to parametric amplification of quantum signals with Josephson circuits”, Comptes Rendus Physique **17**, Quantum microwaves / Micro-ondes quantiques, 740–755 (2016).

[42] J. Y. Mutus, T. C. White, E. Jeffrey, D. Sank, R. Barends, J. Bochmann, Y. Chen, Z. Chen, B. Chiaro, A. Dunsworth, J. Kelly, A. Megrant, C. Neill, P. J. J. O’Malley, P. Roushan, A. Vainsencher, J. Wenner, I. Siddiqi, R. Vijay, A. N. Cleland, and J. M. Martinis, “Design and characterization of a lumped element single-ended superconducting microwave parametric amplifier with on-chip flux bias line”, Applied Physics Letters **103**, 122602, 10.1063/1.4821136 (2013).

[43] L. Planat, R. Dassonneville, J. P. Martínez, F. Foroughi, O. Buisson, W. Hasch-Guichard, C. Naud, R. Vijay, K. Murch, and N. Roch, “Understanding the saturation power of Josephson parametric amplifiers made from squid arrays”, Phys. Rev. Appl. **11**, 034014 (2019).

[44] V. V. Sivak, S. Shankar, G. Liu, J. Aumentado, and M. H. Devoret, “Josephson array-mode parametric amplifier”, Phys. Rev. Appl. **13**, 024014 (2020).

[45] P. Winkel, I. Takmakov, D. Rieger, L. Planat, W. Hasch-Guichard, L. Grünhaupt, N. Maleeva, F. Foroughi, F. Henriques, K. Borisov, J. Ferrero, A. V. Ustinov, W. Wernsdorfer, N. Roch, and I. M. Pop, “Nondegenerate parametric amplifiers based on dispersion-engineered Josephson-junction arrays”, Phys. Rev. Appl. **13**, 024015 (2020).

[46] D. Phan, P. Falthansl-Scheinecker, U. Mishra, W. Strickland, D. Langone, J. Shabani, and A. Higginbotham, “Gate-tunable superconductor-semiconductor parametric amplifier”, Phys. Rev. Appl. **19**, 064032 (2023).

[47] A. Vaartjes, A. Kringhøj, W. Vine, T. Day, A. Morello, and J. J. Pla, “Strong microwave squeezing above 1 Tesla and 1 Kelvin”, arXiv, 2311.07968 (2023).

[48] S. Frasca, C. Roy, G. Beaulieu, and P. Scarlino, “Three-wave mixing quantum-limited kinetic inductance parametric amplifier operating at 6 Tesla and near 1 Kelvin”, arXiv, 2312.00748 (2023).

[49] C. M. Caves, “Quantum limits on noise in linear amplifiers”, Phys. Rev. D **26**, 1817–1839 (1982).

[50] C. K. Andersen, A. Kamal, N. A. Masluk, I. M. Pop, A. Blais, and M. H. Devoret, “Quantum Versus Classical Switching Dynamics of Driven Dissipative Kerr Resonators”, Phys. Rev. Applied **13**, 044017 (2020).

[51] A. Narla, K. M. Sliwa, M. Hatridge, S. Shankar, L. Frunzio, R. J. Schoelkopf, and M. H. Devoret, “Wireless Josephson amplifier”, Applied Physics Letters **104**, 232605, 10.1063/1.4883373 (2014).

[52] G. Liu, T.-C. Chien, X. Cao, O. Lanes, E. Alpern, D. Pekker, and M. Hatridge, “Josephson parametric converter saturation and higher order effects”, Applied Physics Letters **111**, 202603 (2017).

[53] C. Liu, T.-C. Chien, M. Hatridge, and D. Pekker, "Optimizing Josephson-ring-modulator-based Josephson parametric amplifiers via full hamiltonian control", Phys. Rev. A **101**, 042323 (2020).

[54] A. A. Clerk, M. H. Devoret, S. M. Girvin, F. Marquardt, and R. J. Schoelkopf, "Introduction to quantum noise, measurement, and amplification", Rev. Mod. Phys. **82**, 1155–1208 (2010).

[55] L. N. Factory, *Datasheet LNF-LNC4_8F*, (2023) https://lownoisefactory.com/wp-content/uploads/2023/03/lnf-lnc4_8f.pdf, (accessed: 27.09.2023).

[56] L. N. Factory, *Datasheet LNF-LNR4_8art*, (2016) https://quantummicrowave.com/wp-content/uploads/2016/09/lnf-lnr4_8art.pdf, (accessed: 27.09.2023).

[57] MITEQ, *Amplifiers 2009*, (2009) https://nardamiteq.com/docs/MITEQ_Amplifier-AFS.JS_c41.pdf, (accessed: 27.09.2023).

[58] S. Krinner, S. Storz, P. Kurpiers, P. Magnard, J. Heinsoo, R. Keller, J. Lütolf, C. Eichler, and A. Wallraff, "Engineering cryogenic setups for 100-qubit scale superconducting circuit systems", EPJ Quantum Technology **6**, 2 (2019).

[59] J. Gambetta, A. Blais, D. I. Schuster, A. Wallraff, L. Frunzio, J. Majer, M. H. Devoret, S. M. Girvin, and R. J. Schoelkopf, "Qubit-photon interactions in a cavity: measurement-induced dephasing and number splitting", Phys. Rev. A **74**, 042318 (2006).

[60] C. C. Bultink, B. Tarasinski, N. Haandbæk, S. Poletto, N. Haider, D. J. Michalak, A. Bruno, and L. DiCarlo, "General method for extracting the quantum efficiency of dispersive qubit readout in circuit qed", Applied Physics Letters **112**, 092601 (2018).

[61] S. Boutin, D. M. Toyli, A. V. Venkatramani, A. W. Eddins, I. Siddiqi, and A. Blais, "Effect of higher-order nonlinearities on amplification and squeezing in Josephson parametric amplifiers", Phys. Rev. Appl. **8**, 054030 (2017).

[62] R. Meservey and P. M. Tedrow, "Measurements of the Kinetic Inductance of Superconducting Linear Structures", Journal of Applied Physics **40**, 2028–2034 (1969).

[63] A. J. Annunziata, D. F. Santavicca, L. Frunzio, G. Catelani, M. J. Rooks, A. Frydman, and D. E. Prober, "Tunable superconducting nanoinductors", Nanotechnology **21**, 445202 (2010).

[64] J. Zmuidzinas, "Superconducting Microresonators: Physics and Applications", Annual Review of Condensed Matter Physics **3**, 169–214 (2012).

[65] N. Samkharadze, A. Bruno, P. Scarlino, G. Zheng, D. P. DiVincenzo, L. DiCarlo, and L. M. K. Vandersypen, "High-Kinetic-Inductance Superconducting Nanowire Resonators for Circuit QED in a Magnetic Field", Phys. Rev. Applied **5**, 044004 (2016).

[66] D. Niepce, J. Burnett, and J. Bylander, "High Kinetic Inductance NbN Nanowire Superinductors", Phys. Rev. Applied **11**, 044014 (2019).

[67] L. Grünhaupt, M. Spiecker, N. Gusenkova Daria and Maleeva, S. T. Skacel, I. Takmakov, F. Valenti, P. Winkel, H. Rotzinger, W. Wernsdorfer, A. V. Ustinov, and I. M. Pop, "Granular aluminium as a superconducting material for high-impedance quantum circuits", Nature Materials **18**, 816–819 (2019).

[68] P. Kamenov, W.-S. Lu, K. Kalashnikov, T. DiNapoli, M. T. Bell, and M. E. Gershenson, "Granular Aluminum Meandered Superinductors for Quantum Circuits", Phys. Rev. Applied **13**, 054051 (2020).

[69] D. M. Mironov A. Yu. and Silevitch, M. V. Postolova S. V. and Burdastyh, T. Proslier, T. I. Baturina, T. F. Rosenbaum, and V. M. Vinokur, "Supercapacitance and superinductance of TiN and NbTiN films in the vicinity of superconductor-to-insulator transition", Scientific Reports **11**, 16181 (2021).

[70] B. A. Mazin, "Microwave kinetic inductance detectors", PhD thesis (California Institute of Technology, 2005).

[71] A. Blais, S. M. Girvin, and W. D. Oliver, "Quantum information processing and quantum optics with circuit quantum electrodynamics", Nature Physics **16**, 247–256 (2020).

[72] M. Kjaergaard, M. E. Schwartz, J. Braumüller, P. Krantz, J. I.-J. Wang, S. Gustavsson, and W. D. Oliver, "Superconducting Qubits: Current State of Play", Annual Review of Condensed Matter Physics **11**, 369–395 (2020).

[73] A. Blais, A. L. Grimsmo, S. M. Girvin, and A. Wallraff, "Circuit quantum electrodynamics", Rev. Mod. Phys. **93**, 025005 (2021).

[74] Y.-H. Lin, L. B. Nguyen, N. Grabon, J. San Miguel, N. Pankratova, and V. E. Manucharyan, "Demonstration of Protection of a Superconducting Qubit from Energy Decay", Phys. Rev. Lett. **120**, 150503 (2018).

[75] L. B. Nguyen, Y.-H. Lin, A. Somoroff, R. Mencia, N. Grabon, and V. E. Manucharyan, "High-Coherence Fluxonium Qubit", Phys. Rev. X **9**, 041041 (2019).

[76] T. M. Hazard, A. Gyenis, A. Di Paolo, A. T. Asfaw, S. A. Lyon, A. Blais, and A. A. Houck, "Nanowire Superinductance Fluxonium Qubit", Phys. Rev. Lett. **122**, 010504 (2019).

[77] A. Gyenis, P. S. Mundada, A. Di Paolo, T. M. Hazard, X. You, D. I. Schuster, J. Koch, A. Blais, and A. A. Houck, "Experimental Realization of a Protected Superconducting Circuit Derived from the 0–π Qubit", PRX Quantum **2**, 010339 (2021).

[78] A. Gyenis, A. Di Paolo, J. Koch, A. Blais, A. A. Houck, and D. I. Schuster, "Moving beyond the Transmon: Noise-Protected Superconducting Quantum Circuits", PRX Quantum **2**, 030101 (2021).

[79] H. Zhang, S. Chakram, T. Roy, N. Earnest, Y. Lu, Z. Huang, D. K. Weiss, J. Koch, and D. I. Schuster, "Universal Fast-Flux Control of a Coherent, Low-Frequency Qubit", Phys. Rev. X **11**, 011010 (2021).

[80] P. Krantz, M. Kjaergaard, F. Yan, T. P. Orlando, S. Gustavsson, and W. D. Oliver, "A quantum engineer's guide to superconducting qubits", Applied Physics Reviews **6**, 021318 (2019).

[81] A. Palacios-Laloy, F. Nguyen, F. Mallet, D. Bertet P. and Vion, and D. Esteve, "Tunable Resonators for Quantum Circuits", Journal of Low Temperature Physics **151**, 1034–1042 (2008).

[82] O. Naaman, M. O. Abutaleb, C. Kirby, and M. Rennie, "On-chip Josephson junction microwave switch", Applied Physics Letters **108**, 112601 (2016).

[83] M. R. Vissers, J. Hubmayr, M. Sandberg, S. Chaudhuri, C. Bockstiegel, and J. Gao, "Frequency-tunable superconducting resonators via nonlinear kinetic inductance", Applied Physics Letters **107**, 062601 (2015).

[84] M. Xu, X. Han, W. Fu, C.-L. Zou, and H. X. Tang, "Frequency-tunable high-q superconducting resonators via wireless control of nonlinear kinetic inductance", Applied Physics Letters **114**, 192601 (2019).

[85] S. Mahashabde, E. Otto, D. Montemurro, S. de Graaf, S. Kubatkin, and A. Danilov, "Fast Tunable High-Q-Factor Superconducting Microwave Resonators", Phys. Rev. Applied **14**, 044040 (2020).

[86] M. W. A. de Moor, J. D. S. Bommer, D. Xu, G. W. Winkler, A. E. Antipov, A. Bargerbos, G. Wang, N. van Loo, R. L. M. O. het Veld, S. Gazibegovic, D. Car, J. A. Logan, M. Pendharkar, J. S. Lee, E. P. A. M. Bakkers, C. J. Palmstrøm, R. M. Lutchyn, L. P. Kouwenhoven, and H. Zhang, "Electric field tunable superconductor-semiconductor coupling in Majorana nanowires", New Journal of Physics **20**, 103049 (2018).

[87] A. E. Antipov, A. Bargerbos, G. W. Winkler, B. Bauer, E. Rossi, and R. M. Lutchyn, "Effects of Gate-Induced Electric Fields on Semiconductor Majorana Nanowires", Phys. Rev. X **8**, 031041 (2018).

[88] A. E. G. Mikkelsen, P. Kotetes, P. Krogstrup, and K. Flensberg, "Hybridization at superconductor semiconductor interfaces", Phys. Rev. X **8**, 031040 (2018).

[89] G. W. Winkler, A. E. Antipov, B. van Heck, A. A. Soluyanov, L. I. Glazman, M. Wimmer, and R. M. Lutchyn, "Unified numerical approach to topological semiconductor-superconductor heterostructures", Phys. Rev. B **99**, 245408 (2019).

[90] J. Kroll, F. Borsoi, K. van der Enden, W. Uilhoorn, D. de Jong, M. Quintero-Pérez, D. van Woerkom, A. Bruno, S. Plissard, D. Car, E. Bakkers, M. Cassidy, and L. Kouwenhoven, "Magnetic-field-resilient superconducting coplanar-waveguide resonators for hybrid circuit quantum electrodynamics experiments", Phys. Rev. Appl. **11**, 064053 (2019).

[91] A. Kringhøj, T. W. Larsen, O. Erlandsson, W. Uilhoorn, J. G. Kroll, M. Hesselberg, R. P. G. McNeil, P. Krogstrup, L. Casparis, C. M. Marcus, and K. D. Petersson, "Magnetic-Field-Compatible Superconducting Transmon Qubit", Phys. Rev. Applied **15**, 054001 (2021).

[92] R. M. Lutchyn, E. P. A. M. Bakkers, P. Kouwenhoven L. P. and Krogstrup, and Y. Marcus C. M. and Oreg, "Majorana zero modes in superconductor-semiconductor heterostructures", Nature Reviews Materials **3**, 52–68 (2018).

[93] X. Mi, J. V. Cady, D. M. Zajac, J. Stehlik, L. F. Edge, and J. R. Petta, "Circuit quantum electrodynamics architecture for gate-defined quantum dots in silicon", Applied Physics Letters **110**, 043502 (2017).

[94] M. S. Khalil, M. J. A. Stoutimore, F. C. Wellstood, and K. D. Osborn, "An analysis method for asymmetric resonator transmission applied to superconducting devices", Journal of Applied Physics **111**, 054510, 10.1063/1.3692073 (2012).

[95] S. Probst, F. B. Song, P. A. Bushev, A. V. Ustinov, and M. Weides, "Efficient and robust analysis of complex scattering data under noise in microwave resonators", Review of Scientific Instruments **86**, 024706 (2015).

[96] A. Bruno, G. de Lange, S. Asaad, K. L. van der Enden, N. K. Langford, and L. DiCarlo, "Reducing intrinsic loss in superconducting resonators by surface treatment and deep etching of silicon substrates", Applied Physics Letters **106**, 182601 (2015).

[97] E. A. Tholén, A. Ergül, E. M. Doherty, F. M. Weber, F. Grégis, and D. B. Haviland, "Nonlinearities and parametric amplification in superconducting coplanar waveguide resonators", Applied Physics Letters **90**, 253509 (2007).

[98] L. Grünhaupt, N. Maleeva, S. T. Skacel, M. Calvo, F. Levy-Bertrand, A. V. Ustinov, H. Rotzinger, A. Monfardini, G. Catelani, and I. M. Pop, "Loss Mechanisms and Quasiparticle Dynamics in Superconducting Microwave Resonators Made of Thin-Film Granular Aluminum", Phys. Rev. Lett. **121**, 117001 (2018).

[99] E. A. Tholén, A. Ergül, K. Stannigel, C. Hutter, and D. B. Haviland, "Parametric amplification with weak-link nonlinearity in superconducting microresonators", Phys. Scr. **T137**, 014019 (2009).

[100] R. Vijay, M. H. Devoret, and I. Siddiqi, "Invited Review Article: The Josephson bifurcation amplifier", Review of Scientific Instruments **80**, 111101 (2009).

[101] R. Simons, "Coplanar Waveguide Circuits, Components, and Systems", in (John Wiley & Sons, Ltd, 2001) Chap. 8, pp. 203–236.

[102] D. C. Mattis and J. Bardeen, "Theory of the Anomalous Skin Effect in Normal and Superconducting Metals", Phys. Rev. **111**, 412 (1958).

[103] M. Tinkham, *Introduction to Superconductivity* (Dover Publications, 2004).

[104] J. Shen, G. W. Winkler, F. Borsoi, S. Heedt, V. Levajac, J.-Y. Wang, D. van Driel, D. Bouman, S. Gazibegovic, R. L. M. Op Het Veld, D. Car, J. A. Logan, M. Pendharkar, C. J. Palmstrøm, E. P. A. M. Bakkers, L. P. Kouwenhoven, and B. van Heck, "Full parity phase diagram of a proximitized nanowire island", Phys. Rev. B **104**, 045422 (2021).

[105] D. Phan, J. Senior, A. Ghazaryan, M. Hatefipour, W. M. Strickland, J. Shabani, M. Serbyn, and A. P. Higginbotham, "Detecting Induced $p \pm ip$ Pairing at the Al-InAs Interface with a Quantum Microwave Circuit", Phys. Rev. Lett. **128**, 107701 (2022).

[106] T. Kiendl, F. von Oppen, and P. W. Brouwer, "Proximity-induced gap in nanowires with a thin superconducting shell", Phys. Rev. B **100**, 035426 (2019).

[107] C. Reeg, D. Loss, and J. Klinovaja, "Finite-size effects in a nanowire strongly coupled to a thin superconducting shell", Phys. Rev. B **96**, 125426 (2017).

[108] C. Reeg, D. Loss, and J. Klinovaja, "Metallization of a rashba wire by a superconducting layer in the strong-proximity regime", Phys. Rev. B **97**, 165425 (2018).

[109] B. D. Woods, T. D. Stanescu, and S. Das Sarma, "Effective theory approach to the Schrödinger-Poisson problem in semiconductor Majorana devices", Phys. Rev. B **98**, 035428 (2018).

[110] G. C. Ménard, F. K. Malinowski, D. Puglia, D. I. Pikulin, T. Karzig, B. Bauer, P. Krogstrup, and C. M. Marcus, "Suppressing quasiparticle poisoning with a voltage-controlled filter", Phys. Rev. B **100**, 165307 (2019).

[111]V. Mourik, K. Zuo, S. M. Frolov, S. R. Plissard, E. P. A. M. Bakkers, and L. P. Kouwenhoven, “Signatures of Majorana Fermions in Hybrid Superconductor-Semiconductor Nanowire Devices”, Science **336**, 1003–1007 (2012).

[112]Ö. Gül, D. J. van Woerkom, I. van Weperen, D. Car, S. R. Plissard, E. P. A. M. Bakkers, and L. P. Kouwenhoven, “Towards high mobility InSb nanowire devices”, Nanotechnology **26**, 215202 (2015).

[113]I. van Weperen, B. Tarasinski, D. Eeltink, V. S. Pribiag, S. R. Plissard, E. P. A. M. Bakkers, L. P. Kouwenhoven, and M. Wimmer, “Spin-orbit interaction in InSb nanowires”, Phys. Rev. B **91**, 201413(R) (2015).

[114]S. M. Albrecht, A. P. Higginbotham, M. Madsen, F. Kuemmeth, T. S. Jespersen, J. Nygård, P. Krogstrup, and C. M. Marcus, “Exponential protection of zero modes in Majorana islands”, Nature **531**, 206–209 (2016).

[115]F. K. Malinowski, L. Han, D. de Jong, J.-Y. Wang, C. G. Prosko, G. Badawy, S. Gazibegovic, Y. Liu, P. Krogstrup, E. P. A. M. Bakkers, L. P. Kouwenhoven, and J. V. Koski, “Radio-frequency C-V measurements with sub-attofarad sensitivity”, arXiv, 2110.03257 (2021).

[116]S. Ahn, H. Pan, B. Woods, T. D. Stanescu, and S. Das Sarma, “Estimating disorder and its adverse effects in semiconductor Majorana nanowires”, Phys. Rev. Materials **5**, 124602 (2021).

[117]W. Wustmann and V. Shumeiko, “Parametric resonance in tunable superconducting cavities”, Phys. Rev. B **87**, 184501 (2013).

[118]P. Krogstrup, N. L. B. Ziino, S. Chang W. and Albrecht, M. H. Madsen, E. Johnson, J. Nygård, C. M. Marcus, and T. S. Jespersen, “Epitaxy of semiconductor-superconductor nanowires”, Nature Materials **14**, 400–406 (2015).

[119]D. Flanigan, *Resonator*, (2021) https://github.com/danielflanigan/resonator.git.

[120]D. M. Pozar, “Microwave engineering”, in (Fourth edition. Hoboken, NJ : Wiley, 2012).

[121]L. J. Swenson, P. K. Day, B. H. Eom, H. G. Leduc, N. Llombart, C. M. McKenney, O. Noroozian, and J. Zmuidzinas, “Operation of a titanium nitride superconducting microresonator detector in the nonlinear regime”, Journal of Applied Physics **113**, 104501 (2013).

[122]B. Abdo, F. Schackert, M. Hatridge, C. Rigetti, and M. Devoret, “Josephson amplifier for qubit readout”, Applied Physics Letters **99**, 162506 (2011).

[123]R. Vijay, D. H. Slichter, and I. Siddiqi, “Observation of quantum jumps in a superconducting artificial atom”, Phys. Rev. Lett. **106**, 110502 (2011).

[124]P. Krantz, A. Bengtsson, M. Simoen, S. Gustavsson, V. Shumeiko, W. D. Oliver, C. M. Wilson, P. Delsing, and J. Bylander, “Single-shot read-out of a superconducting qubit using a Josephson parametric oscillator”, Nature Communications **7**, 11417 (2016).

[125]T. Walter, P. Kurpiers, S. Gasparinetti, P. Magnard, A. Poto čnik, Y. Salathé, M. Pechal, M. Mondal, M. Oppliger, C. Eichler, and A. Wallraff, “Rapid high-fidelity single-shot dispersive readout of superconducting qubits”, Phys. Rev. Appl. **7**, 054020 (2017).

[126] X. Mi, M. Benito, S. Putz, D. M. Zajac, J. M. Taylor, G. Burkard, and J. R. Petta, “A coherent spin–photon interface in silicon”, Nature **555**, 599–603 (2018).

[127] F. Borjans, X. G. Croot, X. Mi, M. J. Gullans, and J. R. Petta, “Resonant microwave-mediated interactions between distant electron spins”, Nature **577**, 195–198 (2020).

[128] T. Kobayashi, J. Salfi, C. Chua, J. van der Heijden, M. G. House, D. Culcer, W. D. Hutchison, B. C. Johnson, J. C. McCallum, H. Riemann, N. V. Abrosimov, P. Becker, H.-J. Pohl, M. Y. Simmons, and S. Rogge, “Engineering long spin coherence times of spin–orbit qubits in silicon”, Nature Materials **20**, 38–42 (2021).

[129] S. G. J. Philips, M. T. Mądzik, S. V. Amitonov, S. L. de Snoo, M. Russ, N. Kalhor, C. Volk, W. I. L. Lawrie, D. Brousse, L. Tryputen, B. P. Wuetz, A. Sammak, M. Veldhorst, G. Scappucci, and L. M. K. Vandersypen, “Universal control of a six-qubit quantum processor in silicon”, Nature **609**, 919–924 (2022).

[130] A. Mills, C. Guinn, M. Feldman, A. Sigillito, M. Gullans, M. Rakher, J. Kerckhoff, C. Jackson, and J. Petta, “High-fidelity state preparation, quantum control, and readout of an isotopically enriched silicon spin qubit”, Phys. Rev. Appl. **18**, 064028 (2022).

[131] M. Pita-Vidal, A. Bargerbos, R. Žitko, L. J. Splitthoff, L. Grünhaupt, J. J. Wesdorp, Y. Liu, L. P. Kouwenhoven, R. Aguado, B. van Heck, A. Kou, and C. K. Andersen, “Direct manipulation of a superconducting spin qubit strongly coupled to a transmon qubit”, Nature Physics **19**, 1110–1150 (2023).

[132] M. Pita-Vidal, J. J. Wesdorp, L. J. Splitthoff, A. Bargerbos, Y. Liu, L. P. Kouwenhoven, and C. K. Andersen, “Strong tunable coupling between two distant superconducting spin qubits”, arXiv, 2307.15654 (2023).

[133] T. Dvir, G. Wang, N. van Loo, C.-X. Liu, G. P. Mazur, A. Bordin, S. L. D. ten Haaf, J.-Y. Wang, D. van Driel, F. Zatelli, X. Li, F. K. Malinowski, S. Gazibegovic, G. Badawy, E. P. A. M. Bakkers, M. Wimmer, and L. P. Kouwenhoven, “Realization of a minimal Kitaev chain in coupled quantum dots”, Nature **614**, 10.1038/s41586-022-05585-1 (2023).

[134] J. I.-J. Wang, D. Rodan-Legrain, L. Bretheau, D. L. Campbell, B. Kannan, D. Kim, M. Kjaergaard, P. Krantz, G. O. Samach, F. Yan, J. L. Yoder, K. Watanabe, T. Taniguchi, T. P. Orlando, S. Gustavsson, P. Jarillo-Herrero, and W. D. Oliver, “Coherent control of a hybrid superconducting circuit made with graphene-based van der waals heterostructures”, Nature Nanotechnology **14**, 120–125 (2019).

[135] E. Portolés, S. Iwakiri, G. Zheng, P. Rickhaus, T. Taniguchi, K. Watanabe, T. Ihn, K. Ensslin, and F. K. de Vries, “A tunable monolithic squid in twisted bilayer graphene”, Nature Nanotechnology **17**, 1159–1164 (2022).

[136] L. Casparis, M. R. Connolly, M. Kjaergaard, N. J. Pearson, A. Kringhøj, T. W. Larsen, F. Kuemmeth, T. Wang, C. Thomas, S. Gronin, G. C. Gardner, M. J. Manfra, C. M. Marcus, and K. D. Petersson, “Superconducting gatemon qubit based on a proximitized two-dimensional electron gas”, Nature Nanotechnology **13**, 915–919 (2018).

[137] D. Phan, J. Senior, A. Ghazaryan, M. Hatefipour, W. M. Strickland, J. Shabani, M. Serbyn, and A. P. Higginbotham, “Detecting induced $p \pm ip$ pairing at the al-inas interface with a quantum microwave circuit”, Phys. Rev. Lett. **128**, 107701 (2022).

[138]W. M. Strickland, B. H. Elfeky, J. O. Yuan, W. F. Schiela, P. Yu, D. Langone, M. G. Vavilov, V. E. Manucharyan, and J. Shabani, “Superconducting resonators with voltage-controlled frequency and nonlinearity”, Phys. Rev. Appl. **19**, 034021 (2023).

[139]J. G. Kroll, W. Uilhoorn, K. L. van der Enden, D. de Jong, K. Watanabe, T. Taniguchi, S. Goswami, M. C. Cassidy, and L. P. Kouwenhoven, “Magnetic field compatible circuit quantum electrodynamics with graphene Josephson junctions”, Nature Communications **9**, 4615 (2018).

[140]F. E. Schmidt, M. D. Jenkins, K. Watanabe, T. Taniguchi, and G. A. Steele, “A ballistic graphene superconducting microwave circuit”, Nature Communications **9**, 4069 (2018).

[141]M. Mergenthaler, A. Nersisyan, A. Patterson, M. Esposito, A. Baumgartner, C. Schönenberger, G. A. D. Briggs, E. A. Laird, and P. J. Leek, “Circuit quantum electrodynamics with carbon-nanotube-based superconducting quantum circuits”, Phys. Rev. Appl. **15**, 064050 (2021).

[142]M. Meyer, C. Déprez, T. R. van Abswoude, I. N. Meijer, D. Liu, C.-A. Wang, S. Karwal, S. Oosterhout, F. Borsoi, A. Sammak, N. W. Hendrickx, G. Scappucci, and M. Veldhorst, “Electrical control of uniformity in quantum dot devices”, Nano Letters **23**, 2522–2529 (2023).

[143]J. Krause, C. Dickel, E. Vaal, M. Vielmetter, J. Feng, R. Bounds, G. Catelani, J. M. Fink, and Y. Ando, “Magnetic field resilience of three-dimensional transmons with thin-film Al/AlO$_x$/Al Josephson junctions approaching 1 t”, Phys. Rev. Appl. **17**, 034032 (2022).

[144]D. Rieger, S. Günzler, M. Spiecker, A. Nambisan, W. Wernsdorfer, and I. M. Pop, “Fano interference in microwave resonator measurements”, Phys. Rev. Appl. **20**, 014059 (2023).

[145]C. K. Andersen, A. Remm, S. Lazar, S. Krinner, N. Lacroix, G. J. Norris, M. Gabureac, C. Eichler, and A. Wallraff, “Repeated quantum error detection in a surface code”, Nature Physics **16**, 875–880 (2020).

[146]H. Gehring, M. Blaicher, W. Hartmann, and W. H. P. Pernice, “Python based open source design framework for integrated nanophotonic and superconducting circuitry with 2d-3d-hybrid integration”, OSA Continuum **2**, 3091–3101 (2019).

[147]R. Barends, J. Kelly, A. Megrant, D. Sank, E. Jeffrey, Y. Chen, Y. Yin, B. Chiaro, J. Mutus, C. Neill, P. O’Malley, P. Roushan, J. Wenner, T. C. White, A. N. Cleland, and J. M. Martinis, “Coherent Josephson qubit suitable for scalable quantum integrated circuits”, Phys. Rev. Lett. **111**, 080502 (2013).

[148]A. Kringhøj, L. Casparis, M. Hell, T. W. Larsen, F. Kuemmeth, M. Leijnse, K. Flensberg, P. Krogstrup, J. Nygård, K. D. Petersson, and C. M. Marcus, “Anharmonicity of a superconducting qubit with a few-mode Josephson junction”, Phys. Rev. B **97**, 060508 (2018).

[149]W. P. Su, J. R. Schrieffer, and A. J. Heeger, “Solitons in polyacetylene”, Phys. Rev. Lett. **42**, 1698–1701 (1979).

[150]M. Z. Hasan and C. L. Kane, “Colloquium: topological insulators”, Rev. Mod. Phys. **82**, 3045–3067 (2010).

[151] J. K. Asbóth, L. Oroszlány, and A. Pályi, *A short course on topological insulators* (Springer International Publishing, 2016).

[152] N. Batra and G. Sheet, "Physics with coffee and doughnuts", Resonance **25**, 765–786 (2020).

[153] N. Delnour, A. Bissonnette, H. Eleuch, R. MacKenzie, and M. Hilke, "Scanning qubit probe of edge states in a topological insulator", Physics Letters A **466**, 128716 (2023).

[154] G. Jin and E. Greplova, "Topological entanglement stabilization in superconducting quantum circuits", Phys. Rev. Res. **5**, 023088 (2023).

[155] F. Mei, G. Chen, L. Tian, S.-L. Zhu, and S. Jia, "Robust quantum state transfer via topological edge states in superconducting qubit chains", Phys. Rev. A **98**, 012331 (2018).

[156] E. Kim, X. Zhang, V. S. Ferreira, J. Banker, J. K. Iverson, A. Sipahigil, M. Bello, A. González-Tudela, M. Mirhosseini, and O. Painter, "Quantum electrodynamics in a topological waveguide", Phys. Rev. X **11**, 011015 (2021).

[157] C. Vega, M. Bello, D. Porras, and A. González-Tudela, "Qubit-photon bound states in topological waveguides with long-range hoppings", Phys. Rev. A **104**, 053522 (2021).

[158] L.-N. Zheng, X. Yi, and H.-F. Wang, "Engineering a phase-robust topological router in a dimerized superconducting-circuit lattice with long-range hopping and chiral symmetry", Phys. Rev. Appl. **18**, 054037 (2022).

[159] D.-A. Galeano, X.-X. Zhang, and J. Mahecha, "Topological circuit of a versatile non-hermitian quantum system", Science China Physics, Mechanics & Astronomy **65**, 217211 (2021).

[160] M. Zelenayova and E. J. Bergholtz, "Non-hermitian extended midgap states and bound states in the continuum", arXiv, 2310.18270 (2023).

[161] I.-F. Io, C.-Y. Huang, J.-S. You, H.-C. Chang, and H.-c. Kao, "Quasi-hermitian extended ssh models", arXiv, 2308.09874 (2023).

[162] M. Kiczynski, S. K. Gorman, H. Geng, M. B. Donnelly, Y. Chung, Y. He, J. G. Keizer, and M. Y. Simmons, "Engineering topological states in atom-based semiconductor quantum dots", Nature **606**, 694–699 (2022).

[163] S. de Léséleuc, V. Lienhard, P. Scholl, D. Barredo, S. Weber, N. Lang, H. P. Büchler, T. Lahaye, and A. Browaeys, "Observation of a symmetry-protected topological phase of interacting bosons with rydberg atoms", Science **365**, 775–780 (2019).

[164] V. D. Pham, Y. Pan, S. C. Erwin, F. von Oppen, K. Kanisawa, and S. Fölsch, "Topological states in dimerized quantum-dot chains created by atom manipulation", Phys. Rev. B **105**, 125418 (2022).

[165] R.-J. Ren, Y.-H. Lu, Z.-K. Jiang, J. Gao, W.-H. Zhou, Y. Wang, Z.-Q. Jiao, X.-W. Wang, A. S. Solntsev, and X.-M. Jin, "Topologically protecting squeezed light on a photonic chip", Photon. Res. **10**, 456–464 (2022).

[166] Y. Liu, W. Cao, W. Chen, H. Wang, L. Yang, and X. Zhang, "Fully integrated topological electronics", Scientific Reports **12**, 13410 (2022).

[167] T. Iizuka, H. Yuan, Y. Mita, A. Higo, S. Yasunaga, and M. Ezawa, "Experimental demonstration of position-controllable topological interface states in high-frequency Kitaev topological integrated circuits", Communications Physics **6**, 279 (2023).

[168] X. Zhou, W. Zhang, H. Sun, and X. Zhang, "Observation of flat-band localization and topological edge states induced by effective strong interactions in electrical circuit networks", Phys. Rev. B **107**, 035152 (2023).

[169] S. John and J. Wang, "Quantum electrodynamics near a photonic band gap: photon bound states and dressed atoms", Phys. Rev. Lett. **64**, 2418–2421 (1990).

[170] O. Dmytruk and M. Schirò, "Controlling topological phases of matter with quantum light", Communications Physics **5**, 271 (2022).

[171] Y. Ke, J. Huang, W. Liu, Y. Kivshar, and C. Lee, "Topological inverse band theory in waveguide quantum electrodynamics", arXiv, 2301.05481 (2023).

[172] M. Mirhosseini, E. Kim, V. S. Ferreira, M. Kalaee, A. Sipahigil, A. J. Keller, and O. Painter, "Superconducting metamaterials for waveguide quantum electrodynamics", Nature Communications **9**, 3706 (2018).

[173] J. Puertas Martínez, S. Léger, N. Gheeraert, R. Dassonneville, L. Planat, F. Foroughi, Y. Krupko, O. Buisson, C. Naud, W. Hasch-Guichard, S. Florens, I. Snyman, and N. Roch, "A tunable Josephson platform to explore many-body quantum optics in circuit-QED", npj Quantum Information **5**, 19 (2019).

[174] M. Bello, G. Platero, J. I. Cirac, and A. González-Tudela, "Unconventional quantum optics in topological waveguide qed", Science Advances **5**, eaaw0297 (2019).

[175] J. D. Brehm, A. N. Poddubny, A. Stehli, T. Wolz, H. Rotzinger, and A. V. Ustinov, "Waveguide bandgap engineering with an array of superconducting qubits", npj Quantum Materials **6**, 10 (2021).

[176] V. S. Ferreira, J. Banker, A. Sipahigil, M. H. Matheny, A. J. Keller, E. Kim, M. Mirhosseini, and O. Painter, "Collapse and revival of an artificial atom coupled to a structured photonic reservoir", Phys. Rev. X **11**, 041043 (2021).

[177] W. Nie and Y.-x. Liu, "Bandgap-assisted quantum control of topological edge states in a cavity", Phys. Rev. Res. **2**, 012076 (2020).

[178] M. Scigliuzzo, G. Calajò, F. Ciccarello, D. Perez Lozano, A. Bengtsson, P. Scarlino, A. Wallraff, D. Chang, P. Delsing, and S. Gasparinetti, "Controlling Atom-Photon Bound States in an Array of Josephson-Junction Resonators", Phys. Rev. X **12**, 031036 (2022).

[179] C. H. Lee, S. Imhof, C. Berger, F. Bayer, J. Brehm, L. W. Molenkamp, T. Kiessling, and R. Thomale, "Topolectrical circuits", Communications Physics **1**, 39 (2018).

[180] T. Zhang, J. Hu, and X. Qiu, "Topological waveguide quantum sensors", arXiv, 2311.01370 (2023).

[181] P. Pakkiam, N. P. Kumar, M. Pletyukhov, and A. Fedorov, "Qubit-controlled directional edge states in waveguide qed", arXiv, 2212.00108 (2023).

[182] Y. Wang, H. Xu, X. Deng, T. Liew, S. Ghosh, and Q. Xiong, "Topological single photon emission from quantum emitter chains", arXiv, 2303.15807 (2023).

[183] X. Zhang, E. Kim, D. K. Mark, S. Choi, and O. Painter, “A superconducting quantum simulator based on a photonic-bandgap metamaterial”, Science **379**, 278–283 (2023).

[184] A. H. Karamlou, J. Braumüller, Y. Yanay, A. Di Paolo, P. M. Harrington, B. Kannan, D. Kim, M. Kjaergaard, A. Melville, S. Muschinske, B. M. Niedzielski, A. Vepsäläinen, R. Winik, J. L. Yoder, M. Schwartz, C. Tahan, T. P. Orlando, S. Gustavsson, and W. D. Oliver, “Quantum transport and localization in 1d and 2d tight-binding lattices”, npj Quantum Information **8**, 35 (2022).

[185] M. A. Beck, M. Selvanayagam, A. Carniol, S. Cairns, and C. P. Mancini, “Wideband Josephson Parametric Isolator”, arXiv, 2212.08563 (2023).

[186] M. R. Vissers, J. Hubmayr, M. Sandberg, S. Chaudhuri, C. Bockstiegel, and J. Gao, “Frequency-tunable superconducting resonators via nonlinear kinetic inductance”, Applied Physics Letters **107**, 062601 (2015).

[187] X. Dai, D. Tennant, R. Trappen, A. Martinez, D. Melanson, M. Yurtalan, Y. Tang, S. Novikov, J. Grover, S. Disseler, J. Basham, R. Das, D. Kim, A. Melville, B. Niedzielski, S. Weber, J. Yoder, D. Lidar, and A. Lupascu, “Calibration of flux crosstalk in large-scale flux-tunable superconducting quantum circuits”, PRX Quantum **2**, 040313 (2021).

[188] C. N. Barrett, A. H. Karamlou, S. E. Muschinske, I. T. Rosen, J. Braumüller, R. Das, D. K. Kim, B. M. Niedzielski, M. Schuldt, K. Serniak, M. E. Schwartz, J. L. Yoder, T. P. Orlando, S. Gustavsson, J. A. Grover, and W. D. Oliver, “Learning-based calibration of flux crosstalk in transmon qubit arrays”, Phys. Rev. Appl. **20**, 024070 (2023).

[189] A. Hertel, M. Eichinger, L. O. Andersen, D. M. van Zanten, S. Kallatt, P. Scarlino, A. Kringhøj, J. M. Chavez-Garcia, G. C. Gardner, S. Gronin, M. J. Manfra, A. Gyenis, M. Kjaergaard, C. M. Marcus, and K. D. Petersson, “Gate-tunable transmon using selective-area-grown superconductor-semiconductor hybrid structures on silicon”, Phys. Rev. Appl. **18**, 034042 (2022).

[190] I. Mondragon-Shem, T. L. Hughes, J. Song, and E. Prodan, “Topological criticality in the chiral-symmetric aiii class at strong disorder”, Phys. Rev. Lett. **113**, 046802 (2014).

[191] B. Pérez-González, M. Bello, Á. Gómez-León, and G. Platero, “Interplay between long-range hopping and disorder in topological systems”, Phys. Rev. B **99**, 035146 (2019).

[192] Z. Xia, J. Huo, Z. Li, J. Ying, Y. Liu, X.-Y. Tang, Y. Wang, M. Chen, D. Pan, S. Zhang, Q. Liu, T. Li, L. Li, K. He, J. Zhao, R. Shang, and H. Zhang, “Gate-compatible circuit qed in a three-dimensional cavity architecture”, arXiv, 2311.07337 (2023).

[193] T. W. Larsen, M. E. Gershenson, L. Casparis, A. Kringhøj, N. J. Pearson, R. P. G. McNeil, F. Kuemmeth, P. Krogstrup, K. D. Petersson, and C. M. Marcus, “Parity-protected superconductor-semiconductor qubit”, Phys. Rev. Lett. **125**, 056801 (2020).

[194] X.-J. Luo, X.-H. Pan, C.-X. Liu, and X. Liu, “Higher-order topological phases emerging from su-schrieffer-heeger stacking”, Phys. Rev. B **107**, 045118 (2023).

[195] M. Zaimi, C. Boudreault, N. Baspin, N. Delnour, H. Eleuch, R. MacKenzie, and M. Hilke, “Detecting topological edge states with the dynamics of a qubit”, Physics Letters A **388**, 127035 (2021).

[196] Y. Hadad, J. C. Soric, A. B. Khanikaev, and A. Alù, “Self-induced topological protection in nonlinear circuit arrays”, Nature Electronics **1**, 178–182 (2018).

[197] J. M. P. Nair, “Nonlinear construction of topological ssh models”, arXiv, 2211.16440 (2022).

[198] M. J. Rice and E. J. Mele, “Elementary excitations of a linearly conjugated diatomic polymer”, Phys. Rev. Lett. **49**, 1455–1459 (1982).

[199] Y. Zhang, Y.-Q. Ge, and Y.-x. Liu, “Simulation of Kitaev model using one-dimensional chain of superconducting qubits and environmental effect on topological states”, arXiv, 2302.03834 (2023).

[200] U. Vool and M. Devoret, “Introduction to quantum electromagnetic circuits”, International Journal of Circuit Theory and Applications **45**, 897–934 (2017).

[201] M. Scollon and M. P. Kennett, “Persistence of chirality in the su-schrieffer-heeger model in the presence of on-site disorder”, Phys. Rev. B **101**, 144204 (2020).

[202] S. Huang, B. Lienhard, G. Calusine, A. Vepsäläinen, J. Braumüller, D. K. Kim, A. J. Melville, B. M. Niedzielski, J. L. Yoder, B. Kannan, T. P. Orlando, S. Gustavsson, and W. D. Oliver, “Microwave package design for superconducting quantum processors”, PRX Quantum **2**, 020306 (2021).

[203] M. C. Cassidy, A. Bruno, S. Rubbert, M. Irfan, J. Kammhuber, R. N. Schouten, A. R. Akhmerov, and L. P. Kouwenhoven, “Demonstration of an ac Josephson junction laser”, Science **355**, 939–942 (2017).

[204] W. Uilhoorn, J. G. Kroll, D. de Jong, D. J. van Woerkom, J. Nygard, P. Krogstrup, L. P. Kouwenhoven, and M. C. Cassidy, “A semiconductor nanowire Josephson junction laser”, in preparation, 2021.

[205] M. Kjaergaard, M. E. Schwartz, J. Braumüller, P. Krantz, J. I.-J. Wang, S. Gustavsson, and W. D. Oliver, “Superconducting qubits: current state of play”, Annual Review of Condensed Matter Physics **11**, 369–395 (2020).

[206] F. A. et al., “Quantum supremacy using a programmable superconducting processor”, Nature **574**, 505–510 (2019).

[207] O. Mukhanov, A. Kirichenko, C. Howington, J. Walter, M. Hutchings, I. Vernik, D. Yohannes, K. Dodge, A. Ballard, B. L. T. Plourde, A. Opremcak, C. .-. Liu, and R. McDermott, “Scalable quantum computing infrastructure based on superconducting electronics”, 2019 IEEE International Electron Devices Meeting (IEDM), 31.2.1–31.2.4 (2019).

[208] J. Bourassa, F. Beaudoin, J. M. Gambetta, and A. Blais, “Josephson-junction-embedded transmission-line resonators: from Kerr medium to in-line transmon”, Phys. Rev. A **86**, 013814 (2012).

[209] A. D. Armour, M. P. Blencowe, E. Brahimi, and A. J. Rimberg, “Universal quantum fluctuations of a cavity mode driven by a Josephson junction”, Phys. Rev. Lett. **111**, 247001 (2013).

[210] S. Meister, M. Mecklenburg, V. Gramich, J. T. Stockburger, J. Ankerhold, and B. Kubala, “Resonators coupled to voltage-biased Josephson junctions: from linear response to strongly driven nonlinear oscillations”, Phys. Rev. B **92**, 174532 (2015).

[211] S. H. Simon and N. R. Cooper, “Theory of the Josephson junction laser”, Phys. Rev. Lett. **121**, 027004 (2018).

[212] S. Jebari, F. Blanchet, A. Grimm, D. Hazra, R. Albert, P. Joyez, D. Vion, D. Estève, F. Portier, and M. Hofheinz, “Near-quantum-limited amplification from inelastic cooper-pair tunnelling”, Nature Electronics **1**, 223–227 (2018).

[213] M. Hofheinz, F. Portier, Q. Baudouin, P. Joyez, D. Vion, P. Bertet, P. Roche, and D. Esteve, “Bright side of the coulomb blockade”, Phys. Rev. Lett. **106**, 217005 (2011).

[214] M. Westig, B. Kubala, O. Parlavecchio, Y. Mukharsky, C. Altimiras, P. Joyez, D. Vion, P. Roche, D. Esteve, M. Hofheinz, M. Trif, P. Simon, J. Ankerhold, and F. Portier, “Emission of nonclassical radiation by inelastic cooper pair tunneling”, Phys. Rev. Lett. **119**, 137001 (2017).

[215] A. Grimm, F. Blanchet, R. Albert, J. Leppäkangas, S. Jebari, D. Hazra, F. Gustavo, J.-L. Thomassin, E. Dupont-Ferrier, F. Portier, and M. Hofheinz, “Bright on-demand source of antibunched microwave photons based on inelastic cooper pair tunneling”, Phys. Rev. X **9**, 021016 (2019).

[216] C. Rolland, A. Peugeot, S. Dambach, M. Westig, B. Kubala, Y. Mukharsky, C. Altimiras, H. le Sueur, P. Joyez, D. Vion, P. Roche, D. Esteve, J. Ankerhold, and F. Portier, “Antibunched photons emitted by a dc-biased Josephson junction”, Phys. Rev. Lett. **122**, 186804 (2019).

[217] S. Hart, Z. Cui, G. Ménard, M. Deng, A. E. Antipov, R. M. Lutchyn, P. Krogstrup, C. M. Marcus, and K. A. Moler, “Current-phase relations of inas nanowire Josephson junctions: from interacting to multimode regimes”, Phys. Rev. B **100**, 064523 (2019).

[218] B. Dou çot and J. Vidal, “Pairing of cooper pairs in a fully frustrated Josephson-junction chain”, Phys. Rev. Lett. **88**, 227005 (2002).

[219] L. B. Ioffe and M. V. Feigel’man, “Possible realization of an ideal quantum computer in Josephson junction array”, Phys. Rev. B **66**, 224503 (2002).

[220] A. Kitaev, “Protected qubit based on a superconducting current mirror”, arXiv, cond–mat/0609441 (2006).

[221] P. Brooks, A. Kitaev, and J. Preskill, “Protected gates for superconducting qubits”, Phys. Rev. A **87**, 052306 (2013).

[222] P. Campagne-Ibarcq, A. Eickbusch, S. Touzard, E. Zalys-Geller, N. E. Frattini, V. V. Sivak, P. Reinhold, S. Puri, S. Shankar, R. J. Schoelkopf, L. Frunzio, M. Mirrahimi, and M. H. Devoret, “Quantum error correction of a qubit encoded in grid states of an oscillator”, Nature **584**, 368–372 (2020).

[223] M. Pita-Vidal, A. Bargerbos, C.-K. Yang, D. J. van Woerkom, W. Pfaff, N. Haider, P. Krogstrup, L. P. Kouwenhoven, G. de Lange, and A. Kou, “A gate-tunable, field-compatible fluxonium”, arXiv, 1910.07978 (2019).

[224] K. Vogel and H. Risken, “Determination of quasiprobability distributions in terms of probability distributions for the rotated quadrature phase”, Phys. Rev. A **40**, 2847–2849 (1989).

[225] U. Leonhardt and H. Paul, “Realistic optical homodyne measurements and quasiprobability distributions”, Phys. Rev. A **48**, 4598–4604 (1993).

[226] D. T. Smithey, M. Beck, M. G. Raymer, and A. Faridani, “Measurement of the wigner distribution and the density matrix of a light mode using optical homodyne tomography: application to squeezed states and the vacuum”, Phys. Rev. Lett. **70**, 1244–1247 (1993).

[227] M. Hofheinz, H. Wang, M. Ansmann, R. C. Bialczak, E. Lucero, M. Neeley, A. D. O’Connell, D. Sank, J. Wenner, J. M. Martinis, and A. N. Cleland, “Synthesizing arbitrary quantum states in a superconducting resonator”, Nature **459**, 546–549 (2009).

[228] Y. Shalibo, R. Resh, O. Fogel, D. Shwa, R. Bialczak, J. M. Martinis, and N. Katz, “Direct wigner tomography of a superconducting anharmonic oscillator”, Phys. Rev. Lett. **110**, 100404 (2013).

[229] E. Svetitsky, H. Suchowski, R. Resh, Y. Shalibo, J. M. Martinis, and N. Katz, “Hidden two-qubit dynamics of a four-level Josephson circuit”, Nature Communications **5**, 5617 (2014).

[230] M. Reagor, “Superconducting cavities for circuit quantum electrodynamics”, PhD thesis (The school of the thesis, Yale University, Dec. 2015).

[231] K. J. Satzinger, Y. P. Zhong, H.-S. Chang, G. A. Peairs, A. Bienfait, M.-H. Chou, A. Y. Cleland, C. R. Conner, É. Dumur, J. Grebel, I. Gutierrez, B. H. November, R. G. Povey, S. J. Whiteley, D. D. Awschalom, D. I. Schuster, and A. N. Cleland, “Quantum control of surface acoustic-wave phonons”, Nature **563**, 661–665 (2018).

[232] A. Vrajitoarea, Z. Huang, P. Groszkowski, J. Koch, and A. A. Houck, “Quantum control of an oscillator using a stimulated Josephson nonlinearity”, Nature Physics **16**, 211–217 (2020).

[233] J.-C. Besse, S. Gasparinetti, M. C. Collodo, T. Walter, A. Remm, J. Krause, C. Eichler, and A. Wallraff, “Parity detection of propagating microwave fields”, Phys. Rev. X **10**, 011046 (2020).

[234] D. Gottesman, A. Kitaev, and J. Preskill, “Encoding a qubit in an oscillator”, Phys. Rev. A **64**, 012310 (2001).

[235] A. Joshi, K. Noh, and Y. Y. Gao, “Quantum information processing with bosonic qubits in circuit QED”, arXiv, 2008.13471 (2020).

[236] O. Usenko, N. Hoovinakatte, and G. Frossati, *Test report CF-CS110-2PT-2000*, 2019.

[237] G. Batey and G. Teleberg, *Principles of dilution refrigeration - a brief technology guide*, (2015) https://nanoscience.oxinst.com, (accessed: 13.09.2023).

[238] P. Spring, T. Tsunoda, B. Vlastakis, and P. Leek, “Modeling enclosures for large-scale superconducting quantum circuits”, Phys. Rev. Appl. **14**, 024061 (2020).